DIFFUSIONAL GROWTH OF OXIDE SCALES ON COBALT-IRON ALLOYS

DIFFUSIONAL GROWTH OF OXIDE SCALES ON COBALT-IRON ALLOYS

By

PETER MAYER, Dipl. Eng., M. Eng.

A Thesis

Submitted to the School of Graduate Studies

in Partial Fulfilment of the Requirements

for the Degree

Doctor of Philosophy

McMaster University

October, 1973

DOCTOR OF PHILOSOPHY (1973) McMASTER UNIVERSITY
(Metallurgy and Materials Science) Hamilton, Ontario

TITLE: Diffusional Growth of Oxide Scales on Cobalt-Iron Alloys

AUTHOR: Peter Mayer, Dipl. Eng. (Slovak Technical University, Kosice, Czechoslovakia)
M. Eng. (McMaster University, Hamilton, Ontario, Canada)

SUPERVISOR: Professor W.W. Smeltzer

NUMBER OF PAGES: xvii, 207

SCOPE AND CONTENTS:

In this thesis the results of an experimental investigation and theoretical analysis of high temperature oxidation properties of cobalt-iron alloys are presented. Cobalt-iron alloys containing up to 70% iron were subjected to pure oxygen atmospheres with pressures ranging from 10^{-4} to 1 atm at 1200°C. The reaction kinetics, oxide scale morphologies and spatial distributions of the reacting species in the oxidized specimens were determined. It has been established that the reaction is controlled by metal diffusion through the oxide scales separating the reactants. A ternary diffusion model was invoked to describe the high temperature oxidation behaviour of the investigated alloys. The consistency of the model is tested by evaluating the concentration profiles from metal diffusion coefficients and nonstoichiometry of ternary oxides using the Wagner phenomenological equations. The comparison of the results from theoretical calculations and the experimental measurements shows good agreement. This suggests that the theoretical analysis adapted in this work is consistent

with the actual physical and chemical processes governing the oxidation reaction.

ACKNOWLEDGMENTS

I wish to thank my supervisor, Professor W.W. Smeltzer, for having the patience and understanding to allow me to undertake this investigation. His continual suggestions and interest added significantly to the value of my education at McMaster. As a man of rare energy and sensitivity, both to the problems that beset one's personal life and the academic community as a whole, he has shown me a devotion to and creativity in science that I have seldom seen.

Professors J.A. Morrison and D.A.R. Kay are gratefully acknowledged for their helpful suggestions concerning theoretical and experimental aspects of my work as members of my supervisory committee. Professors J.S. Kirkaldy and R. Kelly provided interesting commentary throughout my study and have been especially kind in their interest and encouragement. I thank Dr. A.D. Dalvi for many enlightening discussions and help especially in the early stages of my graduate study.

I am indebted to many of the faculty, post-doctoral fellows, graduate students and technical staff in the Department of Metallurgy and Materials Science for their helpful discussions and aid.

Miss Veronica Komczynski is thanked for typing the final manuscript and Mr. Dave Hodgson for preparing the final illustrations.

The financial support of the Department of Metallurgy and Materials Science of McMaster University in the form of a graduate fellowship and the award of a National Research Council of Canada Bursary allowed me to pursue my studies uninterrupted. The National Research Council of Canada is

acknowledged for its support of the experimental phases of the project in the form of research grants to Dr. W.W. Smeltzer.

Last, but very far from least, I owe a great deal to my wife Tanya, for her long, usually silent suffering over the many years of study, and especially in the last very difficult months. Without her constant support and her practical assistance this research undertaking would never have reached a successful and early conclusion.

TABLE OF CONTENTS

		PAGE
CHAPTER I	INTRODUCTION	1
CHAPTER II	PRINCIPLES OF OXIDATION	4
2.1	Oxide Formation and Growth	4
2.2	Wagner's Theory of Parabolic Oxidation	9
2.3	Oxidation of Alloys	11
CHAPTER III	THEORETICAL ANALYSIS OF DIFFUSION CONTROLLED OXIDATION OF BINARY ALLOYS	16
3.1	Introduction	16
3.2	Theory of Multicomponent Diffusion - Phenomenological Equations	17
3.3	Thermodynamic Stability of the Phases during Oxidation	21
3.4	The Distribution of Cations in the Scales Formed during the Oxidation of Alloys	22
3.4.1	General Presuppositions	22
3 4 2	Co-ordinate Frames and Notation Symbols	23
3.4.3	Formulation of General Equations	26
3.4.4	Summary	32
3.5	Relations between Thermodynamics and Kinetics of Binary Alloys Oxidation	33
3.5.1	Diffusion Paths on Ternary A-B-O Isotherms	34
3.5.2	Internal Oxidation and Alloy-Oxide Interface Stability	39
CHAPTER IV	EXPERIMENTAL DESIGN	42
4.1	Introduction	42
4.2	Requirements on the Experimental System	42
4.3	Preliminary Experiments	43

		PAGE
CHAPTER V	PROPERTIES OF COBALT-IRON-OXYGEN SYSTEM	45
5.1	Introduction	45
5.2	Iron-Oxygen System	45
5.2.1	Defect and Transport Properties of Iron Oxides	45
5.2.2	Oxidation of Iron	49
5.3	Cobalt-Oxygen System	51
5.3.1	Defect and Transport Properties of Cobalt Oxides	51
5.3.2	Oxidation of Cobalt	55
5.4	Cobalt-Iron-Oxygen System	57
5.4.1	Activities and Diffusivities in Co-Fe Alloys	57
5.4.2	Activities, Defect Concentrations and Diffusivities in CoO-FeO	59
5.4.3	Oxidation of Cobalt-Iron Alloys	68
CHAPTER VI	TECHNIQUES AND PROCEDURES OF EXPERIMENTS	71
6.1	Introduction	
6.2	Alloy and Specimen Preparation	71
6.3	Experimental Apparatus	73
6.4	Identification and Analytic Methods	78
6.4.1	Chemical and X-ray Analysis	78
6.4.2	Specimen Preparation for Metallographic and Microprobe Measurements	79
6.4.3	Electrone Probe Microanalysis	79
CHAPTER VII	EXPERIMENTAL RESULTS AND THEIR INTERPRETATION	84
7.1	Introduction	84
7.2	Oxidation Kinetics	84

7.3 Morphological Development of Oxide Scales 111

7.3.1 Characterisation and Topology of External Scales 111

7.3.2 Structures of External Scales Formed at 1 atm Oxygen Pressure 113

7.3.3 Structures of External Scales Formed at 10^{-1} atm Oxygen Pressure 119

7.3.4 Structures of External Scales Formed at 10^{-2} atm Oxygen Pressure 120

7.3.5 Structures of External Scales Formed at 10^{-3} atm Oxygen Pressure 124

7.3.6 Structures of External Scales Formed at 10^{-4} atm Oxygen Pressure 128

7.3.7 Summary - "Oxidation Map" 135

7.4 Concentration Profiles 135

CHAPTER VIII DISCUSSION 151

8.1 Introduction 151

8.2 Analysis of the Experimental Results 151

8.2.1 Oxidation Kinetics 151

8.2.2 Oxidation Modes of Cobalt-Iron Alloys 153

8.2.3 Correlation Between Oxidation Kinetics and Scale Morphologies 154

8.2.4 Composition Paths 155

CHAPTER IX APPLICATION OF THE DIFFUSION MODEL OF BINARY ALLOY OXIDATION TO COBALT-IRON ALLOYS: RESULTS AND DISCUSSION 159

9.1 Introduction 159

9.2 Initial Considerations 159

9.3 Development of Diffusion Equations Describing Concentration Profiles in Cobaltowüstite Scales on Alloys at 1200°C 160

		PAGE
9.4	Numerical Solution	163
9.5	Comparison of Results	166
9.6	Discussion	184
CHAPTER X	CONCLUSIONS	188
APPENDIX A	SUGGESTIONS FOR FUTURE WORK	191
APPENDIX B	ERRORS IN EXPERIMENTS AND CALCULATIONS	192
APPENDIX C	COMPUTER PROGRAM FOR CALCULATIONS OF CONCENTRATION PROFILES IN COBALTOWUSTITE SCALES	195
REFERENCES		201

LIST OF ILLUSTRATIONS

FIGURE	TITLE	PAGE
2-1	Oxidation modes of binary alloys	14
3-1	Co-ordinate frames and notations used in the text	24
3-2	Diffusion model showing the concentration profiles and location of coordinate frames	35
3-3	Schematic representation of an isothermal phase diagram on which is superimposed the "virtual" diffusion path O-Q.	37
3-4	"Virtual" diffusion path which does involve a super-saturation in the alloy	40
5-1	The nonstoichiometry in wüstite, y in $Fe_{1-y}O$, as a function of temperature and partial pressure of oxygen	46
5-2	The Fe-tracer diffusion coefficient as a function of composition and temperature in the wüstite phase	48
5-3	The nonstoichiometry in cobaltous oxide, x in CoO_{1+x}, as a function of temperature and partial pressure of oxygen	52
5-4	Tracer diffusion coefficient of cobalt in CoO as a function of partial pressure of oxygen in temperature range 950° to 1350°C	54
5-5	The oxygen potential phase diagram for Co-Fe-O system at 1200°C	58
5-6	Activity of CoO in contact with metallic phase (Co-Fe alloy) as a function of oxide composition in the system CoO-FeO at 1200°C	61
5-7	Activity of CoO in contact with spinel phase ($(Co,Fe)_3O_4$) as a function of oxide composition in the system CoO-FeO at 1200°C	62

FIGURE	TITLE	PAGE
5-8	Metal vacancy concentration plotted vs. FeO molar fraction in (Co,Fe)O for oxygen pressures ranging from 10^{-9} to 1 atm at 1200°C	64
5-9	Atomic fraction of vacancies per molar fraction of FeO in (Co,Fe)O plotted vs. oxygen pressure	65
5-10	Ratio of tracer diffusion coefficients of Fe^{55} and Co^{60} in single crystal CoO at 1200°C as a function of oxygen potential	69
6-1	Schematic of reaction assembly	75
6-2	Measured relative intensities of X-rays generated by iron and cobalt in Co-Fe alloys at 15 kV	82
6-3	Calculated relative intensities of X-rays generated by iron and cobalt in cobaltowüstite at 15 kV	83
7-1	Oxidation kinetics (10^{0} atm O_2, Co-0÷10% Fe)	85
7-2	Oxidation kinetics (10^{0} atm O_2, Co-20÷70% Fe)	86
7-3	Oxidation kinetics (10^{-1} atm O_2, Co-0÷10% Fe)	87
7-4	Oxidation kinetics (10^{-1} atm O_2, Co-20÷70% Fe)	88
7-5	Oxidation kinetics (10^{-2} atm O_2, Co-0÷10% Fe)	89
7-6	Oxidation kinetics (10^{-2} atm O_2, Co-20÷70% Fe)	90
7-7	Oxidation kinetics (10^{-3} atm O_2, Co-0÷10% Fe)	91
7-8	Oxidation kinetics (10^{-3} atm O_2, Co-20÷70% Fe)	92
7-9	Oxidation kinetics (10^{-4} atm O_2, Co-0÷10% Fe)	93
7-10	Oxidation kinetics (10^{-4} atm O_2, Co-20÷70% Fe)	94
7-11	Parabolic plots (10^{0} atm O_2, Co-0÷10% Fe)	96
7-12	Parabolic plots (10^{0} atm O_2, Co-20÷70% Fe)	97
7-13	Parabolic plots (10^{-1} atm O_2, Co-0÷10% Fe)	98

FIGURE	TITLE	PAGE
7-14	Parabolic plots (10^{-1} atm O_2, Co-20÷70% Fe)	99
7-15	Parabolic plots (10^{-2} atm O_2, Co-0÷10% Fe)	100
7-16	Parabolic plots (10^{-2} atm O_2, Co-20÷70% Fe)	101
7-17	Parabolic plots (10^{-3} atm O_2, Co-0÷10% Fe)	102
7-18	Parabolic plots (10^{-3} atm O_2, Co-20÷70% Fe)	103
7-19	Parabolic plots (10^{-4} atm O_2, Co-0÷10% Fe)	104
7-20	Parabolic plots (10^{-4} atm O_2, Co-20÷70% Fe)	105
7-21	Parabolic oxidation rate constant (k_p) as a function of oxygen pressure and iron concentration in cobalt-iron alloys	110
7-22(a)-(b)	Cross sections of oxide scales formed at 1 atm O_2 (Co-0÷4% Fe)	116
7-22(e)-(h)	Cross sections of oxide scales formed at 1 atm O_2 (Co-6÷20% Fe)	117
7-22(i)-(l)	Cross sections of oxide scales formed at 1 atm O_2 (Co-30÷70% Fe)	118
7-23(a)-(d)	Cross sections of oxide scales formed at 10^{-1} atm O_2 (Co-0÷4% Fe)	121
7-23(e)-(h)	Cross sections of oxide scales formed at 10^{-1} atm O_2 (Co-6÷20% Fe)	122
7-23(i)-(l)	Cross sections of oxide scales formed at 10^{-1} atm O_2 (Co-30÷70% Fe)	123
7-24(a)-(b)	Cross sections of oxide scales formed at 10^{-2} atm O_2 (Co-0÷4% Fe)	125
7-24(e)-(h)	Cross sections of oxide scales formed at 10^{-2} atm O_2 (Co-6÷20% Fe)	126

FIGURE	TITLE	PAGE
7-24(i)-(j)	Cross sections of oxide scales formed at 10^{-2} atm O_2 (Co-40 and 50% Fe)	127
7-25(a)-(b)	Cross sections of oxide scales formed at 10^{-3} atm O_2 (Co-0÷4% Fe)	129
7-25(e)-(h)	Cross sections of oxide scales formed at 10^{-3} atm O_2 (Co-6÷20% Fe)	130
7-25(i)-(l)	Cross sections of oxide scales formed at 10^{-3} atm O_2 (Co-30%÷70% Fe)	131
7-26(a)-(b)	Cross sections of oxide scales formed at 10^{-4} atm O_2 (Co-0÷4% Fe)	132
7-26(e)-(h)	Cross sections of oxide scales formed at 10^{-4} atm O_2 (Co-6%÷20% Fe)	133
7-26(i)-(l)	Cross sections of oxide scales formed at 10^{-4} atm O_2 (Co-30%÷70% Fe)	134
7-27	Types of oxide scales formed on cobalt-iron alloys at 1200°C in oxygen atmospheres	136
7-28	"Oxidation map" for cobalt-iron alloys oxidized in oxygen at 1200°C	137
7-29(a)	Concentration profiles of FeO in CoO-FeO scales (10^{-4} atm O_2, Co-1,4,8% Fe)	140
7-29(b)	Concentration profiles of FeO in CoO-FeO scales (10^{-3} atm O_2, Co-1,4,8% Fe)	141
7-29(c)	Concentration profiles of FeO in CoO-FeO scales (10^{-2} atm O_2, Co-1,4,8% Fe)	142
7-29(d)	Concentration profiles of FeO in CoO-FeO scales (10^{-1} atm O_2, Co-1,4,8% Fe)	143
7-29(e)	Concentration profiles of FeO in CoO-FeO scales (1 atm O_2, Co-1,4,8% Fe)	144

FIGURE	TITLE	PAGE
7-30(a)	Concentration profiles of FeO in CoO-FeO scales (10^{-4} atm O_2, Co-2,6,10% Fe)	145
7-30(b)	Concentration profiles of FeO in CoO-FeO scales (10^{-3} atm O_2, Co-2,6,10% Fe)	146
7-30(c)	Concentration profiles of FeO in CoO-FeO scales (10^{-2} atm O_2, Co-2,6,10% Fe)	147
7-30(d)	Concentration profiles of FeO in CoO-FeO scales (10^{-1} atm O_2, Co-2,6,10% Fe)	148
7-30(e)	Concentration profiles of FeO in CoO-FeO scales (1 atm O_2, Co-2,6,10% Fe)	149
8-1	Schematic plot of composition path on ternary isotherm for the investigated alloys oxidized in oxygen at 10^{-4} to 10^{-3} atm	156
8-2	Schematic plot of composition path on ternary isotherm for the investigated alloys oxidized in oxygen at 10^{-2} to 1 atm	157
9-1	Calculated and measured concentration profiles of FeO in CoO-FeO scales (10^{-4} atm, Co-1,4,8% Fe)	167
9-2	Calculated and measured concendration profiles of FeO in CoO-FeO scales (10^{-3} atm, Co-1,4,8% Fe)	168
9-3	Calculated and measured concentration profiles of FeO in CoO-FeO scales (10^{-2} atm, Co-1,4,8% Fe)	169
9-4	Calculated and measured concentration profiles of FeO in CoO-FeO scales (10^{-1} atm, Co-1,4,8% Fe)	170
9-5	Calculated and measured concentration profiles of FeO in CoO-FeO scales (1 atm, Co-1,4,8% Fe)	171
9-6	Calculated and measured concentration profiles of FeO in CoO-FeO scales (10^{-4} atm, Co-2,6,10% Fe)	172

FIGURE	TITLE	PAGE
9-7	Calculated and measured concentration profiles of FeO in CoO-FeO scales (10^{-3} atm, Co-2,6,10% Fe)	173
9-8	Calculated and measured concentration profiles of FeO in CoO-FeO scales (10^{-2} atm, Co-2,6,10% Fe)	174
9-9	Calculated and measured concentration profiles of FeO in CoO-FeO scales (10^{-1} atm, Co-2,6,10% Fe)	175
9-10	Calculated and measured concentration profiles of FeO in CoO-FeO scales (1 atm, Co-2,6,8% Fe)	176
9-11	Oxygen activity profile in (Co,Fe)O scale formed on Co-10% Fe alloy at 10^{-3} atm O_2	177
9-12	Oxygen activity profile in (Co,Fe)O scale formed on Co-10% Fe alloy at 1 atm O_2	178

LIST OF TABLES

TABLE	TITLE	PAGE
5-1	Parabolic Oxidation Constants of Cobalt	56
5-2	Interdiffusion Coefficients in Co-Fe at 1200°C	59
5-3	Cation and Vacancy Diffusivities and Defect Concentration in CoO_{1+x} at 1200°C	67
5-4	Diffusivities of Co^{60} and Fe^{55} in CoO at 1200°C as a Function of Oxygen Potential	70
6-1	Chemical Compositions of Used Iron and Cobalt	72
6-2	Actual Chemical Composition of Prepared Alloys	74
7-1	Parabolic Oxidation Rate Constants (10^{0}÷10^{-2} atm, Co-0÷10% Fe)	106
7-2	Parabolic Oxidation Rate Constants (10^{-3}÷10^{-4}, Co-0÷10% Fe)	107
7-3	Parabolic Oxidation Rate Constants (10^{0}÷10^{-2} atm, Co-20÷70% Fe)	108
7-4	Parabolic Oxidation Rate Constants (10^{-3}÷10^{-4} atm, Co-20÷70% Fe)	109
7-5	The Comparison of Parabolic Oxidation Rate Constants for Pure Co at 1200°C	112
7-6	Spalling Tendency of Scales Forming on Cobalt-Iron Alloys at 1200°C	114
9-1	Extrapolated Values of ξ at the Oxide-Gas Interface	179

TABLE	TITLE	PAGE
9-2	Iterated Values of ξ at the Alloy-Oxide Interface	179
9-3	Oxygen Activities at the Oxide-Gas Interface (10^{-4} atm)	180
9-4	Oxygen Activities at the Oxide-Gas Interface (10^{-3} atm)	180
9-5	Oxygen Activities at the Oxide-Gas Interface (10^{-2} atm)	181
9-6	Oxygen Activities at the Oxide-Gas Interface (10^{-1} atm)	181
9-7	Oxygen Activities at the Oxide-Gas Interface (1 atm)	182
9-8	The Position of the Maximum in ξ Profile and Corresponding Oxygen Potentials	183
C1	Computer Program Used for Numerical Integrations	198
C2	Computer Output (calculated Profile for Co-10% Fe Alloy at 10^{-3} atm O_2)	200

CHAPTER I

INTRODUCTION

Successful prediction of the application of an alloy under high temperature service conditions requires extensive knowledge of physical, chemical, and mechanical properties of the material and the service conditions to which it will be submitted, e.g. temperature, atmosphere, stress, vibration, etc. Among the properties to be considered most seriously is oxidation and/or corrosion resistance. Therefore, the development of experimental techniques and analytical methods for monitoring the oxidation kinetics and morphological development of oxide scales is a technological necessity. Theoretical understanding of the processes involved is also an important scientific challenge.

The present investigation is part of a broad research project concerning oxidation and sulphidation of pure metals and alloys at high temperatures. The problem of reaction between the metal and environment is studied from both theoretical as well as experimental point of view. In the case of alloy oxidation and sulphidation these two factors are very closely related. Therefore, theoretical analysis of this very complex process is essential, in order to gain an understanding of the experimental results.

The purpose of the present work is the experimental study of the diffusion controlled oxidation of binary alloys and further development of the diffusion model based on the concept of local equilibrium and

multicomponent diffusion. This task involves experimental investigations of the oxidation kinetics, morphological development and compositions of the oxide scales, and theoretical analysis.

Preliminary experiments showed that cobalt-iron alloys (cobalt base alloys are very important structural materials used in aircraft jet engines) satisfy all the conditions of the theoretical model describing the diffusion controlled oxidation of binary alloys. In addition, the thermodynamics and transport properties of the allpy and oxide phases are known. Accordingly, the oxidation kinetics and morphological development of oxide scales on cobalt-iron alloys were determined for iron alloy contents up to 70% exposed to various oxygen pressures (from 10^{-4} atm to 1 atm) at 1200°C. Measurements were also made of the metal compositional profiles in the scales in order that a diffusion model could be invoked to correlate the parabolic oxidation kinetics of the alloys.

In the following presentation, Chapters II and III contain a general discussion on the oxidation of pure metals and binary alloys. Various theoretical considerations discussed in these chapters are applied subsequently to the design of the experimental system described in Chapter IV. Chapter V contains a literature survey of the high temperature properties of Co-Fe-O system. Experimental techniques are described in Chapter VI. In the following two chapters the experimental results are presented, interpreted and discussed. Application of the diffusion model and discussion of theoretical calculations in the light of experimental findings is presented in Chapter IX. Chapter X contains the summarized conclusions of this work. Appendix A contains proposals for future work. A complete error analysis of the measurements and calculations is given in Appendix B

and Appendix C describes in detail the computation method.

CHAPTER II

PRINCIPLES OF OXIDATION

2.1 Oxide Formation and Growth

Metals form one of the most important classification of materials used for centuries in all fields of human activity. Because of their widespread use metals are often exposed to chemically and physically aggressive environments containing oxygen, nitrogen, sulphur and other reactive gases and vapors. Unfortunately, with a few exceptions they react with such environments, in reactions designated by the term "oxidation".

When a clean surface of metal is exposed to the attack of a gas, the reaction commences at the metal-gas interface, and unless the reaction products are volatile, they form an intermediate layer between the metal and gas. This reaction is governed by two factors. One is the thermodynamic equilibrium determining which compounds, if any, are formed. The second factor is the rate at which compound formation occurs and it is a kinetic problem. The study of the oxidation processes of metallic materials is therefore concerned with their response to various environments under various conditions of temperature and pressure.

A metal in a gaseous environment constitutes therefore a complex chemical system and in most cases an interpretation of the reaction behaviour can be achieved only with great difficulty. The equation for the reaction between oxygen and metal to form metal oxide may be written as:

$$a\ Me + \frac{b}{2}\ O_2 \rightarrow Me_aO_b \qquad (2.1)$$

However, because the oxidation behaviour of a metal depends upon many variables reaction mechanisms prove to be complicated. The initial step involves the adsorption of the gases on the metal surface. As the reaction progresses, oxygen may dissolve in the metal; then oxide is formed on the surface either as a film or as discrete oxide nuclei. Both adsorption and initial oxide formation are functions of surface orientations, crystal defects on the surface, impurities in the metal and gas, and surface preparation.

The oxide frequently appears as a compact phase with the metal and oxygen gas spatially separated from each other, and further reaction is only possible by passage of the reactants through this superficial layer. In such situations, the course of the reaction is no longer determined by Eq. (1.1), but by diffusion and phase boundary processes for which the mechanisms are complex. One must consider, in general, several partial processes. First, phase boundary reactions involving chemisorption of oxygen molecules with subsequent formation of oxide by transfer of oxygen into the metal or of metal into the adsorbed oxygen layer. This formation stage involves nucleation and crystal growth processes. Second, predominant transport processes in a space charge boundary layer in case of films, especially at low temperatures, where the electrical potential gradient is the major driving force. And third, diffusion of cations, anions and electrons through the oxide film or scale, the driving force for this process being the electrochemical potential gradient in the oxide layer.

One of these above processes is usually the slowest and hence rate-determining reaction step.

The methods for investigation of oxidation processes include the reaction product identification by standard chemical and metallographical methods and reaction rate monitoring. The reaction rate monitoring includes determinations of the changes in thickness of scale, in weight of sample or in the volume of oxygen consumed from the atmosphere as a function of time. Because of the very complexity of the processes, the reaction rate laws may take various forms. Most of the quantitative experimental data are obtained as changes in weight (Δm) per unit surface area (A) which are directly proportional to the oxide thickness, if it can be assumed, that density is constant throughout the oxide layer.

$$\frac{\Delta m}{A} = \frac{\text{mol. wt. of oxygen}}{\text{mol. wt. of oxide}} \cdot \rho \cdot x \qquad (2.2)$$

where ρ = density of oxide

x = thickness

The simplest rate law observed is the linear relationship,

$$\frac{\Delta m}{A} = k_L t \qquad (2.3)$$

where k_L = linear scaling constant

t = time

This type of behaviour is associated with growth of porous films where the direct contact occurs between metal and gas, such as for the alkali metals. It was also observed in growth of compact scales, such as wüstite in CO_2-CO atmospheres when diffusion in the scale is sufficiently rapid and the controlling step is chemical reaction at the oxide-gas interface.

The most common type of oxidation behaviour, and also best described theoretically is the parabolic relationship which will be discussed in more detail later. In this case the oxidation rate is inversely proportional to the film thickness

$$\frac{dx}{dt} = \frac{k_p}{x} \qquad (2.4)$$

Integration of the equation (2.4) and substitution into (2.2) gives the parabolic relationship

$$(\frac{\Delta m}{A})^2 = k_p t + C \qquad (2.5)$$

where k_p is parabolic rate scaling constant. In this case the rate controlling step is diffusion of either cations and/or anions across a compact scale.

Experimental values have occasionally been found to agree with cubic relationship

$$(\frac{\Delta m}{A})^3 = k_k \cdot t \qquad (2.6)$$

or logarithmic

$$\frac{\Delta m}{A} = k_\ell \cdot \log(a \cdot t + t_o) \qquad (2.7)$$

and also inverse logarithmic

$$\frac{A}{\Delta m} = b - k_{i\ell} \log t \qquad (2.8)$$

These relationships are most applicable in describing the formation of very thin films at lower temperatures. Combinations of two or more of these rate laws in a single oxidation-time curve are also quite common. In most cases, the temperature effect can be expressed by an Arrhenius

relationship

$$k = k_o e^{-Q/RT} \tag{2.3}$$

where Q is the activation energy of the process.

Usually the oxides formed on the surface of the metal are not stoichiometric compounds. The degree of nonstoichiometry in oxides is generally equivalent to the presence of point defects at concentrations dependent on the temperature and on oxygen partial pressure. For metal excess oxides it is found that nonstoichiometry increases with decreasing oxygen pressure. It has been shown that these oxides have principal oxygen pressure dependence ranging from $p_{O_2}^{-1/2}$ to $p_{O_2}^{-1/6}$ for concentrations of oxygen vacancies and metal interstitials respectively. In metal deficit oxides, the concentration of defects increase with oxygen pressure by a dependence ranging from $p_{O_2}^{1/2}$ to $p^{1/6}$ for concentrations of metal vacancies of different charge.

The knowledge and understanding of defect structures in oxides is essential for theoretical calculations of reaction rates in connection with thermodynamic equilibrium data and transport properties in the form of self-diffusion coefficients. If the concentrations and mobilities of ionic and electronic defects in a metal oxide as a function of the respective independent thermodynamic variables are known and, furthermore, the rates of the phase boundary reactions involved are known, it is possible to calculate the scaling rate of a metal provided that no irregularities such as break away of the oxide from the metal occurs. Conversely, it is possible to obtain information regarding lattice defects or phase boundary reactions from the observations on the oxidation kinetics.

2.2 Wagner's Theory of Parabolic Oxidation

In the early 1920's Tamman[1] and Pilling and Bedworth[2] reported that a number of metals absorb oxygen according to a parabolic law. This empirical result was explained by Wagner[3] who formulated a general theory of high-temperature oxidation of metals. He postulated that the transport of reactants across an oxide reaction product layer under conditions of interfacial equilibria proceeded by the independent migration of ions and electrons under the influence of an electrochemical potential gradient. The prerequisite for the ionic species to be mobile is that the sublattice contains pointdefects like interstitials and vacancies. Under these restrictions, the current of a species i in equivalents per cm^2 equals

$$J_i = z_i \nu_i c_i = z_i c_i B_i \left(\frac{d\mu_i}{dx} + z_i F \frac{d\psi}{dx}\right) \qquad (2.10)$$

Here $z_i c_i$ represents the concentration in equivalents per cm^3, ν_i and B_i are the particle velocity and mobility and the term in brackets is the electrochemical potential gradient for the species i consisting of the chemical and electrical potentials μ_i and $z_i F\psi$ respectively where F is the Faraday. The derivation of expressions for the parabolic rational rate constant from this relationship is lengthy but well documented in recent monographs.[4,5]

When an oxide exhibits transport by only one component and its conductivity is predominantly electronic, the parabolic rational rate constant may be expressed as

$$k_r(\text{equivalent/cm sec}) = \frac{RT}{|z_2|F^2} \int_{a_0'}^{a_0''} t_i \sigma \, d\ln a_0 \qquad (2.11)$$

Here t_i is ionic transport number, σ is the electrical conductivity and a_0 is the oxygen activity. This is the original form of k_r, but not the most popular. The more useful form of the relation is expressed in terms of self-diffusion coefficients. In the case of metal migration only, this equation reduces to

$$k_r(\text{equivalent/cm sec}) = \bar{C}_2 \int_{a_0'}^{a_0''} \frac{Z_1}{|Z_2|} D_1 \, d\ell n a_0 \qquad (2.12)$$

where D_1 is self-diffusion coefficient of metal and $\bar{C}_2$ is the average oxide composition in equivalents/cm^3.

The validity of the assumptions has been tested for the parabolic oxidation of copper, cobalt and iron.[4,5] The comparison with experimental data shows close agreement. But this simple and elegant model has been questioned in several respects in recent years. The lattice defect and electron defect properties of oxides are probably much more complex than originally suggested. The ionization state of vacancies, complex formation and interactions of these variously charged species might well influence the oxidation kinetics. Furthermore, diffusion studies in polycrystalline materials have shown that structural defects such as pores, grain boundaries and dislocations act as low resistance paths and may be an important mode of transport, especially at intermediate temperatures.

Smeltzer et al.[4] have proposed a theory to describe the non-parabolic oxidation kinetics of titanium, hafnium and zirconium. In this theory, lattice diffusion and diffusion along low resistance paths, which decrease in density with time, were assumed to occur simultaneously. More recently, Perrow, Smeltzer and Embury[5] have employed the model for non-parabolic

oxidation based on combination of diffusion along grain boundaries and lattice diffusion to explain the deviations from the parabolic law in oxidation of nickel. The contribution of grain boundary diffusion to the effective diffusion coefficient, D_{eff}, is weighted according to the grain size:

$$D_{eff} = D_L(1-f) + D_B f$$

where D_L and D_B are the lattice and boundary diffusion coefficients, respectively. The fraction of available sites lying within the low resistance paths is f and is inversely proportional to the grain size.

2.3 Oxidation of Alloys

Although the problem of alloy oxidation has a history as that of elementary oxidation because of its practical importance (Pilling and Bedworth also published papers on alloy oxidation), the theory for the processes involved in the oxidation of alloys is relatively undeveloped. The reasons for this are twofold: from the theoretical point of view, the theory of diffusion in multicomponent systems has only lately been studied in detail; and from the experimental point of view, the empirical description of the processes was, until recently, very difficult. This difficulty arises because an important variable in the oxidation of alloys is the spacial redistribution of the components in the alloy as oxidation proceeds. Before the development of the electron-probe microanalyser, it was possible to determine this distribution in only a few special cases.

If an alloy is subjected to oxidation, one component is, in general, oxidized preferentially because the alloy components have different affinities

to oxygen. Differences in diffusion rates for different alloy components in the metal and oxide phases also give rise to concentration gradients within them. Consequently the compositions of scale and alloy may change in a complicated manner with time. The second component may enter the scale, affecting its lattice defect structure, or may accumulate as a metal or oxide beneath the main scale. Also, if oxygen diffuses into the alloy in atomic form, precipitation of the less noble metal oxide may occur as internal oxide.

Thermodynamics, usually in the form of ternary equilibrium diagrams involving two alloying elements and oxygen, is useful in predicting the alloying element likely to be preferentially oxidized and sometimes the likely steady-state scale.

The kinetic data obtained from alloy oxidation experiments often deviate from idealized relationships mentioned earlier and a series of rate transitions may be observed. In particular, the conditions necessary for the parabolic relationship to hold in alloy systems are as follows. The sequence of reaction layers must not change with time and alterations in oxide structure due to cracking and phase transformations must not occur. Interface reactions must be quite rapid to ensure local thermodynamic equilibrium. In order to obtain tractable mathematical expressions with appropriate boundary conditions, it has been necessary to assume that the composition of the alloy at some point must be the initial composition (semi-infinite plate) and the compositions at the interfaces must be time independent.

It is clear from the number of kinetic and thermodynamic factors to be considered that oxidation of alloys is extremely complex. It is often

useful, therefore, to consider certain limiting cases, applicable specially to binary alloys, which can be treated qualitatively as well as quantitatively.

A classification of different modes of binary alloy oxidation due to Moreau and Bernard[6] and Wood[7] permits the following work to be seen in the perspective of the entire binary alloy oxidation scene. An alloy AB represents the general alloy under consideration, in which A is the more noble metal and B the less noble metal. Initially, the special case for the exclusive oxidation of one alloy component is considered before proceeding to the more general case where both components oxidize (Fig. 2-1).

Class I - Only one of the elements oxidizes under the prevailing conditions, giving BO.

(A) The solute element B oxidizes under the given conditions:

(1) internally, giving BO particles in a matrix of A, e.g. dilute Fe-Al alloys which oxidize internally to produce Al_2O_3 particles in iron matrix (Fig. 2-1 (I_A^1)). The oxygen pressure in the atmosphere is less than the equilibrium dissociation pressure of AO.

(2) exclusively externally, giving a single layer of BO above an alloy matrix depleted in B, e.g., Cu-Si alloys richer in silicon producing an external SiO_2 layer (Fig. 2-1 (I_A^2)). The oxygen pressure in the atmosphere is generally less than the dissociation pressure of AO.

(B) The element B is now the major element and oxidizes exclusively

(1) leaving the non-oxidizable metal A dispersed in BO, e.g., Cu-Au alloys rich in copper (Fig. 2-1 (I_B^1)).

(2) leaving the non-oxidizable metal A in a A-enriched zone beneath the BO scale, e.g. Ni-Pt alloys (Fig. 2-1(I_B^2)).

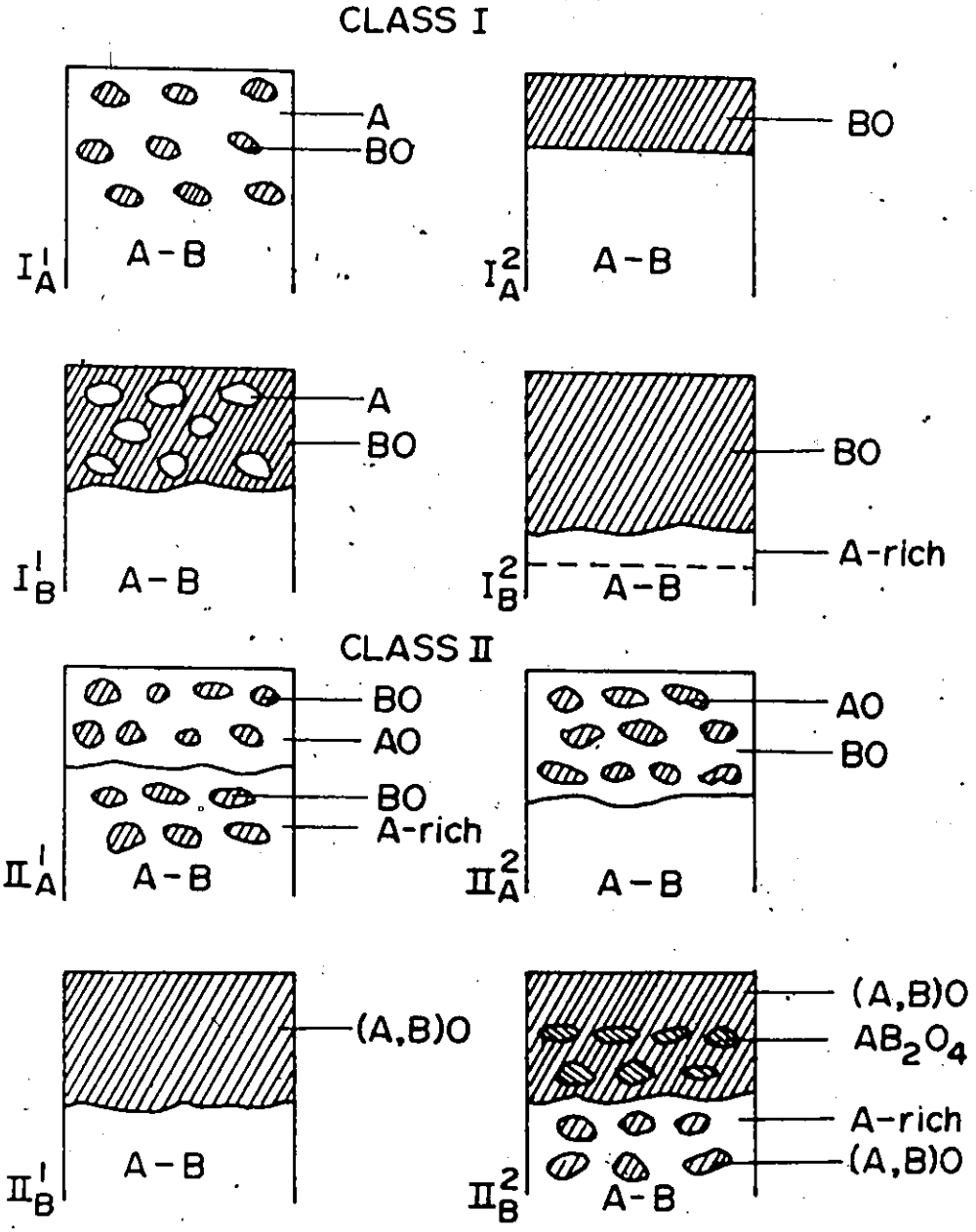

Fig. 2-1

Oxidation modes of binary alloys

Class II - Both alloying elements oxidize simultaneously to give AO and BO, the oxygen pressure in the atmosphere being greater than the equilibrium dissociation pressure of both oxides.

(A) AO and BO are virtually insoluble in each other:

(1) The less noble metal B is the minor component. An internal oxide of BO lies beneath a two-phase layer of AO-BO, e.g., certain Cu-Ni alloys (Fig. 2-1 (II_A^1)).

(2) The less noble metal is the major component so that no internal oxidation is now observed, e.g. Cu-Ni alloys rich in Ni (Fig. 2-1 (II_A^2)).

(B) AO and BO react to form a mixed oxide.

(1) AO and BO form a single solid solution (A,B)O, e.g., Fe-Mn alloys (Fig. 2-1 (II_B^1)).

(2) A double oxide is formed, often as spinel, which may give a complete surface layer of variable composition or give particles incorporated into a matrix of AO with BO formed internally, e.g., Fe-Co alloys (Fig. 2-1 (II_B^2)).

In many alloy systems several types of behaviour are possible depending on the composition, oxidation atmosphere, temperature, pressure, time, etc. Changes from one type of behaviour to another may occur on a single specimen.

CHAPTER III

THEORETICAL ANALYSIS OF DIFFUSION CONTROLLED OXIDATION OF BINARY ALLOYS

3.1 Introduction

A theoretical description of the high temperature oxidation behaviour of binary alloys must consider the diffusional processes taking place in both the oxide scale and the alloy. Since three species are involved (i.e. the alloying elements A and B, and oxygen O), a completely general description must also involve the elements of ternary diffusion theory. At high temperatures, one can generally assume that a condition of local thermodynamic equilibrium prevails at the gas-scale and scale-alloy interfaces. The requirement that the various diffusing species be conserved at the interfaces and the local equilibrium conditions lead to a coupling or interdependence of the diffusion fields in the oxide and alloy phases. This interplay between diffusion in the two phases involves thermodynamic as well as kinetic considerations. It follows that a knowledge of the thermodynamics of the ternary system A-B-O, preferably in the form of a ternary phase diagram is a necessity.

The most effective means of presenting the relationship between the kinetic and thermodynamic aspects of binary alloy oxidation and corresponding oxide scale and subscale structures is by means of diffusion path on the appropriate A-B-O ternary isotherm.

In the following the theory of multicomponent diffusion, concept of diffusion path, thermodynamics and diffusion model for oxidation of binary alloys II_B^1 type will be discussed in detail.

3.2 Theory of Multicomponent Diffusion - Phenomenological Equations

The n-component system at equilibrium is uniquely determined by specifying all the potentials e.g. chemical potential, electric potential, etc. If now the system is displaced slightly from equilibrium, the rate of return to equilibrium is proportional to the deviation from this equilibrium. This is the phenomenological basis for multicomponent diffusion formulated by Onsager.[8] According to this formulation, for a system near equilibrium the flux-force relations for an n-component isotropic system are linear, i.e.,

$$J_i = \sum_{k=1}^{n} L_{ik} X_k \tag{3.1}$$

where J_i is the flux of component i, X_k are the forces (the gradients of present potentials) and L_{ik} are empirical proportionality coefficients. In the absence of electrical, thermal and pressure gradients the only forces X_k are the negative values of chemical potential gradients. Equation (3.1) becomes

$$J_i = -\sum_{k=1}^{n} L_{ik} \frac{\partial \mu_k}{\partial x} \tag{3.2}$$

where μ_k are the chemical potentials. As a consequence of Onsager's reciprocity theorem, the matrix $[L_{ik}]$ is symmetric, viz.,

$$L_{ik} = L_{ki} \tag{3.3}$$

L_{ik} also satisfies the equalities

$$\sum_i L_{ik} = \sum_k L_{ik} = 0 \tag{3.4}$$

and the inequalities

$$L_{ii} > 0;\ L_{ii}L_{kk} - L_{ik}L_{ki} > 0, \text{ etc.} \tag{3.5}$$

Since the μ_k are not convenient variables for mathematical and experimental analysis and are functions of n-1 independent atom fractions, we can expand Eq. (3.2) to obtain a relation which involves molar concentrations c_k:

$$J_i = -\sum_{k=1}^{n-1} D_{ik} \frac{\partial c_k}{\partial x} \tag{3.6}$$

where

$$D_{ik} = \sum_{j=1}^{n} L_{ij} \frac{\partial \mu_j}{\partial c_k} \tag{3.7}$$

Equation (3.6) is recognized as a generalization of Fick's first law. It is invariably assumed that the molar volume of the system is independent of composition. As a result, the concentration of one of the components, usually taken as the n^{th}, is independent.

Because multicomponent diffusion is a cooperative process, the flux of the i^{th} component is dependent on the fluxes of the remaining components. The coupling between the fluxes is represented by the L_{ik} coefficients. Although the off-diagonal coefficients L_{ik} are not, in general, zero, according to Darken[10] it is reasonable to assume, that

$$L_{ik} << L_{ii} \quad (i \neq k) \tag{3.8}$$

Inserting this assumption into Eq. (3.2) and (3.7) we obtain

$$J_i = -L_{ii} \frac{\partial \mu_i}{\partial x} \tag{3.9}$$

and

$$D_{ik} = L_{ii} \frac{d\mu_i}{dc_k} \tag{3.10}$$

This simplifies the mathematics considerably, but nevertheless it should be treated as an approximation.

If the force on an atom (F) is taken to be the gradient of the appropri. potential and v_i is the mean velocity of the atom i when acted upon by F_i, the mobility B_i is given by the equation

$$B_i = \frac{v_i}{F_i} \tag{3.11}$$

So the flux J_i can then be defined as

$$J_i = C_i v_i \tag{3.12}$$

$$= B_i F_i C_i \tag{3.13}$$

$$= -B_i C_i \frac{d\mu_i}{dx} \tag{3.14}$$

$$= -L_{ii} \frac{d\mu_i}{dx} \tag{3.15}$$

Comparing Eqs. (3.14) and (3.15) we obtain

$$L_{ii} = B_i C_i \tag{3.16}$$

In the Eq. (3.15) the μ_i is given by

$$\mu_i = \mu_i^o + RT \ln a_i \tag{3.17}$$

where μ_i^o is the standard chemical potential of component i, a_i is the activity of the component i based on the standard state, R is the universal

gas constant and T is the absolute temperature.

Thus Eq. (3.15) becomes

$$J_i = -L_{ii} RT \frac{\partial \ell n a_i}{\partial x} \tag{3.18}$$

which in the view of Eq. (3.16) is

$$J_i = -B_i RT\, C_i \frac{\partial \ell n a_i}{\partial x} \tag{3.19}$$

If correlation effects are neglected, then the self-diffusion coefficient, D_i, of species i is given by the Nerst-Einstein relation[11]

$$D_i = B_i RT \tag{3.20}$$

The flux of species i is obtained by combining Eqs. (3.19) and (3.20)

$$J_i = -D_i C_i \frac{\partial \ell n a_i}{\partial x} \tag{3.21}$$

Usually, in the growing oxide scales strong thermodynamic interactions can exist. Consequently it is convenient to use equation (3.21) where activity gradients are utilized.

If the thermodynamic interactions are not strong, an alternative formalism due to Wagner[12] for activity coefficients may be used. Thus from Eq. (3.6) for a ternary system

$$J_i = -D_{ii} \frac{\partial c_i}{\partial x} - D_{ij} \frac{\partial c_j}{\partial x}, \quad i,j = 1,2 \tag{3.22}$$

It can be shown from Eq. (3.7) that

$$D_{ii} = D_i\left(1 + c_i \frac{\partial \ell n \gamma_i}{\partial c_i}\right), \quad i = 1,2 \tag{3.23}$$

and

$$D_{ij} = D_i c_i \frac{\partial \ell n \gamma_i}{\partial c_j}, \quad i = 1,2 \tag{3.24}$$

where D_i is given by Eq. (3.20) and γ_i is the activity coefficient of component i. The term D_{ij} as defined by (3.24) is called the diffusion interaction term.

3.3 Thermodynamic Stability of the Phases during Oxidation

The phase rule for a heterogeneous system of components is formulated as

$$F = C + 2 - P \tag{3.25}$$

where C is the number of components, P is the number of phases present, 2 stands for pressure and temperature and F represents the thermodynamic degrees of freedom. In the case of diffusion controlled oxidation, the fluxes J_i are proportional to the gradient of chemical potentials. Consequently, at least one degree of freedom is required within a phase region for diffusion to occur and hence for the oxidation reaction to proceed. Thus, in oxidation of pure metals the phases must be arranged in the unique sequence of single-phase layers, given by thermodynamic stability of the oxides. The chemical potential gradients within each phase act as a driving force for diffusion. If the metal is a binary alloy the Gibbs' rule does not exclude the formation of two phase regions, since under isobaric and isothermal conditions there is one degree of freedom. Thus the possibility of chemical gradient and hence that of diffusion exists. So the oxide scale on a binary alloy is often made up of two-phase regions, which appear as mixtures of two oxides, zones of internal oxidation or nonplanar interfaces.

3.4 The Distribution of Cations in the Scales Formed during the Oxidation of Alloys[15]

When an alloy of metals A and B reacts with nonmetal X, e.g. oxygen or sulphur, a scale consisting of a solid solution of the corresponding compounds may be formed. In general, the ratio of the number of moles of metals A and B in the scale is not equal to the ratio in the alloy inasmuch as the less noble metal tends to enter the scale preferentially. Further in the view of different cations diffusivities, the ratio of metals A and B in the scale varies with distance x from the alloy-scale interface. For a theoretical calculation of the overall scaling rate as a function of alloy composition, it is necessary to know the local distribution of A and B in the scale. Thus this section is concerned with methods of calculating the local distribution of A and B in the scale as a basis for calculating the scaling rate.

3.4.1 General Presuppositions

The following presuppositions are made:

1. The alloy A-B may be one or two-phase alloy with uniform initial composition N_B^o (mole fraction).

2. In the scale, only a single phase is supposed to be present.

3. Exclusive diffusion control is presumed, i.e. at the alloy-scale and scale-gas interface local thermodynamic equilibrium is supposed to prevail.

4. The alloy is assumed to be given as a flat sample of virtually infinite thickness.

5. The alloy-scale interface is assumed to be plane at any time $t > 0$. No voids are presumed to be present.

6. In view of the last two presuppositions, equations are formulated in one direction only.

7. In the scale, electronic conduction is presumed to prevail, and diffusion of cations of metals A and B rather than diffusion of anions of X is supposed to account for transport of matter across the scale.

8. Only small deviations from the ideal metal-to-nonmetal ratio are presumed to occur.

9. The compounds in the scale are denoted by A(x) and B(x) without specification of the molar ratio of the constituent elements. The equivalent volume V_{eq} of the solid solution A(x)-B(x) is presumed to be independent of composition in accord with the fact that in most systems the volume is predominantly determined by the volume of the larger anions rather than by the volume of the smaller cations.

3.4.2 Co-ordinate Frames and Notation Symbols

In describing the diffusion processes in the alloy and oxide it is convenient to use two different frames of reference. Firstly, the origin of the u-frame is located at the original alloy surface. Because the alloy lattice is stationary with respect to this coordinate system, it is used to describe diffusion in the alloy. The x-frame is attached to the scale-alloy interface and is utilized for the description of diffusion in the oxide. The coordinate frames are summarized in Fig. (3-1) together with the diffusion profiles of various variables used in the formulation of the problem.

The following symbols are introduced:

t time

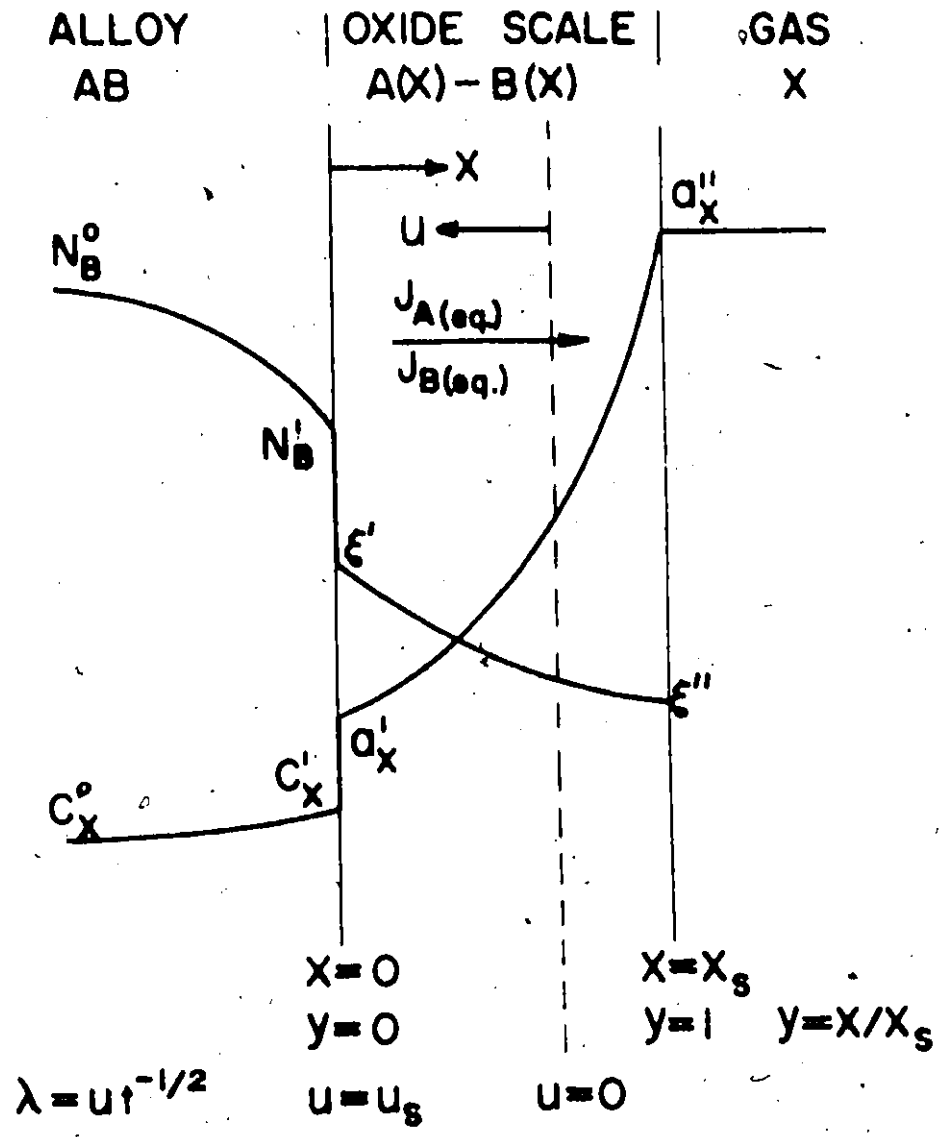

Fig. 3-1

Co-ordinate frames and notations used in the text

x	distance from the alloy-scale interface in outward direction
x_s	thickness of the scale at time t
$y = x/x_s$	dimensionless variable of distance in oxide phase
u	distance from the initial surface of alloy in inward direction
u_s	distance of the alloy-scale interface from the initial surface of the alloy at time t
$\lambda = u/t^{1/2}$	dimensionless variable of distance in alloy
$v = du_s/dt$	rate of recession of the alloy-scale interface
$k = x_s(dx_s/dt)$	rate constant for growth of the scale according to Tamman
N_A, N_B	mole fractions of A and B, in alloy,
N_A^o, N_B^o	mole fraction of A and B, in bulk alloy
V_m	molar volume of the alloy
V_{eq}	volume per equivalent of compound A(x) and B(x) in the scale
μ_i^o	chemical potential of i in its standard state per mole
a_i	activity of constituent i
R	general gas constant
T	temperature
z_i	absolute valence of ions of type i
ξ	local equivalent fraction of compound B(x) in the scale, i.e. ratio of the number of equivalents of cations B to the sum of the number of equivalents of cations of metals A and B

ξ_{av}	average equivalent fraction of compound B(X) in the scale
ξ_{alloy}	equivalent fraction of B in the bulk alloy
D_{AB}	interdiffusion coefficient in alloy
D_A, D_B	self-diffusion coefficient = tracer diffusion coefficients of ions of metals A and B, respectively, in the scale.

Subscripts are used in order to denote quantities referring to element A, B and X, and A(X) and B(X), respectively. Superscripts ' and " denote quantities at the alloy-scale and scale-gas interface, respectively.

3.4.3 Formulation of the General Equations

In general, the flux of the ions A and B in the scale is due to both a concentration gradient and a gradient of electrical potential.[3] It is, however, not necessary to consider details of the driving force for movement of the ions. In the following formulation, originally given by Wagner,[15] correlation effects are disregarded. Thus equations for the flux of cations of metals A and B in a scale involving prevailing electronic conduction with respect to the oxide ion lattice in the view of the equations in the section 3.2, may be written as:

$$J_A(eq) = -\frac{D_A(1-\xi)}{V_{eq}} \cdot \frac{\partial \xi n a_A}{\partial x} \tag{3.26}$$

$$J_B(eq) = -\frac{D_B \xi}{V_{eq}} \cdot \frac{\partial \xi n a_B}{\partial x} \tag{3.27}$$

where $(1-\xi)/V_{eq}$ and ξ/V_{eq} are the local concentrations of cation metals A and B, respectively.

A solid solution A(X)-B(X) involving deviations from the ideal metal-to-nonmetal ratio must be treated as a ternary system. In addition to

pressure P, temperature T and equivalent fraction ξ, one has, therefore, a fourth independent variable, which may be chosen to be the activity a_X of nonmetal X. Thus one may rewrite Eqs. (3.26) and (3.27) upon expressing the activities a_A and a_B of metals A and B in the scale by a_X and ξ. The activities of elements A, B and X and the compounds A(X) and B(X) are interrelated by

$$\mu_A^o + RT\,\ell n a_A + \left(\frac{z_A}{z_X}\right)(\mu_X^o + RT\ell n a_X) = \mu_{A(X)}^o + RT\ell n a_{A(X)} \qquad (3.28)$$

$$\mu_B^o + Rt\ell n\, a_B + \left(\frac{z_B}{z_X}\right)(\mu_X^o + RT\, n a_X) = \mu_{B(X)}^o + RT\ell n\, a_{B(X)} \qquad (3.29)$$

With the help of Eqs. (3.28) and (3.29) one may express a_X and a_B in terms of $a_{A(X)}$, $a_{B(X)}$ and a_X. In the case of small deviations from the ideal stoichiometric metal-to-nonmetal ratio, the activities $a_{A(X)}$ and $a_{B(X)}$ are practically determined by P, T and ξ. Thus one obtains from Eqs. (3.26) to (3.29)

$$J_{A(eq)} = -\frac{D_A(1-\xi)}{V_{eq}}\left(\frac{\partial \ell n a_{A(X)}}{\partial \xi}\cdot\frac{\partial \xi}{\partial x} - \frac{z_A}{z_X}\,\frac{\partial \ell n a_X}{\partial x}\right) \qquad (3.30)$$

$$J_{B(eq)} = -\frac{D_B \xi}{V_{eq}}\cdot\left(\frac{\partial \ell n a_{B(X)}}{\partial \xi}\cdot\frac{\partial \xi}{\partial x} - \frac{z_B}{z_X}\cdot\frac{\partial \ell n a_X}{\partial x}\right) \qquad (3.31)$$

where values of $\frac{\partial \ell n a_{A(X)}}{\partial \xi}$ and $\frac{\partial \ell n a_{B(X)}}{\partial \xi}$ are supposed to be known quantities, which are characteristic of the thermodynamics of mixing of the quasi-binary system A(X)-B(X).

Since the rate of scaling is supposed to be controlled by diffusion, the rate of thickening of the scale is presumed to be inversely proportional

to the instantaneous thickness x_s,

$$\frac{dx_s}{dt} = \frac{k}{x_s} \tag{3.32}$$

where k is a constant. Integration of Eq. (3.32) yields the parabolic rate law

$$x_s = (2kt)^{1/2} \tag{3.33}$$

The sum of the fluxes of A and B at any distance x multiplied by the volume per equivalent V_{eq}, is equal to the rate of increase in volume of the scale per unit cross-section, i.e. equal to the rate of increase in thickness x_s,

$$(J_{A(eq)} + J_{B(eq)}) V_{eq} = \frac{dx_s}{dt} \tag{3.34}$$

From dimensional analysis it follows that in the case of exclusive diffusion control the local equivalent fraction ξ and the local activity of nonmetal a_X depend only on the ratio y of distance x to the instantaneous thickness x_s of the scale,

$$y = x/x_s \tag{3.35}$$

From Eqs. (3.30), (3.31) and (3.34) using Eq. (3.35) one obtains

$$D_A(1-\xi)\left(-\frac{\partial \ell n a_{A(X)}}{\partial \xi} \cdot \frac{d\xi}{dy} + \frac{z_A}{z_X}\frac{d\ell n a_X}{dy}\right) + D_B\xi\left(-\frac{\partial \ell n a_{B(X)}}{\partial \xi} \cdot \frac{d\xi}{dy} + \frac{z_B}{z_X}\frac{d\ell n a_X}{dy}\right) = k \tag{3.36}$$

Application of the continuity equation to Eq. (3.31) and assuming again that ξ and a_X are functions of y only, Wagner obtains the equation

$$yk \frac{d\xi}{dy} = - \frac{d}{dy}[D_B \xi (\frac{\partial \ell n a_B(X)}{\partial \xi} \cdot \frac{d\xi}{dy} - \frac{z_B}{z_X} \frac{d \ell n a_X}{dy})], \qquad (3.37)$$

which gives the rate at which the concentration changes in the scale.

Similarly it is possible to derive the expression for the rate of concentration change in the alloy from Fick's second law using the dimensionless variable $\lambda = u/t^{1/2}$. So

$$\frac{1}{2}\lambda \frac{dN_B}{d\lambda} = - \frac{d}{d\lambda}[D_{AB} \frac{dN_B}{d\lambda}] \qquad (3.38)$$

for $\lambda > \frac{u_s}{t^{1/2}}$.

In order to calculate the constant k of the parabolic rate law, which appears as a parameter in equation (3.36) and (3.37), further ξ and a_X as function of y, and N_B as a function of u from the ordinary differential equations of second order (3.40) and (3.38) six boundary conditions have to be specified.

The needed additional conditions are as follows:

(1) The initial composition of the alloy is supposed to be uniform with the mole fraction N_B^o. Thus

$$N_B = N_B^o \quad \text{at } u \geq 0, \quad t = 0, \quad \text{i.e. at } \lambda = \infty \qquad (3.39)$$

(2) The thermodynamics of ternary system A-B-X is supposed to be known. Thus a value of ξ' at the alloy-scale interface corresponds to definite values of N_B' and a_X'. Hence, using the symbols f_1 and f_2 for respective functions,

$$N_B' = f_1(\xi') \quad \text{at } \lambda = u_s/t^{1/2} \qquad (3.40)$$

and

$$a_X' = f_2(\xi') \quad \text{at } y = 0. \qquad (3.41)$$

(3) At the outer interface of the scale, the activity of nonmetal X is supposed to be given. Thus

$$a_X(y = 1) = a''_X \tag{3.42}$$

(4) At the outer surface of the scale, $x = x_s$, ions of metals A and B are used for the expansion of the lattice. For metal B one has the material balance

$$J_{B(eq)}(x = x_s) = \frac{\xi''}{V_{eq}} \frac{dx_s}{dt} \tag{3.43}$$

Substitution of equation (3.31) with $x = yx_s$ and equation (3.32) in equation (3.43) yields

$$-[D_B \xi (\frac{\partial \ell n a_{B(X)}}{\partial \xi} \frac{d\xi}{dy} - \frac{z_B}{z_X} \frac{d\ell n a_X}{dy})]_{y=1} = \xi'' k \tag{3.44}$$

(5) Next an equation of material balance at the alloy-scale interface can be formulated. The ratio of the recession u_s of the alloy-scale interface to the thickness of the scale, x_s, equals the ratio of the molar volume of the alloy to the equivalent volume of the scale multiplied by the sum of the number of moles of metals A and B per equivalent of the two metals

$$\frac{u_s}{x_s} = \frac{V_m}{V_{eq}} (\frac{1-\xi_{av}}{z_A} + \frac{\xi_{av}}{z_B}) \tag{3.45}$$

where ξ_{av} is the average equivalent fraction of B(X) in the scale,

$$\xi_{av} = \int_0^1 \xi \, dy \tag{3.46}$$

From Eq. (3.33) and (3.45) it follows that recession u_s of the alloy-scale interface at time t is

$$u_s = (2kt)^{1/2} \frac{V_m}{V_{eq}} \left(\frac{1-\xi_{av}}{z_A} + \frac{\xi_{av}}{z_B}\right) \tag{3.47}$$

Thus, the rate of recession of the alloy-scale interface is

$$v = \frac{du_s}{dt} = \left(\frac{k}{2t}\right)^{1/2} \frac{V_m}{V_{eq}} \left(\frac{1-\xi_{av}}{z_A} + \frac{\xi_{av}}{z_B}\right) \tag{3.48}$$

During the time interval dt the alloy-scale interface moves inward by the distance $v\,dt$. The number of equivalents of metal B in the alloy reacting per unit cross-section is, therefore $z_B(N_B'/V_m)\,dt$ plus the number of equivalents diffusing toward the interface

$$z_B \left[\frac{N_B'}{V_m} v + D_{AB} \left(\frac{\partial N_B}{\partial u V_m}\right)_{u=u_s}\right] dt \tag{3.49}$$

which must be equal to the flux of B in the scale away from the interface $J_{B(eq)}$ (X=0) given by Eq. (3.31). Thus the material balance after substitutions and rearrangement is

$$z_B N_B' \left(\frac{1-\xi_{av}}{z_A} + \frac{\xi_{av}}{z_B}\right) + \frac{2^{1/2} z_B D_{AB} V_{eq}}{k^{1/2} V_m} \left(\frac{dN_B}{d\lambda}\right)_{\lambda=u_s/t^{1/2}} =$$

$$= -\left[\frac{D_B \xi}{k} \left(\frac{\partial \ell n a_B(x)}{\partial \xi} \frac{d\xi}{dy} - \frac{z_B}{z_X} \frac{d\ell n a_X}{dy}\right)\right]_{y=0} \tag{3.50}$$

There are two limiting cases

(a) If diffusion in the alloy is fast in comparison to diffusion in the scale, i.e. if $D_{AB} >> D_A$ and $D_{AB} >> D_B$, concentration differences in the alloy are negligible and, therefore, $N_B' = N_B^o$. (3.51)

Using the inverse function introduced in Eq. (3.40), it is possible to obtain the value of ξ' and a_X from equation (3.41) without use of Eq. (3.50).

(b) If diffusion in the alloy is slow in comparison to diffusion in the scale, i.e. if $D_{AB} << D_A$ and $D_{AB} << D_B$, the ratio of the fluxes of B and A in the scale at y = 0 in equivalents per unit cross-section per unit time must be equal to the ratio of the number of equivalents of B and A in the bulk alloy. Thus one has in the view of (3.30), (3.31), (3.35) and (3.36)

$$\xi_{alloy} = \frac{1}{k}[D_B \xi(- \frac{\partial \ell n a_B(x)}{\partial \xi} \frac{d\xi}{dy} + \frac{z_B}{z_X} \frac{d\ell n a_X}{dy})]_{y=0} \qquad (3.52)$$

which in the case of negligible diffusion in the alloy equals the average equivalent-fraction ξ_{av} in the scale defined by Eq. (3.46). Hence

$$\xi_{av} = \xi_{alloy} \quad \text{if} \quad D_{AB} << D_A, D_B \qquad (3.53)$$

3.4.4 Summary

Equations (3.39), (3.40), (3.41), (3.42), (3.44), (3.45) and (3.50) are necessary auxillary equations in order to calculate the oxidation constant k, the average equivalent fraction ξ_{av} of B(X) in the scale, Further ξ and a_X as functions of y, and N_B as a function of λ can be calculated from the differential equation Eq. (3.36) of first order and the two differential equations of second order, Eqs. (3.37) and (3.38), if D_A and D_B are given as functions of ξ and a_X. This calculation is a tremendous task even with the help of modern computers. Consequently, it is necessary to obtain results for special cases which permit introduction of appropriate simplifications.

3.5 Relations between Thermodynamics and Kinetics of Binary Alloys Oxidation

In 1940, Rhines[16] made use of A-B-O type phase diagrams in an attempt to predict the sequence of oxide layer formation during the oxidation of copper alloys. He used the expedient of drawing, upon the appropriate A-B-O ternary isotherm, a straight line connecting the oxygen corner with the bulk alloy composition and then noting the order and identity of the one and two phase regions crossed. Rhines was aware that this is an oversimplification; nevertheless, using this approach he was able to indicate how scale structure depends on the bulk alloy composition.

Thomas[17] studied the high temperature oxidation of Cu-Pd and Cu-Pt alloys. On the basis of observed scale and subscale structures corresponding to various bulk alloy compositions, he superimposed diffusion paths on the appropriate schematic ternary isotherm. On this basis, Thomas was able to interpret the five modes of oxide scale structure which he observed for Cu-Pd alloys.

Clark and Rhines[18] studied the ternary diffusion in Al-Mg-Zn alloys. On the basis of their observations they postulated fourteen general rules governing the course of diffusion paths corresponding to multilayered ternary diffusion structures. A few of these rules have subsequently been shown to be incorrect.

Kirkaldy and Brown[19] have more recently established general principles for the description of diffusion structures in ternary systems. These authors developed a set of seventeen general theorems or rules pertaining to the construction of diffusion paths on a ternary isotherm. They also introduced a concept of "virtual path" as an aid to path

prediction in multiphase systems. These fundamental principles can be readily applied to the oxide scale and subscale formation during binary alloy oxidation.

3.5.1 Diffusion Paths on Ternary A-B-O Isotherms[20]

The concentration distributions (corresponding to binary alloy oxidation) determined theoretically using treatments similar to those mentioned in Sec. 3.4 or experimentally, for example, by microprobe analyses could be related to the ternary phase diagrams. Consider as an example, the case in which a single oxide $A_{n-x}B_xO$ forms on the binary alloy AB. There are assumed to be no restrictions on the solubility of B in the oxide or that of O in the alloy. In order to simplify the considerations the dependent variables used in this formulation are different than those used in Sec. 3.4. So the components under consideration are A, B and O. In Fig. 3-2, the concentrations in moles per unit volume of the arbitrary chosen independent variables A and O are shown for time t. It is necessary to consider only two variables since it follows from the phase rule that concentration of one of the components is dependent for given conditions.

In the general case, the distributions of C_A and C_O are functions of distance and time. If it can be shown that C_A and C_O are parametric solutions to the diffusion equations (that is, for all values of distance (x) and time (t), $C_A = C_A(\lambda)$ and $C_O = C_O(\lambda)$ where λ is a function of x and t) then elimination of λ between these expressions will yield a distance and time-independent relation

$$C_A = C_A(C_O) \tag{3.54}$$

The plot of this relation on the corresponding ternary phase

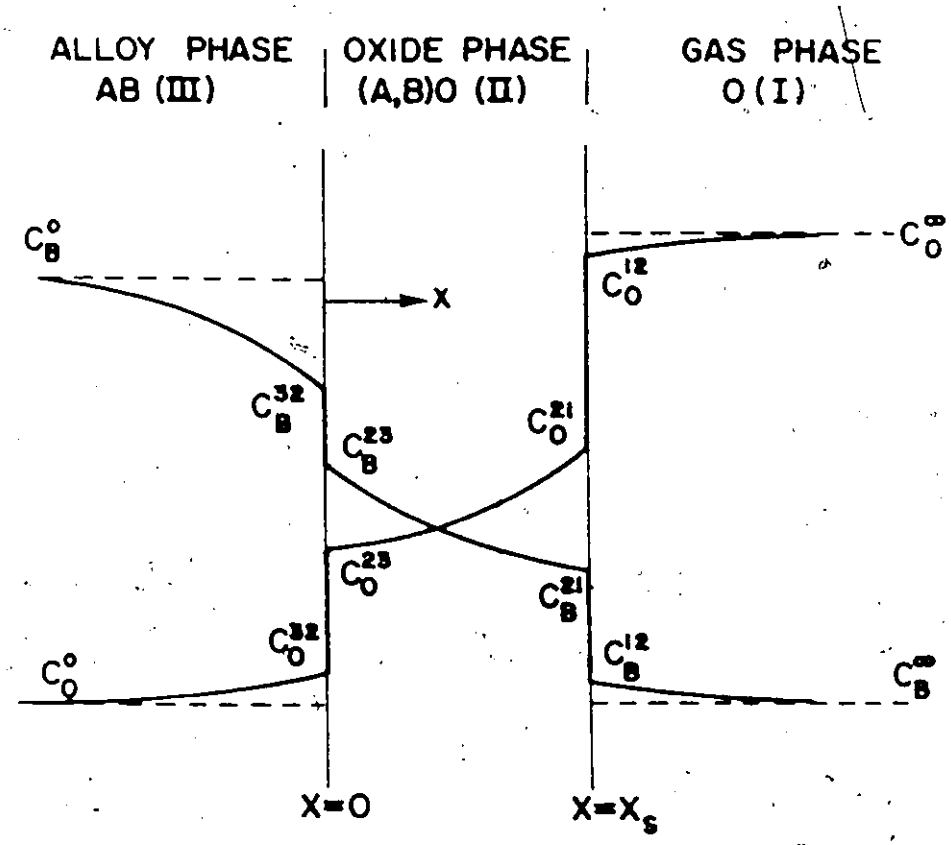

Fig. 3-2

Diffusion model showing the concentration profiles and location of coordinate frame

diagram, the path O-Q in Fig. 3-3, will therefore be stationary with time. For transformations which are diffusion controlled and involve infinite or semiinfinite boundary conditions, the parametric substitution

$$\lambda = xt^{-1/2} \tag{3.55}$$

is valid and this leads to the familiar parabolic oxidation kinetics. The invariant path O-Q is unique for the given terminal compositions and given set of experimental conditions, e.g., temperature, pressure, etc.[19]

When the oxidation process is diffusion controlled and therefore the concentration distributions are parametric in distance and time, the interfacial concentrations (C_A^{12}, C_O^{12}),(C_A^{21}, C_O^{21}), (C_A^{23}, C_O^{23}) and (C_A^{32}, C_O^{32}) are independent of time. However, these concentrations are not known ab initio, rather they are obtained as a part of the solution to the diffusion equations. This is quite unlike isothermal oxidation of pure metal in which case the binary phase diagram uniquely specifies the interface concentrations if local equilibrium is assumed to prevail at the interfaces.

If the diffusion path is obtained from calculations based on diffusion models which involve only planar interfaces and an assumed sequence of single-phase regions, then it may have to be regarded as being a "virtual" diffusion path. For example, assume the calculated path dips from a single phase field into a two-phase field, thereby cutting the lines and returns to the single phase region. This path is a "virtual" one since the situation is unstable, in view of the isolated zone of supersaturated material. The actual diffusion path may involve nonplanar interfaces or internal precipitates or both. These develop in an effort

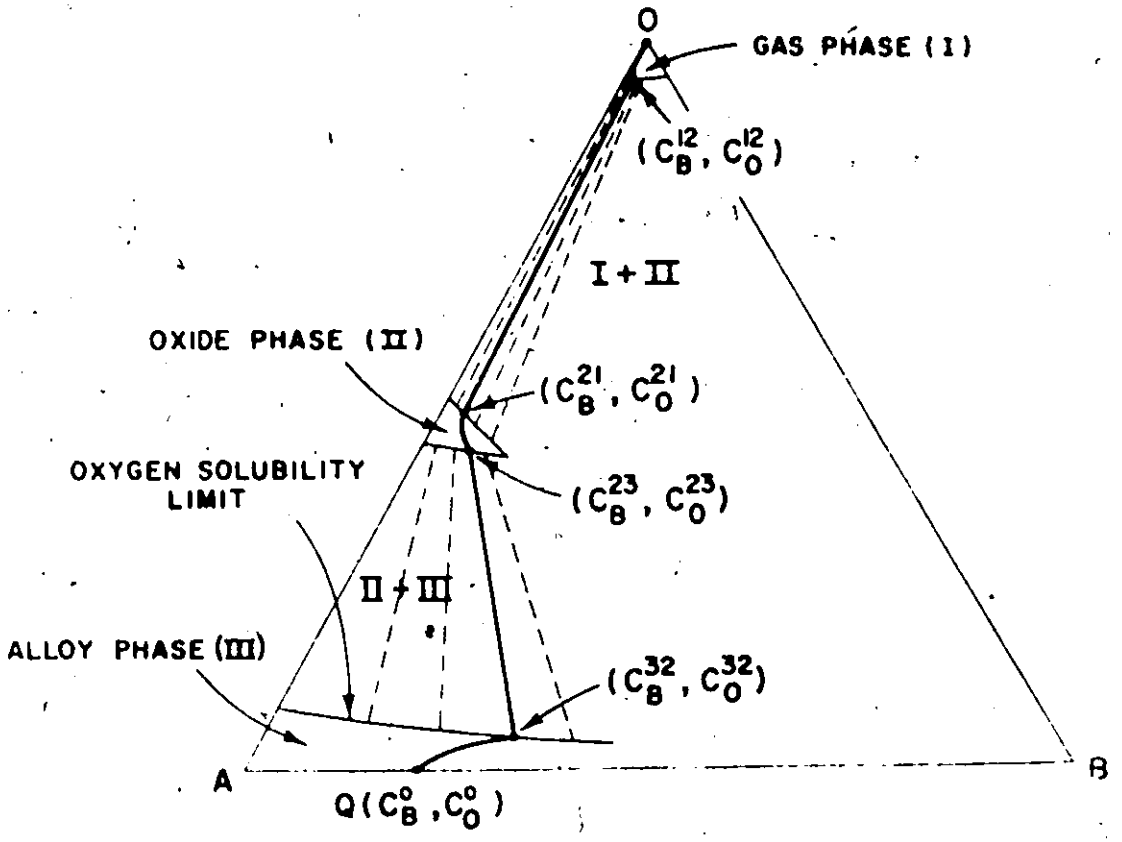

Fig. 3-3

Schematic representation of an isothermal phase diagram on which is superimposed the "virtual" diffusion path O-Q

to eliminate the supersaturation. On the other hand, if the calculated diffusion path does not enter a two-phase field, other than to cross it and is coincident with a tie line, then this path will coincide with the actual (experimentally observed) diffusion path if no kinetic instability occurs.

It was mentioned earlier that Kirkaldy and Brown[19] gave a list of 17 theorems pertaining to the construction of ternary diffusion paths. Dalvi and Coates[20] have given the more relevant of these rules for metal alloy oxidation and shown how they apply to several specific binary alloy systems. It is assumed that there is no evaporation of the alloying elements A and B and, for simplicity, that the atmospheric oxygen potential is unity.

(a) The shift in the alloy composition from the bulk alloy to the alloy-oxide interface is away from the component which is preferentially oxidized.

(b) The diffusion path must, at least once, cross the straight line joining the oxygen corner of the phase diagram to the bulk alloy composition.

(c) At a given temperature, the diffusion path is defined uniquely only by the bulk alloy composition and oxidizing atmosphere.

(d) In order to maintain monotonic activity gradients, a diffusion path in a two-phase region can not reverse its order of crossing tie lines.

(e) To the extent that the effect of lateral diffusion and nonplanar interfaces can be ignored or averaged out, the diffusion paths involving two-phase regions are time invariant.

3.5.2 Internal Oxidation and Alloy-oxide Interface Stability

In the previous section, it was mentioned that if the "virtual" diffusion path for the alloy cuts through a two-phase field (alloy + oxide) as indicated in Fig. 3-4, then a thermodynamic force exists for internal oxidation and for morphological breakdown of a planar alloy-oxide interface. Accordingly a "virtual" diffusion path predicts supersaturation and ultimate existence of configurations involving two-phase regions. The actual diffusion path can then be calculated by taking such predictions into account and reformulating the problem in such a way as to involve the appropriate two-phase regions.

Numerous quantitative treatments have been attempted to account for internal precipitation in the alloy; some important contributions are due to Rhines et al.,[21] Darken,[22] Thomas,[17] Wagner[23,24] and Kirkaldy.[25,26]

To account for morphological breakdown of a planar alloy-oxide interface, a method must be used involving application of mathematical perturbation theory. Wagner[23,28] has employed this method on certain limiting (pseudo-binary) situations, while Coates and Kirkaldy[29] have more recently generalized the treatment for application to systems of arbitrary constitution.

The interface could be unstable in the absence of supersaturation for purely kinetic reasons. On the basis of the simple argument,[28] the interface will maintain a stable planar shape if the oxidation rate is determined exclusively by mass transport in the oxide. On the other hand, if the rate determining process is transport in the alloy, there is a strong tendency for the interface to break down. If a planar interface is kinetically stable, supersaturation could be relieved by internal

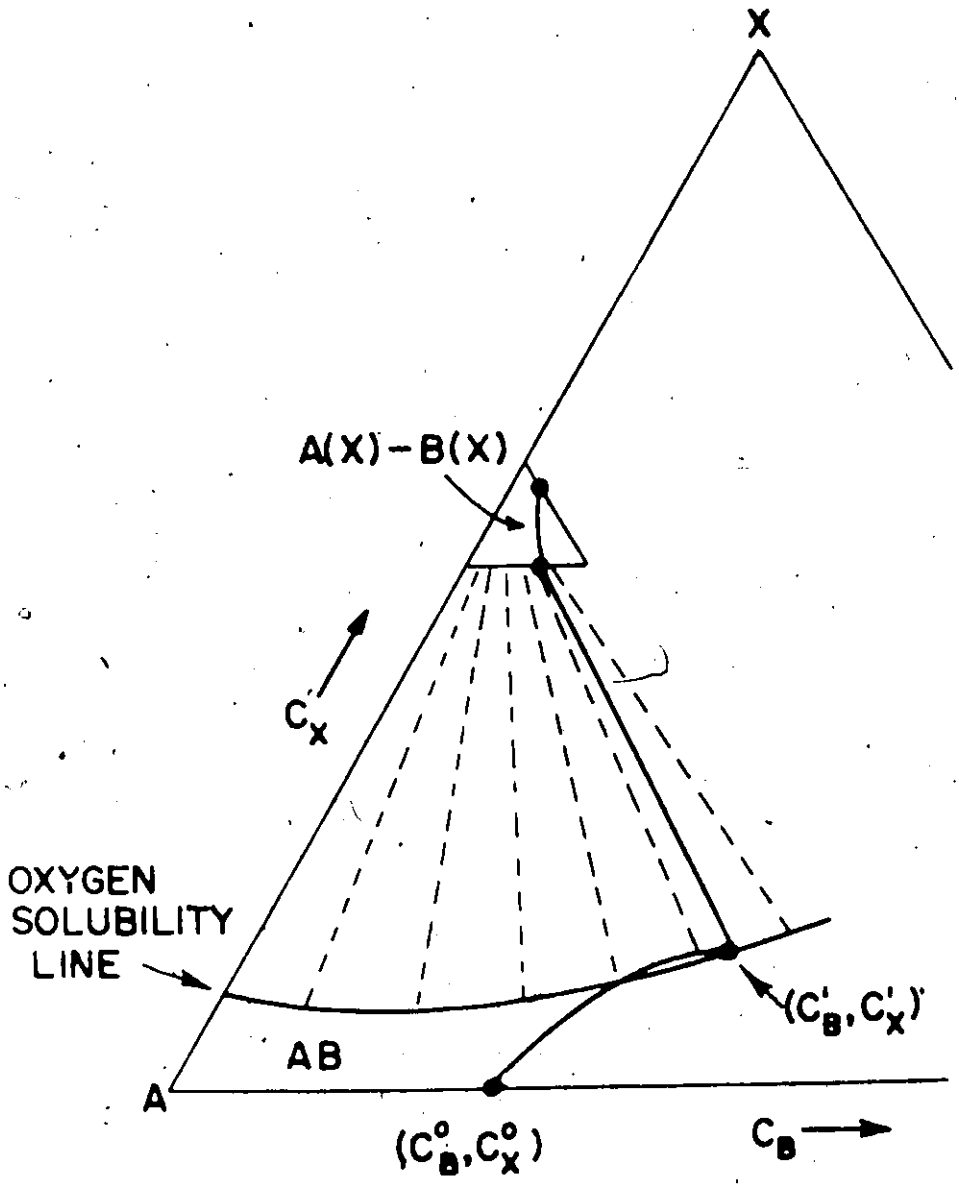

Fig. 3-4

"Virtual" diffusion path which does involve a supersaturation in the alloy

oxidation only. On the other hand if the interface is not stable the internal oxidation need not occur.

CHAPTER IV

EXPERIMENTAL DESIGN

4.1 Introduction

The aims of this work outlined in the first chapter and requirements of the theoretical treatment of diffusion controlled binary alloy oxidation were considered and correlated to select alloy systems for study and to design appropriate experimental tests. The basic requirements on the experimental system and the preliminary experiments leading to the selection of the alloy system are briefly described. In the last part of this section a brief description of the system chosen for experimentation is presented.

4.2 Requirements on the Experimental System

In order to apply and extend the general diffusion model[15] of binary alloy oxidation it was necessary to find a suitable experimental binary alloy system. There are two basic requirements of the theoretical analysis which have to be satisfied. The first is that the oxidation product should preferably be a one-phase oxide scale. The second gives a condition, that the interfaces must remain morphologically stable exhibiting a planar shape.

The solution of the diffusion equations requires that the thermodynamics and transport properties of the system be known to obtain the data for boundary conditions. Therefore, all or part of these data leading to suitable approximations should be available from the literature. Those

not available must be obtained from appropriate experiments or from iterations of numerical solutions.

For an experimental investigation of oxidation kinetics, the rate of the reaction should be measurable within a reasonable length of time with sufficient accuracy at achievable experimental conditions (temperature and pressure of oxidizing atmosphere). The limitations of the analytical and metallographical methods should also be taken into account. For example, the compositions of alloys should be high enough to be measurable quantitatively using an electron-probe microanalyzer which exhibits limitations based upon the type of alloy micro-structure and atomic number corrections for the constituents.

4.3 Preliminary Experiments

Initially a survey was made of the oxide systems forming solid solutions from known binary phase diagrams.[30] The oxides had to be those which were most stable if a given metal formed more than one oxide.

Since the oxidation behaviour of most of these systems had not been investigated previously, "oxidation mapping" was carried out for a total of seven binary alloys. The "oxidation mapping" is the determination of the type of scale forming during oxidation as a function of temperature, oxygen potential and alloy composition. All experiments were carried out at temperatures above the minimum at which the mobility of the ions ensured reasonable high rates of diffusion. The temperatures were estimated by Tamman's rule which relates the temperature T_a, at which lattice diffusion first becomes appreciable, to the absolute melting point (m.p.)T_m°K.

for metals $T_a \simeq 0.33\ T_m$

for salts and oxides $T_a \simeq 0.57\ T_m$

for covalent compounds $T_a \approx 0.90\ T_m$

For most metals this temperature is sufficiently low, but for oxides, which usually have very high melting points, this temperature may be fairly high. The following binary alloys were prepared and oxidized in CO_2-CO atmospheres or laboratory air depending on the stability of the oxidation product: Al-Cr, Al-Zn, Ni-Zn, Ni-Zr, Ni-Mn, Co-Mn and Co-Fe.

Only the Co-Fe system up to 10% Fe satisfied the two basic requirements which were a single-phase oxidation product and reasonable planar interfaces. A careful review of the literature established that the thermodynamics at 1200°C for Co-Fe-O system was known. Information pertaining to the transport properties of the alloy, pure and doped oxides, and the nonstoichiometry of the CoO-FeO solid solution are available from the literature. Therefore, the Co-Fe-O system was found to be suitable for theoretical analysis and appropriate for experimental investigations. In addition, the oxidation properties of Co-Fe alloys were not investigated previously. Since cobalt alloys are very important technological materials, the oxidation properties were examined over the whole range of compositions at five different oxygen pressures ranging from 10^{-4} to 1 atm.

CHAPTER V

PROPERTIES OF COBALT-IRON-OXYGEN SYSTEM

5.1 Introduction

The system utilized to demonstrate the relations between the diffusional properties and growth of oxide scales on binary alloys is based on Co-Fe alloys. Since the theoretical analysis of the oxidation phenomena is based upon limiting properties of the pure metal-oxygen systems, Fe-O and Co-O, pertinent results from these systems are presented in great detail.

5.2 Iron-Oxygen System

The system contains three oxides:[32] wüstite (FeO), magnetite (Fe_3O_4), and hematite (Fe_2O_3). Of these oxides, wüstite is only stable above 570°C. Wüstite and magnetite are both based on a face-centred cubic oxygen lattice; wüstite has the NaCl structure, while magnetite has the spinel structure. Hematite has the corundum structure.

5.2.1 Defect and Transport Properties of Iron Oxides

Wüstite (FeO)

The nonstoichiometry[33-43] of $Fe_{1-y}O$ as a function of partial pressure of oxygen has been extensively studied using thermogravimetry and solid state electrochemical techniques. The results of various studies are generally in a good agreement. The results of Vallet and Raccah[34] are shown in Fig. 5-1. It may be noted that the deviation from nonstoichiometry y varies from 0.05 at the iron-wüstite phase boundary up to 0.15 (depending on temperature) at the wüstite-magnetite boundary. In contrast to the

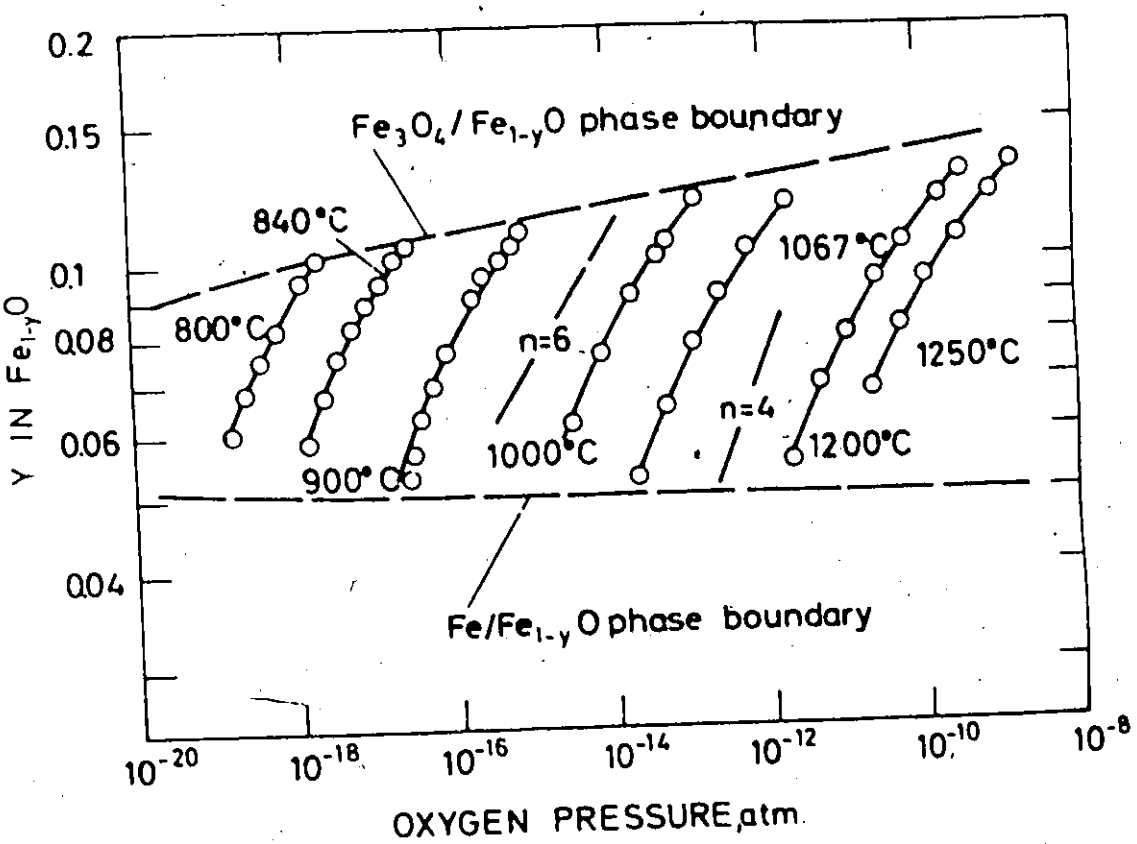

Fig. 5-1

The nonstoichiometry in wüstite, y in $Fe_{1-y}O$, as a function of temperature and partial pressure of oxygen

behaviour of most oxides, the nonstoichiometry of $Fe_{1-y}O$ at constant partial pressure of oxygen increases with decreasing temperature. The pressure dependence above 1000°C, $y \propto p_{O_2}^{1/n}$, can be characterized by values of n ranging from approximately 4 to 6. In many of the earlier interpretations of the defect structure of wüstite, it was commonly assumed that point defects constituted unassociated doubly or singly charged vacancies. These simple models do not appear to be presently tenable since structural investigation suggests[44-48] that the defects are complex. Kofstad and Hed[49] and Libowitz[50] both propose that the basic point defect is complex and consists of a tetrahedral ion and two associated octahedral vacancies as suggested by the structural studies.[44,46] Both models provide good agreement between experimental and calculated values of y as a function of oxygen activity. In spite of this fact, the controversy about the defect structure of $Fe_{1-y}O$ is not yet resolved.

The self-diffusion of a radioactive iron tracer in $Fe_{1-y}O$ as a function of nonstoichiometry and temperature has been studied by Himmel, Mehl and Birchenal,[42] Carter and Richardson[51] and Desmarescaux et al.[52] The tracer diffusion coefficient as a function of the composition reported by Himmel et al.[51] is shown in Fig. 5-2. These results are in fair agreement with others.[51,52]

Magnetite (Fe_3O_4)

Magnetite is a metal-deficit oxide relative to its stoichiometric composition and the formula may accordingly be written as $Fe_{3-y}O_4$.[32,53,54] The value of y increases with decreasing temperature at constant partial pressure of oxygen. Schmalzried[55] found an oxygen pressure dependence of

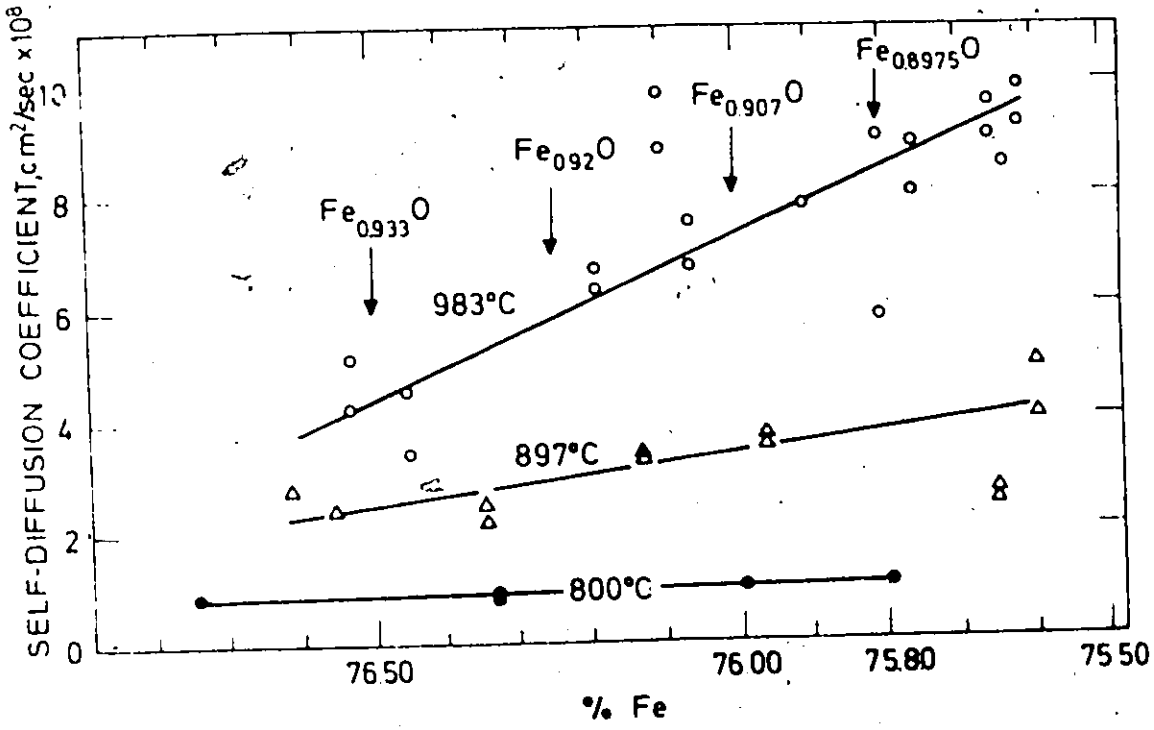

Fig. 5-2

The Fe-tracer diffusion coefficient as a function of composition and temperature in the wüstite phase

$D_{Fe} \propto P_{O_2}^{0.4}$ over the magnetite phase field at 1115°C. The detailed interpretation of the diffusion mechanism is difficult, particularly as the nature of the defects is in question. It is generally believed that these defects correspond to iron vacancies in the octahedral or tetrahedral metal lattice sites.

Hematite (Fe_2O_3)

Salmon[54] reported that Fe_2O_3 is oxygen deficient, and for Fe_2O_3 in equilibrium with Fe_3O_4 the value of x in Fe_2O_{3-x} ranges from 0.0015 at 1000°C to 0.011 at 1500°C. This result suggests that the predominating point defects are oxygen vacancies and/or interstitial iron ions.

Both Fe and O tracer diffusion in Fe_2O_3 have been studied. The results obtained by different workers[56-59] are in a fair agreement. It has been found that Fe and O ions diffuse at approximately the same rate in Fe_2O_3 at high temperatures.

5.2.2 Oxidation of Iron

A multilayer scale consisting of the three oxides is formed when iron is exposed at elevated temperatures to oxygen or dry air at ambient pressure. At temperatures above 700°C the growth proceeds very rapidly and scales become several microns thick within a few minutes. After a short initial period of non-steady state the oxidation proceeds by parabolic kinetics. During this period the relative proportions of the oxide layers remain unchanged being approximately 100:5:1 for $X_{FeO}:X_{Fe_3O_4}:X_{Fe_2O_3}$.

Davies et al.,[60] Paidassi[61] and Schmahl et al.[62] have presented a large body of results on parabolic scaling amenable to theoretical analysis when combined with the previously discussed results on Fe-O thermodynamics.

defect structures and diffusional properties of wüstite. Himmel et al.[63] first applied the Wagner theory[3] to the oxidation of iron. They used their determinations of the iron self-diffusion constants and data from the Fe-O diagram on wüstite compositions and oxygen activities to evaluate the parabolic oxidation constants. These calculations however are only valid to a first approximation for relating theoretical and experimental values of the parabolic rate constants since the small amounts of higher oxides formed were not taken into account.

The influence of oxygen pressure on the oxidation properties of iron was extensively studied in two temperature ranges. At temperatures between 200°-550°C[64-69] the early oxidation stage involves processes of nucleation and growth of magnetite. Later the growth of hematite on a developed magnetite layer or separation of this scale from the metal leads to a decrease in oxidation rate. In the temperature range 550°-600° there are large discrepancies among results[70-75] reported for the influence of oxygen pressure on the form of the oxidation curve and the reaction rates. In recent work Goursat and Smeltzer[76] established the rates and mechanism of iron oxidation in the pressure range 2.5×10^{-3} to 3×10^{-1} Torr at 800°C. The reaction exhibits initially an increasing oxidation rate followed by a stage of linear kinetics before onset of parabolic kinetics. The first oxidation state is associated with the growth of wüstite crystals over an oxide base film while linear kinetics govern the growth of a uniformly thick wustite scale. The scaling rate was proportional to the oxygen pressure due to reaction control by nondissociative oxygen adsorption; the sticking coefficient of oxygen was 0.067. Parabolic kinetics governed the

growth of duplex scales containing layers of wüstite and magnetite. The parabolic oxidation rate was independent of oxygen pressure since the transport through the wüstite scale was rate limiting.

The results[60,77] for iron oxidation in oxygen at temperatures higher than 1000°C do not indicate the presence of the non-parabolic initial period. The data for oxidation at reduced pressures of oxygen are not available.

5.3 Cobalt-Oxygen System

There are three oxides of cobalt, namely CoO, Co_3O_4 and Co_2O_3 which have respectively cubic, spinel and hexagonal structures.[78] Of those three oxides, Co_2O_3 is unstable above 300°C, so will not be considered further, and Co_3O_4 above 850-950°C at pressures lower than atmospheric. CoO and Co_3O_4 are thought to be metal-deficit semiconductors.

5.3.1 Defect and Transport Properties of Cobalt Oxides

Cobaltous Oxide (CoO)

Cobaltous oxide is generally assumed to be approximately stoichiometric at its decomposition pressure (which ranges from 10^{-12} atm O_2 at 840°C to 10^{-6} atm at 1440°C). At a partial pressure of oxygen higher than that of decomposition, the concentration of cation vacancy defects increase with increasing oxygen pressure.

Fisher and Tannhauser[79] determined the phase diagram of CoO_{1+x} in the range of temperatures 900°C-1450°C and the range of pressures bounded by $p(O_2)$ = 1 atm. and the phase boundary as shown in Fig. 5-3. This phase diagram was determined by combining thermogravimetric and electrical measurements. Fisher and Tannhauser identified a range (A) where V_M' (single charged vacancy)

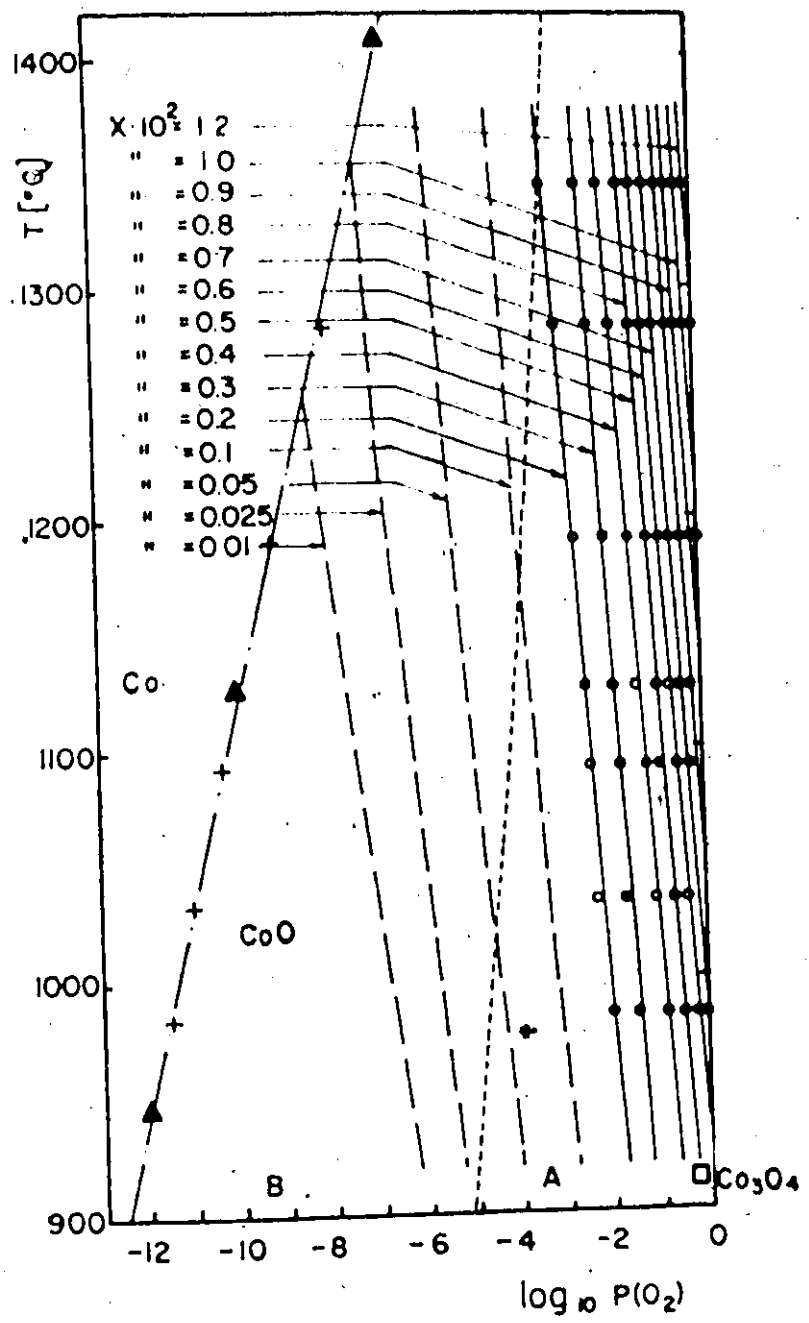

Fig. 5-3

The nonstoichiometry in cobaltous oxide, x in CoO_{1+x}, as a function of temperature and partial pressure of oxygen

was the dominant defect species (the slope of log σ vs. log $p(O_2)$ being 1/4), and a second range (B) where V_M'' (double charged vacancy) was the dominant defect, with slope 1/6. These two regions have been confirmed by Henri Lé Brusq et al.[80] at 1000°C. Also Eror and Wagner[81] found a slope of about 1/4 for the conductivity and deviation from stoichiometry. In the range 1000°C-1200°C, Eror's measurements were confined to the region of pressures called A in Ref. (79). His measurements were made on single crystals, whereas Fisher used polycrystals. Sockel and Schmalzried[82] measured at 1200°C the deviation from stoichiometry x by a coulometric method down to $p(O_2) = 10^{-7}$ atm. They found a slope 1/4, whereas Fisher's[79] conductivity results at the same temperature gave a slope of 1/6 at log $p(O_2) \simeq -3.0$. The difference in slopes is explainable if one keeps in mind, that the transition from slope 1/4 to 1/6 in log σ vs. log $p(O_2)$ should occur about four orders of magnitude of $p(O_2)$ before the transition in log x vs. $p(O_2)$.

The self-diffusion of cobalt in CoO as a function of temperature (950°C to 1400°C) and partial pressures of oxygen (1 to 10^{-5} atm) has been studied by tracer techniques by Carter and Richardson,[83] Chen et al.[84] and Crow.[85] The tracer diffusion coefficient is plotted as a function of the oxygen pressure in Fig. 5-4.[83] At 1 atm O_2 the tracer diffusion coefficient[83] is given by $D_{Co}^t = 2.15 \times 10^{-3} \exp(-34{,}500/RT)$ and $D_{Co}^t = 5 \times 10^{-3} \exp(-38{,}390/RT)$ measured by Chen et al.[84] in air. The data of Crow[84] will be shown later in the section on diffusion in mixed CoO-FeO oxide. The diffusion coefficient[83] is proportional to about $p_{O_2}^{1/3}$ at 1 atm and to about $p_{O_2}^{1/4}$ at 10^{-3} atm. This is in agreement with the nonstoichiometry

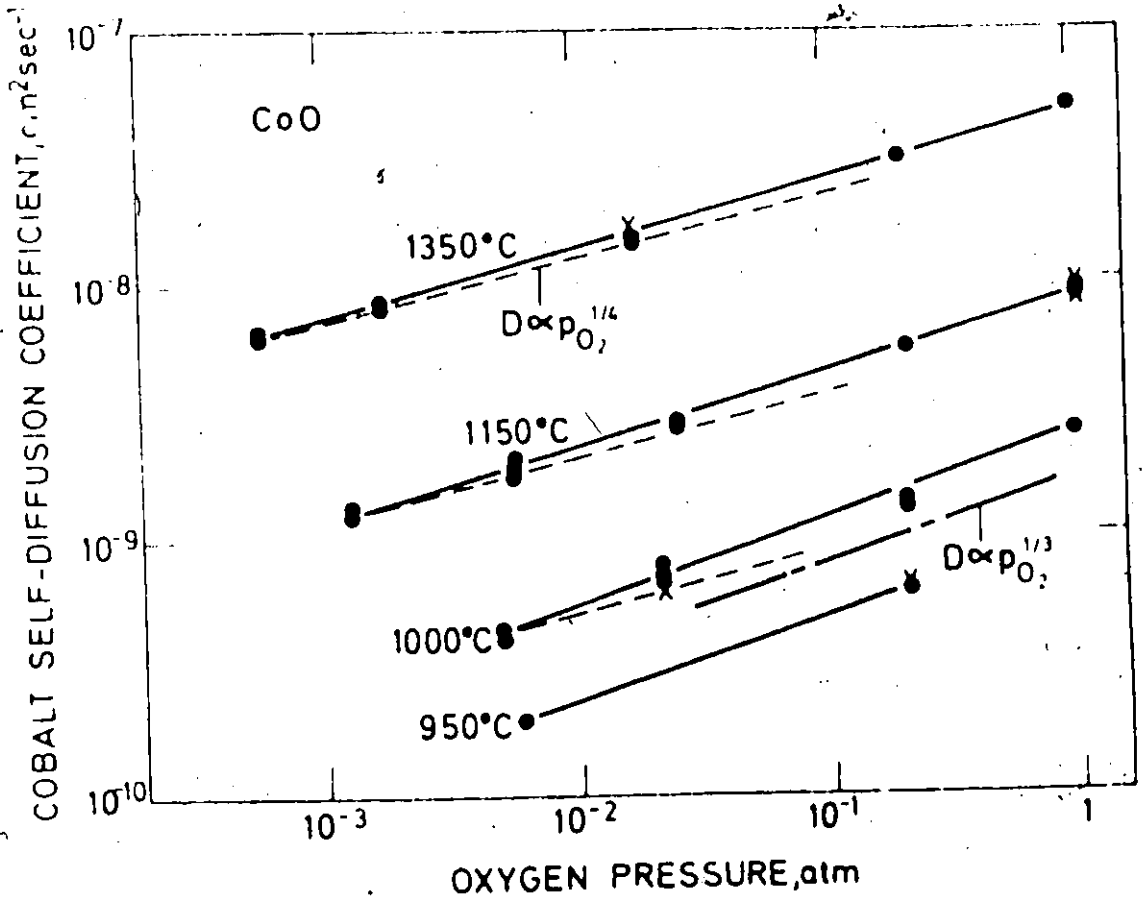

Fig. 5-4

Tracer diffusion coefficient of cobalt in CoO as a function of partial pressure of oxygen in temperature range 950° to 1350°C

studies[79] in that the vacancies are singly charged at reduced pressures and that neutral vacancies make a contribution close to 1 atm O_2.

Oxygen diffusion in CoO has been studied by Thompson,[86] Chen and Jackson[87] and Holt[88] and it has been found to be several orders of magnitude slower than that of cobalt at the same oxygen pressure. The mechanism of oxygen diffusion has not been definitely determined.

Co_3O_4

The structure of Co_3O_4, according to Schmalzried,[89] can be best described as inverse spinel. There are but limited data available on diffusion in Co_3O_4. Oxygen diffusion has been studied by Thompson,[86] who reported a diffusion coefficient $D_o = 2.4 \times 10^{-22} \exp(-176{,}000/RT)$. Wagner and Koch[90] have reported that the electrical conductivity of Co_3O_4 is essentially independent of the partial pressure of oxygen between 1 and 0.21 atm O_2 at 900°C.

5.3.2 Oxidation of Cobalt

The two layer scale consisting of CoO and Co_3O_4 forms when cobalt is exposed to oxygen at 1 atm pressure at temperatures below 750°C, and one layer scale consisting of CoO only above 950°C.

The oxidation kinetics of cobalt have been extensively studied and the results were reviewed by Paidassi,[91] Wood[92] and more recently by Morin and Rigaud.[93] It has been found that between 400°C and 1400°C a parabolic relationship is obeyed with some initial deviations between 400°C and 800°C. The Arrhenius plot of the parabolic oxidation rate constants as a function of temperature[93] exhibits three distinct regions where the activation energy is constant. The first region at temperatures above 950°C corresponds

to scale formation of CoO only. The Wagner theory of parabolic oxidation[3] was successfully used by Carter and Richardson[94] to calculate the theoretical rates of parabolic oxidation from diffusion constants measurements. The experimental and theoretically calculated rates are in good agreement. The transition region between 950°C and 750°C is characterized by a sharp decrease in oxidation rate with temperature. Below 750°C the oxidation product is composed of two layers of CoO and Co_3O_4. In the latter two regions the influence of oxygen pressure on the oxidation rate was found to be not very pronounced.[93]

The parabolic oxidation rate constant could be expressed as

$$k_p = k_o \cdot p_{O_2}^{1/n} \cdot e^{(-Q/RT)} \qquad (5.1)$$

where k_o is constant, n is the coefficient of oxygen pressure dependence for k, Q is activation energy and T is temperature in °K. The numerical values of k_p's obtained from numerical analysis of numerous experimental results accumulated in the literature on the parabolic oxidation of cobalt in the view of Eq. 5.1 are listed in table 5.1

Table 5-1

Temperature range C°	k_o (g^2/cm^4-s)	n	Q (kcal/mole)
above 950°C	6.43×10^{-2}	2.8	37.5
750°C-950°C	1.50×10^{2}	-	56.3
450°C-750°C	2.96×10^{-5}	-	24.9

5.4 Cobalt-Iron-Oxygen System

An oxygen potential diagram for Co-Fe-O system was established by Ankrust and Muan[95] using their data obtained by a thermogravimetric method and data obtained by Roiter and Paladino.[96] The diagram shown in Fig. 5-5 illustrates the equilibrium existence of the phases Co-Fe alloy, (Co, Fe)O and $(Co, Fe)_3O_4$ at 1200°C as a function of oxygen pressure. This diagram is in essence complementary to the classical ternary phase diagram (Co-Fe-O). These two different ways of plotting phase equilibrium data are related through the Gibbs-Duhem relation. This type of representation of thermodynamic information about ternary systems is rational and is used extensively in oxidation practice because metal compositions of various phases are directly related to oxygen pressures.

5.4.1 Activities and Diffusivities in Co-Fe Alloys

The thermodynamic properties of Co-Fe alloys were studied by Satow et al.[97] In the temperature region[98] of γ phase stability, (for all alloys above 1020°C), the entropy of mixing and heat of mixing show almost ideal behaviour, and the activity obeys Raoult's law. Therefore, the alloys in the entire range of compositions at 1200°C could be considered as being ideal.

Interdiffusion studies using Co-Fe diffusion couples were completed by Badia[99] for temperatures in the range from 1136°C to 1356°C. The electron probe microanalyser was used to measure the concentration profiles from which utilizing Boltzman-Matano analysis[100,101] the interdiffusion coefficients D_{FeCo} were calculated. The diffusion constant at 1200°C increases from 2.3×10^{-11} cm^2/sec for pure iron with increasing cobalt content to a maximum

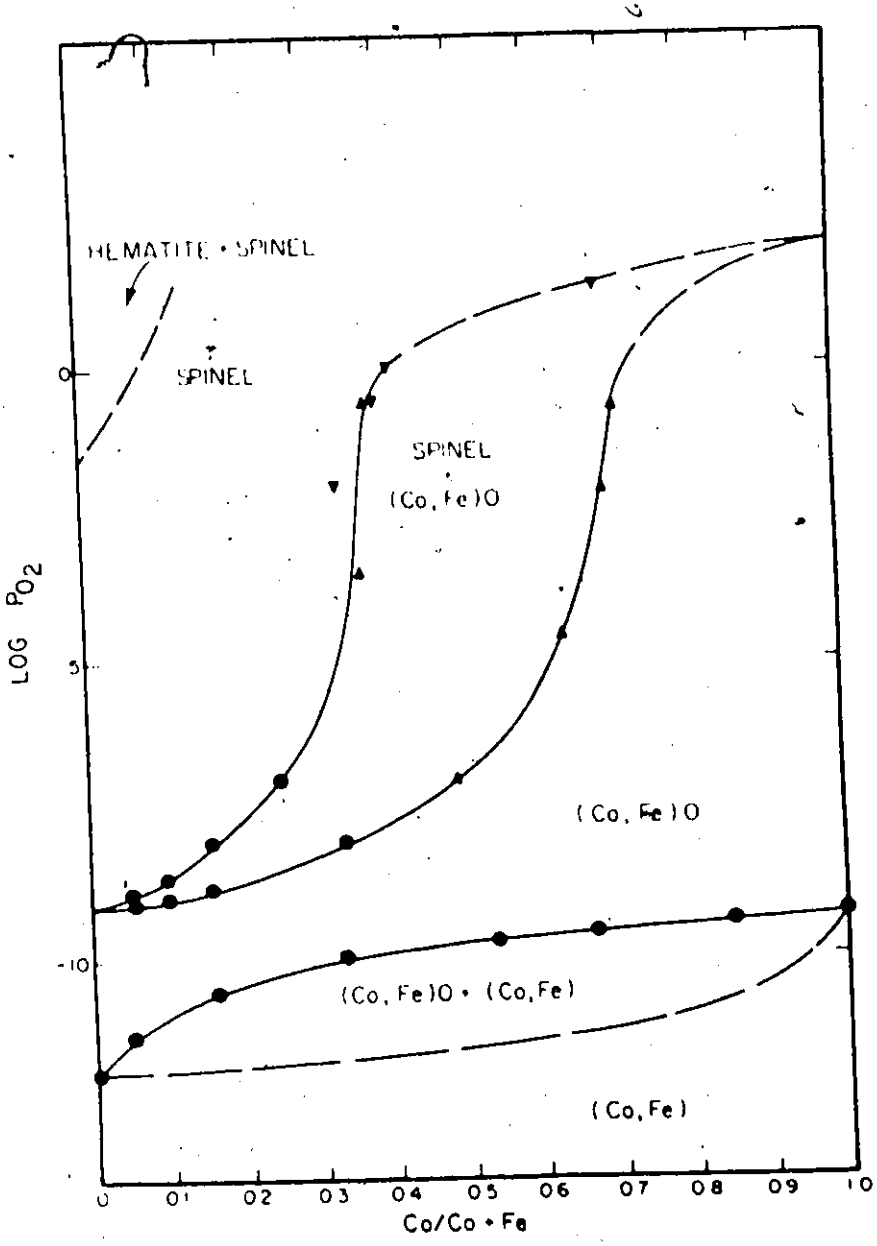

Fig. 5-5

The oxygen potential phase diagram for Co-Fe-O system at 1200°C

value of 1.19×10^{-10} cm^2/sec at about 70 atomic percent of Co in the alloy. It subsequently decreases being equal to 9.2×10^{-11} cm^2/sec for pure cobalt. The numerical data for 1200°C are shown in Table 5-2

Table 5-2

Interdiffusion coefficients in Co-Fe at 1200°C

Iron content in alloy [atomic fraction]	$\tilde{D}_{FeCo} \times 10^{10}$ [cm^2/sec]
0.0	0.92
0.1	1.05
0.2	1.15
0.3	1.19
0.4	1.14
0.5	0.94
0.6	0.81
0.7	0.52
0.8	0.41
0.9	0.29
1.0	0.23

5.4.2 Activities, Defect Concentrations and Diffusivities in CoO-FeO

Both cobaltous oxide and wüstite are isomorphic, i.e. they have the rock salt structure and the cations are similar in size, weight and electronic structure. At 1200°C they form a solid solution over a wide range of compositions and oxygen potentials as illustrated by the phase diagram in Fig. 5-5.

A knowledge of the activities of the oxide components in solid solution is necessary for the calculation of cation distributions in oxide scales formed on Fe-Co alloys exposed to oxygen. Ankrust and Muan[102]

determined experimentally the activity of CoO in cobaltowüstite in equilibrium with Co-Fe alloys at 1200°C. The results are shown graphically in Fig. 5-6. The CoO activity curve shows a slight positive deviation from ideality, but at low concentrations of CoO in cobaltowüstite Henry's law is obeyed since the activity of CoO is linearly dependent on concentration. Because of the large defect concentrations in wüstite and cobaltowüstite,[95] it is reasonable to assume that the activity-composition relations in the oxide phase coexisting with a spinel phase at relatively high oxygen pressures will not be the same as those prevailing in the oxide solid solution coexisting with metal. The Gibbs-Duhem integration due to Schuhmann[103] was used to determine the activities of CoO and FeO from a knowledge of oxygen potentials in the cobaltowüstite phase field.[95] The CoO activity curve shown in Fig. 5-7 exhibits only slight positive deviations from ideality. The corresponding FeO activities can be obtained by a simple binary Gibbs-Duhem integration by assuming ideal behavior for the Co-Fe phase.

Cobalt oxide behaves as a p-type semiconductor containing metal vacancies in the singly and doubly ionized states, the former being predominant over a major portion of its oxygen stability range.[79,81] Iron substituted into this oxide is considered to give rise to the following defect equilibrium

$$1/2\ O_2 + \alpha Fe^{+2} \rightarrow O^{2-} + V_M^{\alpha-} + \alpha Fe^{+3} \qquad (5.2)$$

where the designated iron and oxygen ions occupy normal lattice sites and $V_M^{\alpha-}$ is a vacancy in the metal sublattice with electrical charge $\alpha-$. There are insufficient results, however, for analyzing this defect equilibrium

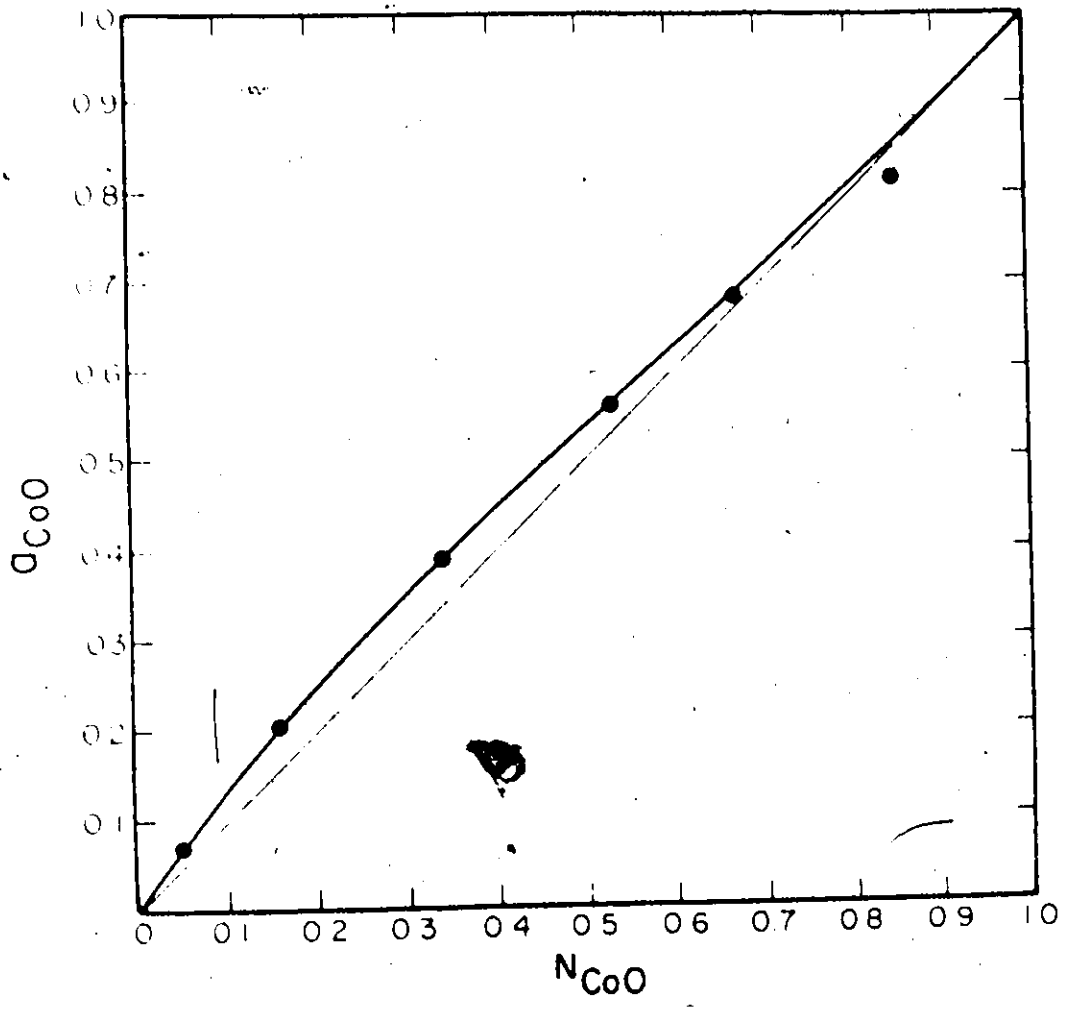

Fig. 5-6

Activity of CoO in contact with metallic phase (Co-Fe alloy) as a function of oxide composition in the system CoO-FeO at 1200°C

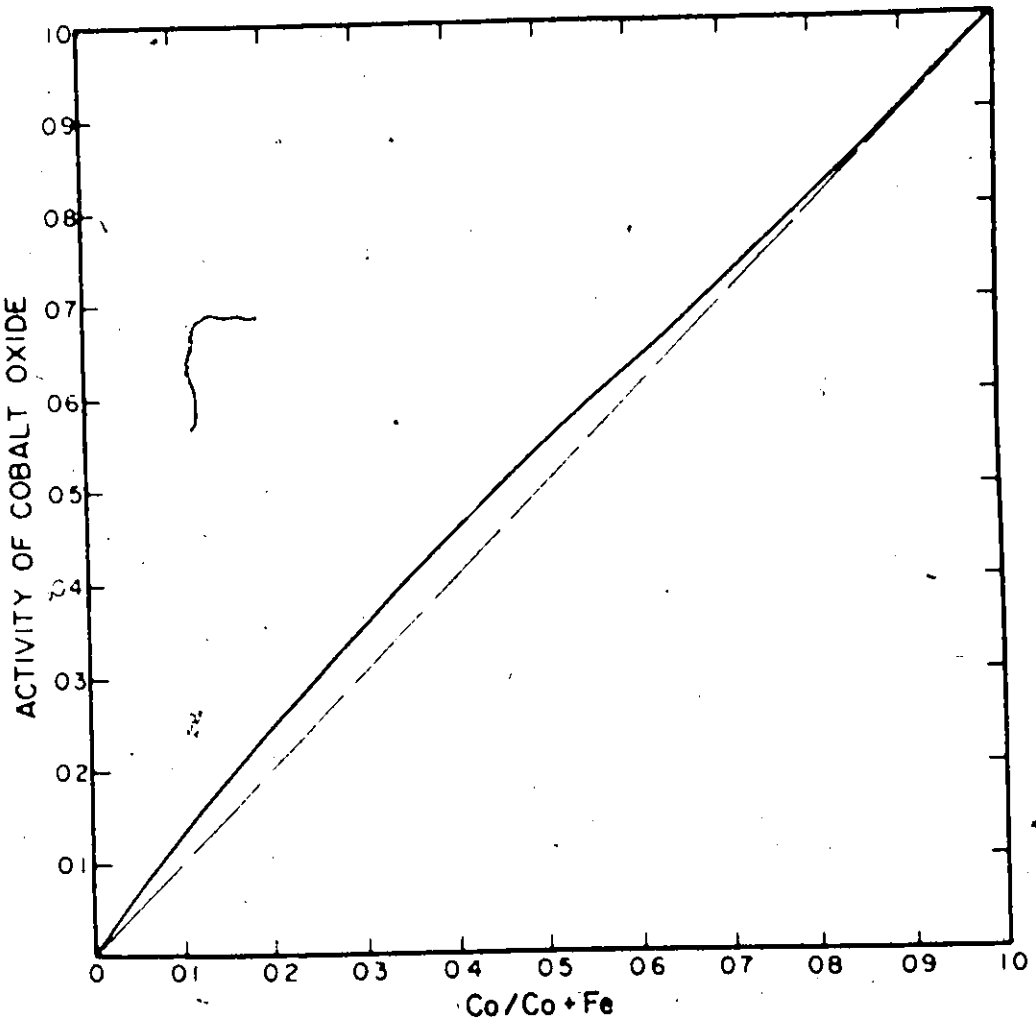

Fig. 5-7

Activity of CoO in contact with spinel phase ($(Co,Fe)_3O_4$) as a function of oxide compositions in the system CoO-FeO at 1200°C

in detail. It is reasonable, nevertheless, to suggest that the vacancies occur predominantly from the influence of iron by the displacement of the above reaction far to the right. Assuming to a first approximation, that the fraction of the total iron content ionized to the ferric remains constant, at fixed oxygen activity, the atom fraction of vacancies is of the form

$$N_V = \gamma a_o^{n} \xi \qquad (5.3)$$

Here , a_o is the oxygen activity, ξ is the iron atom fraction in the cation sublattice of (Co,Fe)O, ν and n are empirical constants.

Vacancy concentrations were calculated from the compositions of (CoFe)O reported by Ankrust and Muan[95] using the formula $N_V = X - 1/X$ where X is the oxygen atom fraction per metal atom fraction (X = O/Fe + Co). N_V is plotted vs. ξ for several values of oxygen pressure in Fig. 5-8. Linear plots relate these variables for oxide compositions encountered in the present work. Fig. 5-9 shows the slopes N_V/ξ plotted as a function of corresponding oxygen potentials on logarithmic scales. It is seen that a constant power relationship for the oxygen activity dependence is an adequate approximation although the additionally depicted plot exhibiting a small curvature may account in a more factual manner for the vacancy behaviour. Accordingly the constants in Eq. (5.3) are expressed as $\gamma = 0.60 \pm 0.11$ and $n = 0.15 \pm 0.03$.

It is essential to represent the metal self-diffusion coefficients by appropriate analytical expressions involving their dependence on the iron concentrations and oxygen activities in order to numerically integrate the differential equations introduced in Chapter 3. The following formalism

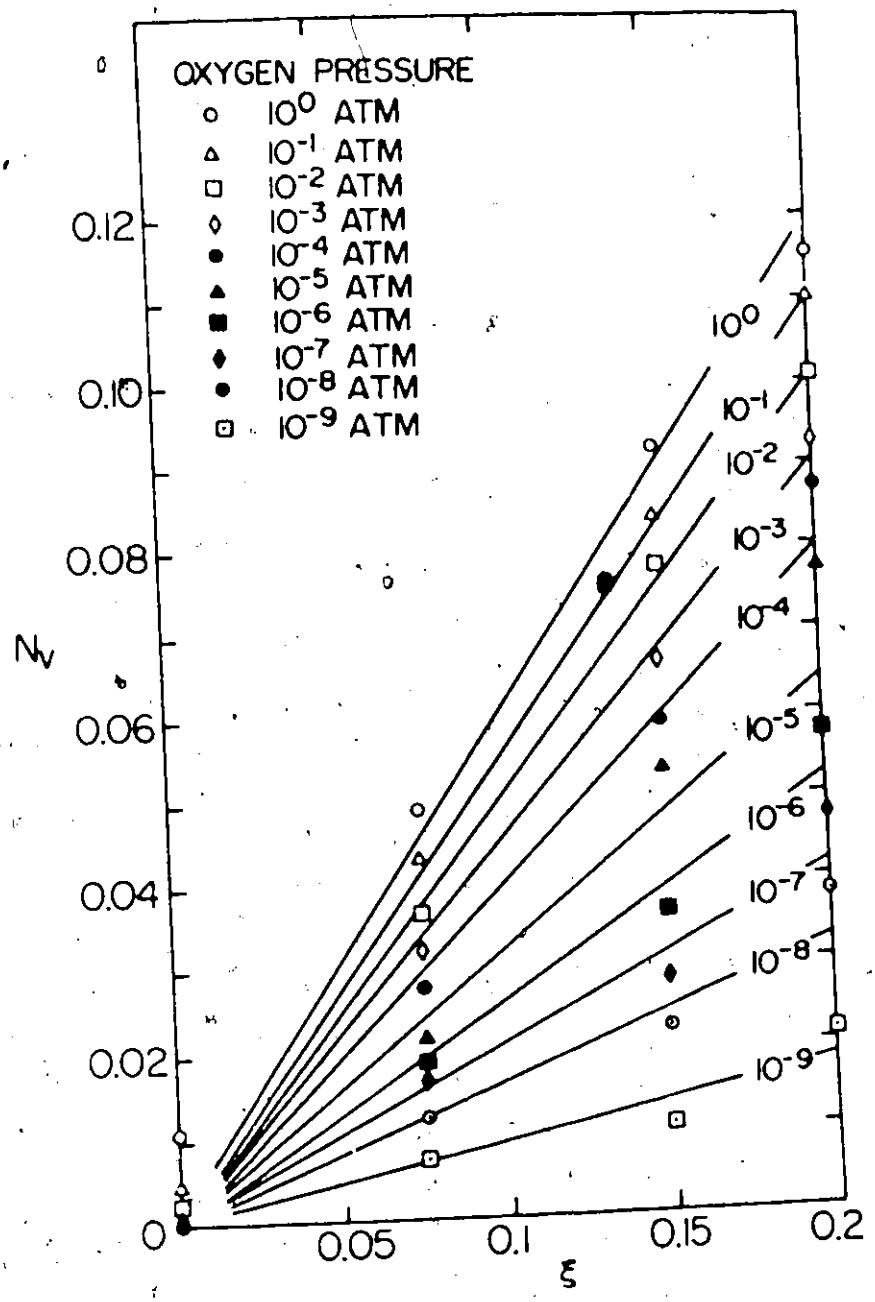

Fig. 5-8

"etal vacancy concentration plotted vs. Fe^ molar fraction in (Co,Fe)O for oxygen pressures ranging from 10^{-9} to 1 atm at 1200°C

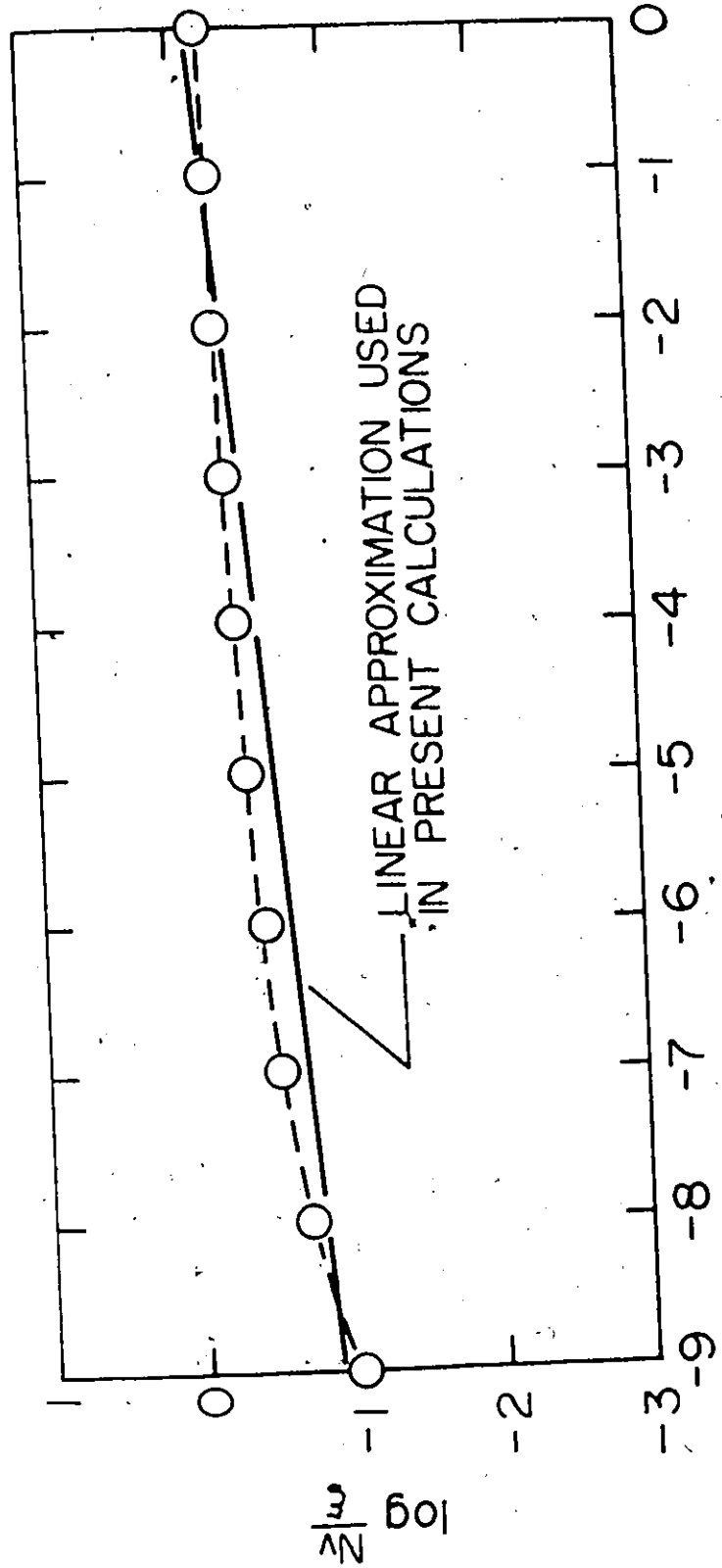

Fig. 5-9

Atomic fraction of vacancies per molar fraction of FeO in (Co,Fe)O plotted vs. oxygen pressure

is used to relate the self-diffusivity to the vacancy diffusivity, vacancy concentration and chemical composition of (CoFe)O:

$$D_{Co} = D^{V}_{Co} N_V = D^{O}_{Co} \gamma a_O^{n} \quad (5.4)$$

$$D_{Fe} = D^{V}_{Fe} N_V = D^{O}_{Fe} \gamma a_O^{n} \quad (5.5)$$

and $$p = D_{Co}/D_{Fe} = D^{O}_{Co}/D^{O}_{Fe} \quad (5.6)$$

In the absence of direct experimental measurements of tracer or self-diffusion coefficients of cobalt, the vacancy diffusivity must be calculated from the data for pure CoO. Using this constant and experimentally obtained values for defect concentrations in cobaltowüstite, the self-diffusion constant for cobalt cations could be calculated from Eq. (5.4) as a function of composition and pressure. Carter and Richardson[83] expressed the tracer diffusion coefficient of cobalt in cobalt oxide as a function of oxygen activity by a constant power relationship. Using these results and those reported by Fischer and Tannhauser[79] for the dependence of cobalt vacancy concentration on oxygen activity, the cobalt vacancy diffusivity at 1200°C was calculated to be $D^{O}_{Co} = 1.46 \pm 0.04 \times 10^{-6}$ cm^2/sec. The actual numerical values used in this estimation are shown in Table 5.3

The ratio p, of cobalt and iron cation diffusivities in cobaltowüstite on the cobalt side was estimated from tracer diffusion measurements of Co^{60} and Fe^{55} in single crystals of CoO reported by Crow.[85] The interpolated data for 1200°C are shown in Table 5-4. These measurements are suitable for calculation of p because the level of impurities and consequently the level of defect concentration was altered to a negligible extent by

Table 5-3

Cation and vacancy diffusivities and defect concentrations in CoO_{1+x} at 1200°C

P_{O_2} (atm)	D^t_{CoO} (cm^2/sec)	N_V	$D^o_{Co}xf$ (cm^2/sec)
10^{-0}	1.35×10^{-8}	0.0119	1.13×10^{-6}
10^{-1}	6.5×10^{-9}	0.00566	1.14×10^{-6}
10^{-2}	3.7×10^{-9}	0.00299	1.23×10^{-6}
10^{-3}	2.9×10^{-9}	0.00169	1.12×10^{-6}

Average value of D^o_{Co} xf = 1.14×10^{-6} cm^2/sec.

From $D_{Co} = D^o_{Co} \gamma a^n \xi^m = D^t_{CoO} \frac{1}{f}$, if f = 0.78

the vacancy diffusivity is

$$D^o_{Co} = 1.46\pm0.04\times10^{-6}\ cm^2/sec$$

adding the radioactive tracer for penetration measurements.[85] The calculated values are listed in Table 5-4 and graphically represented in Fig. 5-10.

5.4.3 Oxidation of Cobalt-Iron Alloys

A comprehensive study of Co-Fe alloy oxidation over the entire range of composition was carried out by Voitovich[104] at temperatures between 500°C and 900°C. The scales were compact and protective at all temperatures. The sharp increase of the oxidation rate was observed at temperatures higher than 700°C. This effect was caused by the appearance of wüstite in the scale layer which contained a high concentration of cationic defects. The oxidation rate as a function of the cobalt content passed through a shallow minima corresponding to cobalt contents in the range of 30-70% at all temperatures. It was established that Fe-Co alloys, especially the alloy with 50% cobalt, have higher oxidation resistance than the pure metals at all temperatures. A compact and mechanically strong dark gray scale was formed except on alloys containing high iron contents at 900°C. In these cases, the scale layer formed cracks during oxidation. The decrease in oxidation rate for the alloys was attributed to spinel formation, which hinders the diffusion of oxygen and metal.

Additions of 2 to 6% Co have been reported[105] to lengthen the lifetime of iron wires at higher temperatures (1050°C). Above this temperature experimental results are not available on the oxidation properties of Co-Fe alloys.

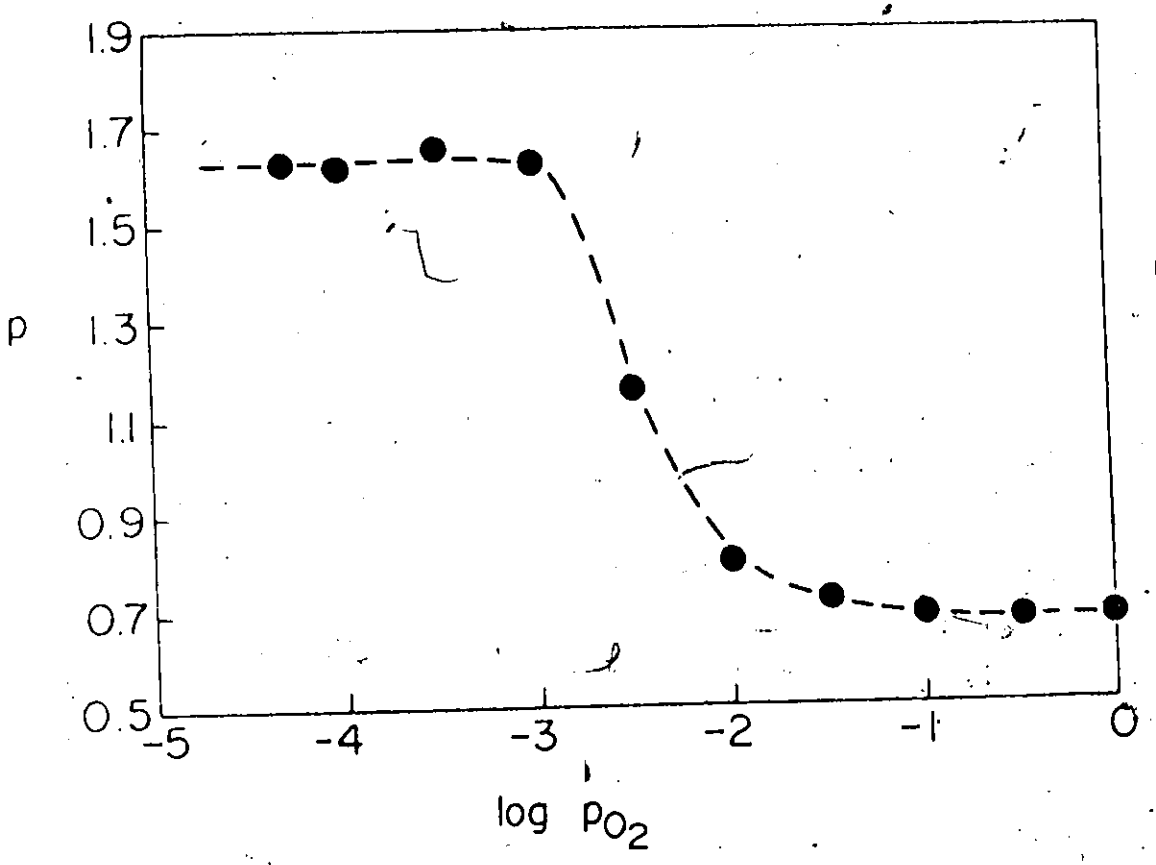

Fig. 5-10

Ratio of tracer diffusion coefficients of Fe^{55} and Co^{60} in single crystal CoO at 1200°C as a function of oxygen potential

Table 5-4

Diffusivities of Co^{60} and Fe^{55} in CoO at 1200°C as a function of oxygen potential[85]

$\log_{10} P_{O_2}$	$D^{Fe^{55}}_{CoO} \times 10^8$ (cm^2/sec)	$D^{Co^{60}}_{CoO} \times 10^8$ (cm^2/sec)	p*
0.0	1.70	2.50	0.68
-0.5	1.16	1.71	0.68
-1.0	0.83	1.22	0.68
-1.5	0.59	0.82	0.72
-2.0	0.48	0.60	0.80
-2.5	0.46	0.40	1.15
-3.0	0.45	0.28	1.63
-3.5	0.43	0.26	1.66
-4.0	0.39	0.24	1.61
-4.3	0.37	0.23	1.62

* $p = \frac{D^{Fe^{55}}_{CoO}}{D^{Co^{60}}_{CoO}}$

CHAPTER VI

TECHNIQUES AND PROCEDURES OF EXPERIMENTS

6.1 Introduction

A variety of experimental techniques and procedures were used for preparation and analysis of materials, for carrying out the oxidation investigations and for identification and analyses of oxidation products. These techniques include argon arc melting, vacuum annealing, chemical analysis of materials, a thermogravimetric method of weight gain measurements, optical and electron metallography, X-ray diffraction and electron probe microanalysis.

The experimental procedure involved preparation of Fe-Co alloys. Specimens prepared from these alloys were exposed to oxygen atmospheres of various pressures at 1200°C. Oxidized alloys were then subjected to identification and analytic examinations.

6.2 Alloy and Specimen Preparation

The iron and cobalt used in this investigation were supplied by A.D. Mackay Co. and by Johnson Matley Chemical Ltd., respectively. The chemical compositions of the metals as supplied by the companies is given in Table 6-1.

The portions of each material, mechanically and chemically cleaned, were accurately weighed to yield alloys with nominal composition of 0, 1, 2, 4, 6, 8, 10, 20, 30, 40, 50, 70, 80 atomic percent of iron in cobalt. Approximately 300 g of material were placed in the melting chamber

Table 6-1

Chemical Composition of Used Iron and Cobalt

Composition of Iron:

ELEMENT	PERCENT
Aluminum	0.003
Calcium	0.001
*Carbon, Total	0.004
Chromium	0.003
Cobalt	0.005
Copper	0.001
Magnesium	0.0005
Manganese	0.001
Nickel	0.020
*Oxygen	0.05
Silicon	0.001
*Sulfur	0.004
Zirconium	0.001

*Determined by chemical analysis.

Composition of Cobalt:

ELEMENT	Parts per million
Silicon	10
Nickel	5
Iron	2
Aluminum	1
Calcium	<1
Copper	<1
Magnesium	<1
Silver	<1

of a nonconsumable arc furnace with a tungsten electrode operating under argon atmosphere. In order to prevent any long range segregations, each charge was melted, inverted and then remelted until a total of four melting operations had been completed. The alloys were in the form of rods, 3 inches long and 1/2 inch in diameter. They were sealed in a quartz tube partially filled with argon and annealed for different periods of time at 1000°C to completely homogenize the composition depending on the size of the rod. After this, they were machined to uniform diameter and cut with a multiple wire saw to the final specimen shape. So obtained flat discs 10 x 2 mm were mounted in Bakelite and metallographically polished on all surfaces to 1μ diamond abrasive using kerosene as lubricant. After removal from Bakelite mountings, the specimens were cleaned with petroleum ether and stored under dried acetone until required. Immediately before an experimental test a specimen was dried and weighted to ±0.1 micrograms, and its surface area was computed by measuring the specimen dimensions with a micrometer.

The actual chemical compositions of the used alloys were determined by the two methods. The atomic absorption photometry, a modern and now commonly used way of chemical analysis, was backed by standard ASM wet chemical analysis for Co. The list of alloy compositions is shown in Table 6-1.

6.3 Experimental Apparatus

The experimental assembly was comprised of three parts: reaction gas supply system, reaction chamber with a suspension device for specimens and a continuous recording semiautomatic microbalance. The schematic diagram on Fig. 6-1 represents an overall view of the basic components of

Table 6-2

Actual Chemical Composition of Prepared Alloys

Nominal Composition	Actual Composition Fe	
	w/o	a/o
Co-1% Fe	0.93	0.98
Co-2% Fe	2.1	2.2
Co-4% Fe	4.1	4.3
Co-6% Fe	5.5	5.8
Co-8% Fe	7.7	8.1
Co-10% Fe	9.6	10.1
Co-20% Fe	19.3	20.2
Co-30% Fe	28.6	29.7
Co-40% Fe	38.6	39.9
Co-50% Fe	49.9	51.3
Co-70% Fe	69.3	70.4

Fig. 6-1: Schematic of reaction assembly containing RV Ainsworth continuously recording semiautomatic microbalance: 1 - oxygen purifier containing silica gel, 2 - reflection mirror, 3 - observation window, 4 - Pirani gage, 5 - supporting ring for heating element, 6 - silicone carbide heating element, 7 - furnace, 8 - mullite tube, 9 - thermocouples, 10 - Pirani gage, 11 - loading inlet, 12 - soft iron core, 13 - magnet, 14 - outer tube, 15 - suspension tube, 16 - specimen, 17 - suspension wire, 18 - expansion bellow, 19 - automatically switched weights, 20 - glass bell, 21 - transducer, 22 - cold trap, 23 - diffusion pump, 24 - mechanical pump.

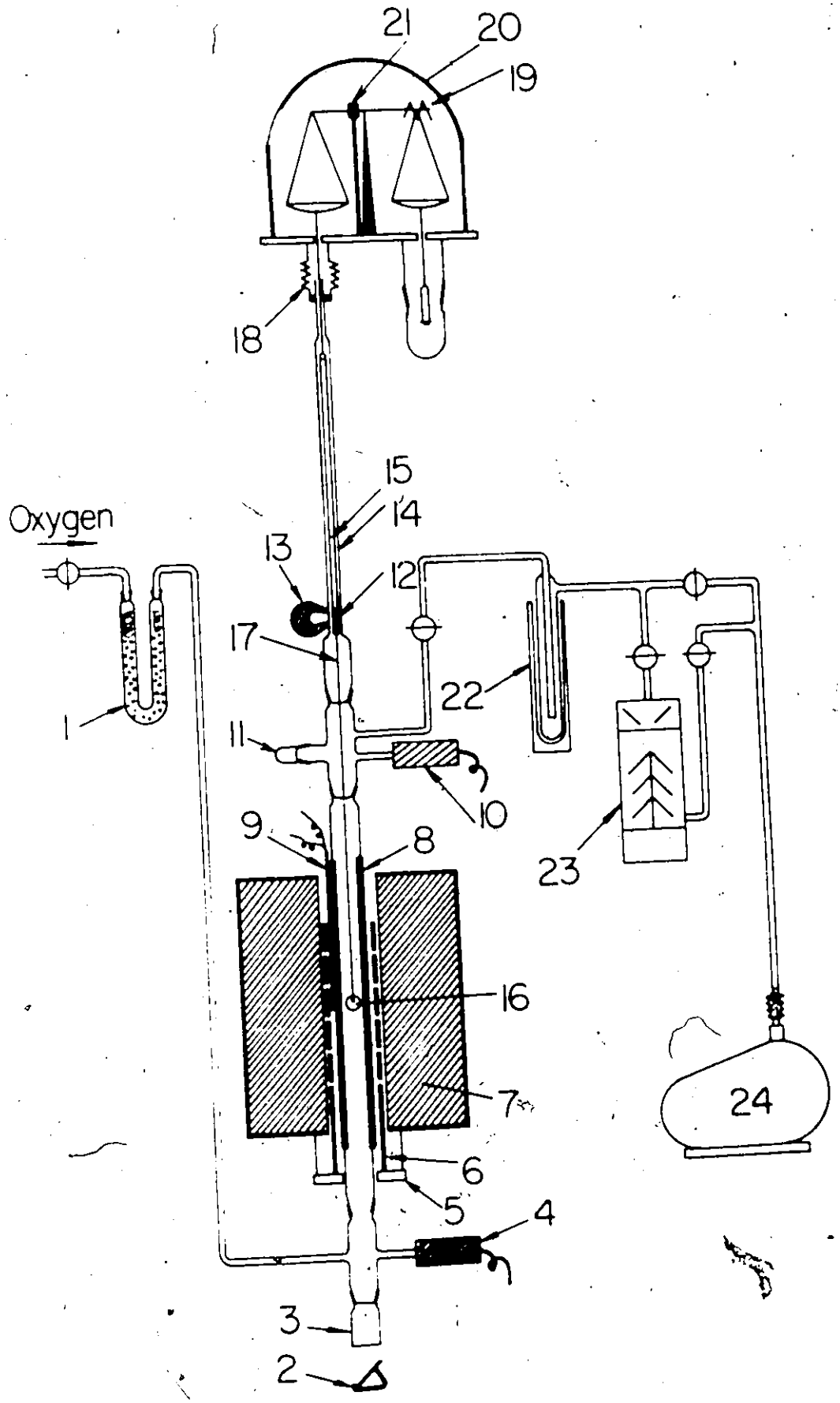

Fig. 6-1

the assembly. The numbers mark the essential parts and are explained in the figure caption.

Oxidation rates in flowing oxygen atmospheres were measured with an Ainsworth, Type RV, continuously recording semiautomatic balance. The balance had a sensitivity of 0.01 mg and the weight gain was recorded on an Ainsworth, Type AU-1, recorder unit with Bristol's recorder. Temperature in the mullite tube reaction chamber was controlled to within ±2°C by a proportional controller, Thermoelectric type 400, and the power was supplied continuously to the silicon carbide heating element, Crusilite, single muffle type. Two controlling Pt/Pt-13 Rh thermocouples were placed between the heating element and mullite tube. The actual temperature profile inside the reaction chamber was obtained by measuring the temperature by means of a calibrated thermocouple suspended into the reaction zone at different depths. This calibration procedure was repeated before each series of experiments. The sample to be oxidized was attached to the microbalance by a two-stage magnetic suspension device, which consisted of a Pyrex tube closed at the top and partially open at the bottom. It was connected to one beam of the microbalance by nylon fibre. An Armco iron core inside the tube could be manipulated by the magnet outside the assembly. The specimen was suspended in the furnace by means of platinum wire attached to the iron core. This arrangement allowed the test specimen to be raised and lowered in the furnace without any direct contact from outside. A dish suspended from the second beam of the balance permitted delicate balancing of the balance. Prior to the lowering of the sample into the hot zone of the furnace, the desired oxygen pressure was set by leaking dry oxygen (Matheson U.H.P. grade) through a metering needle valve into the reaction chamber continuously pumped with a Speedivac

mechanical vacuum pump, ED150 type. This type of dynamic regulation was found to be very effective in maintaining constant oxygen pressure in the reaction chamber, especially at the low pressures. Zero time for oxidation was taken at the instant when the sample was lowered into the hot zone.

After the specimens had been oxidized to the desired extent, they were raised out of the hot zone. The system was backfilled with oxygen and the specimens were taken out. The specimens were then weighed and mounted edgewise in cold self-setting resin for metallographic observations.

6.4 Identification and Analytic Methods

6.4.1 Chemical and X-ray Analysis

The compositions of the alloys were determined by two methods: the standard chemical wet analysis (ASM) and atomic absorption determination.

In the first method, a metal sample was dissolved in HCl (1:1). After dissolution and addition of stannous chloride, potassium permanganate and mercuric chloride, the total iron was determined by titrating with potassium dichromate. In the second method the metal samples, accurately weighed, were dissolved in boiling concentrated HCl. After cooling, the solutions were diluted to yield the approximate concentrations acceptable for the atomic absorption photometer, model No. 303 by Perkin-Elmer Ltd. The measured values were recalculated to yield the contents of cobalt in weight percent.

X-ray analysis was used to identify the phases present in oxide scales. Oxide scales were scraped off the exposed samples and ground in an agate mortar to a fine powder. The samples were prepared by filling

very fine glass capillaries with powder and placing them in the Debye-Scherer camera exposed to copper K_α radiation. From so obtained radiograms, it was possible to identify the oxide phases.

6.4.2 Specimen Preparation for Metallographic and Microprobe Measurements

The mounted specimens were polished on silicon carbide papers through 200, 320, 400 and 600 grit, with final polishing on 6 and 1μ diamond paste impregnated napless cloths using kerosene as lubricant. In all the polishing operations only kerosene was used as lubricant because it was found that water eroded the oxide surface. The mounting compound, plastic epoxy No. 20-8130 AB supplied by Buehler Ltd. was found to be hard enough after setting to reduce the surface area relief arising in polished cross-section due to various constituents of various hardness.

The microstructures of the specimens after polishing were examined by means of the Zeiss optical microscope. A 1 to 5 minute etch in 80 parts lactic acid, 5 parts HCl, 10 parts hydrogen peroxide, and 10 parts HNO_3 was utilized to accent the oxidized cross-sections.

Before measurements on the microprobe, a thin layer of carbon was evaporated on the surface of the polished cross-section to prevent electric charge build up on nonconductive parts of the sample.

6.4.3 Electron Probe Microanalysis

The theory and practice of electron probe microanalyses is completely described in the following references.[106,107,108,109] In the present investigation a Cameca MS-64 model electron probe microanalyser was used to measure the chemical compositions of investigated alloys and oxide scales. The instrument has the take-off angle 18° for the exited X-rays.

The best operating conditions found for the Co-Fe-O system were at an acceleration voltage of 15 kV and specimen current between 100 and 150 nano-amperes. The K_α lines for Fe and Co are well separated and therefore were selected for the purpose of analysis. However, Co fluoresces Fe, especially in samples rich in Co and causes an increase in intensity of X-rays emitted by iron. Accordingly, calibration of the microprobe is necessary, if it is used for quantitative analysis. In the process of calibration the relative intensities of the X-rays from the element of interest, are obtained as a function of the composition. The relative intensity is the ratio of the X-rays from a given element in alloy or oxide minus the background intensity and the X-ray intensity from a pure element minus the background intensity. The background intensity could be obtained by counting with the spectrometer set a few degrees off the peak, or as in the present measurements on Co-Fe alloys, by setting the spectometer for Co and counting pure Fe and vice-versa. The X-ray intensity from a given element minus the background intensity is proportional to the amount present in the alloy or oxide. Since this observed, corrected absolute intensity varies from day to day, only the relative intensity is of interest because it does not vary with subjective factors such as instrument set up, etc. The calibration curves of relative intensity versus the composition could be obtained by two methods. The first method makes use of standards containing known amounts of elements and is a relatively simple process. The second method is a calculation procedure which allows one to calculate theoretically the desired relation using all available knowledge of the various necessary corrections.

The first method was used to calibrate the probe for Co-Fe alloys. The standards were actual alloys used in the present experiments. The results of the measurements are shown in Fig. 6-2. As previously mentioned the fluorescence effect of Co on Fe gave rise to the higher relative intensities for iron. On the other hand, the lower relative intensities for cobalt indicate absorption of the X-rays.

The second method was used to obtain the calibration curves for cobaltwüstite. This method was chosen because it was impractical to prepare separately the cobaltowüstite standards. The method described by Friskney and Howorth[110,111] consisted of successively applying atomic number,[112] absorption[113] and fluorescence[114,115] corrections to an assumed compositional set. A computer was used to limit numerical operations. Tables of theoretical relative intensity ratios for Fe and Co were generated. The calculated values are plotted in Fig. 6-3. The calibration procedure was verified only for pure cobaltous oxide.

The measurements were done on specimens prepared the same way as for optical examinations. However, it was necessary to deposit a thin layer of carbon on the surface to be examined to prevent any build up of charge on the non-conductive oxide phases present. To insure accurate results the method of point counts was used. The readings were obtained within the oxide and alloy phases at various distances from the alloy-oxide interface. Corrections were applied to these readings and phase compositions were thus obtained as a function of the distance from the interface for samples oxidized for different time periods. It was necessary in this procedure that the polished edge of a sample be perpendicular to its surface and the movement of the sample be perpendicular to the detector axis.

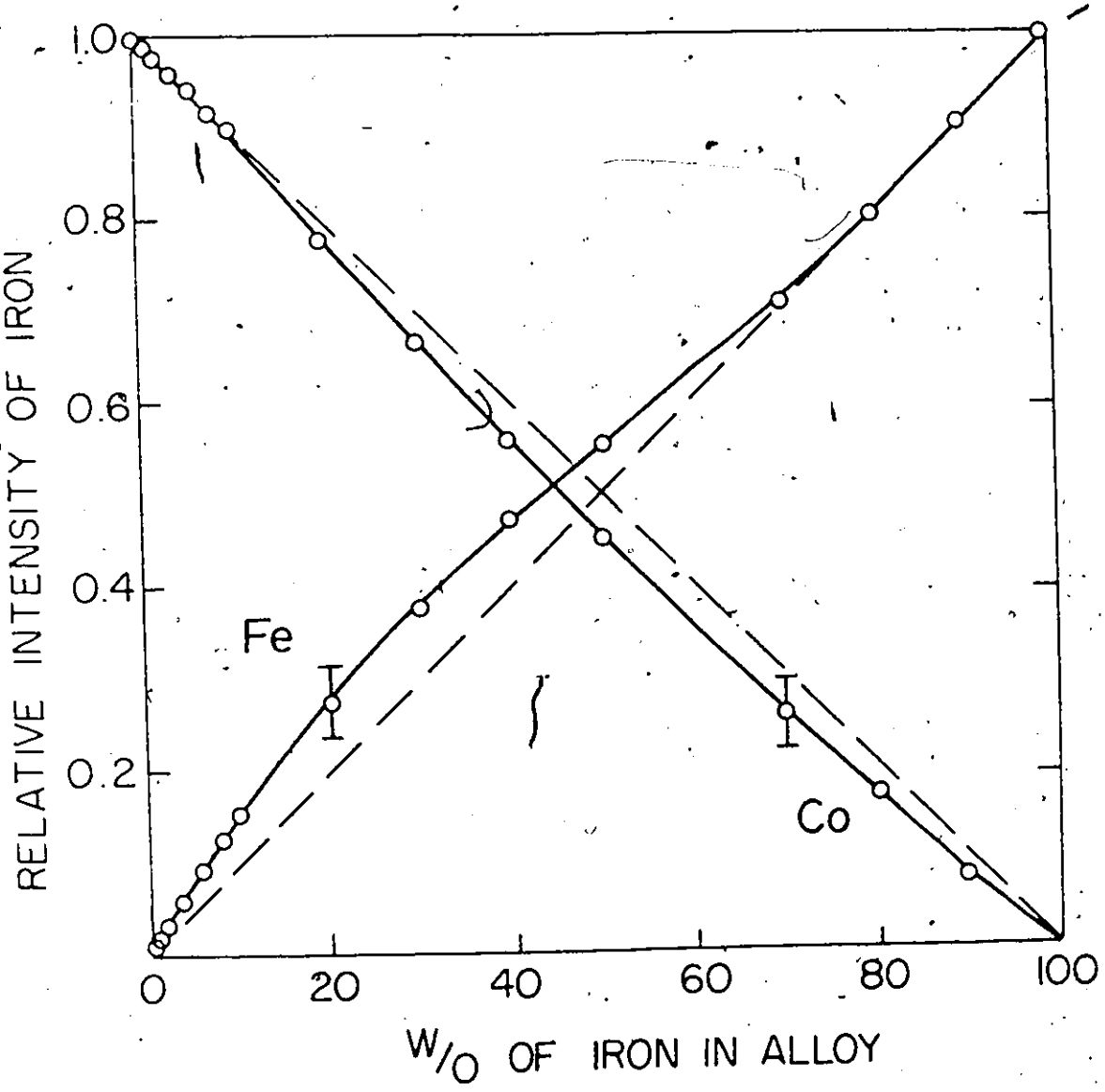

Fig. 6-2

Measured relative intensities of X-rays generated by iron and cobalt in Co-Fe alloys at 15 kV

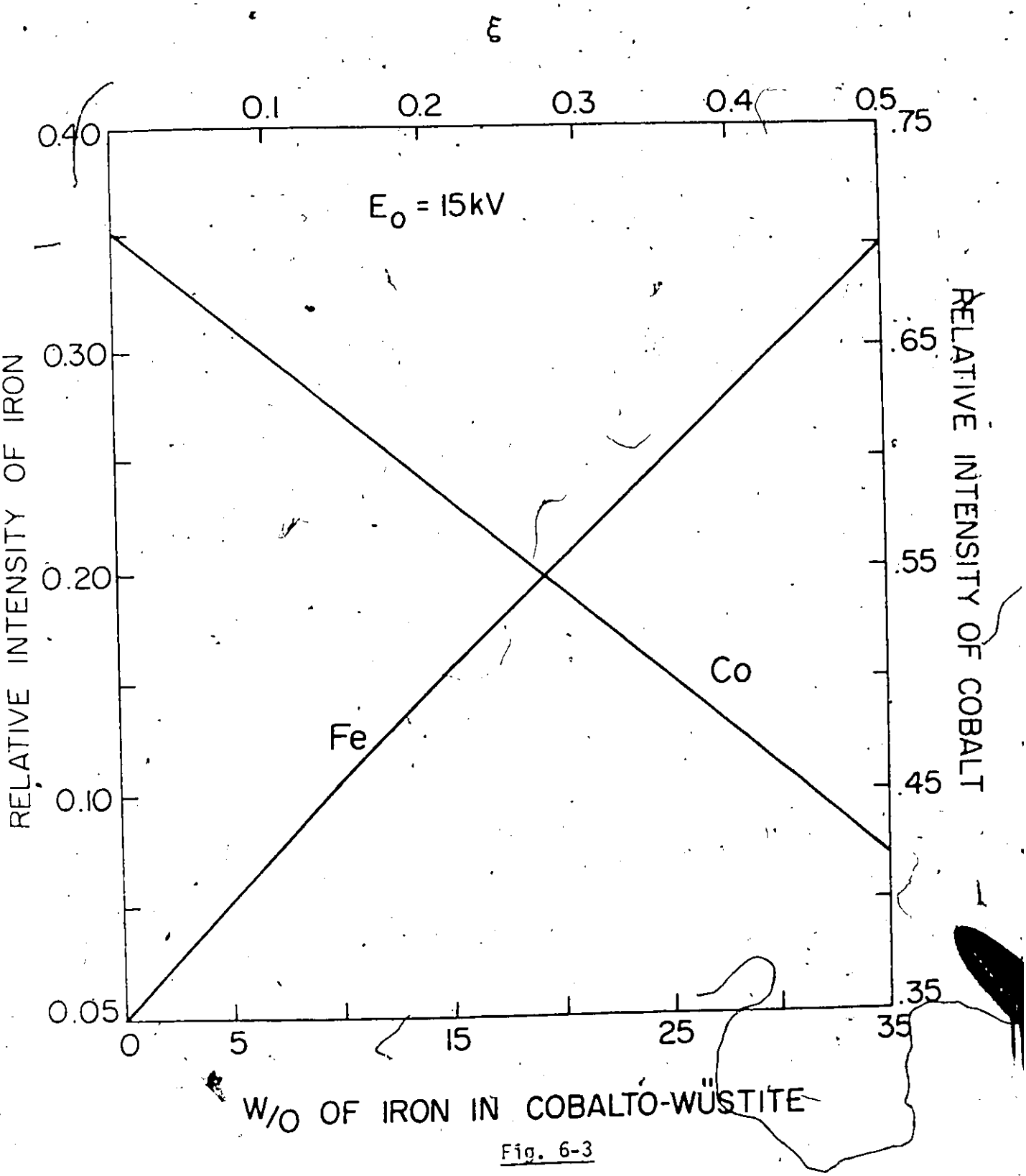

Fig. 6-3

Calculated relative intensities of X-rays generated by iron and cobalt in cobaltowüstite at 15 kV

CHAPTER VII

EXPERIMENTAL RESULTS AND THEIR INTERPRETATION

7.1 Introduction

A detailed investigation of oxidation properties of Co-Fe alloys exposed to oxygen atmospheres of various pressures at 1200°C is described in the following chapter. The oxidation properties are characterised by reaction rates, morphological development of scales and concentration profiles in the alloy and oxide phases. These characteristics are presented as results obtained from the various experimental and analytical tests described in the previous chapter in the form of diagrams, tables and photomicrographs. The behaviour of the alloys is followed as a function of iron content in cobalt and oxygen pressure at constant temperature 1200°C (2192°F).

7.2 Oxidation Kinetics

The results from the investigations on the oxidation kinetics obtained by recording the increase in specimen weight (consumption of oxygen) as a function of time are presented as smooth curves since a continuous recording balance was used. The weight gains are expressed in mg/cm^2 and time in minutes in Figs. 7-1 to 7-10. The experimental conditions, the temperature and oxygen pressure from 10^{-4} atm to 1 atm, are indicated on the graphs. There are two plots for each pressure: for alloys containing 0% Fe to 10% Fe and for alloys containing 20% Fe to 80% Fe. The period of oxidation varied from 10 minutes to 120 minutes depending on

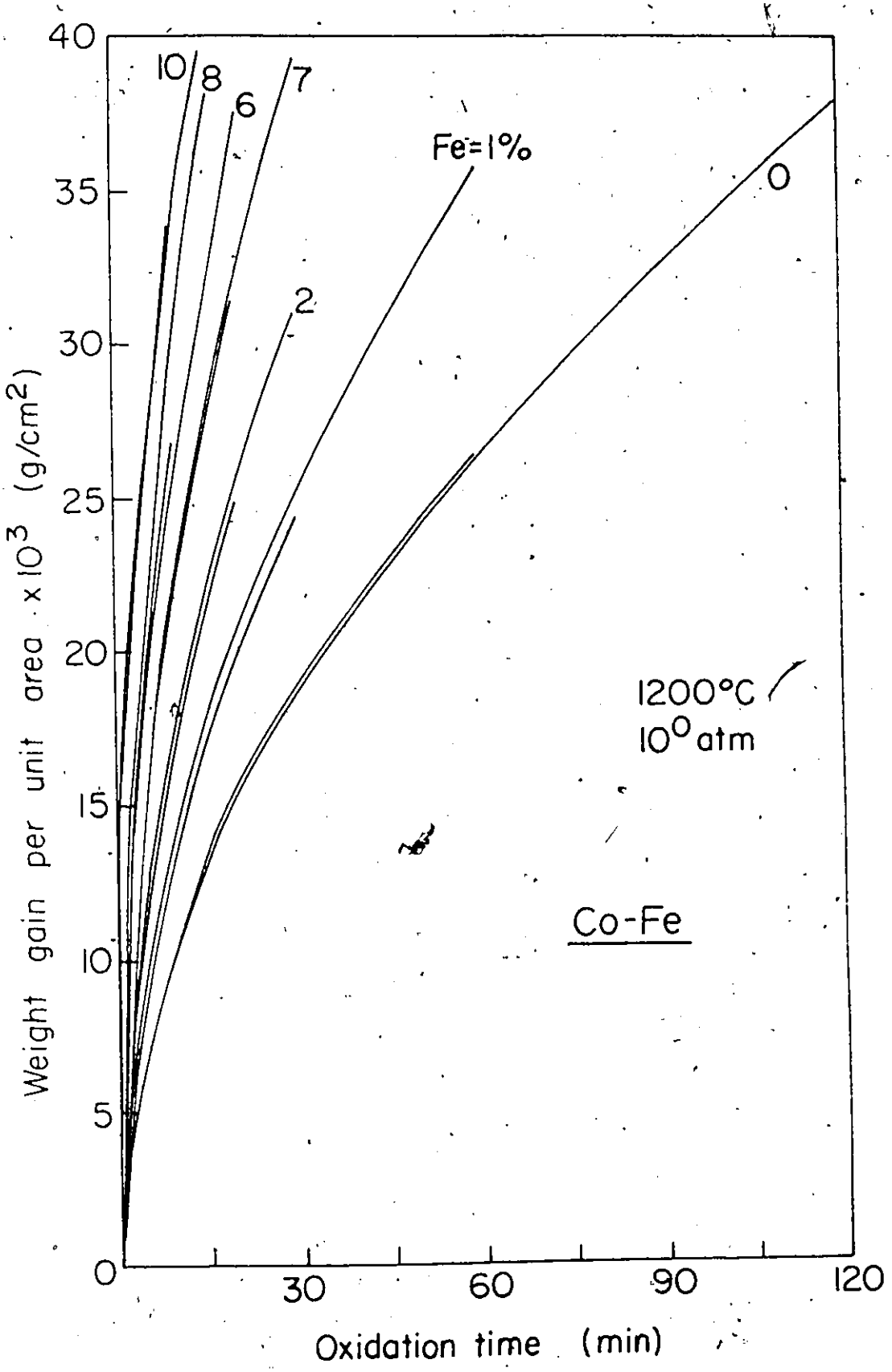

Fig. 7-1

Oxidation kinetics

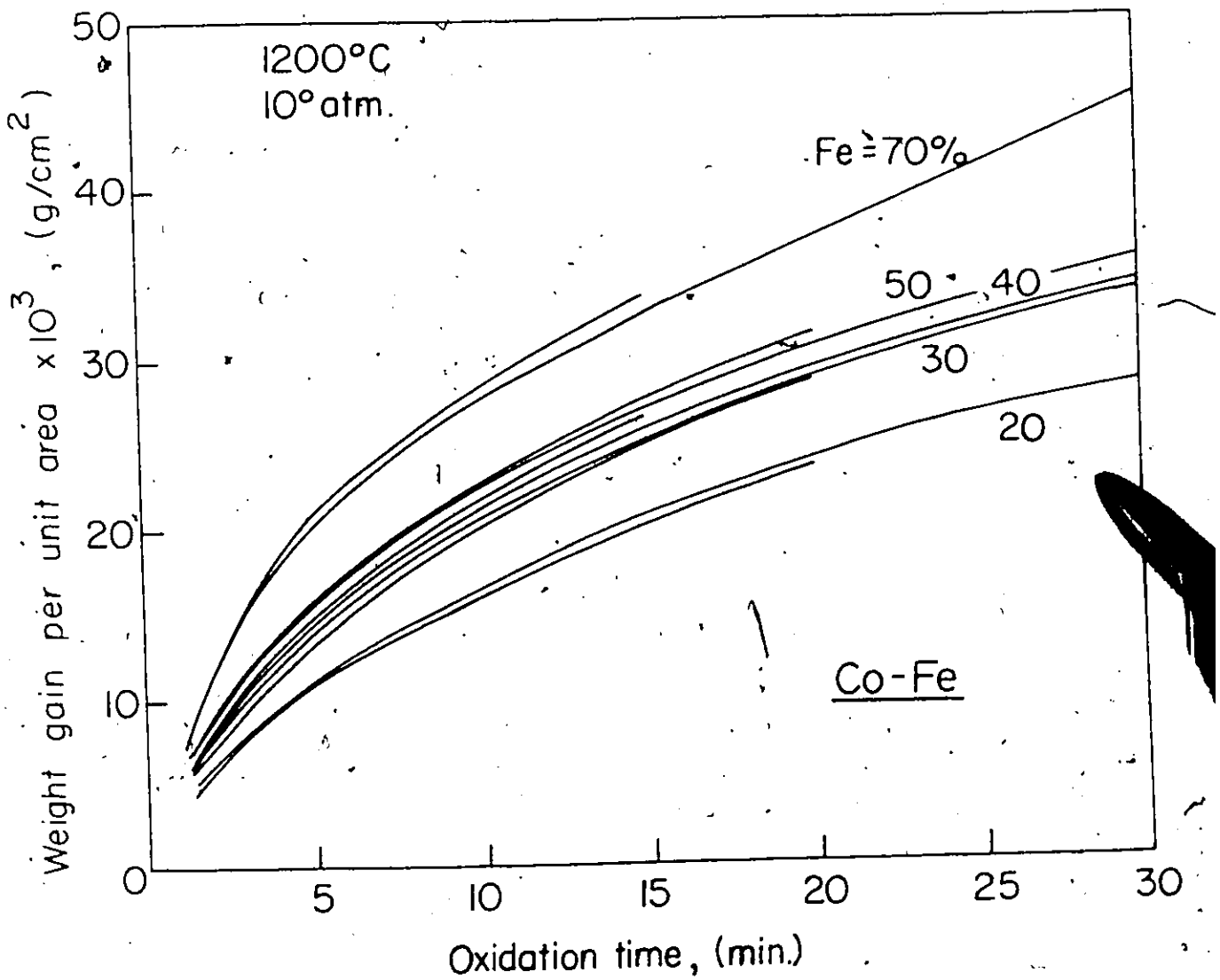

Fig. 7-2

Oxidation kinetics

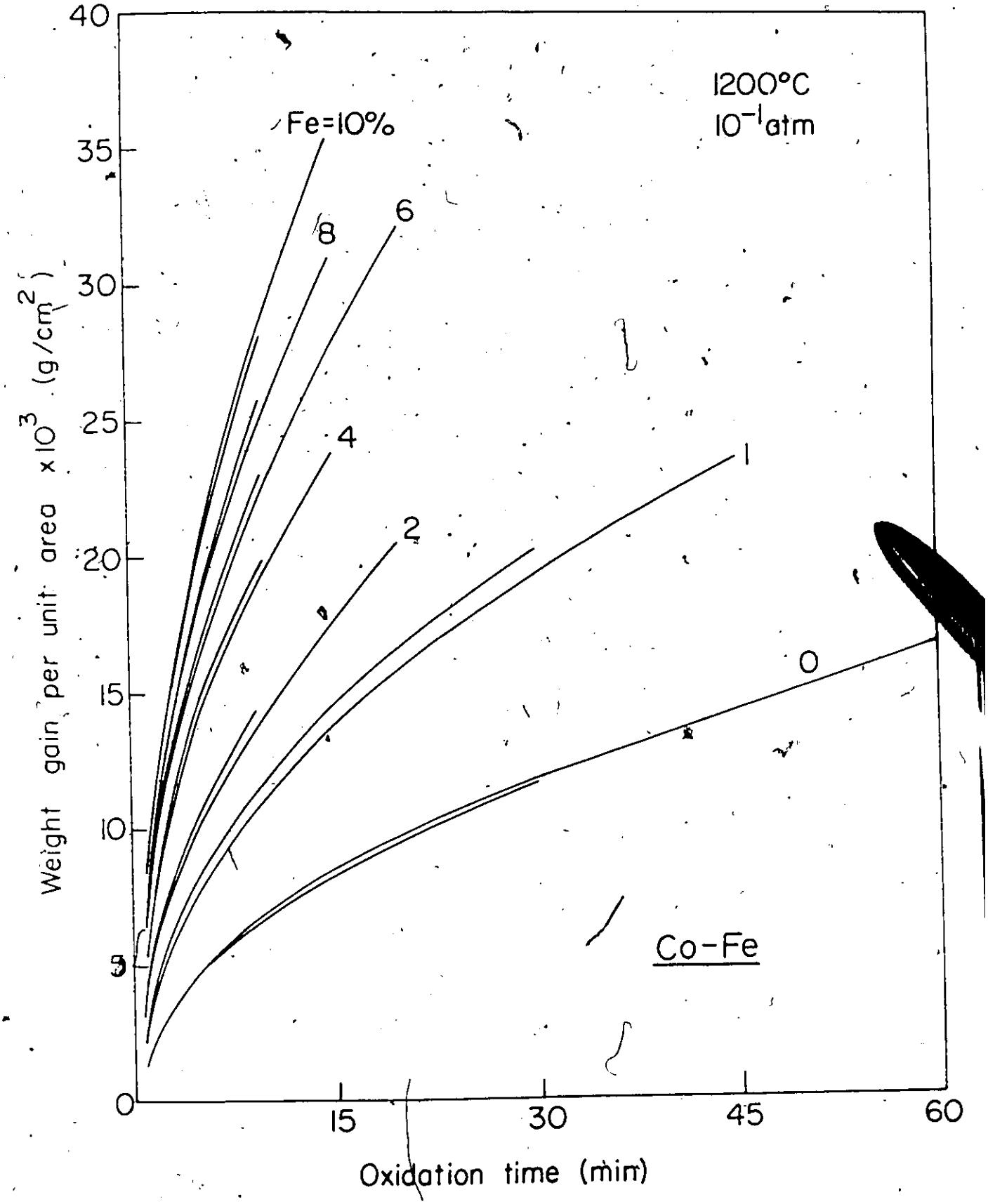

Fig. 7-3

Oxidation kinetics

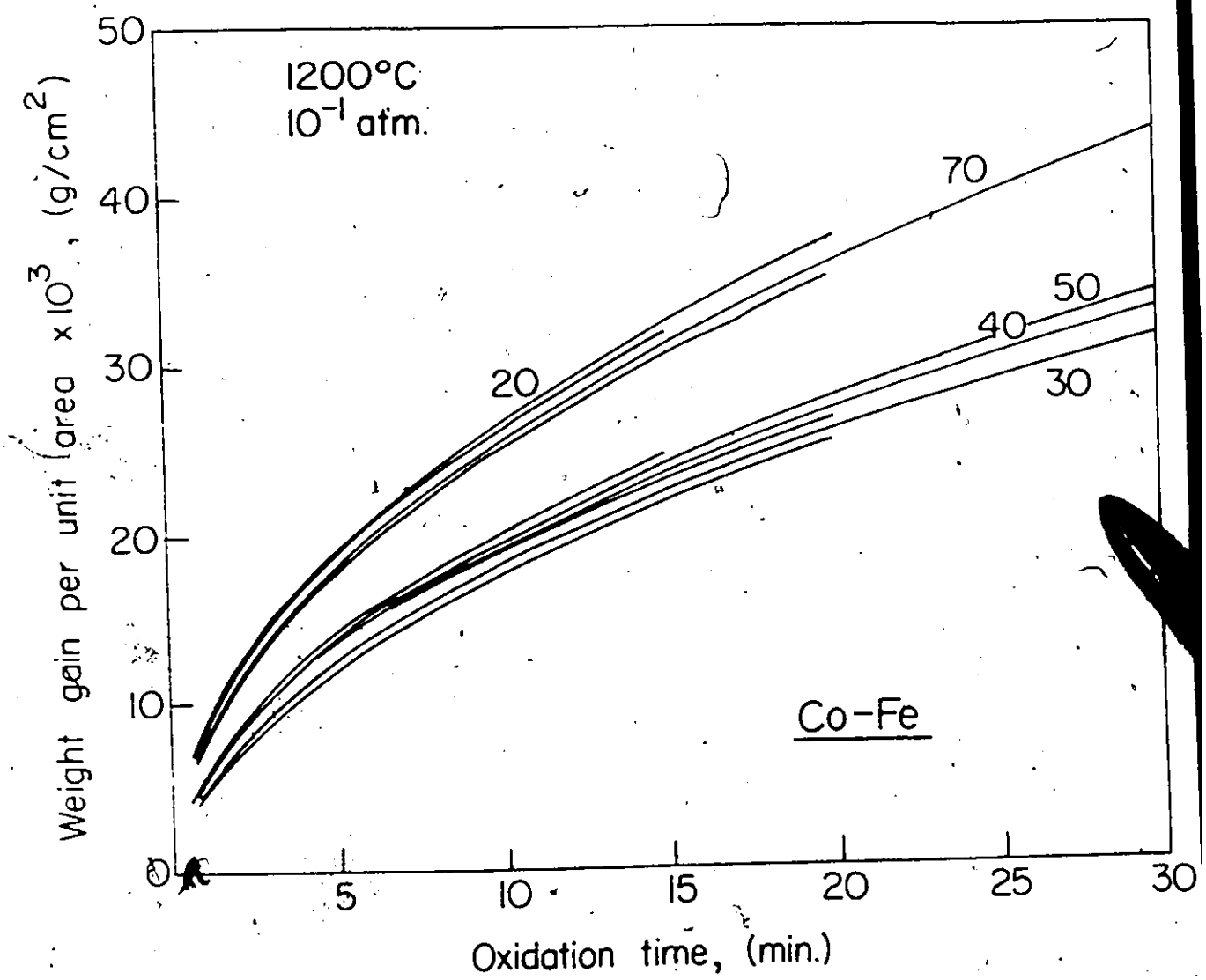

Fig. 7-4

Oxidation kinetics

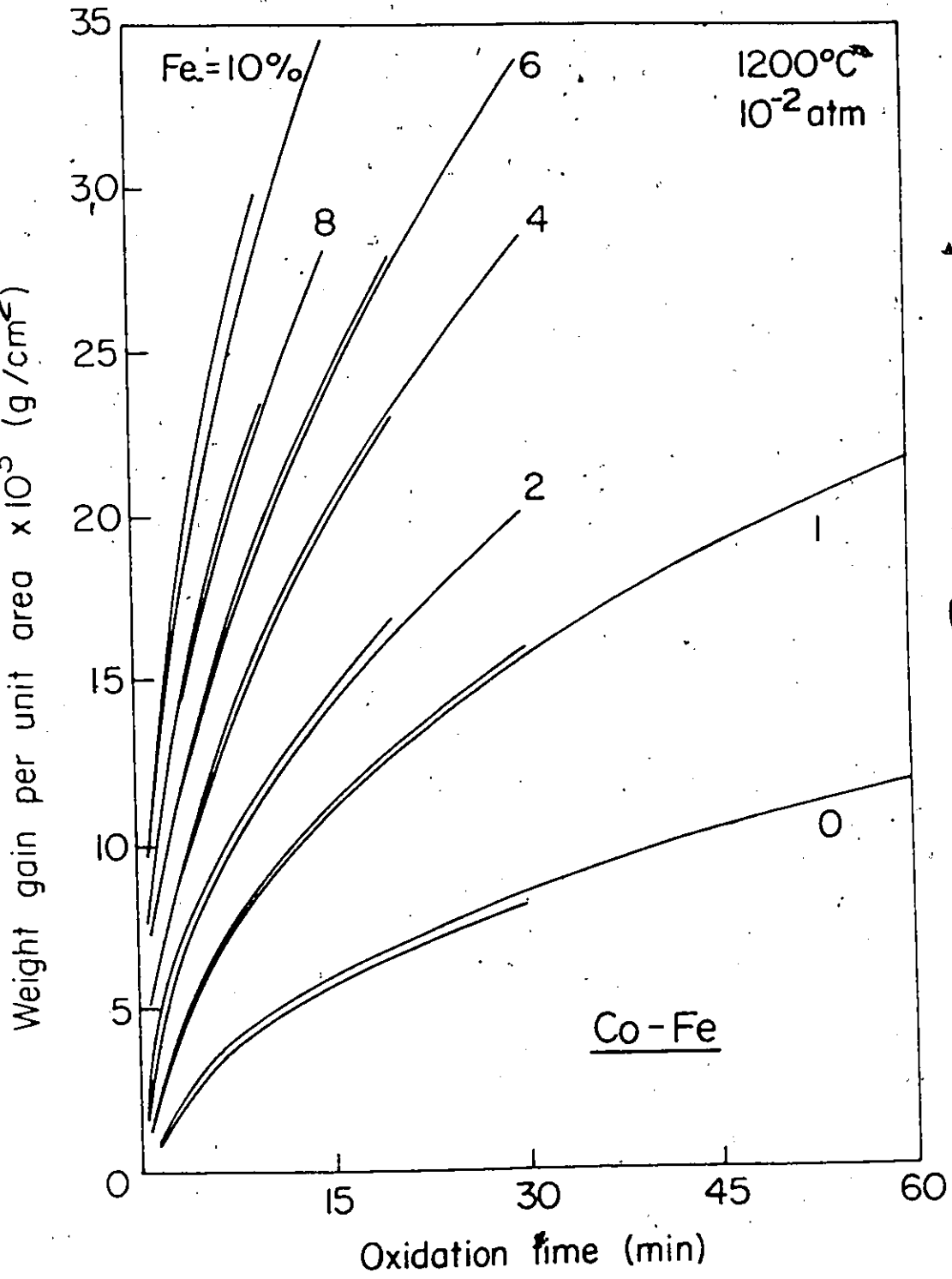

Fig. 7-5

Oxidation kinetics

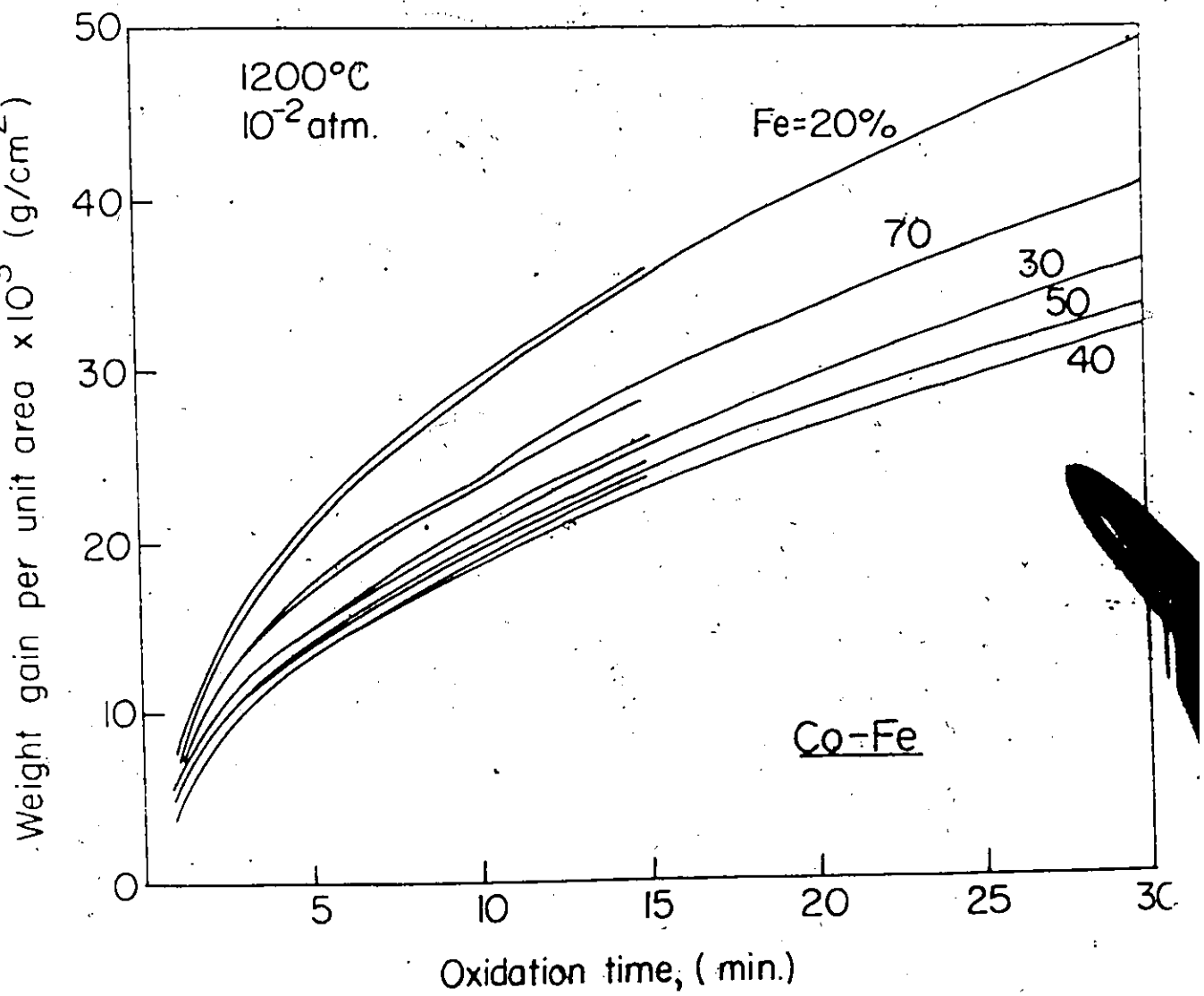

Fig. 7-6

Oxidation kinetics

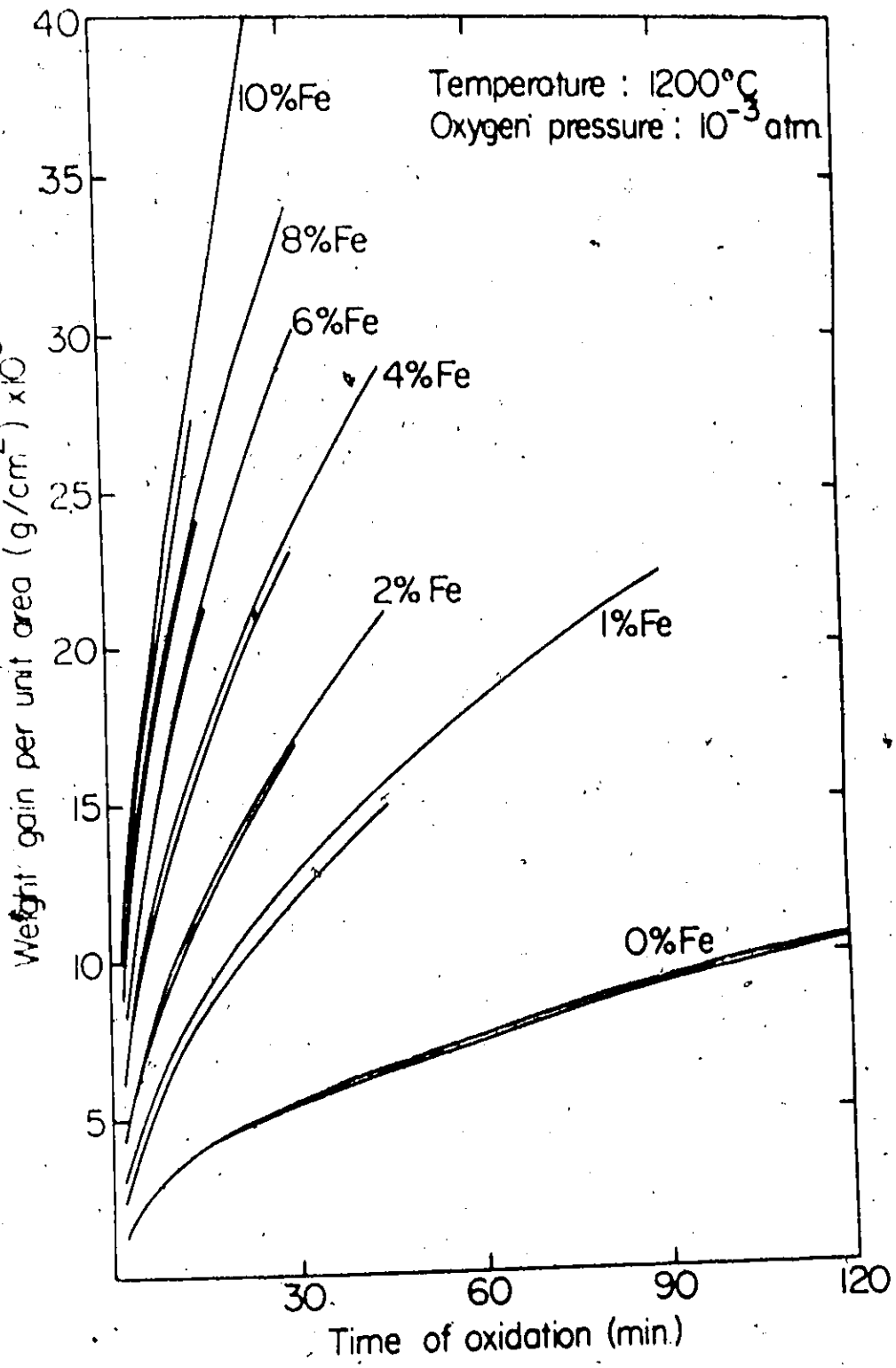

Fig. 7-7

Oxidation kinetics

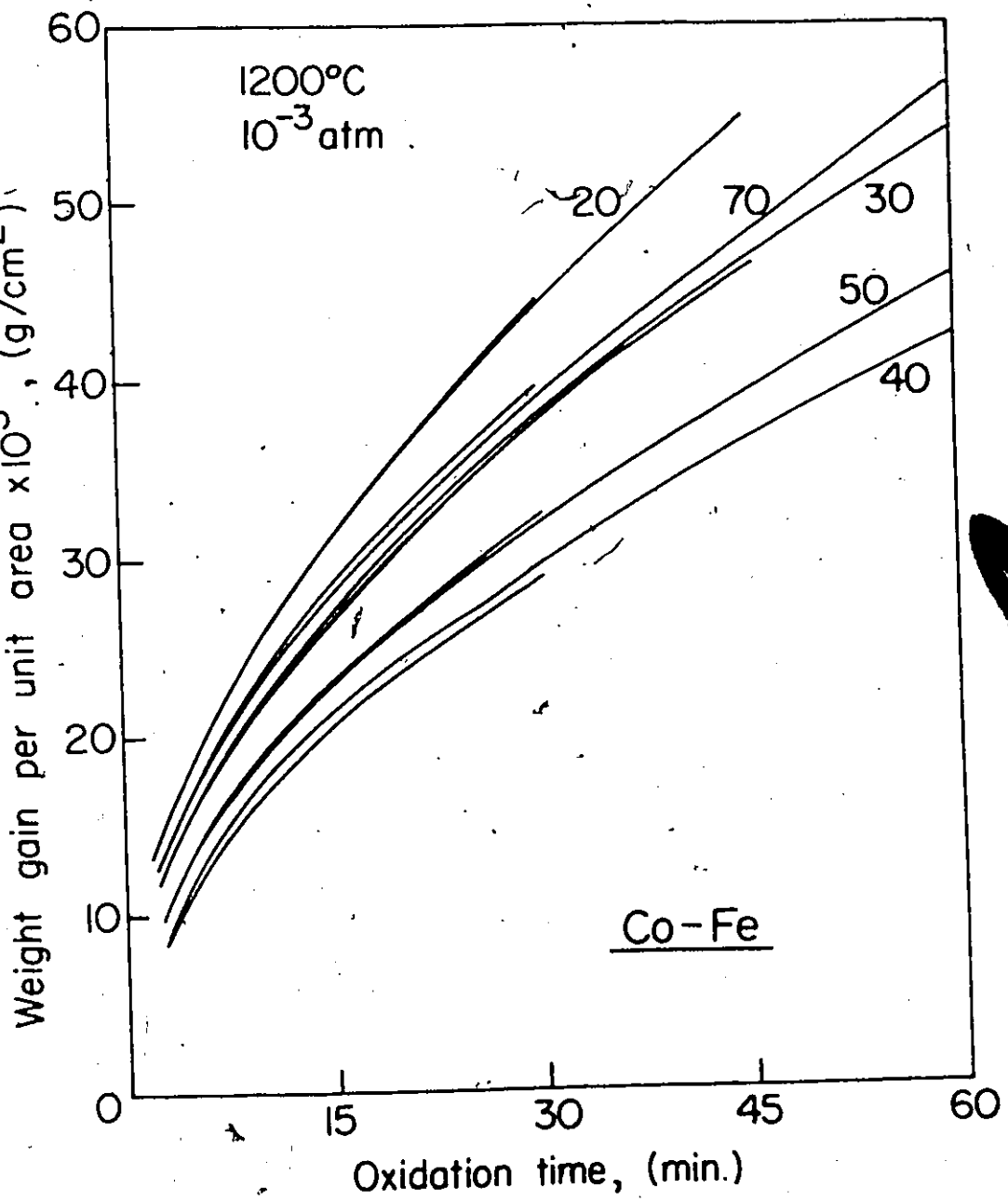

Fig. 7-8

Oxidation kinetics

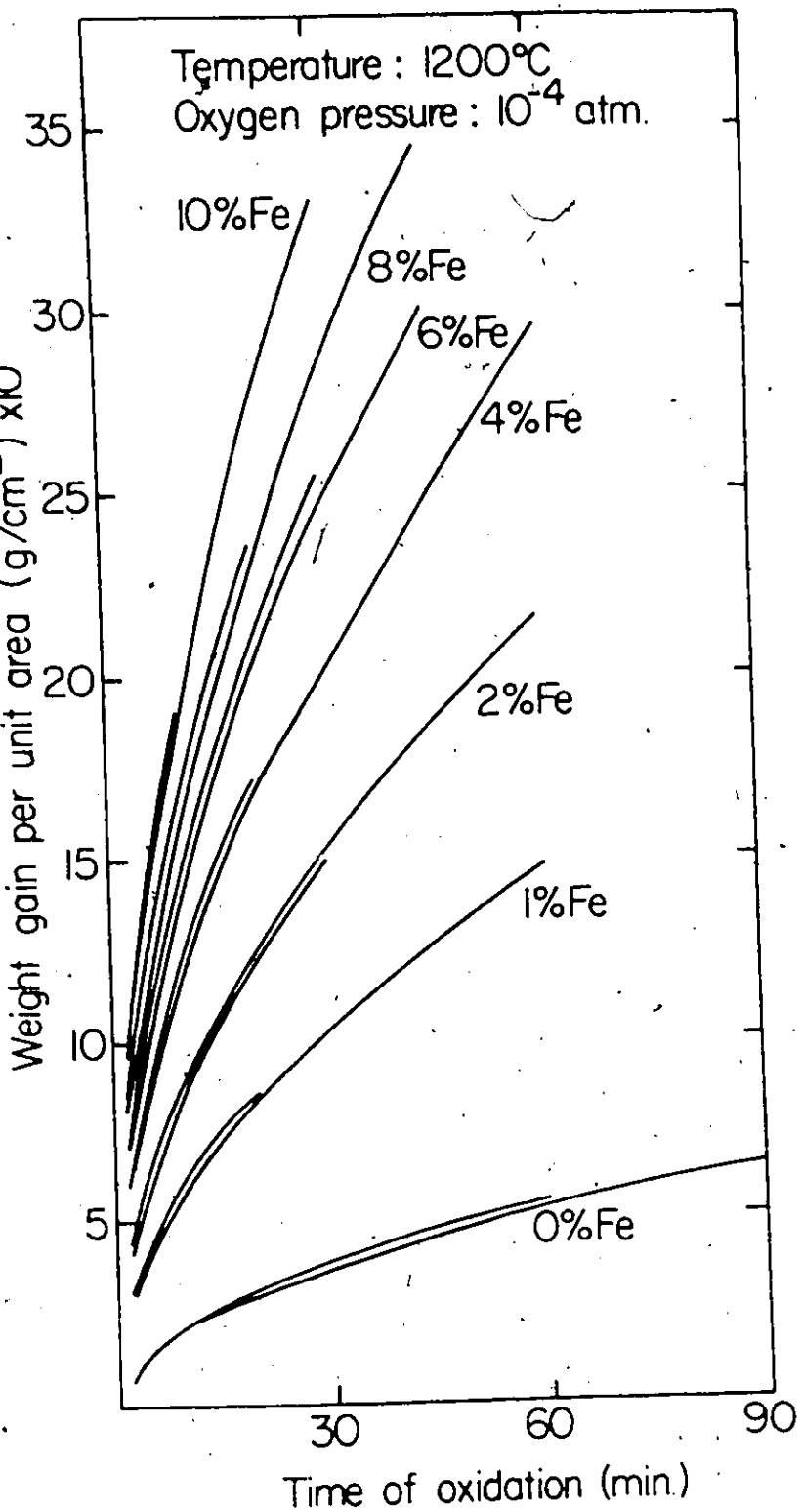

Fig. 7-9

Oxidation kinetics

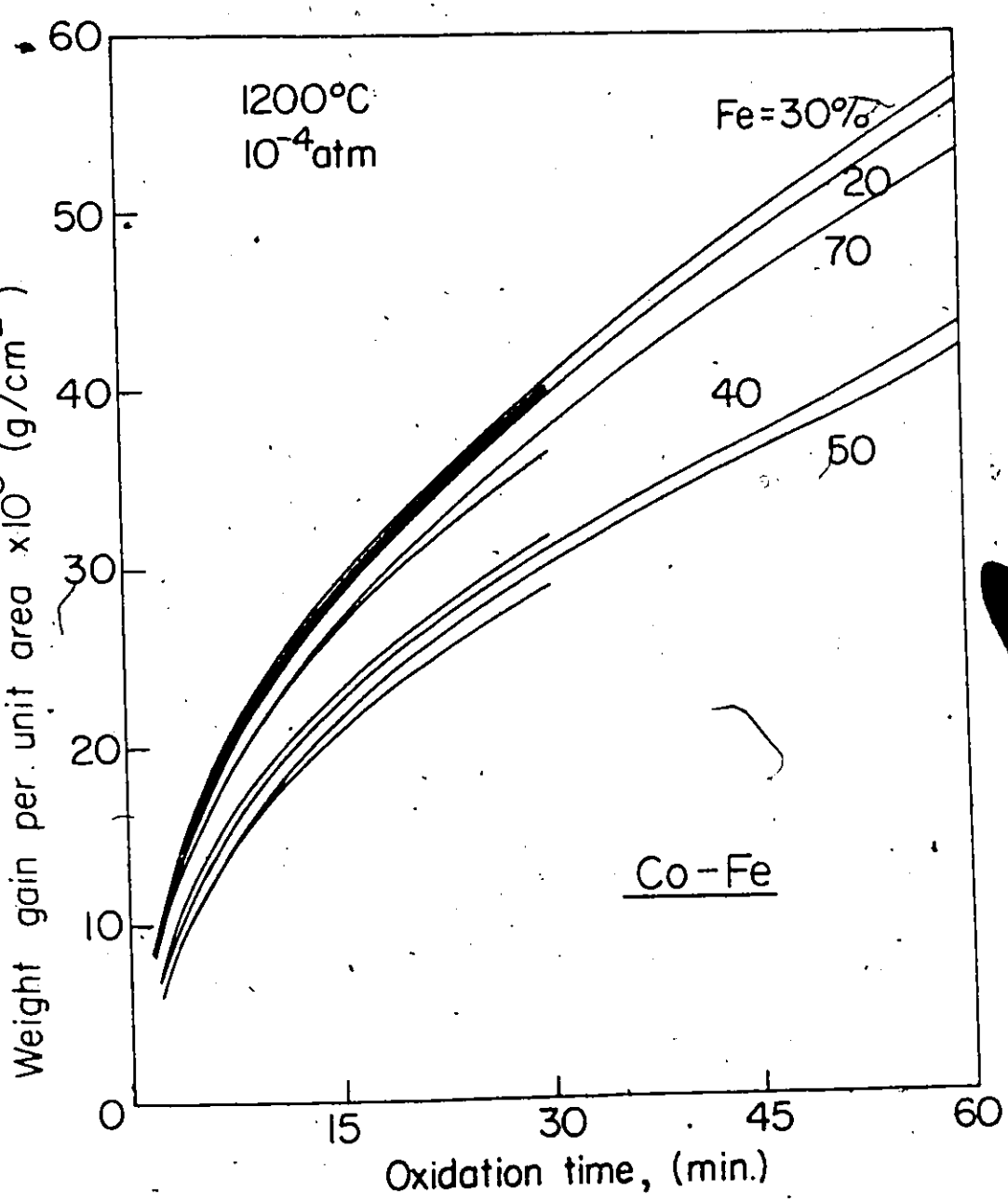

Fig. 7-10

Oxidation kinetics

the rate of reaction. The time period for oxidation was determined by the final weight gain, being generally between 20 mg/cm^2 and 50 mg/cm^2, in order to obtain reasonably thick scales for metallographic observations and microprobe measurements. In each case at least two samples were oxidized, to check the reproducibility of the experiments. In addition, the extent of reaction was checked by measuring the final oxide thickness on cross-sectioned samples. The thickness of the scale could be converted into weight gain per unit area, since 7.6μ of wüstite corresponds approximately to a weight gain of 1 mg/cm^2.

Parabolic plots [(weight gain per unit area)^2 vs. time] corresponding to the kinetic data in Figs. 7-1 to 7-10 are shown in Figs. 7-11 to 7-20. These plots suggest that the parabolic law is obeyed in the whole recorded reaction period. The measure of the oxidation rate when the kinetics are parabolic is the parabolic oxidation rate constant usually designated as k_p from Eq. (2.5). Weight gain curves were plotted from the end of the exposure period using the difference in weight of the sample before and after oxidation as starting point. Then using the chart from the balance recorder the weight gains were totaled for equal time periods and the total weight gain subtracted from the final weight. This method of plotting experimental data eliminates the error introduced by the initial unrecorded period of reaction.

The parabolic rate constants for the alloys investigated determined from the slopes of the parabolic plots are given in Tables 7-1 to 7-4. The values of k_p are the arithmetical average from the data obtained in these experimental investigations. These k_p's are graphically represented in Fig. 7-21.

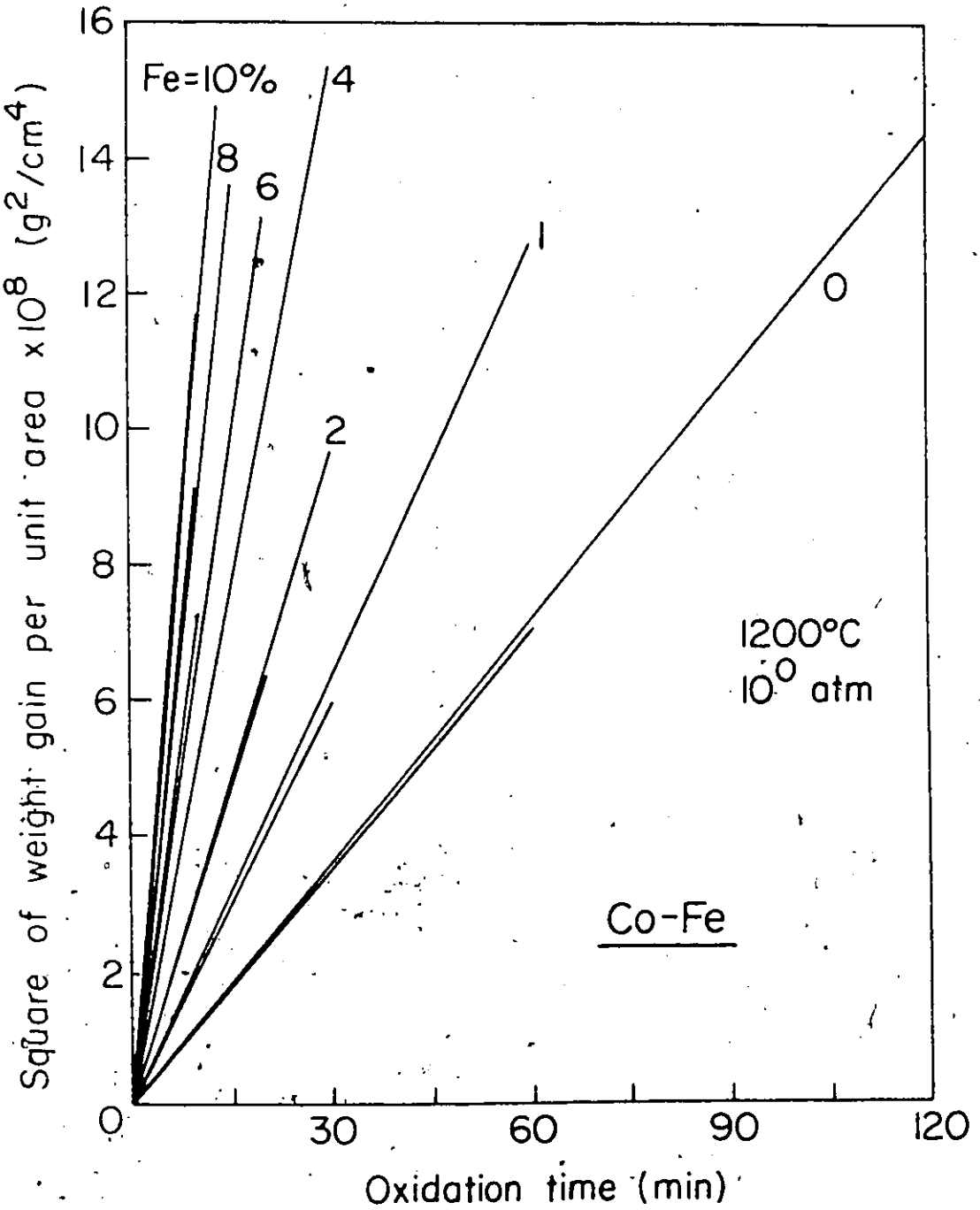

Fig. 7-11

Parabolic plots

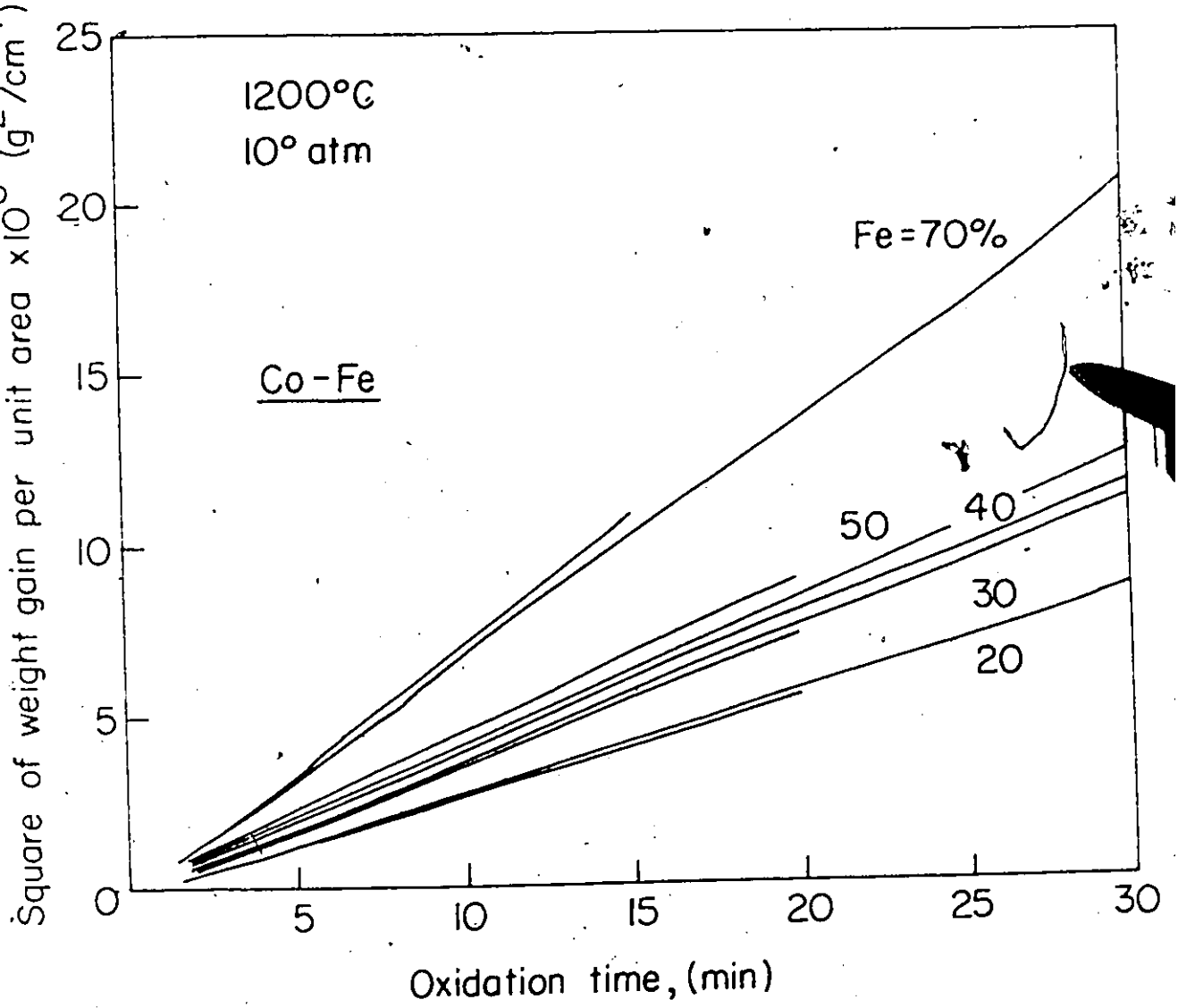

Fig. 7-12

Parabolic plots

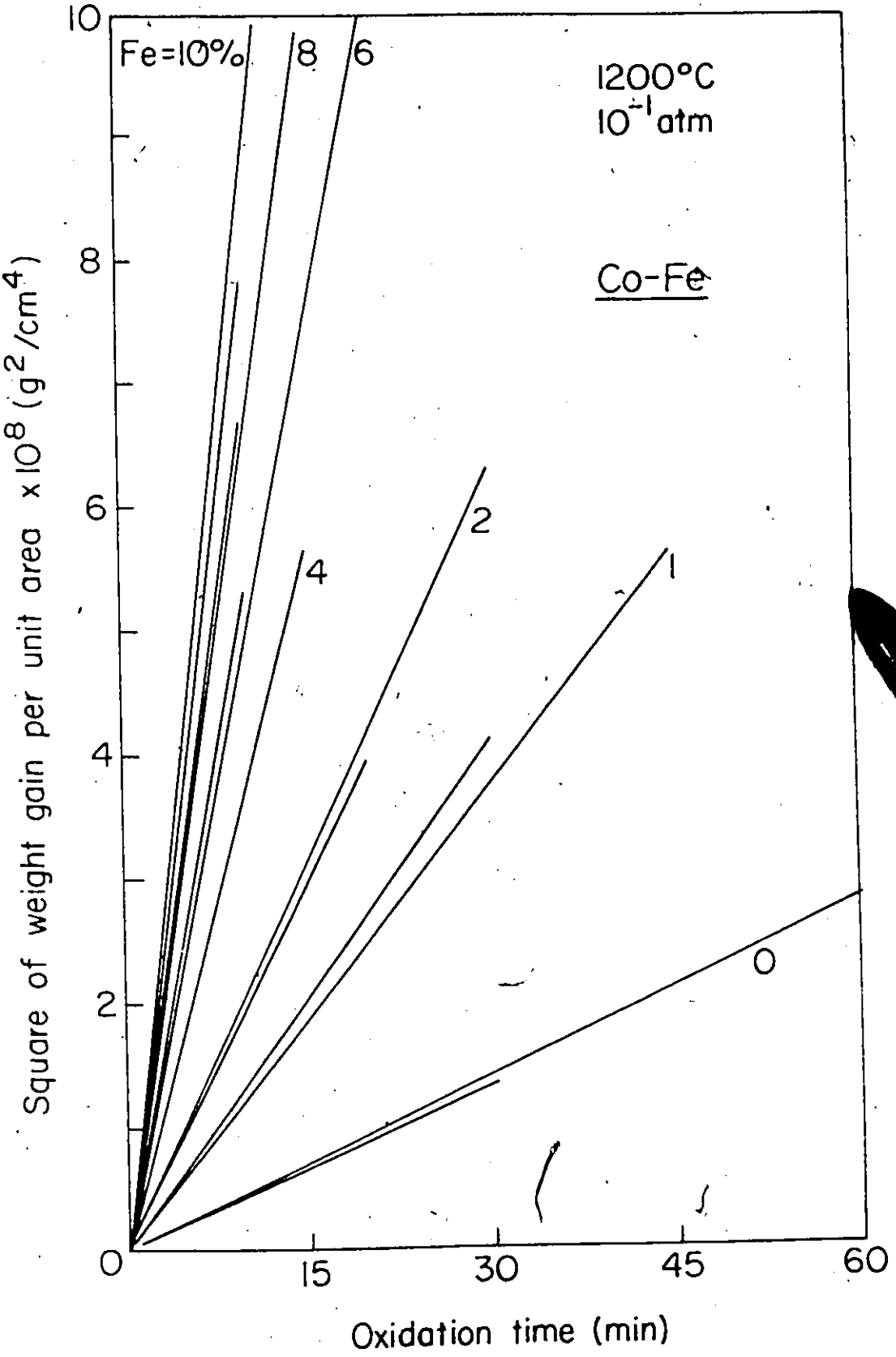

Fig. 7-13
Parabolic plots

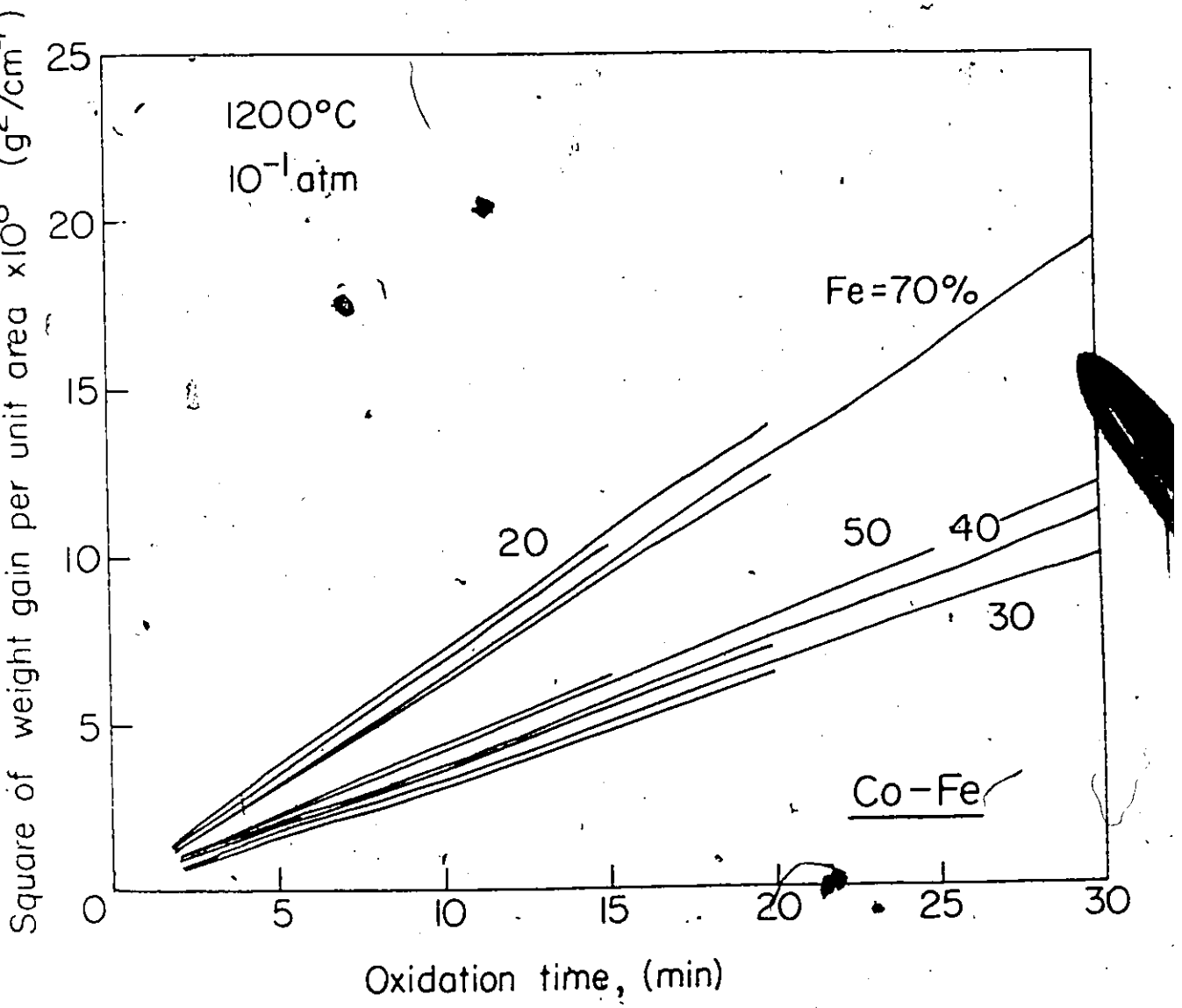

Fig. 7-14

Parabolic plots

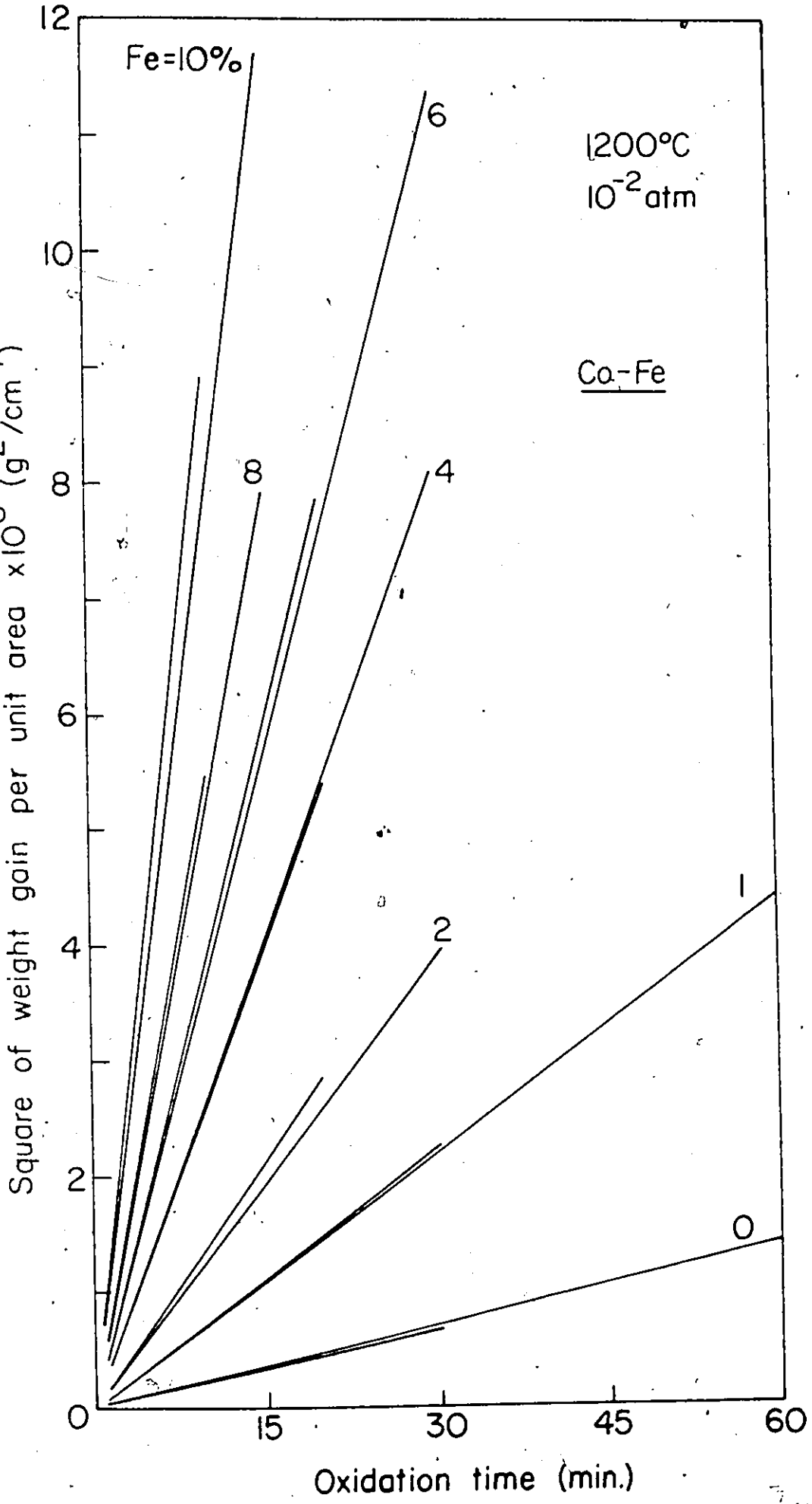

Fig. 7-15 Parabolic plots

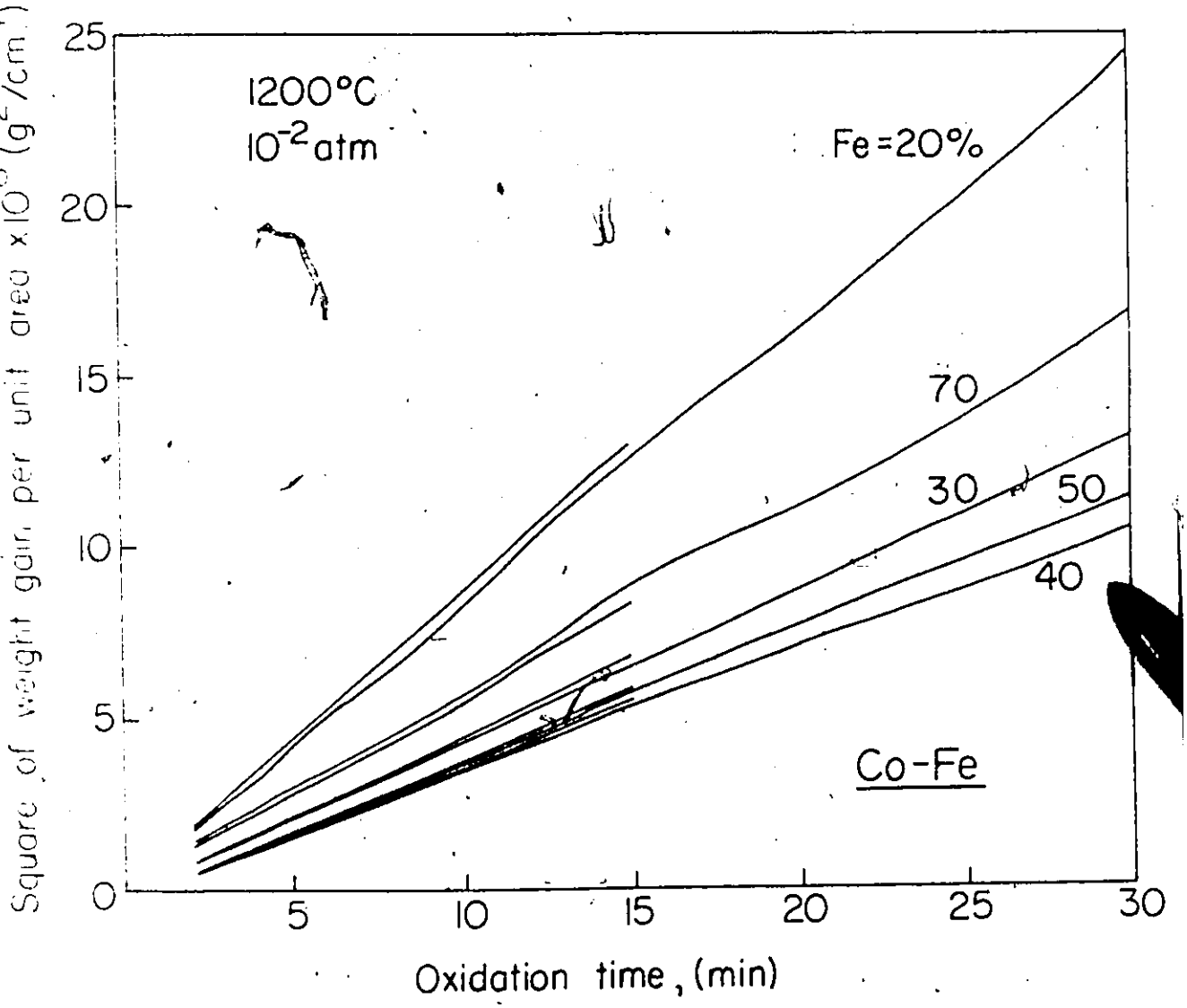

Fig. 7-16

Parabolic plots

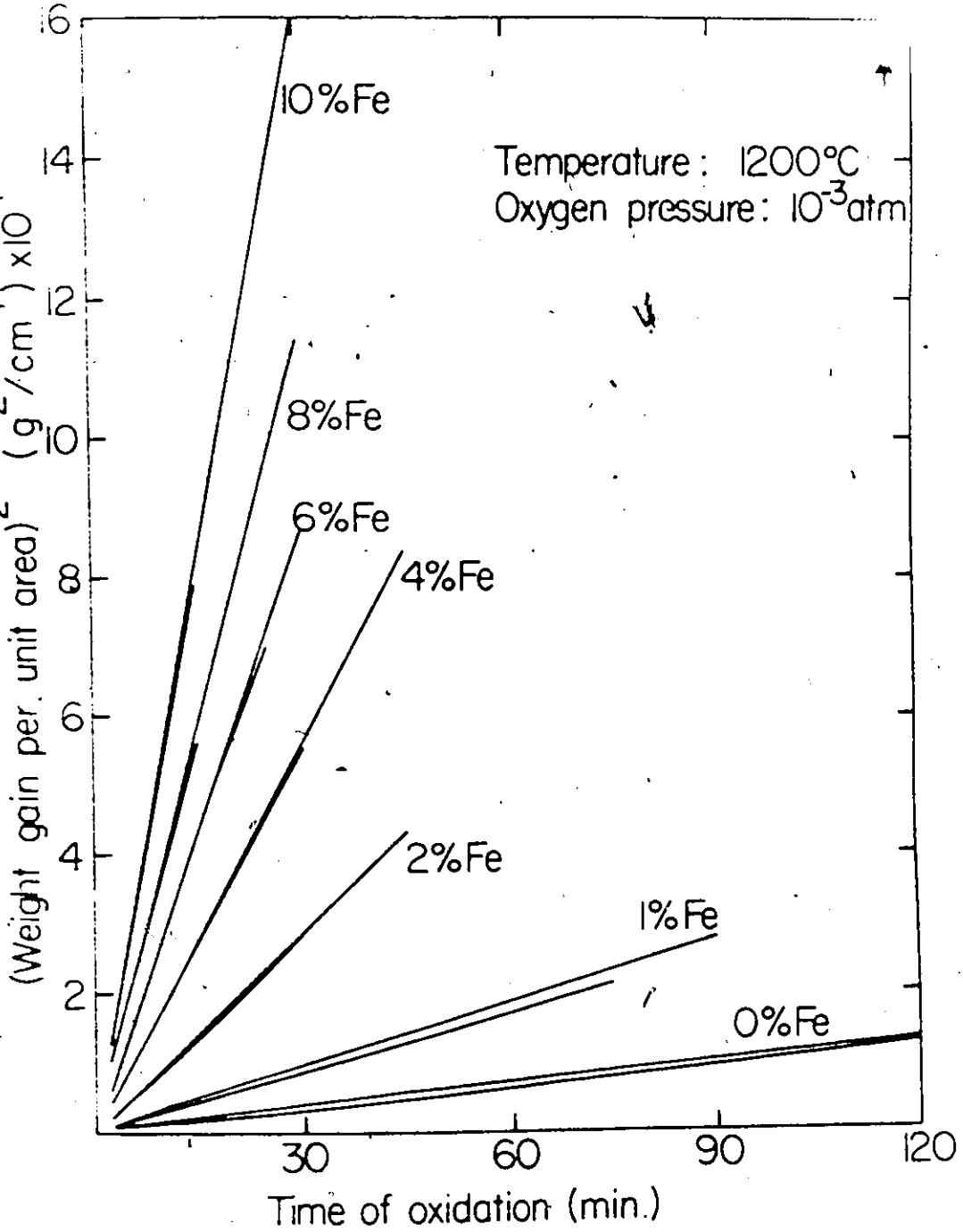

Fig. 7-17

Parabolic plots

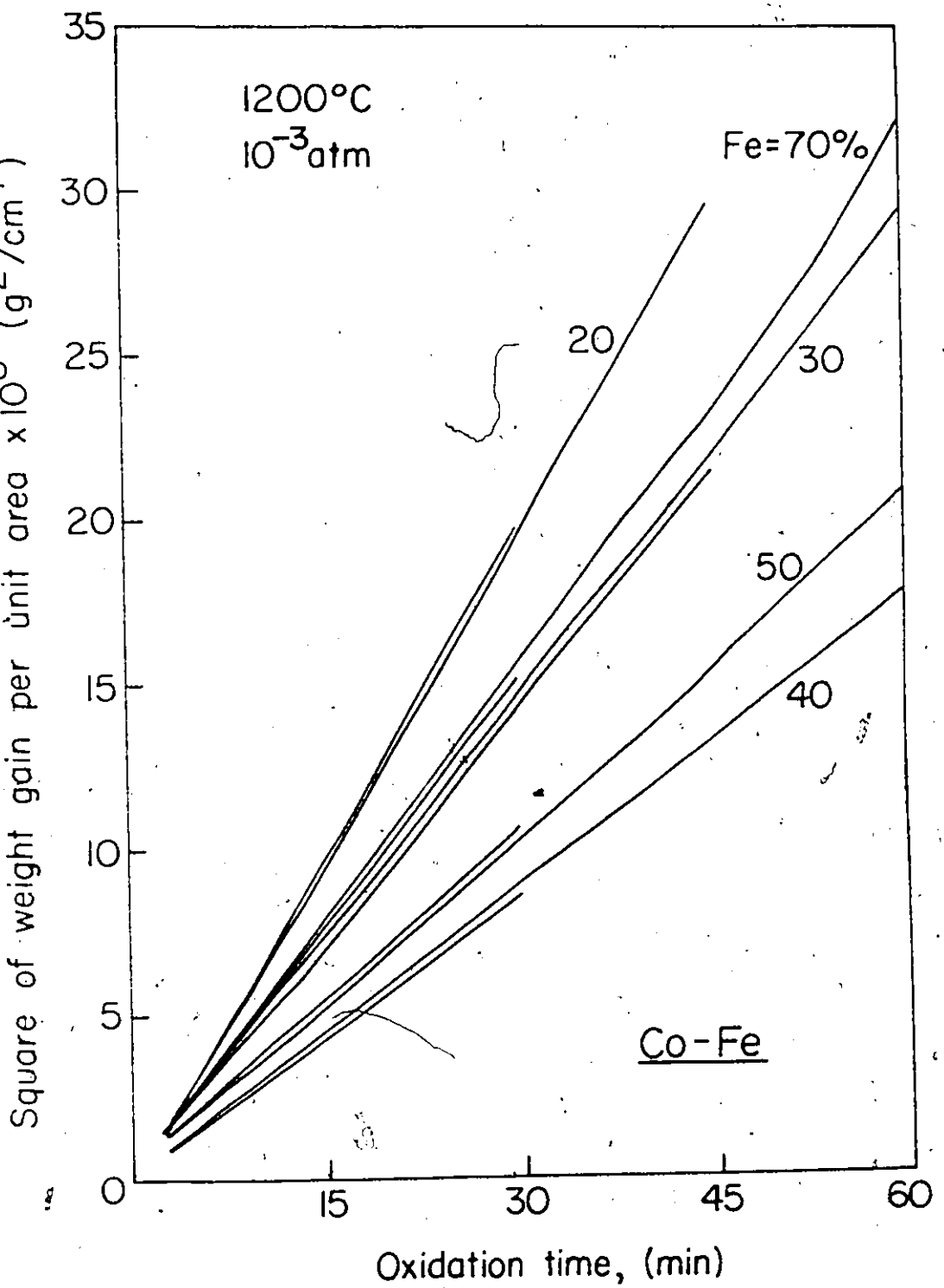

Fig. 7-18

Parabolic plots

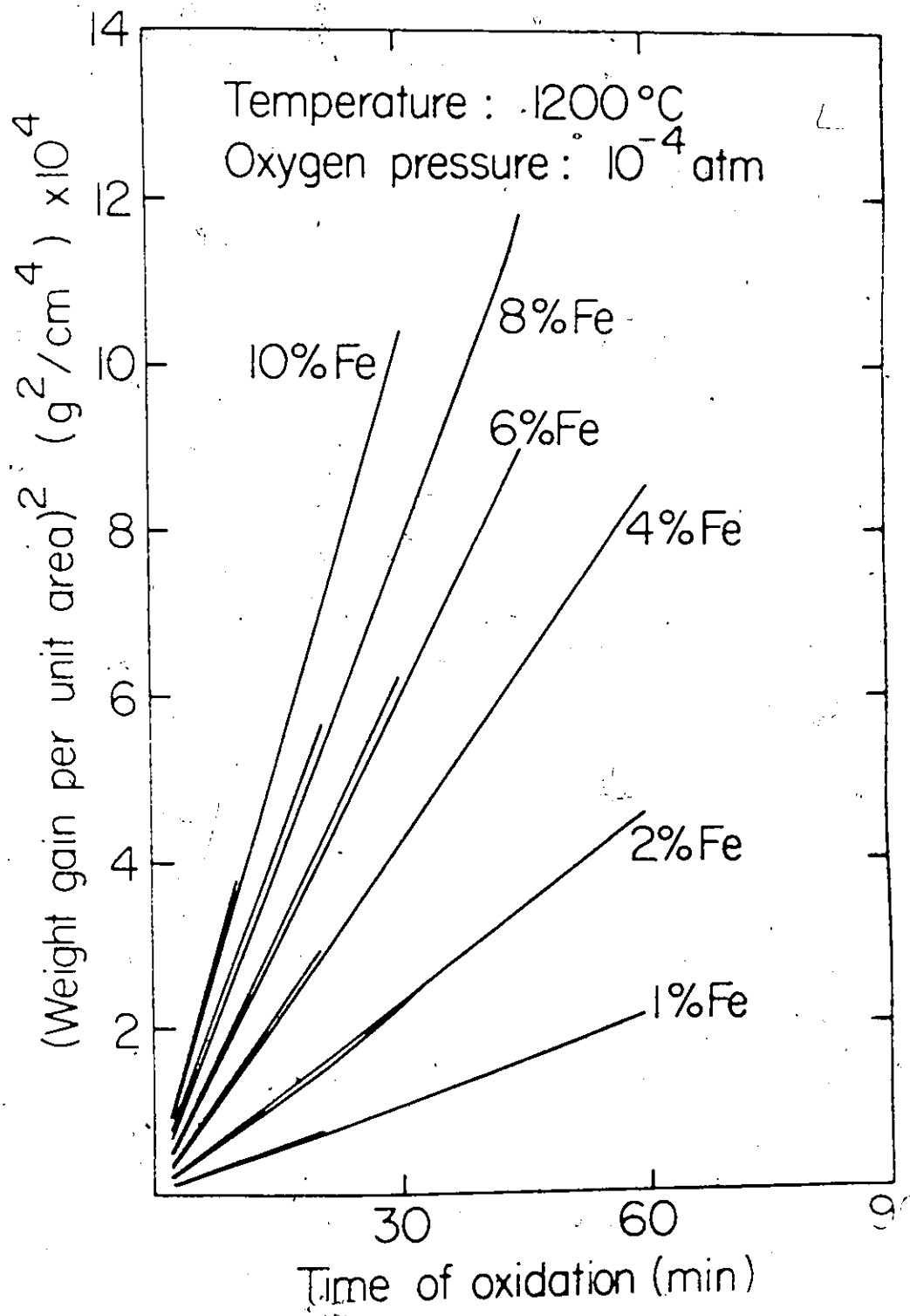

Fig. 7-19

Parabolic plots

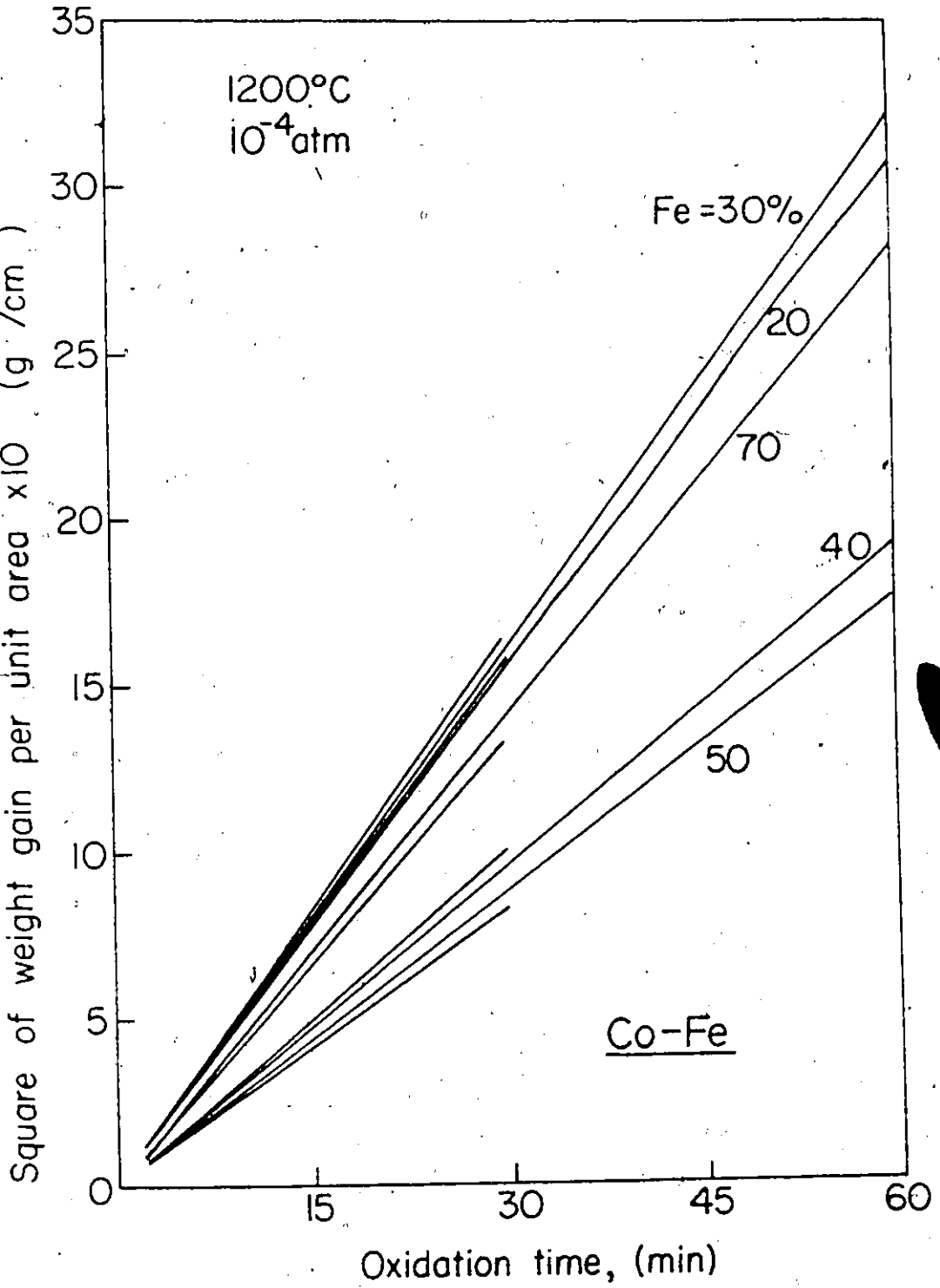

Fig. 7-20

Parabolic plots

Table 7-1

Nominal Iron Content In Alloy [%]	k_p [g^2/cm^4 sec] x 10^6 Oxygen Pressure[atm] 10^0	10^{-1}	10^{-2}
0	$0.1787^{+0.0162}_{-0.0201}$	$0.0834^{+0.0120}_{-0.0064}$	$0.0385^{+0.0013}_{-0.0009}$
1	$0.3099^{+0.0442}_{-0.0426}$	$0.2154^{+0.0128}_{-0.0120}$	$0.1294^{+0.0105}_{-0.0044}$
2	$0.5214^{+0.0208}_{-0.0556}$	$0.3335^{+0.0173}_{-0.0229}$	$0.2389^{+0.0143}_{-0.0205}$
4	$0.8391^{+0.0219}_{-0.0249}$	$0.6311^{+0.0239}_{-0.0307}$	$0.4424^{+0.0458}_{-0.0366}$
6	$1.1501^{+0.0959}_{-0.0970}$	$0.8499^{+0.0507}_{-0.0611}$	$0.6500^{+0.0371}_{-0.0264}$
8	$1.5001^{+0.0200}_{-0.0474}$	$1.1299^{+0.0548}_{-0.0469}$	$0.9011^{+0.0147}_{-0.0192}$
10	$1.8104^{+0.0595}_{-0.1710}$	$1.3501^{+0.1087}_{-0.1340}$	$1.035^{+0.1295}_{-0.1034}$

Table 7-2

Nominal Iron Content in Alloy [%]	k_p [g^2/cm^4 sec] x 10^6 Oxygen Pressure[atm]	
	10^{-3}	10^{-4}
0	$0.0178^{+0.0012}_{-0.0015}$	$0.0083^{+0.0004}_{-0.0004}$
1	$0.0830^{+0.0182}_{-0.0127}$	$0.0620^{+0.0049}_{-0.0038}$
2	$0.1603^{+0.0089}_{-0.0082}$	$0.1254^{+0.0037}_{-0.0064}$
4	$0.3089^{+0.0418}_{-0.0263}$	$0.2470^{+0.0162}_{-0.0087}$
6	$0.4789^{+0.0235}_{-0.0292}$	$0.3550^{+0.0109}_{-0.0309}$
8	$0.6432^{+0.0323}_{-0.0428}$	$0.4706^{+0.0341}_{-0.0309}$
10	$0.8291^{+0.0647}_{-0.0392}$	$0.6000^{+0.0110}_{-0.0266}$

Table 7-3

Nominal Iron Content in Alloy [%]	k_p [g^2/cm^4 sec] x 10^6 Oxygen Pressure[atm] 10^0	10^{-1}	10^{-2}
20	$0.4957^{+0.0121}_{-0.0112}$	$1.1345^{+0.1000}_{-0.0994}$	$1.3714^{+0.0313}_{-0.0421}$
30	$0.6189^{+0.0614}_{-0.0583}$	$0.5471^{+0.0374}_{-0.0293}$	$0.7533^{+0.0199}_{-0.0154}$
40	$0.6400^{+0.0412}_{-0.0501}$	$0.6251^{+0.0514}_{-0.0608}$	$0.5348^{+0.0127}_{-0.0342}$
50	$0.7625^{+0.0314}_{-0.0611}$	$0.6634^{+0.0317}_{-0.0399}$	$0.6104^{+0.0418}_{-0.0182}$
70	$1.1643^{+0.0834}_{-0.0719}$	$1.0777^{+0.0913}_{-0.0898}$	$0.9245^{+0.0427}_{-0.0934}$

Table 7-4

Nominal Iron Content in Alloy [%]	k_p [g^2/cm^4 sec] x 10^6	
	Oxygen Pressure[atm]	
	10^{-3}	10^{-4}
20	$1.0944^{+0.0031}_{-0.0813}$	$0.9358^{+0.0643}_{-0.0485}$
30	$0.8438^{+0.0292}_{-0.0348}$	$0.9012^{+0.0734}_{-0.0539}$
40	$0.5272^{+0.0062}_{-0.0241}$	$0.4853^{+0.0397}_{-0.0410}$
50	$0.5924^{+0.0092}_{-0.0098}$	$0.5257^{+0.0063}_{-0.0138}$
70	$0.8574^{+0.0501}_{-0.0123}$	$0.8313^{+0.0734}_{-0.0197}$

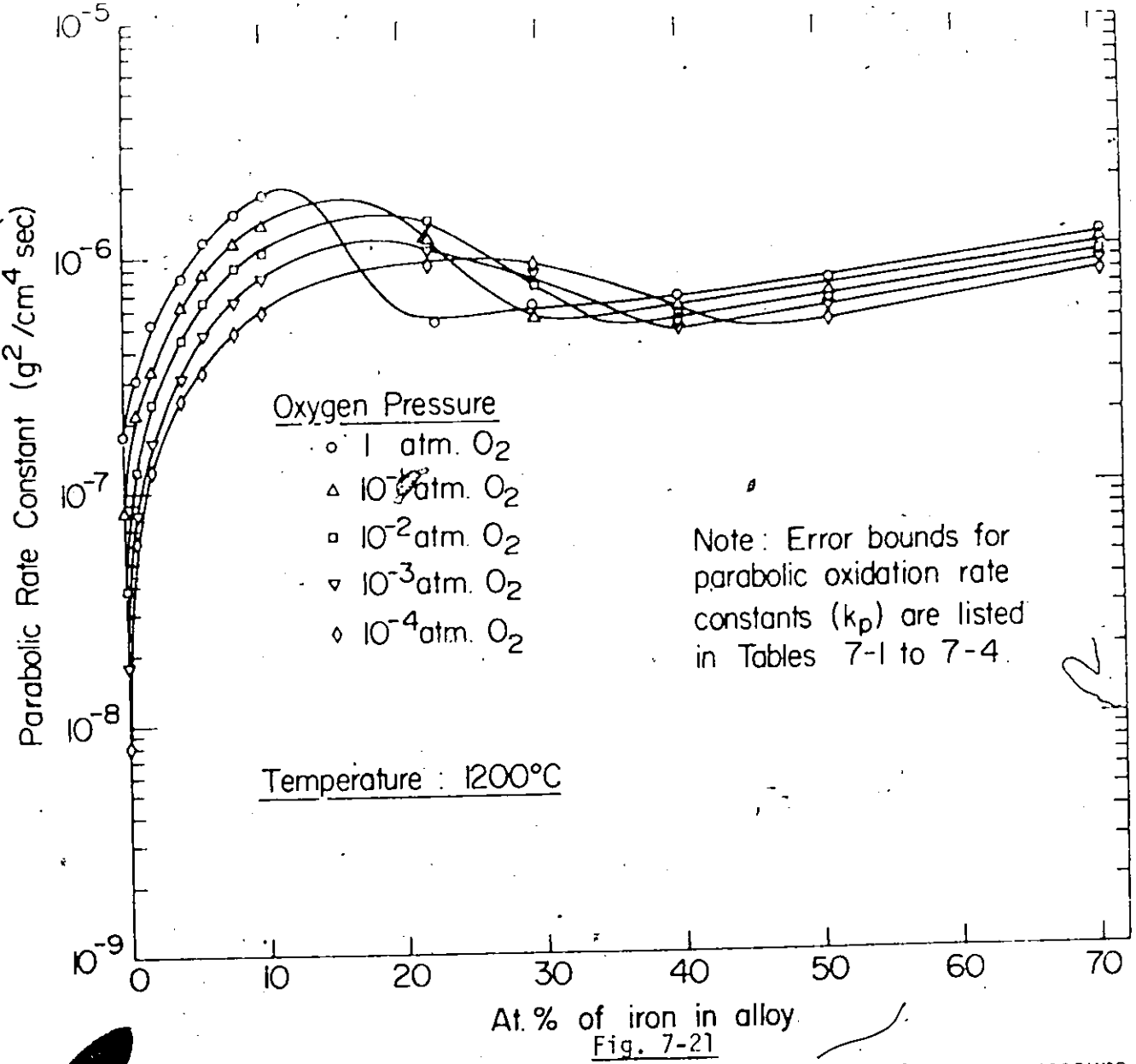

Fig. 7-21

Parabolic oxidation rate constant (k_p) as a function of oxygen pressure and iron concentration in cobalt-iron alloys.

The oxidation rate constants of cobalt-iron alloys increase upon addition of iron to cobalt up to 10% Fe, then they decrease from 10 to 20% Fe followed by a small increase in values. The reasons for this type of behaviour will be elucidated later by correlating the structure and morphology of the oxide scales with kinetic results. The rate of pure cobalt oxidation obtained from these experiments is compared with results from the literature[93] in Table 7-5. The k_p's are in good agreement within the limits of experimental error of the investigations.

7.3 Morphological Development of Oxide Scales

7.3.1 Characterisation and Topology of External Scales

Adherence of oxide scales during the high temperature tests was very good since the kinetics did not show any irregular periods which could be ascribed to the blister formation or scale break-away. However, scales formed on some alloys showed a tendency to blister or spall during quenching. In general, the spalling resistance decreased with increasing iron alloy content. This is due to a change in the mechanical properties of cobalt oxide by addition of iron and spinel phase formation. Those scales which became brittle cracked upon quenching. The stress for cracking is generated by the difference in the thermal expansion coefficients between scale and alloy.

Oxide scales formed on pure cobalt showed excellent spalling resistance in all oxidizing atmospheres. Addition of iron to the alloy causes the spalling resistance of the oxide scales to deteriorate. Experimentally this was observed as a partial detachment of the scale or in some cases complete scale spalling after quenching of the oxidized

Table 7-5

The comparison of Parabolic Oxidation Rate Constants for pure Co at 1200°C

Oxygen pressure [atm]	Data from literature[93] $k_p x 10^6 [gm^2/cm^4 sec]$	Mean experimental values $k_p x 10^6 [gm^2/cm^4 sec]$
10^{0}	0.1727	0.1787
10^{-1}	0.0759	0.834
10^{-2}	0.0333	0.0385
10^{-3}	0.0146	0.0178
10^{-4}	0.0064	0.0083

samples. Table 7-6 shows the summary of these observations. From this table it is clear, that the tendency for an oxide scale to spall increases with increasing alloy iron content and oxygen pressure in the reaction atmosphere.

Surface topographies of oxidized samples were investigated by means of scanning electron microscopy. The grain size at the oxide-gas interface decreased with decreasing oxygen pressure and increased with iron content in the base alloy. The surface of CoO formed on Co at 1 atm oxygen pressure was smooth and glassy. With increasing iron content and decreasing oxygen potential the surface lost its glassy appearance. The tarnishing of the oxide surface was due to preferential growth of the oxide grains in the most favorable crystallographic direction. The resulting terraced and ledged structure of the surface causes the dull appearance. The preferential growth of oxide grains was most pronounced during oxidation at 10^{-4} atm oxygen pressure.

7.3.2 Structures of External Scales Formed at 1 atm Oxygen Pressure

Pure Cobalt

A scale formed on pure cobalt is composed of dense CoO exhibiting a small degree of porosity at the metal-scale interface and Co_3O_4 resulting from precipitation during cooling from 1200°C to room temperature. Fig. 7-22(a) shows the metallographic cross-section of pure cobalt oxidized for 120 minutes. Precipitates of Co_3O_4 outline the grain boundaries and they could be found also in the middle of the CoO grains. The shape of the precipitates appears to be spherical, approximately 0.5μ in diameter.

Table 7-6

Spalling Tendency of Scales Forming on Cobalt-iron Alloys at 1200°C

Nominal Iron Content in Alloy [%]	Oxygen Pressure [atm]				
	10^{0}	10^{-1}	10^{-2}	10^{-3}	10^{-4}
0	A	A	A	A	A
1	A	A	A	A	A
2	D	A	A	A	A
4	D	D	A	A	A
6	D	A	A	A	A
8	D	D	A	A	A
10	D	A	A	D	A
20	D	D	D	D	A
30	D	D	D	D	A
40	D	D	D	D	A
50	D	D	D	D	D
70	D	D	D	D	A

A - oxide scale attached to the metal

D - oxide scale detached from the metal

Co-1% Fe to 10% Fe Alloys

Figs. 7-22(b) and 7-22(g) show single phase cobaltowüstite scales formed during oxidation and spinel precipitates which most likely formed during cooling. Precipitate formation is caused by oxygen supersaturation of cobaltowüstite upon cooling from 1200°C. The phenomena are analogous to precipitation at a temperature within a two-phase region $CoO-Co_3O_4$. The shape of the precipitates changes with increasing iron content in the oxide. The precipitates, as shown in Fig. 7-22(b) for oxide formed on Co-1% Fe alloy, retain globular form. However, the precipitates in Fig. 7-22(c) found in the oxide formed on the Co-2% Fe alloy are elongated in one dimension. The elongation of the precipitates increased with concentration of iron. Figs. 7-22(f) and 7-22(g) show a needle type network of $(Co,Fe)_3O_4$ in cobaltowüstite matrix of a scale on alloys of higher iron concentrations.

These micrographs show that dense scales are formed with some porosity at the alloy-oxide interface. This interface was morphologically stable retaining a planar shape during the course of oxidation. Internal oxidation was not observed.

Co-20% Fe to Co-70% Fe alloys

The structures of oxide scales formed on these alloys are shown in Figs. 7-22(h) to 7-22(l). Each scale is composed of three layers, the outer and inner layers being cobaltowüstite with spinel precipitates with a continuous layer of $(Co,Fe)_3O_4$ between them. The relative position of the spinel layer in the scale changed with iron alloy content but this position did not change with time. The ratio of the outer to inner cobaltowüstite layer thickness decreased with increasing iron content in alloy and

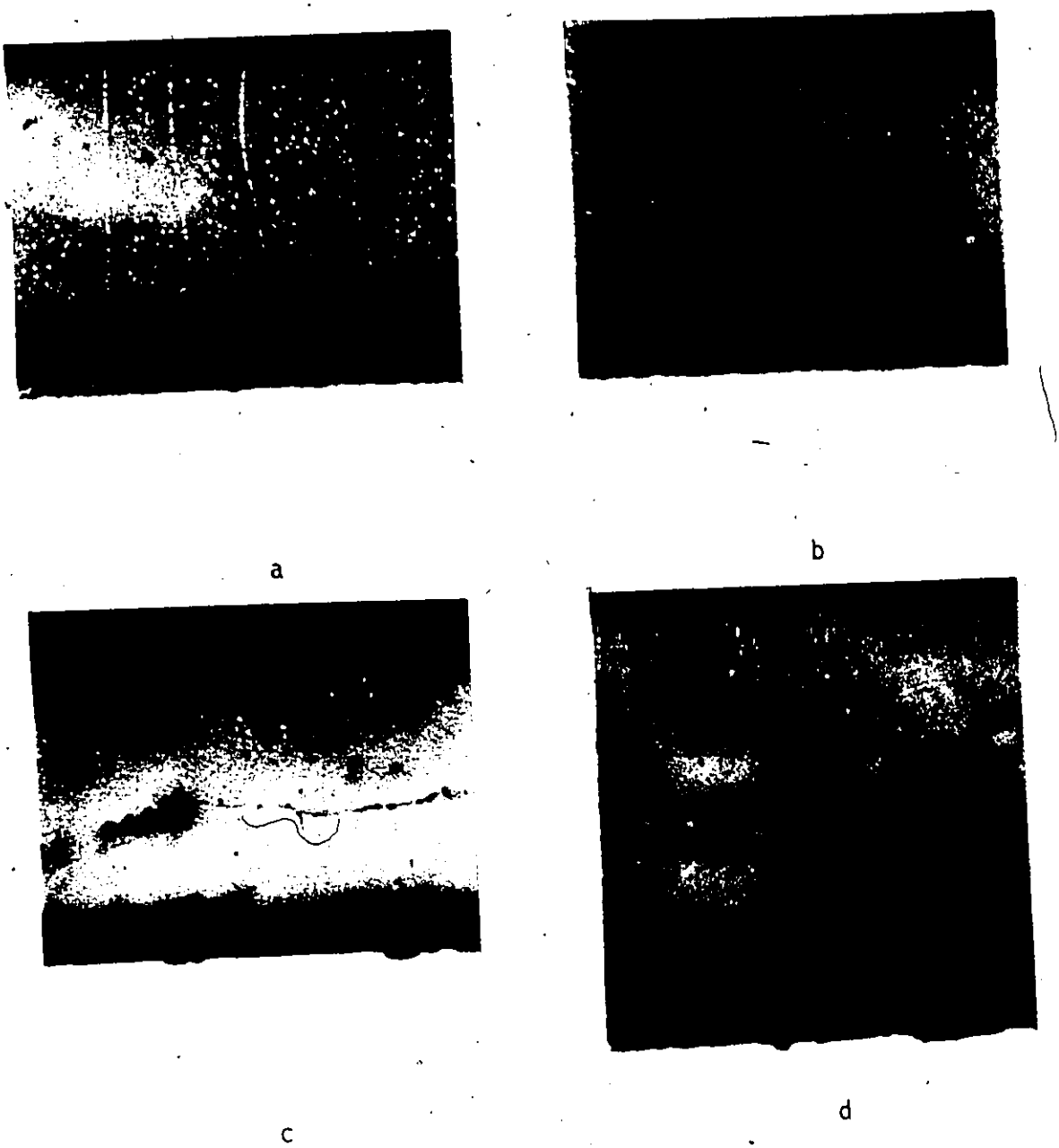

Fig. 7-22

Cross sections of oxide scales formed at 1 atm oxygen pressure: (a) pure cobalt oxidized for 30 min - (200X, unetched); (b) Co-1% Fe alloy oxidized for 60 min - (200X, unetched); (c) Co-2% Fe alloy oxidized for 30 min - (200X, unetched); (d) Co-4% Fe alloy oxidized for 30 min - (200X, unetched)

e

f

g

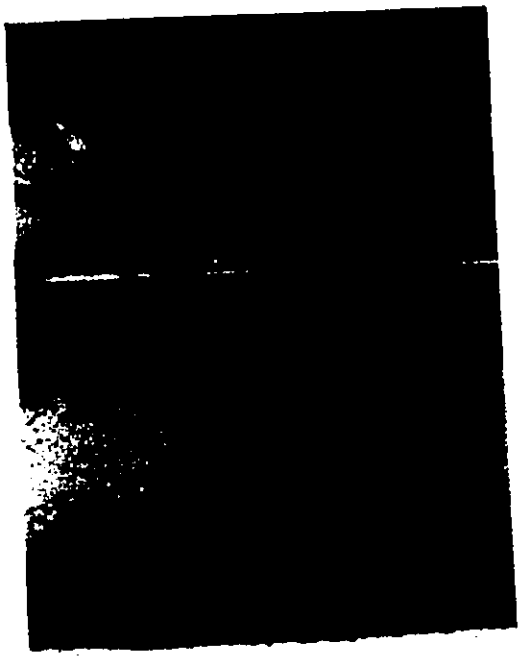

h

Fig. 7-22

Cross sections of oxide scales formed at 1 atm oxygen pressure: (e) Co-6% Fe alloy oxidized for 10 min - (200X, unetched); (f) Co-8% Fe alloy oxidized for 10 min - (200X, unetched); (g) Co-10% Fe alloy oxidized for 15 min - (200X, unetched); (h) Co-20% Fe alloy oxidized for 30 min - (320X, unetched).

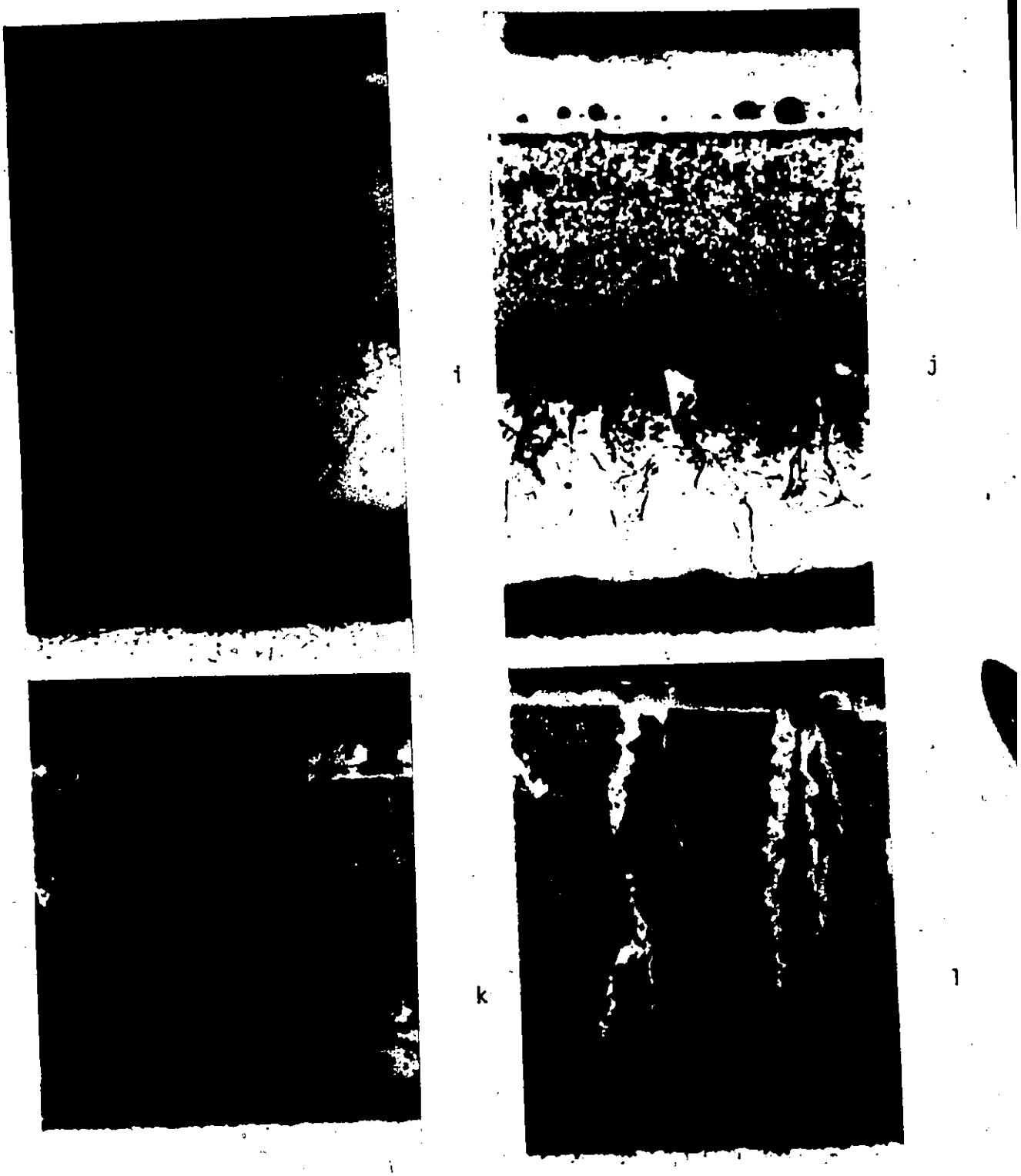

Fig. 7-22

Cross sections of oxide scales formed at 1 atm oxygen pressure: (i) Co-30% Fe alloy oxidized for 30 min - (320X, etched); (j) Co-40% Fe alloy oxidized for 30 min - (320X, etched); (k) Co-50% Fe alloy oxidized for 30 min - (200X, etched); (l) Co-70% Fe alloy oxidized for 30 min - (200X, etched).

it was 1/3, 1/4, 1/5, 1/10 and 1/25, for scales formed on Co-20% Fe, Co-30% Fe, Co-40% Fe, Co-50% Fe and Co-70% Fe alloy, respectively.

7.3.3 Structures of External Scales Formed at 10^{-1} atm Oxygen Pressure

Pure Cobalt

Fig. 7-23(a) shows the CoO scale formed on pure cobalt after 30 minutes. The scale was compact and adherent to the metal with some porosity at the metal-oxide interface. The Co_3O_4 precipitates are located in the outer half of the scale and appear to be smaller than those formed in the CoO scale during quenching in 1 atm of oxygen.

Co-2% Fe to Co-10% Fe alloys

The scales formed on alloys containing 1, 2, 4, 6, 8 and 10% iron were single phase compact cobaltowüstite layers (Fig. 7-23(b) to 7-23(g)). The porosity at the scale-alloy interface is of limited extent. The porosities in the scales shown in Figs. 7-23(f) and 7-23(g) are artifacts created during metallographic polishing.

The precipitation of a $(Co,Fe)_3O_4$ spinel phase in (Co,Fe)O scale during quenching was not observed. The oxide-alloy interface was planar with very limited porosity due to coagulation of the cation vacancies and "metallographic pull-out" of fine-grained oxide at this interface. Internal oxidation was not observed.

Co-20% Fe Alloy

The external scale shown in Fig. 7-23(h) was formed during oxidation for 15 minutes. The scale is pore free except at the metal-oxide interface. The tests revealed presence of two phases (Co,Fe)O and $(Co,Fe)_3O_4$. The spinel phase is concentrated in the form of precipitates in the outer part

of the scale. It is interesting to observe that the maximum density of the particles is at the same location in the scale, where the continuous layer of spinel phase was found in the scale on an oxidized Co-20% Fe alloy at 1 atm O_2.

Co-30 to Co-70% Fe Alloys

The scales shown in Figs. 7-23(i) to 7-23(l) exhibit three layers. The outer and inner layers are cobaltowüstite containing spinel precipitates and a continuous layer of $(Co,Fe)_3O_4$ occurs between them. The change in ratio of outer and inner (Co,Fe)O layer thickness with the iron content in alloy is similar to the behaviour found for oxidation at 1 atm oxygen pressure. Internal oxidation was observed in the metal near the regions of the alloy-oxide interfaces in all alloys.

7.3.4 Structures of External Scales Formed at 10^{-2} atm Oxygen Pressure

Pure Cobalt

Fig. 7-24(a) shows a CoO oxide scale formed on cobalt after 60 minutes of exposure. Precipitates of Co_3O_4 are present but the size of the particles is much smaller than in the case of cobalt oxidation in oxygen at 1 atm and 10^{-1} atm. The scale is compact and adherent with some porosity at the alloy-oxide interface.

Co-1% Fe to Co-10% Co Alloys

The scales formed on these alloys are illustrated in Figs. 7-24(b) to 7-24(g). They are compact and adherent layers of cobaltowüstite. Internal oxidation was not observed and the interface between alloy and oxide was planar. The minor irregularities at this interface are due to coagulation of vacancies and plastic flow of the oxide phase to fill up the cavities.

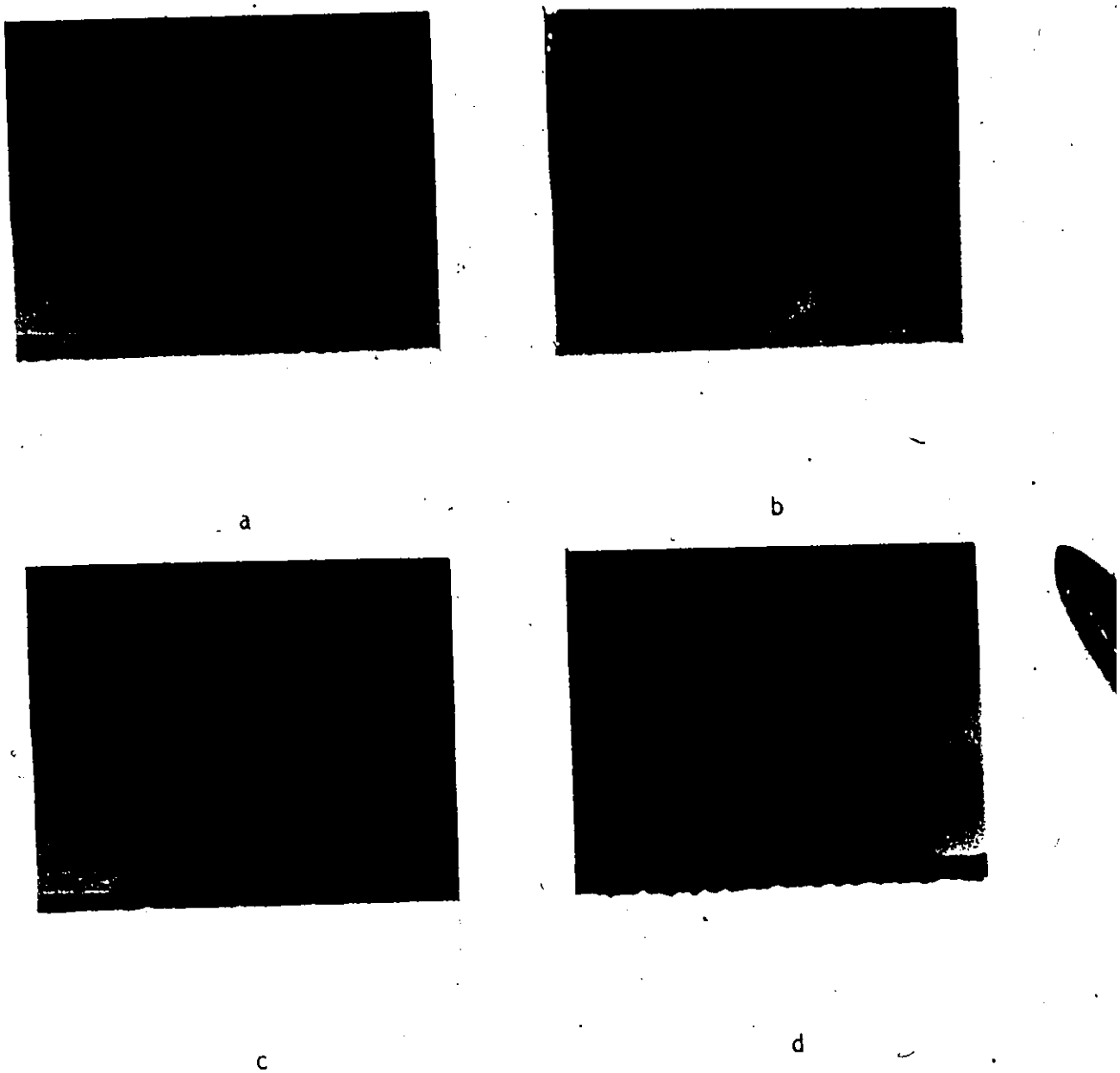

Fig. 7-23

Cross sections of oxide scales formed at 10^{-1} atm oxygen pressure: (a) pure cobalt oxidized for 30 min - (200X, unetched); (b) Co-1% Fe alloy oxidized for 30 min - (200X, unetched); (c) Co-2% Fe alloy oxidized for 20 min - (200X, unetched); (d) Co-4% Fe alloy oxidized for 10 min - (200X, unetched).

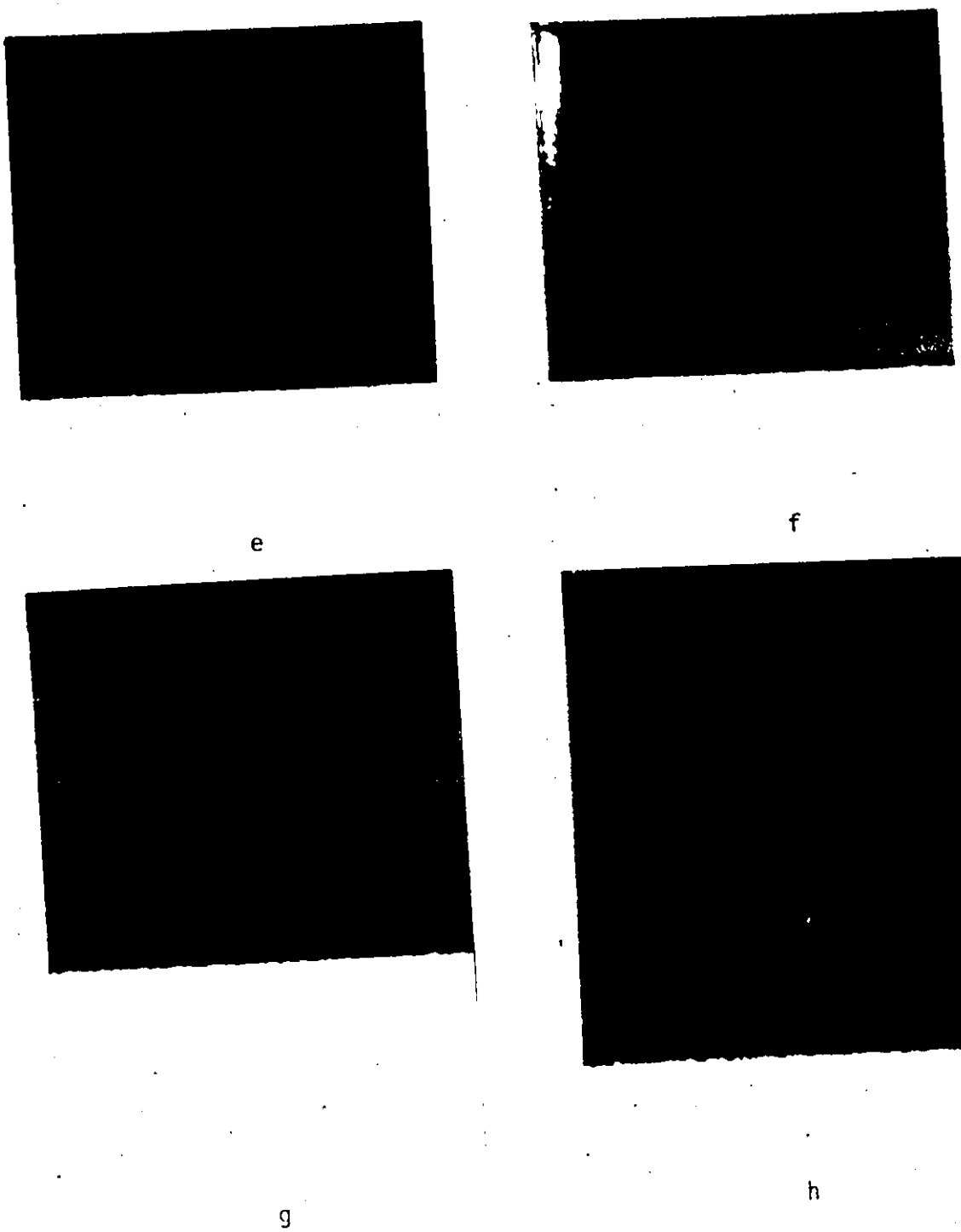

Fig. 7-23

Cross sections of oxide scales formed at 10^{-1} atm oxygen pressure: (e) Co-6% Fe alloy oxidized for 20 min - (200X, unetched); (f) Co-8% Fe alloy oxidized for 15 min - (200X, unetched); (g) Co-10% Fe alloy oxidized for 15 min - (200X, unetched) (h) Co-20% Fe alloy oxidized for 15 min - (320X, unetched).

Fig. 7-23

Cross sections of oxide scales formed at 10^{-1} atm oxygen pressure: (i) Co-30% Fe alloy oxidized for 30 min - (320X, etched); (j) Co-40% Fe alloy oxidized for 30 min - (160X, etched); (k) Co-50% Fe alloy oxidized for 30 min - (160X, etched); (l) Co-70% Fe alloy oxidized for 30 min - (160X, etched).

Co-20% Fe Alloy

The external scale shown in Fig. 7-24(h) has a structure similar to the scale formed on the same alloy at 10^{-1} atm oxygen pressure. The precipitates are particles of $(Co,Fe)_3O_4$ imbedded in a compact cobaltowüstite scale.

Co-30% Fe to Co-70% Fe Alloys

The oxide scales formed in these alloys have a similar structure to those formed during oxidation in 1 atm and 10^{-1} atm oxygen pressure. For illustration, the scales on the Co-40% Fe and Co-50% Fe alloys are shown in Figs. 7-24(i) and 7-24(j).

7.3.5 Structures of External Scales Formed at 10^{-3} atm Oxygen Pressure

Pure Cobalt

The oxide scale shown in Fig. 7-25(a) is compact and adherent CoO. Spinel particles as found in the scales formed at higher oxygen pressures were not observed.

Co-1% Fe to Co-10% Alloys

The cross-sections of the scales on these alloys are shown in Figs. 7-25(b) to 7-25(g). They are adherent compact one phase cobaltowüstite layers. The interface retains planar shape throughout the course of oxidation at all alloy concentrations. Internal oxidation was not observed except for the Co-10% Fe alloy. The cross-section in Fig. 7-25(g) shows some irregularities at the alloy-oxide interface.

Co-20% Fe alloy

An oxide scale on this alloy is composed of a cobaltowüstite oxide layer containing particles of $(Co,Fe)_3O_4$ in the outer part of the scale (Fig. 7-25(h)).

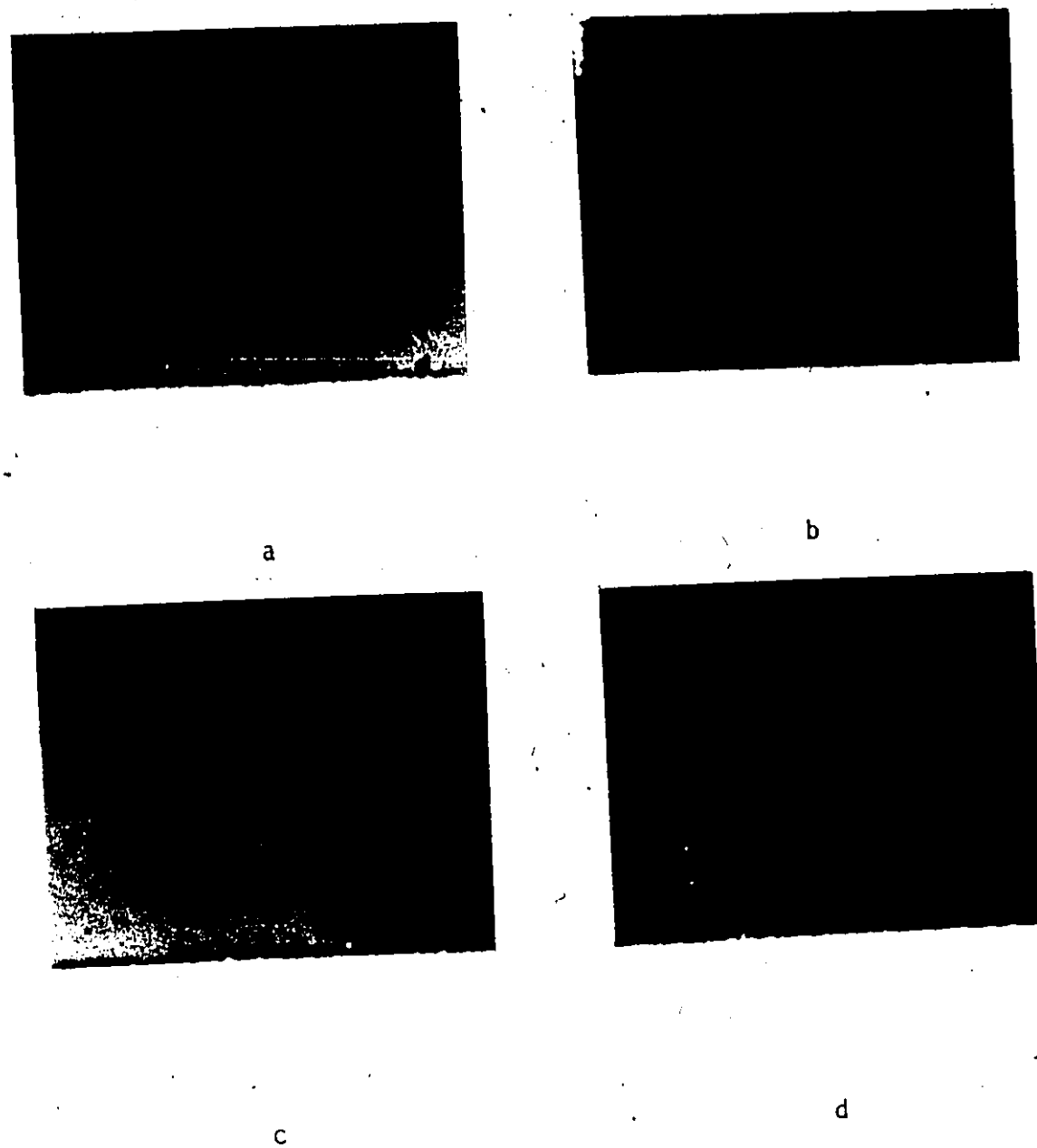

Fig. 7-24

Cross sections of oxide scales formed at 10^{-2} atm oxygen pressure: (a) pure cobalt oxidized for 60 min - (200X, unetched); (b) Co-1% Fe alloy oxidized for 60 min - (200X, unetched); (c) Co-2% Fe alloy oxidized for 30 min - (200X, unetched); (d) Co-4% Fe alloy oxidized for 30 min - (200X, unetched).

e

f

g

h

Fig. 7-24

Cross sections of oxide scales formed at 10^{-2} atm oxygen pressure: (e) Co-6% Fe alloy oxidized for 30 min - (200X, unetched); (f) Co-8% Fe alloy oxidized for 15 min - (200X, unetched); (g) Co-10% Fe alloy oxidized for 15 min - (200X, unetched); (h) Co-20% Fe alloy oxidized for 30 min - (160X, unetched).

i j

Fig. 7-24

Cross sections of oxide scales formed at 10^{-2} atm oxygen pressure: (i) Co-40% Fe alloy oxidized for 30 min - (160X, etched); (j) Co-50% Fe alloy oxidized for 30 min - (160X, etched).

Co-30% Fe Alloy

A cross-section of the scale on this alloy is shown in Fig. 7-25(i). The cobaltowüstite layer with dispersed small particles of $(Co,Fe)_3O_4$ contains a region of large semicontinuous spinel phase formations near the outer interface. Internal oxidation is confined to a narrow region at the metal-oxide interface.

Co-40% Fe to Co-70% Fe Alloys

Figs. 7-25(j) to 7-25(l) show the cross-sections of scales formed on these alloys. The scales have the same structural features as those formed at higher oxygen pressures: two cobaltowüstite layers containing spinel particles with a continuous $(Co,Fe)_3O_4$ layer between them. Again internal oxidation is confined to the narrow zone at the metal-oxide interface.

7.3.6 Structures of External Scales Formed at 10^{-4} atm Oxygen Pressure

Pure Cobalt

Fig. 7-26(a) shows the compact CoO scale formed after 60 minutes. The polishing revealed the columnar structure of the scale. No porosity was observed at the metal-oxide interface. Porosity in the scale was created by "metallographical pull out".

Co-1% Fe to Co-10% Fe Alloys

The scales on these alloys are shown in Figs. 7-26(b) to 7-26(g). An oxide layer is a single compact phase of cobaltowüstite with an irregular outer interface caused by outward preferential growth of large columnar grains. Inner interface between alloy-scale is planar with limited amounts of internal oxide occurring in alloys with iron content higher than 0.

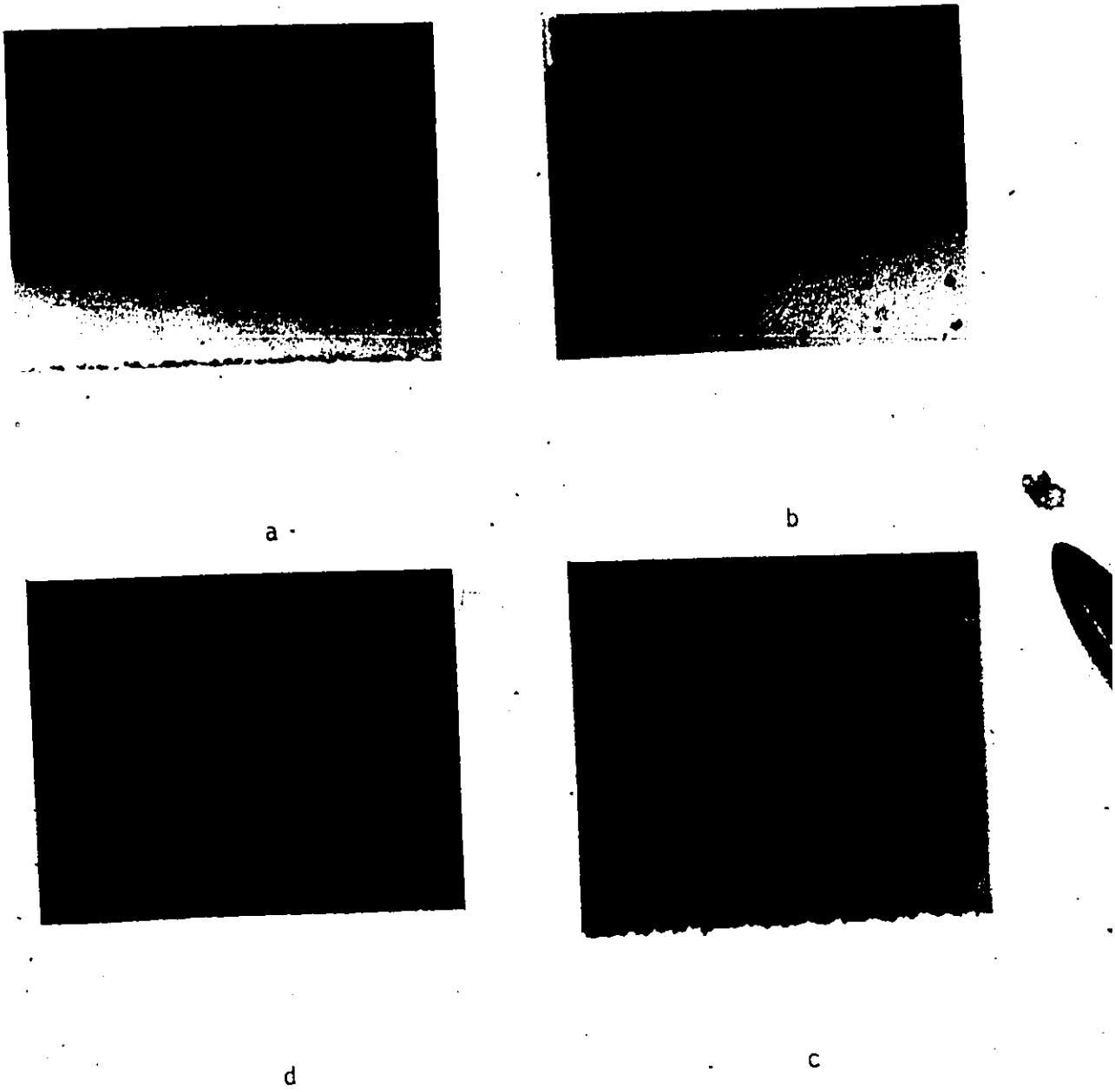

Fig. 7-25

Cross sections of oxide scales formed at 10^{-3} atm oxygen pressure: (a) pure cobalt oxidized for 120 min - (200X, unetched); (b) Co-1% Fe alloy oxidized for 45 min - (200X, unetched); (c) Co-2% Fe alloy oxidized for 45 min - (200X, unetched); (d) Co-4% Fe alloy oxidized for 45 min - (200X, unetched).

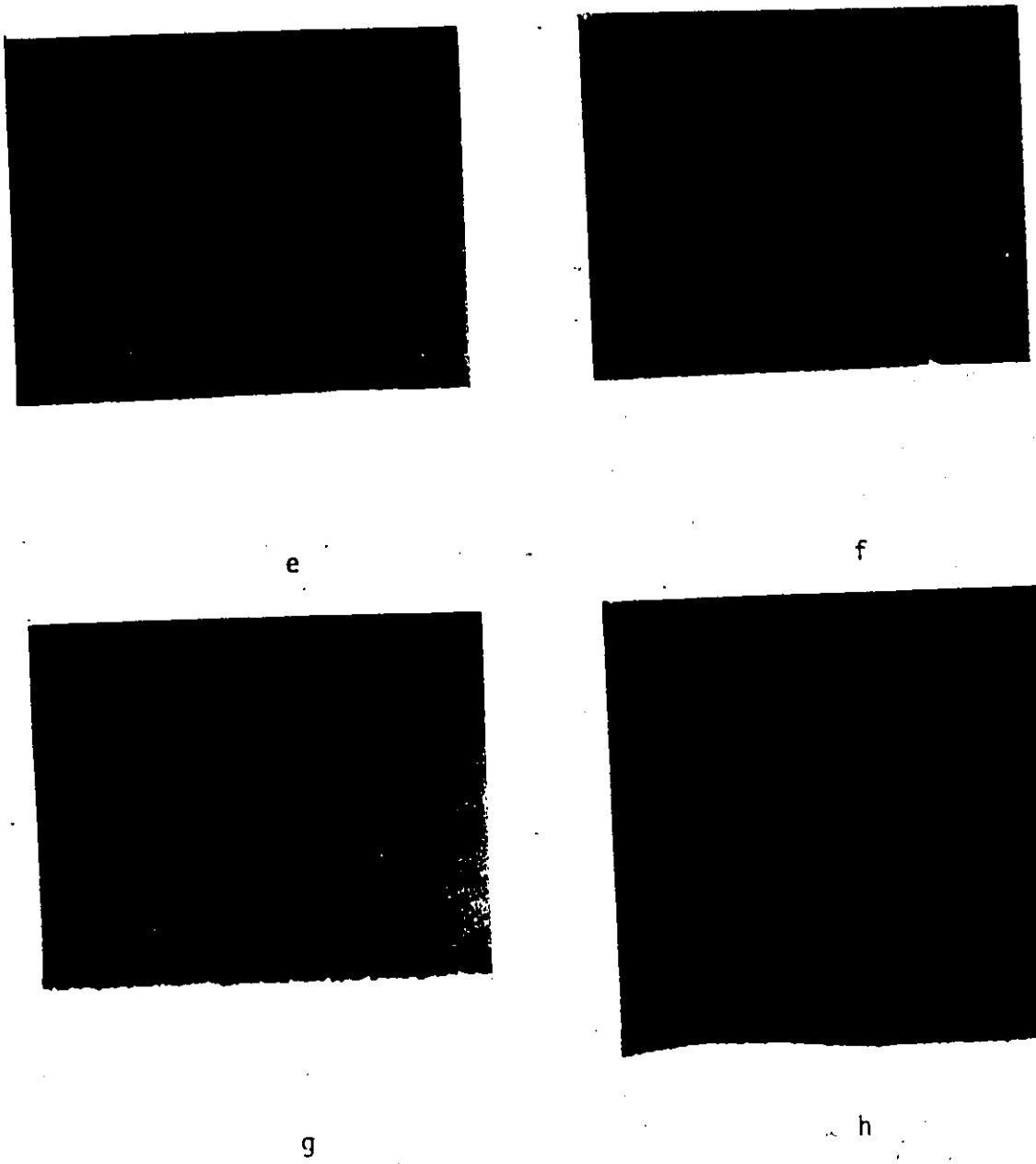

e f

g h

Fig. 7-25

Cross sections of oxide scales formed at 10^{-3} atm oxygen pressure: (e) Co-6% Fe alloy oxidized for 25 min - (200X, unetched); (f) Co-8% Fe alloy oxidized for 15 min - (200X, unetched); (g) Co-10% Fe alloy oxidized for 15 min - (200X, unetched); (h) Co-20% Fe alloy oxidized for 30 min - (200X, unetched).

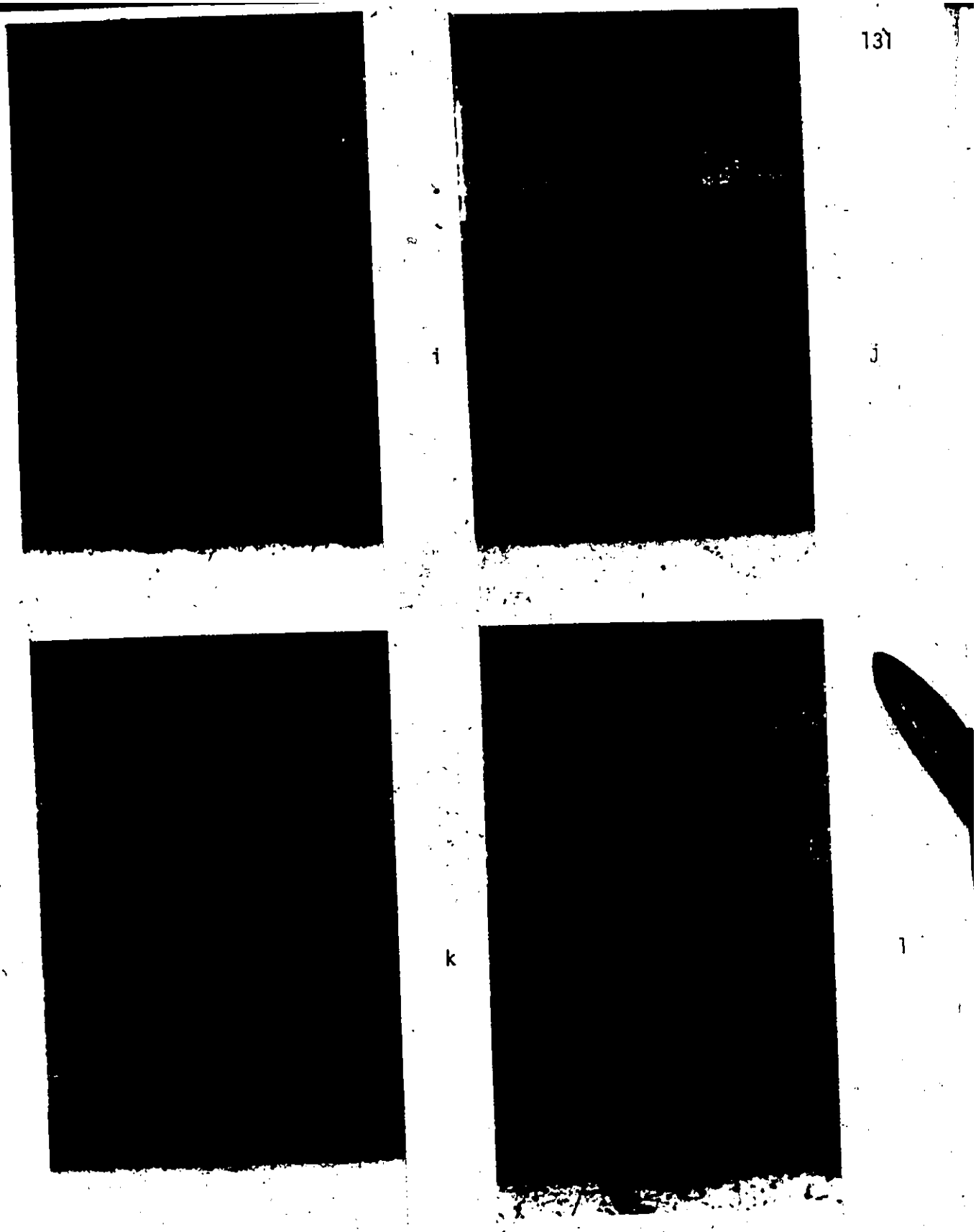

Fig. 7-25

Cross sections of oxide scales formed at 10^{-3} atm oxygen pressure: (i) Co-30% Fe alloy oxidized for 45 min - (200X, unetched); (j) Co-40% Fe alloy oxidized for 60 min - (200X, etched); (k) Co-50% alloy oxidized for 60 min - (200X, etched); (l) Co-70% Fe alloy oxidized for 60 min - (200X, etched).

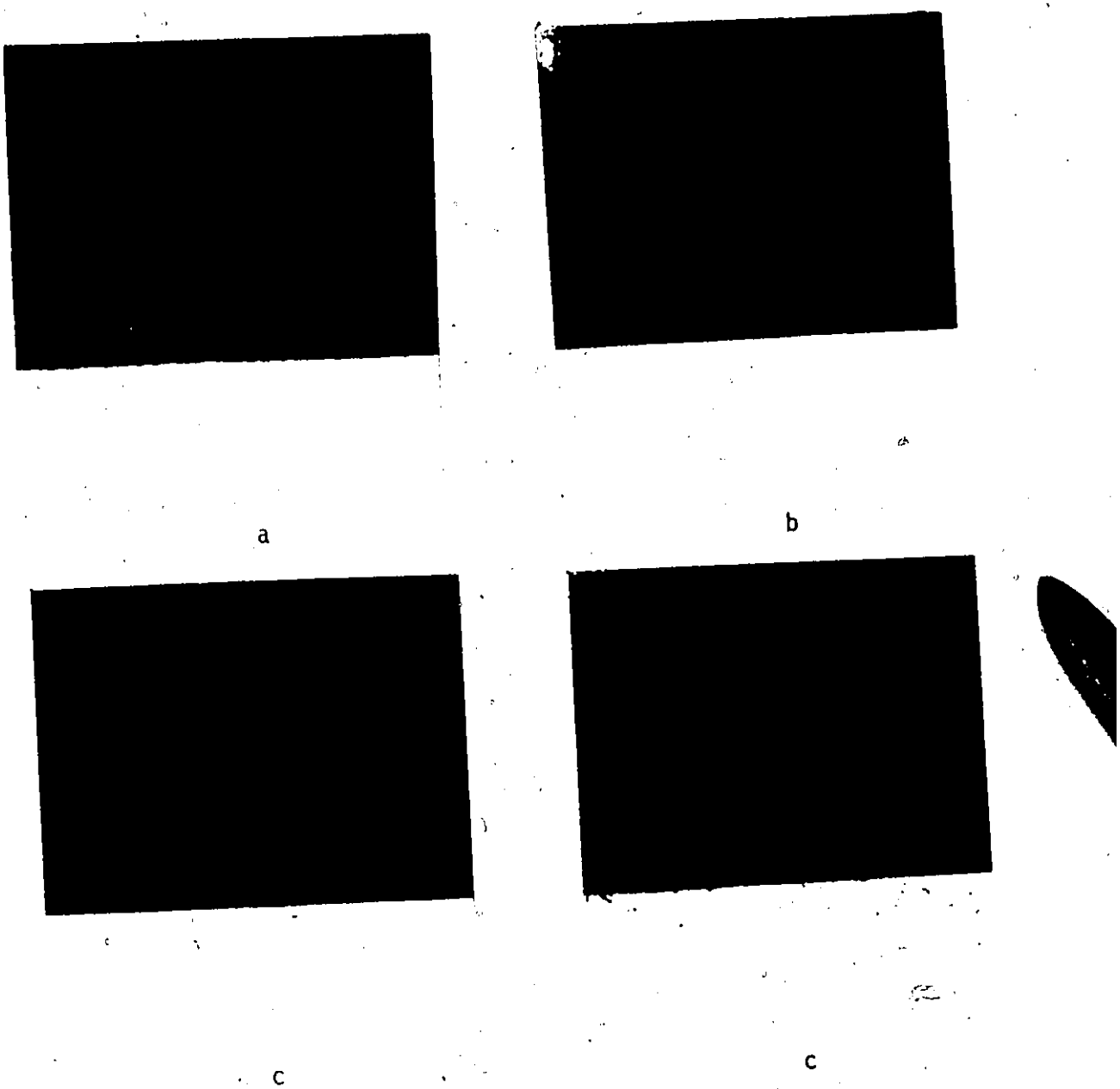

Fig. 7-26

Cross sections of oxide scales formed at 10^{-4} atm oxygen pressure: (a) pure cobalt oxidized for 60 min - (200X, unetched); (b) Co-1% Fe alloy oxidized for 20 min - (200X, unetched); (c) Co-2% Fe alloy oxidized for 30 min - (200X, unetched); (d) Co-4% Fe alloy oxidized for 20 min - (200X, unetched).

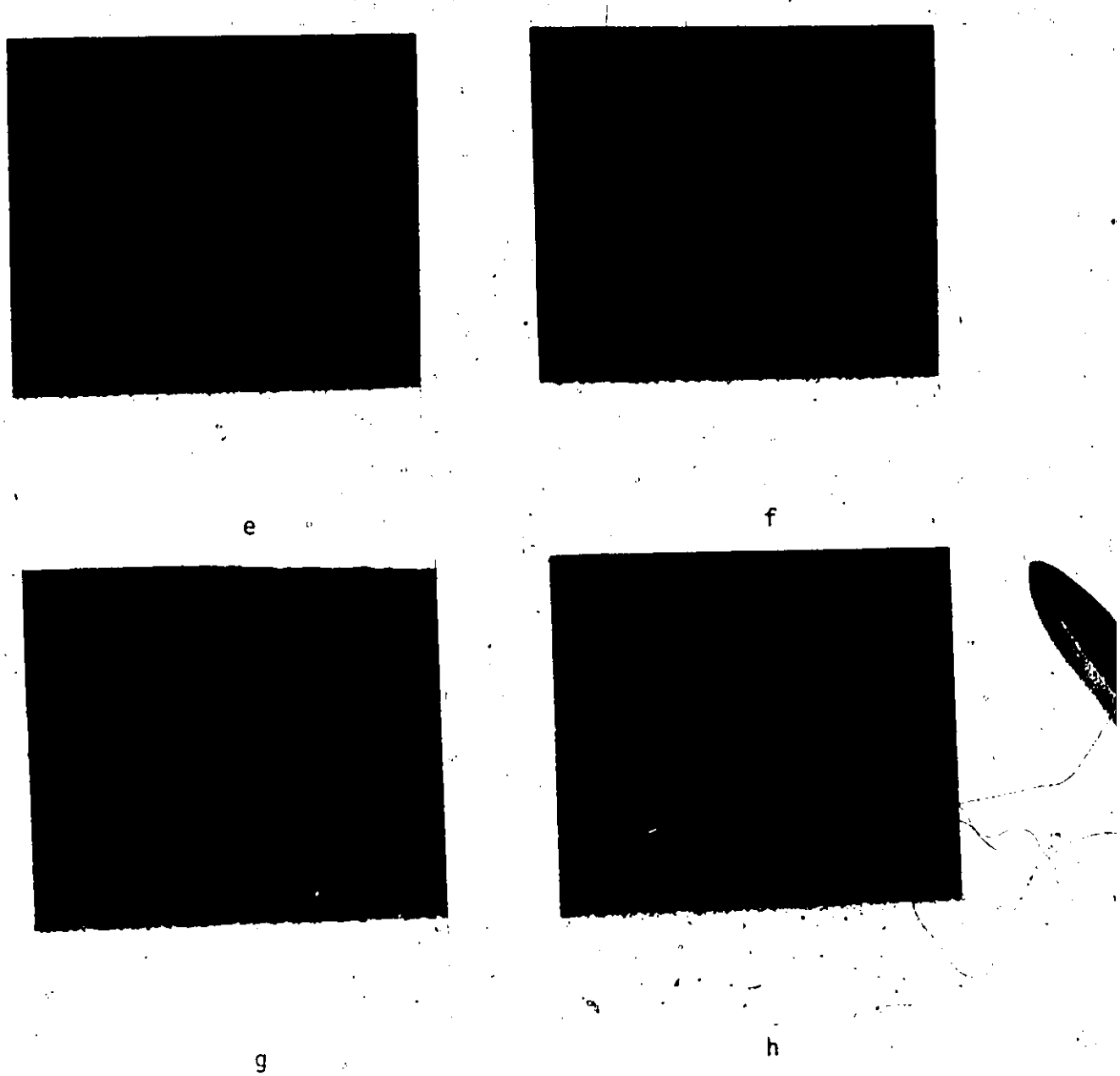

Fig. 7-26

Cross sections of oxide scales formed at 10^{-4} atm oxygen pressure: (e) Co-6% Fe alloy oxidized for 30 min - (200X, unetched); (f) Co-8% Fe alloy oxidized for 20 min - (200X, unetched); (g) Co-10% Fe alloy oxidized for 10 min - (200X, unetched); (h) Co-20% Fe alloy oxidized for 30 min - (200X, unetched).

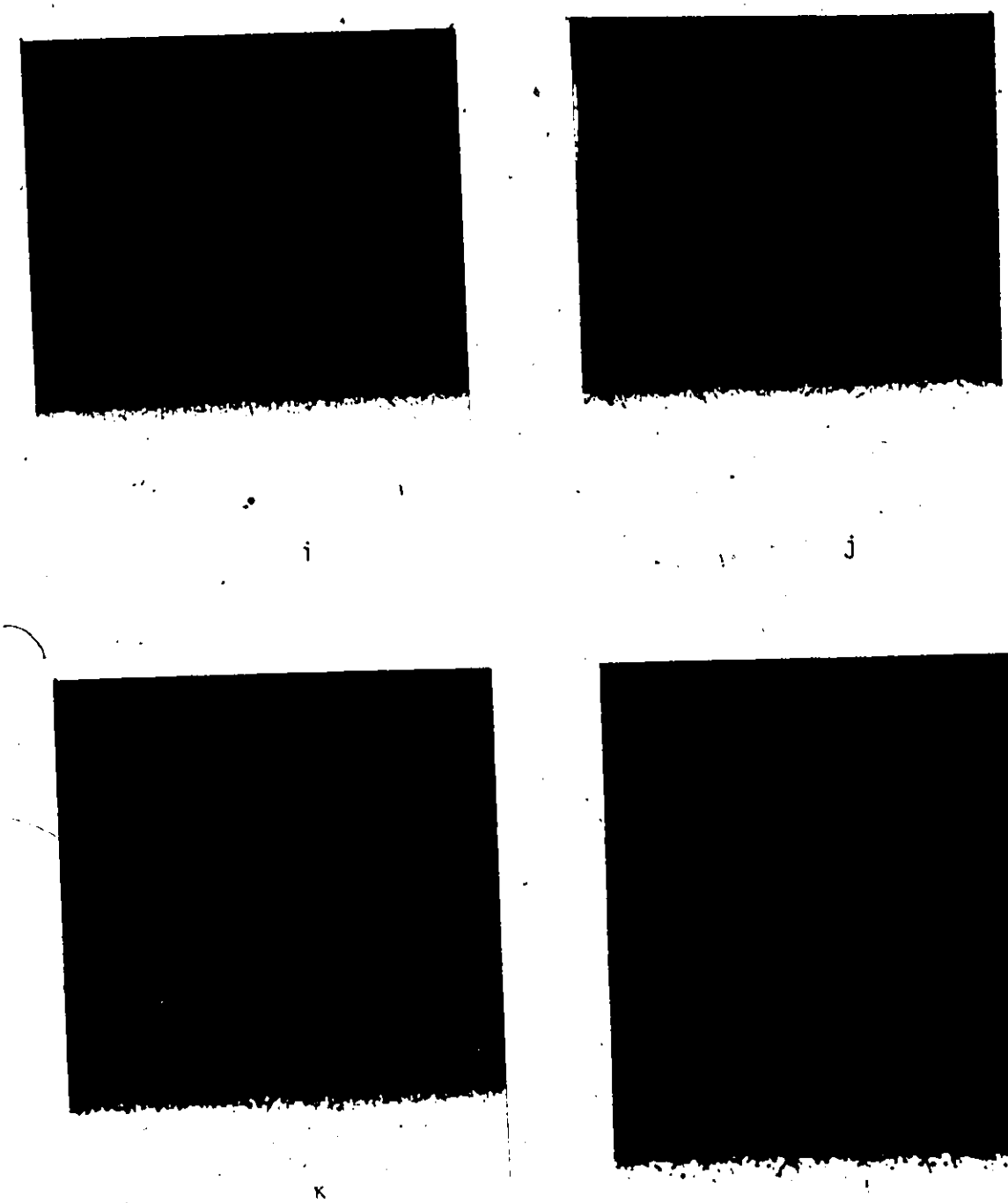

Fig. 7-26

Cross sections of oxide scales formed at 10^{-4} atm oxygen pressure: (i) Co-30% Fe alloy oxidized for 30 min - (200X, unetched); (j) Co-40% Fe alloy oxidized for 60 min - (200X, unetched); (k) Co-50% Fe alloy oxidized for 60 min - (200X, unetched); (l) Co-70% Fe alloy oxidized for 60 min - (200X, unetched).

Co-20 Fe to Co-70% Fe Alloys

The structure of the scales is two-phase cobaltowüstite and spinel. There is a gradual change in the distribution of the spinel phase. Cross sections of the scales are illustrated in Figs. 7-26(h) to 7-26(l). The density of dispersed spinel particles at an outer interface increases with iron alloy content. A continuous spinel phase is formed in the scales on alloys containing greater than 40% Fe.

7.3.7 Summary - "Oxidation Map"

The morphological development of the scales can be summarized concisely and informatively by using an "oxidation map". This is a diagram indicating the type of oxide scales forming on the alloys as a function of iron alloy content and oxygen pressure.

Five distinct structural types of oxide scales which developed at 1200°C are illustrated in Fig. 7-27. Symbols in the brackets designate the particular type of structure, and are used in Fig. 7-28. The latter figure is an "oxidation map" for cobalt-iron alloys exposed to oxygen at 1200°C. The diagram can be divided into two parts: single phase and multiple phase scale formation. Since this work will be concerned with the theory of alloy oxidation when only a one-phase scale is forming during the course of oxidation, alloys containing up to 10% Fe will be considered in the following section.

7.4 Concentration Profiles

Spatial distributions of the constituent elements within the oxidized specimens were measured using an electron probe microanalyser. The measured concentrations were recorded as a function of the position in the cross sectioned samples. The point count method was used at regular distance

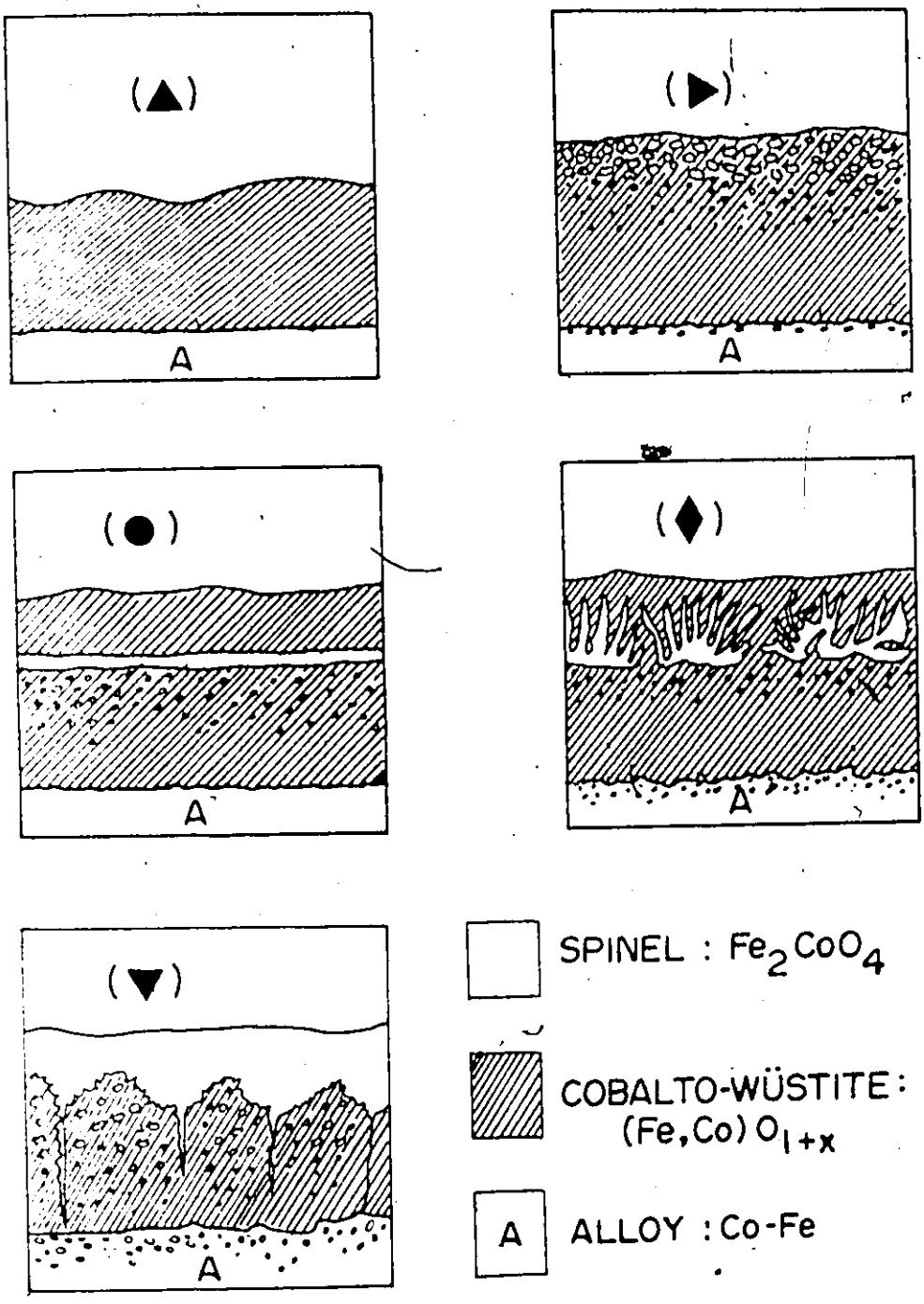

Fig. 7-27

Types of oxide scales formed on cobalt-iron alloys at 1200°C in oxygen atmospheres.

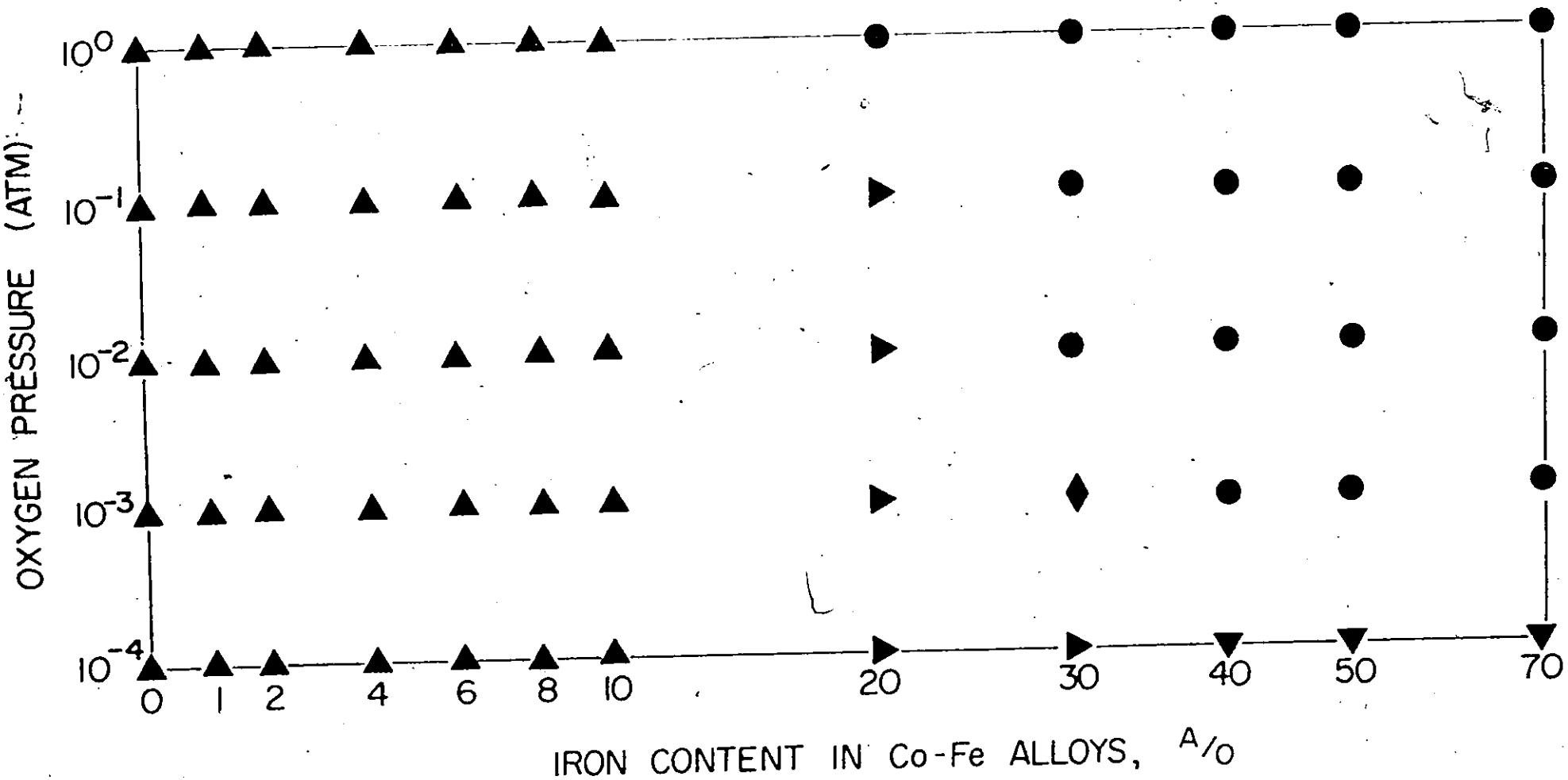

Fig. 7-28

"Oxidation map" for cobalt-iron alloys oxidized in oxygen at 1200°C. (Symbols are explained in Fig. 7-27)

intervals scanning the sample in the direction of the prevailing diffusion process, i.e. perpendicular to the alloy-oxide and oxide-gas interfaces.

Iron, cobalt and oxygen are the constituents of the experimental system apart from impurities, and therefore, the measurements of their distributions are essential for an understanding of the oxidation process. To measure oxygen concentrations in the alloy is impractical because of its low solubility in cobalt-iron alloys. Similarly impractical are measurements of oxygen in the oxide phase, in spite of its high concentrations. Oxygen concentrations measured by the microprobe technique contain large errors which are due to the fact that oxygen has a very low atomic number. Elements with atomic numbers lower than 11 are at the lower detection limit of the instrument, and naturally the measured concentrations are not accurate. However, oxygen concentrations in the oxide phases could be easily calculated from the iron and cobalt profiles knowing the oxide stoichiometric composition. Any error introduced by this calculation is smaller than the measurement error. Moreover, the concentration measurements of one metal component are generally sufficient because in binary alloy and oxide systems the concentrations are chemically complementary.

Concentration profiles were quantitatively determined in oxidized samples with original iron concentration 1%, 2%, 4%, 6%, 8% and 10%. Since the cobalt content of the samples is high, the most significant error is involved in its measurement. Accordingly it was more accurate to determine the iron concentration profile in the alloy and oxide phases.

The line scans for the distribution of iron in the oxidized alloys exhibited very little change in concentration. Any sharp decrease in iron concentration at the alloy-oxide interface is not possible to measure, since

the spatial extent of the corresponding iron profile at this interface is smaller than the size of the electron beam. Under this condition, the interference from the alloy with high iron content and from the oxide phase smears out the actual concentration profiles. This situation was observed in all analysed samples, and therefore the concentration profiles in the alloys are not included in the following diagrams.

Metal concentrations in the external scales were plotted as a function of the dimensionless parameter y defined by the Eq. (3.35)

$$y = x/x_s$$

where x is the distance from the alloy-oxide interface and x_s is the thickness of the external scale. The concentration of iron is expressed as the equivalent fraction of FeO in the scale, i.e. ratio of the number of equivalents of cations of Fe to the sum of the number of equivalents of iron and cobalt cations. The equivalent fraction is designated by symbol ξ. Figs. 7-29(a) to (e) and 7-30(a) to (e) show the results of microprobe measurements. The experimental conditions and original alloy concentrations are listed in each figure. A full line was drawn through the points representing the means of the measured values to emphasize the most probable form of the actual concentration profile. The errors involved in the measurements of these profiles include tilting of the samples during mounting, uncertainty in measurement of the total thickness of the oxide scale due to edge rounding during polishing and preferential growth of oxide grains, and errors associated with electron probe microanalysis.

The form of the concentration profiles changes with the oxygen pressure in the reaction atmosphere. Figs. 7-29(a) to (e) illustrate the concentration profiles in external scales formed on Co-8% Fe, Co-4% Fe and

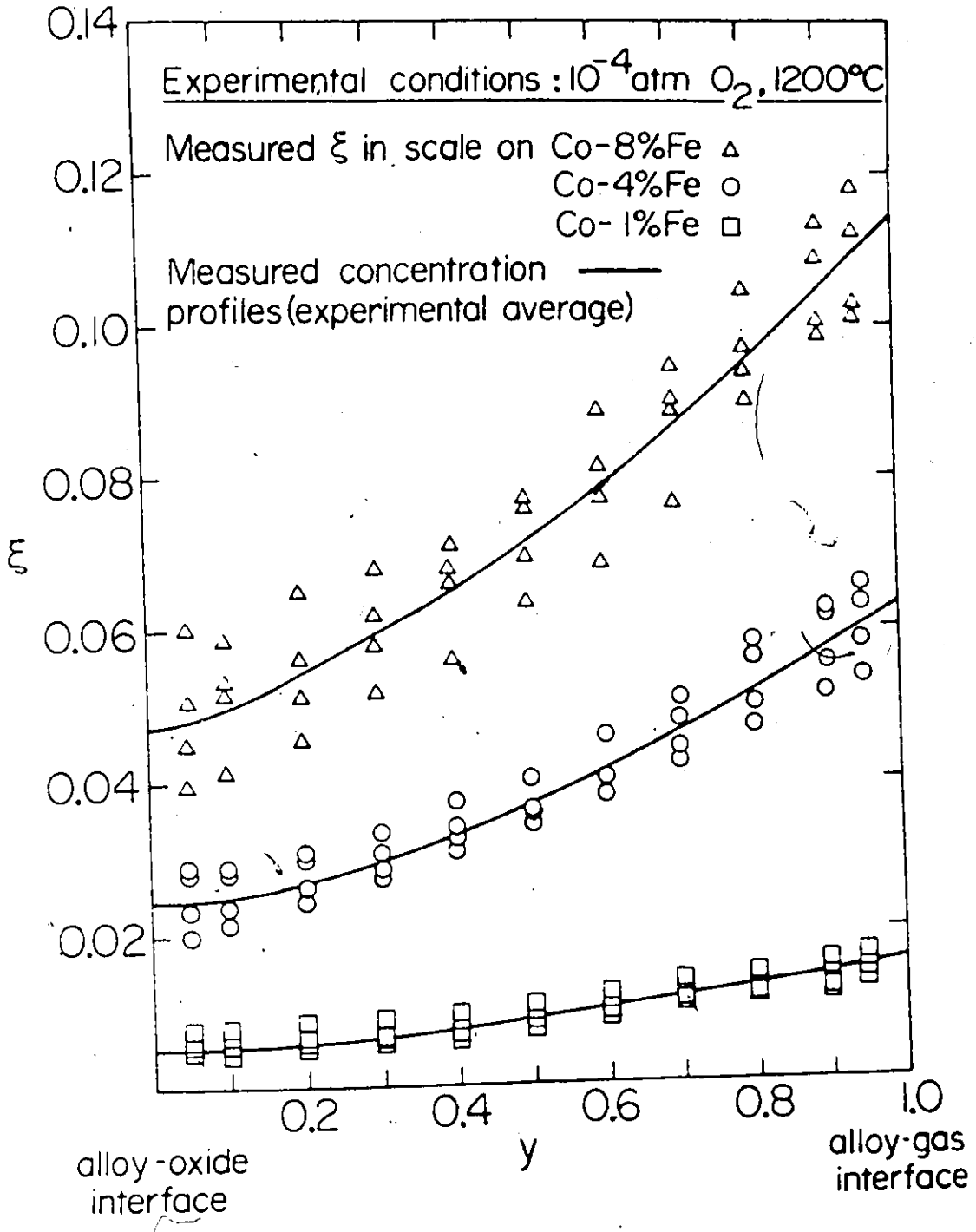

Fig. 7-23(a)

Mole fraction of FeO, ξ, as a function of normalized distance coordinate y in the CoO-FeO oxide scale

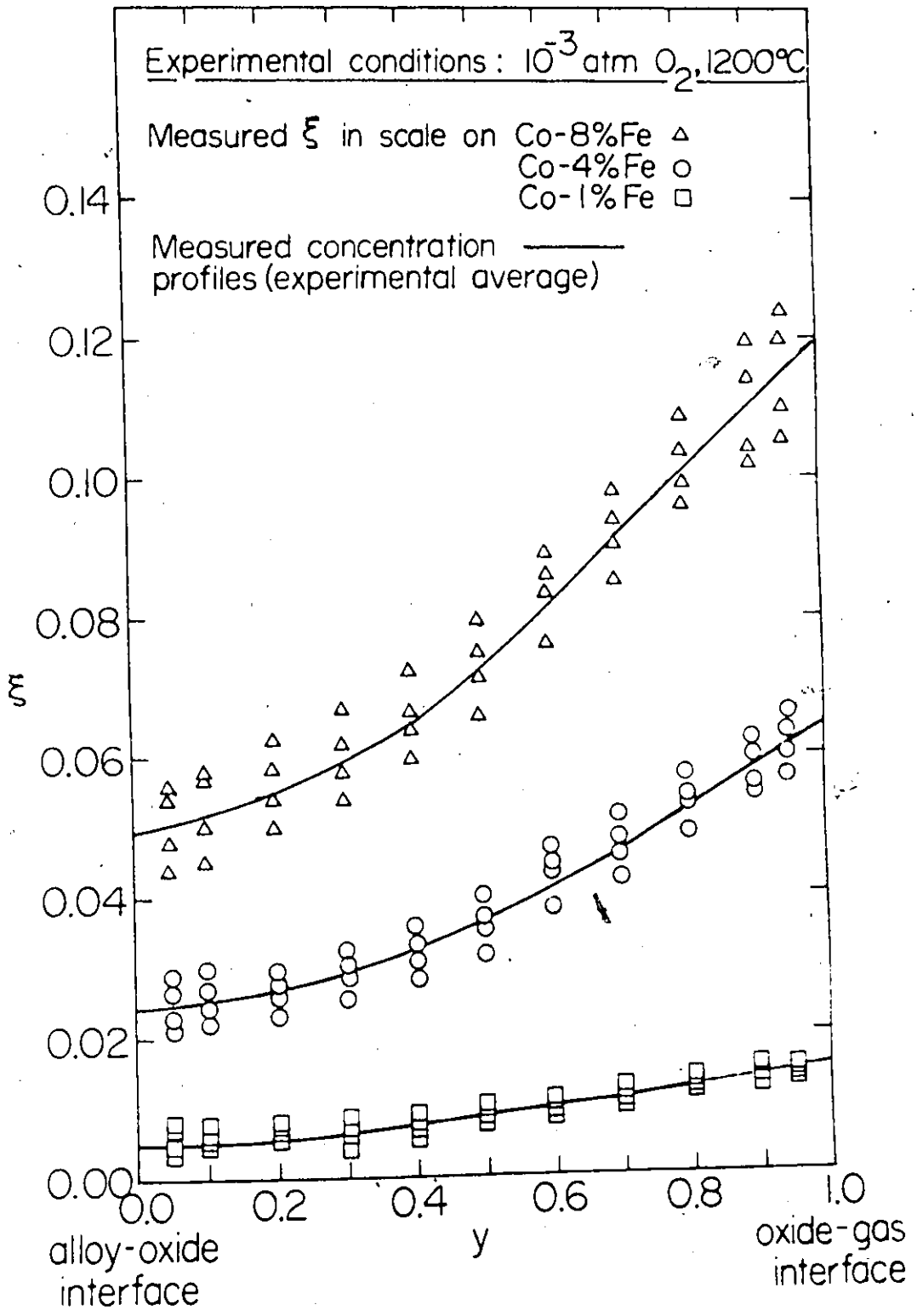

Fig. 7-29(b)

Mole fraction of FeO, ξ, as a function of normalized distance coordinate y in the CoO-FeO oxide scale

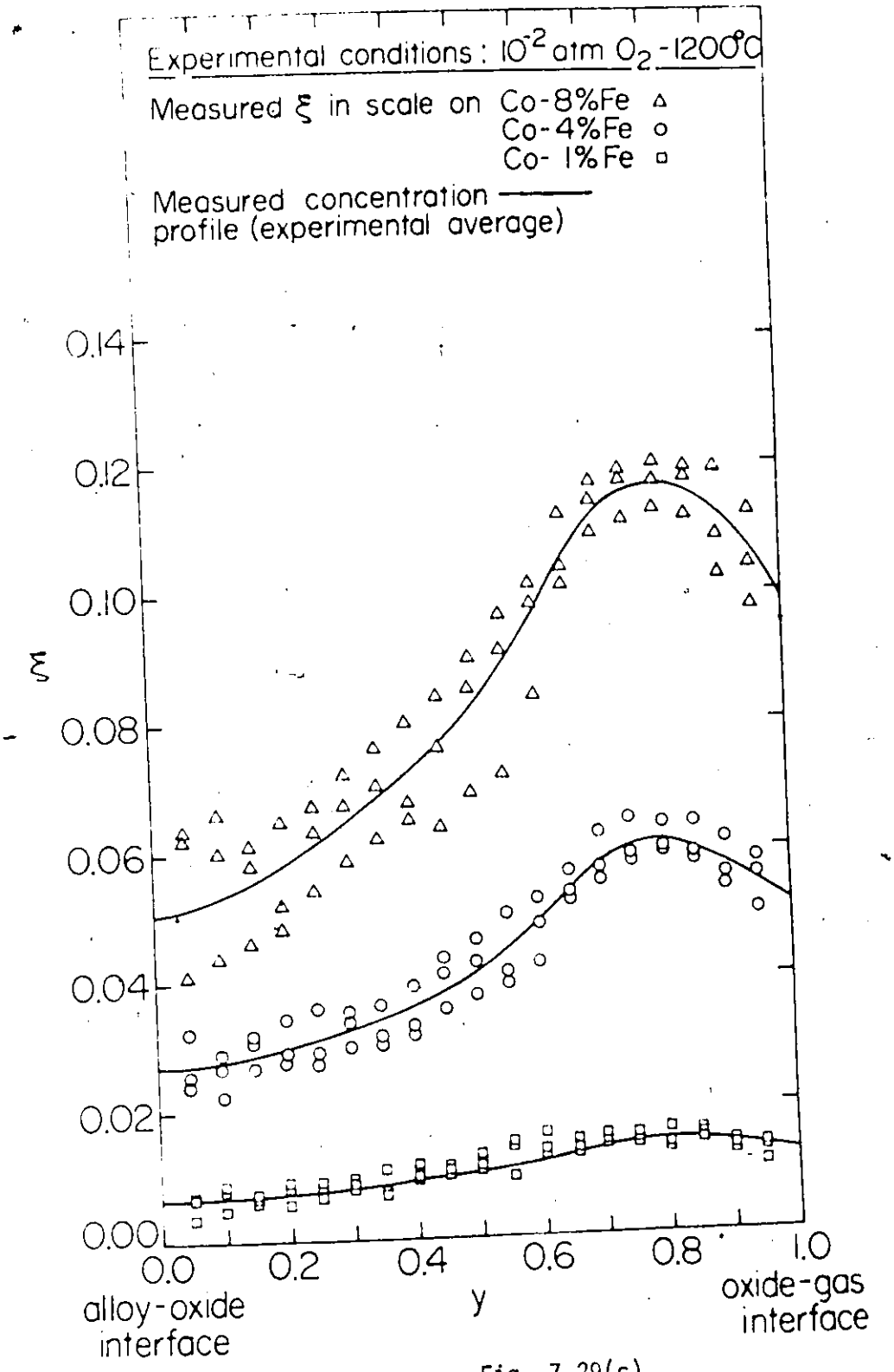

Fig. 7-29(c)

Mole fraction of FeO, ξ, as a function of normalized distance coordinate y in the CoO-FeO oxide scale

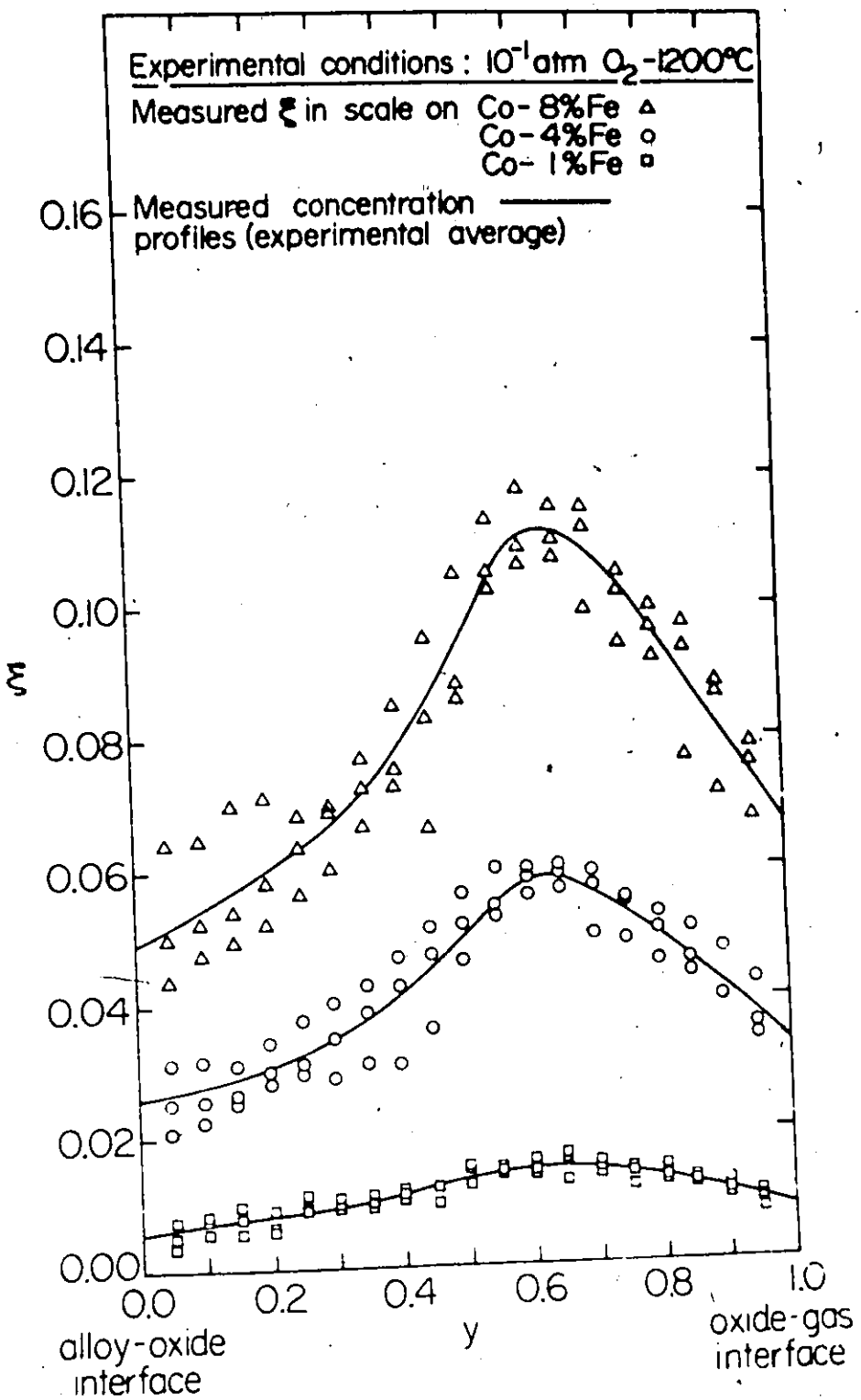

Fig. 7-29(d)

Mole fraction of FeO, ξ, as a function of normalized distance coordinate y in the CoO-FeO oxide scale

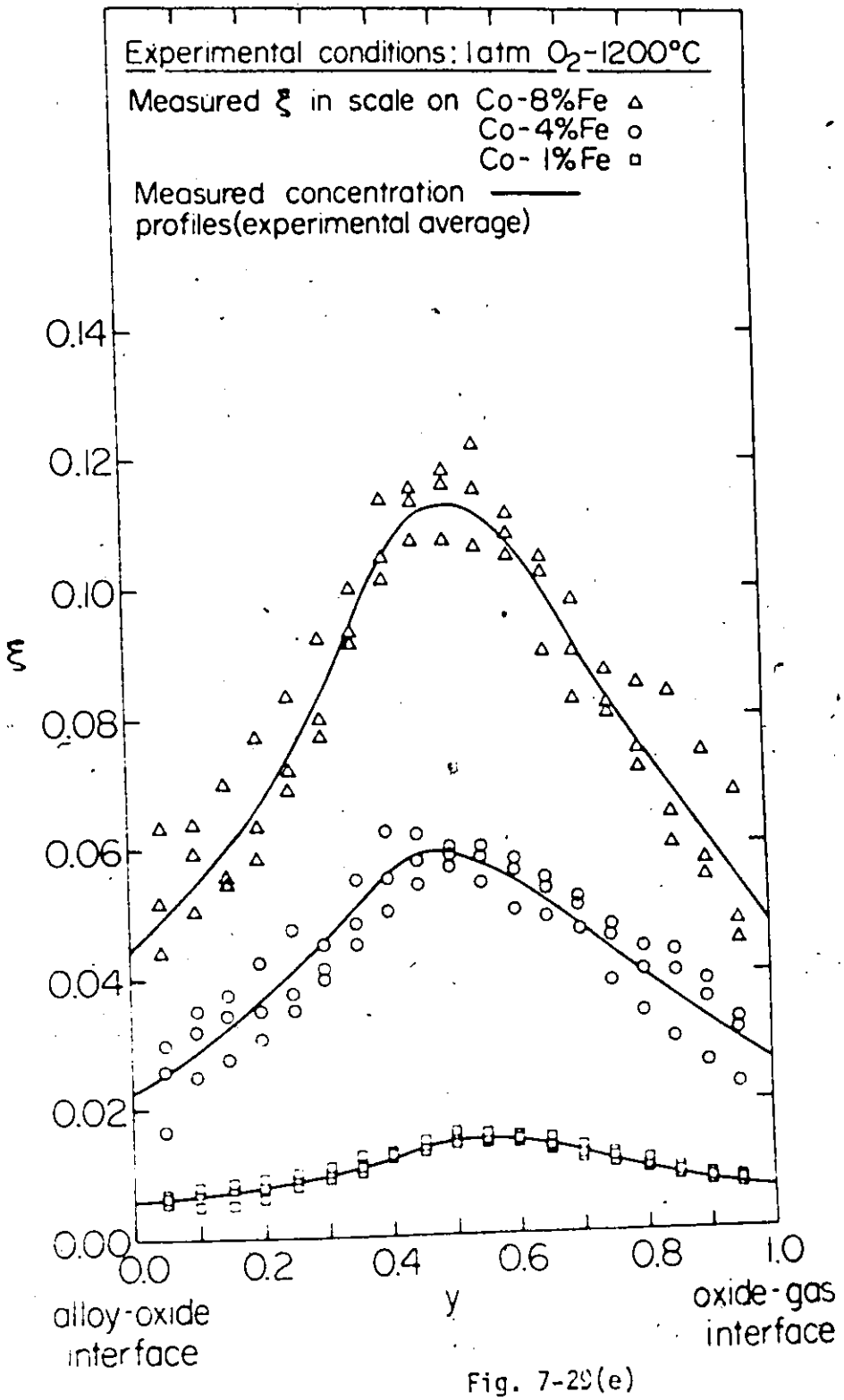

Fig. 7-29(e)

Mole fraction of FeO, ξ, as a function of normalized distance coordinate y in the CoO-FeO oxide scale

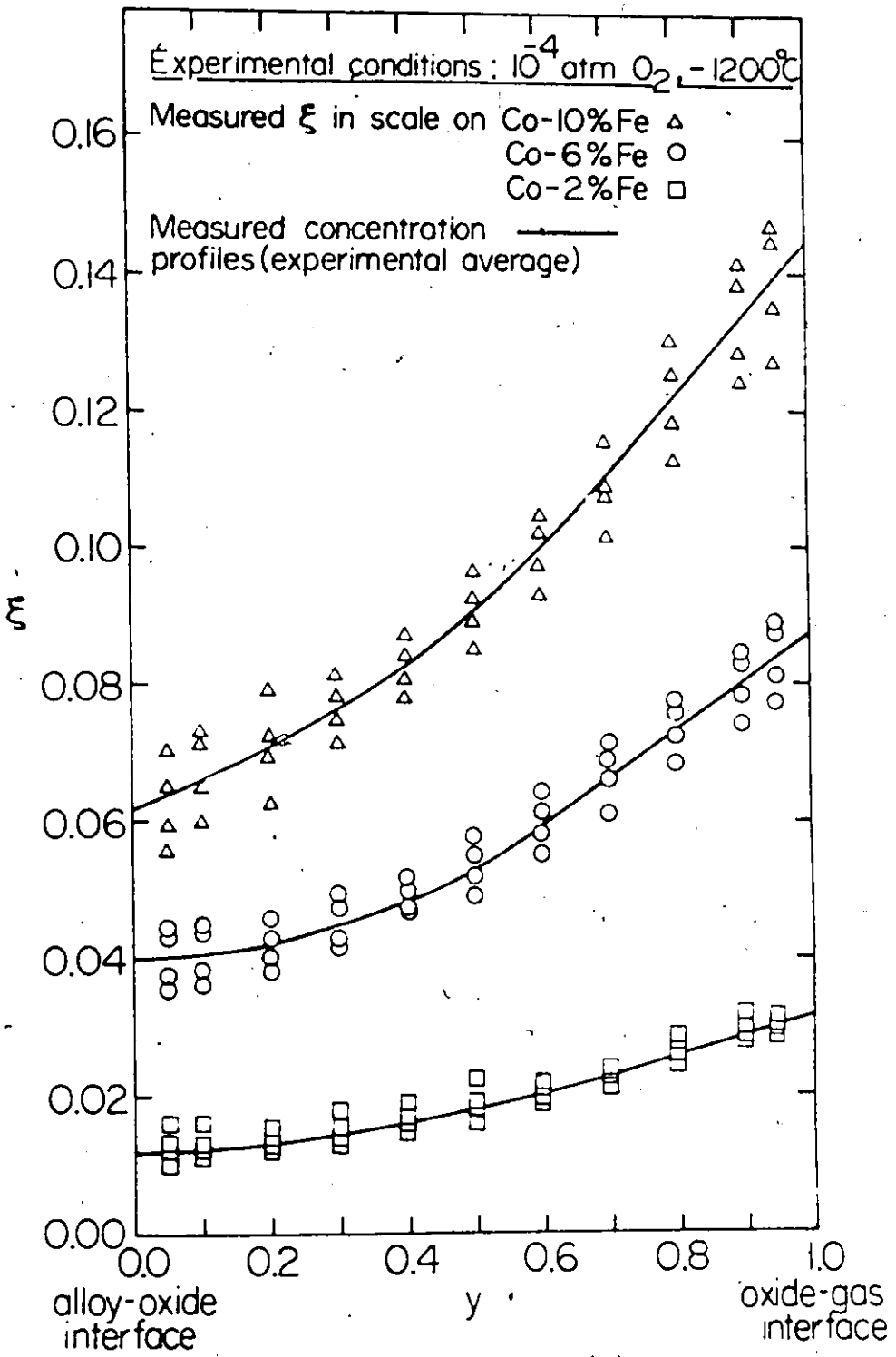

Fig. 7-33(a)

Mole fraction of FeO, ξ, as a function of normalized distance coordinate y in the CoO-FeO oxide scale

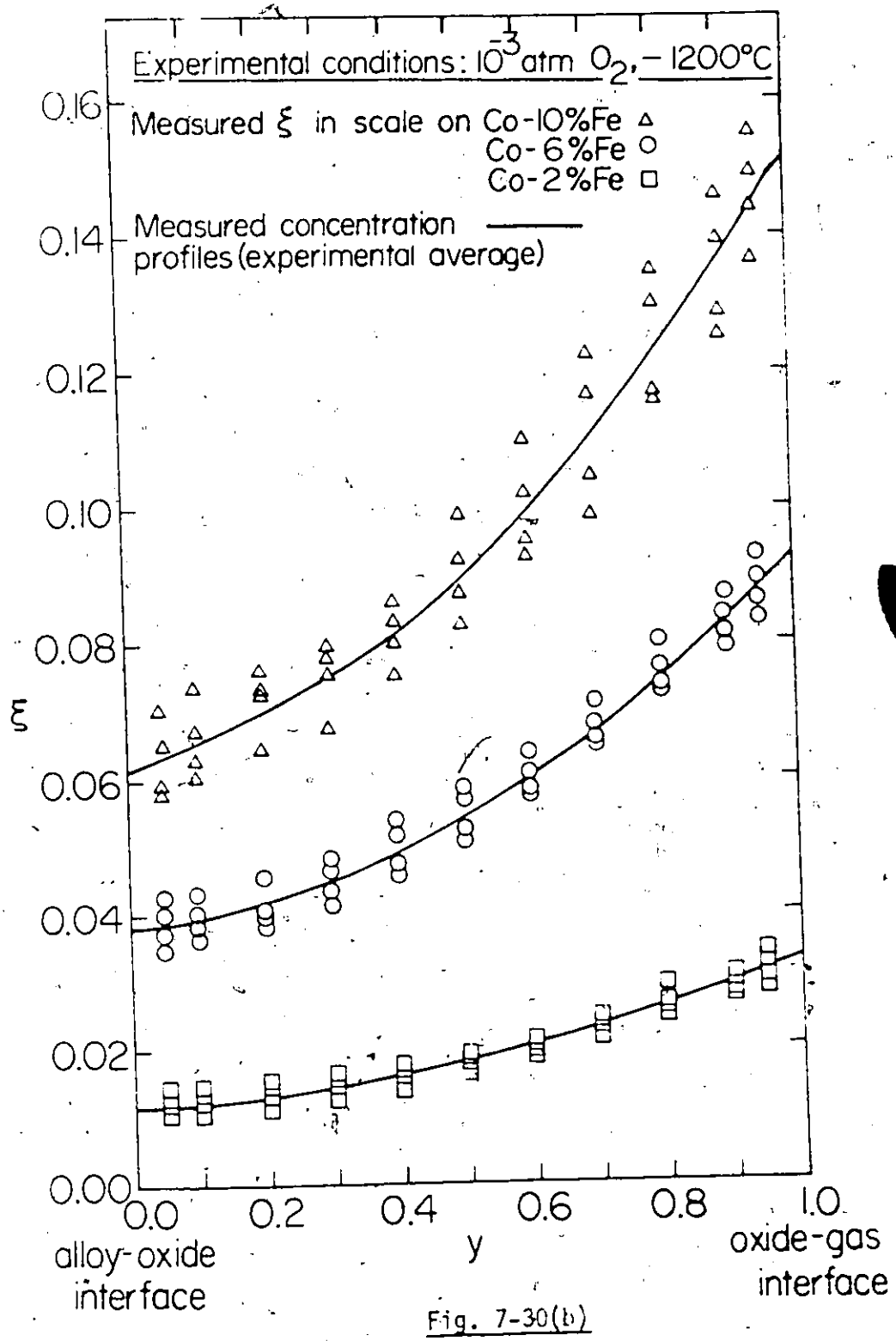

Fig. 7-30(b)

Mole fraction of FeO, ξ, as a function of normalized distance coordinate y in the CoO-FeO oxide scale.

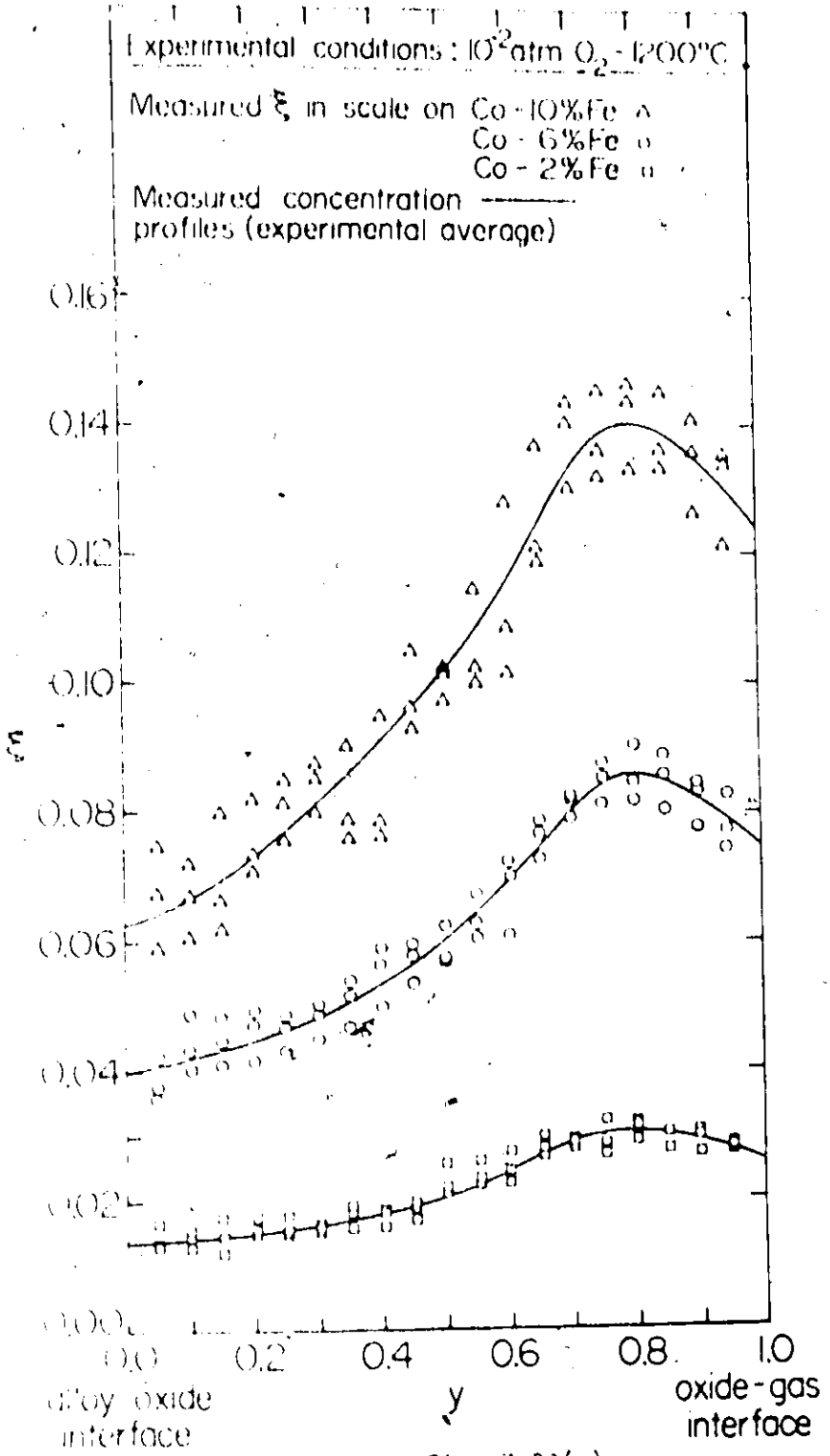

Fig. 7-30(c)

Mole fraction of FeO, ξ, as a function of normalized distance coordinate y in the CoO-FeO oxide scale

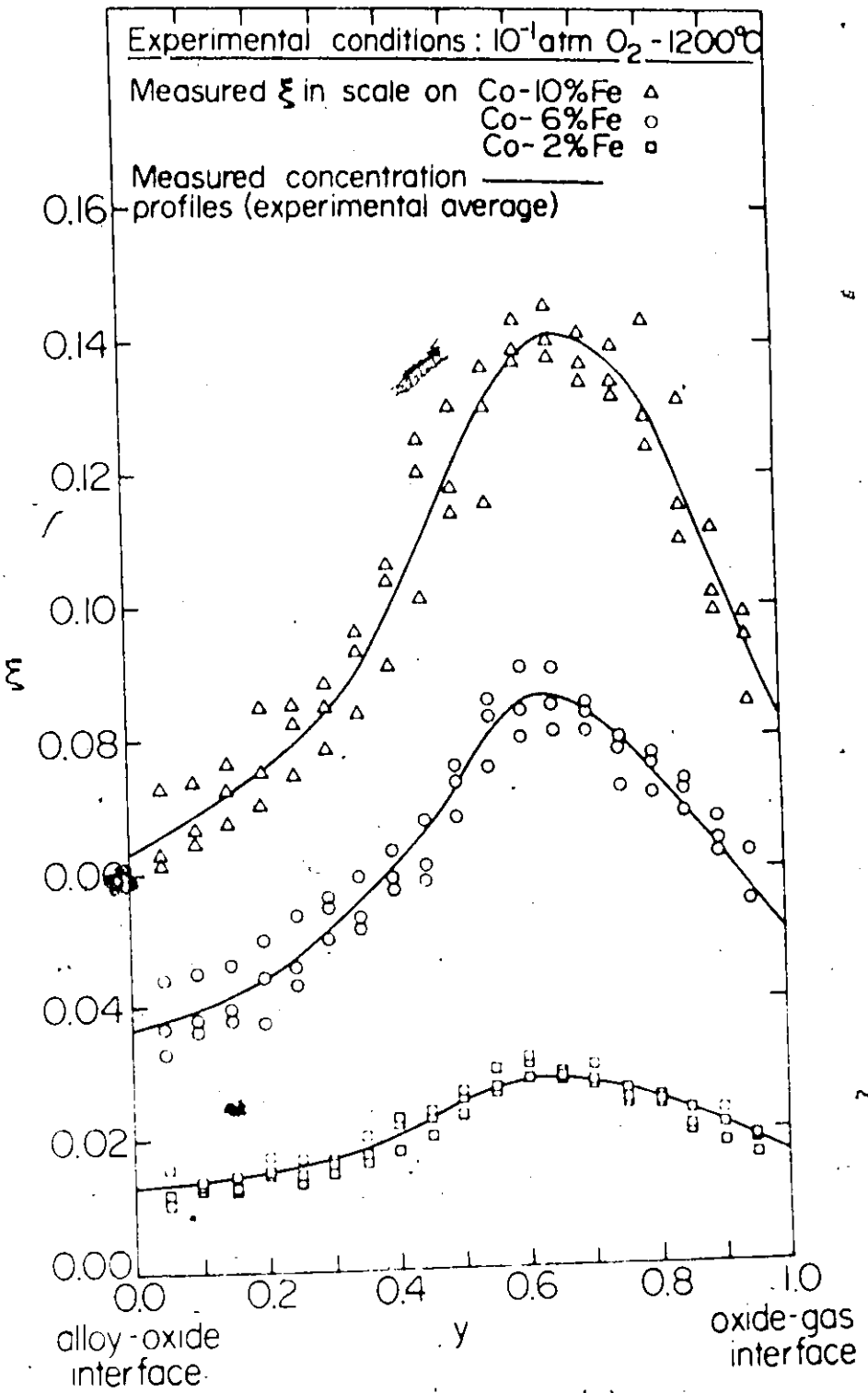

Fig. 7-30(d)

Mole fraction of FeO, ξ, as a function of normalized distance coordinate y in the CoO-FeO oxide scale

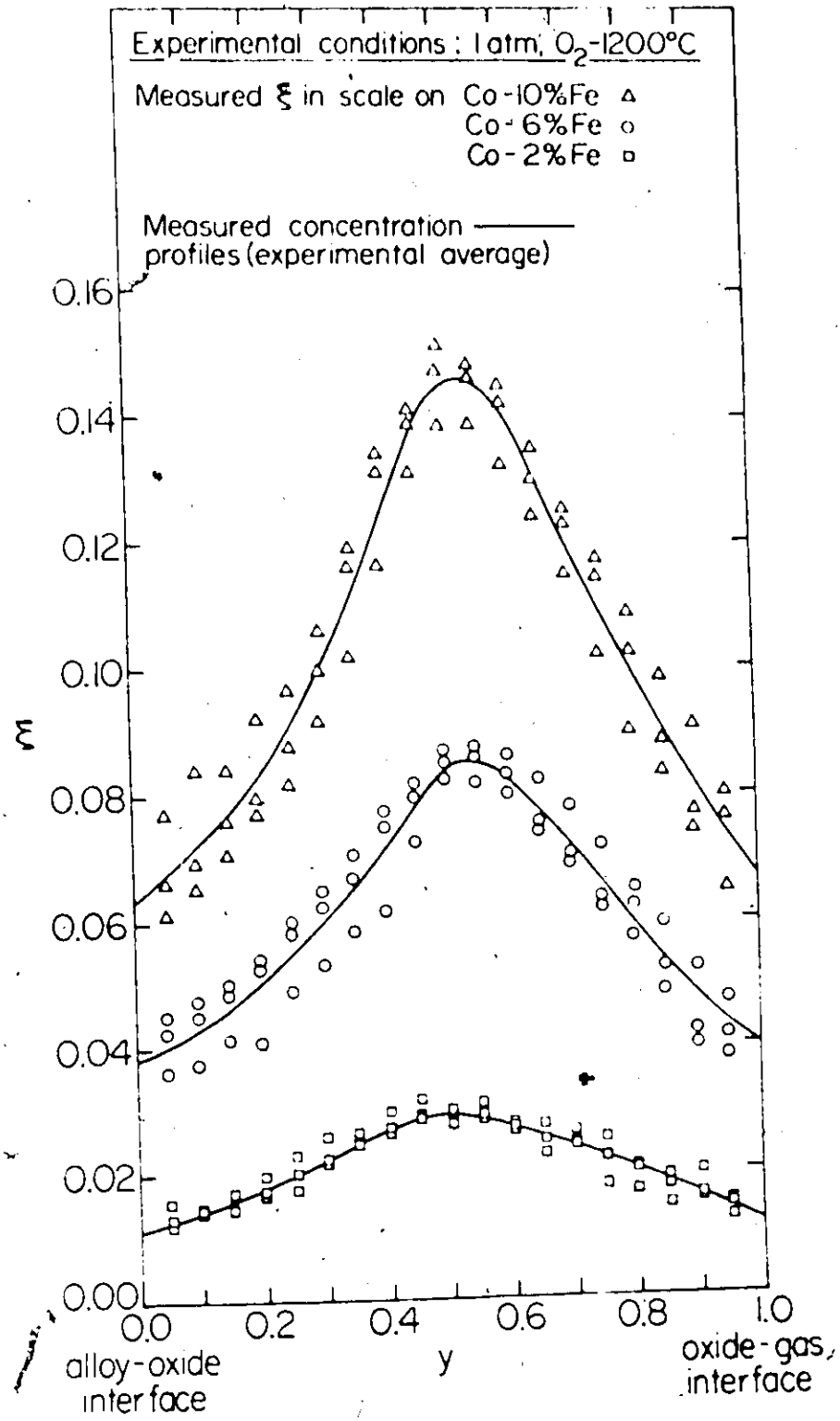

Fig. 7-30(e)

Mole fraction of FeO, ξ, as a function of normalized distance coordinate y in the CoO-FeO oxide scale

Co-1% Fe alloys. At the lowest oxygen pressure 10^{-4} atm a monotonic increase of iron concentration towards the outer interface was observed. The profile for 10^{-3} atm oxygen pressure has the same form; however, the increase in iron concentration is more pronounced. With further increase in oxygen pressure the iron profile exhibits a maximum. The position of this maximum shifts toward the centre of the scale, away from the outer interface with increasing oxygen pressure. Finally, in the scales formed at 1 atm oxygen pressure the iron concentration profile exhibits a bell-shaped form. A similar pattern was observed for scales on Co-10% Fe, Co-6% Fe and Co-2% Fe alloys. The corresponding iron concentration profiles are illustrated in Figs. 7-30(a) to (e).

These measurements showed that the concentration profiles are invariant in y-space within the experimental accuracy limited by the method of analysis.

CHAPTER VIII

DISCUSSION

8.1 Introduction

The results of thermogravimetric experiments, metallographic observations and microprobe measurements are correlated and put into broader perspective in relation to the general principles of binary alloy oxidation in this chapter.

8.2 Analysis of the Experimental Results

8.2.1 Oxidation Kinetics

The parabolic plots shown in Figs. 7-11 to 7-20 demonstrate that the weight-gains measured in the thermogravimetric experiments follow parabolic relationships. This correlation suggests that the oxidation rate of Co-Fe alloys is controlled by transport phenomena. Consequently, the rates of interfacial reactions are higher than transport by diffusion through the scale and local chemical equilibrium is achieved.

In the view of the following analysis, it is necessary to re-introduce the concept of "local equilibrium", which has been tacitly assumed in the previous theoretical discussions. The reactants, in case of oxidation, are separated by an oxide scale and the total free energy change takes place over a large distance; hence, one can consider any microscopic volume element as being substantially in equilibrium within itself even during the course of reaction. It is very important to establish whether local equilibrium prevails because if this condition is satisfied the reaction attains a steady state. The requirement that the various diffusing

species must be conserved at the interfaces leads to a coupling or interdependence of the diffusion fields. This signifies that the concentrations at the interfaces are not functions of time and that the metallographic structure is well defined and stable. Thus the transverse cross-sectional concentrations are stable in y and λ space (viz. Section 3.4).

The fact that the reaction rates followed parabolic kinetics is the main experimental evidence that steady state oxidation actually occurs. However, additional experimental evidence will be discussed in a following section based on concentration paths.

As shown in Fig. 7-21, the parabolic oxidation rate increases rapidly with increasing iron concentration up to 10% in the base alloy. Then the oxidation rate drops sharply with further increase in iron content with a subsequent steady moderate increase. The position of the maximum in reaction rate is a function of iron content in the base alloy and oxygen potential in the reaction atmosphere. With decreasing oxygen pressure the maximum shifts toward higher concentrations of iron in the alloy. This type of scaling behaviour is typical for a number of binary alloys namely Ni-Cr,[116,117,118] Ni-Fe[119] and Co-Cr.[120]

It is to be emphasized that the analysis in this work concerns the oxidation reaction when a steady state is achieved. Therefore, no attempt has been made to study the processes occurring at the very early stages and during long periods of oxidation. The oxidation kinetics in these periods can exhibit deviations from parabolic behaviour due to numerous factors, e.g. mechanical stress, changes in crystal structure, accumulation of large quantities of defects and porosity in the scale, etc. Irregularities in the weight-gain kinetics curves have been reported

for Co-Cr,[120,121] Fe-Cr[122] and Ni-Cr[123] alloy oxidation. Therefore, the present experiments were confined to intermediate reaction times, when the reaction rate is diffusion controlled and follows a parabolic type of dependence.

8.2.2 Oxidation Modes of Cobalt-Iron Alloys

At least five different types of scale morphology occur as a function of oxygen pressure and iron content in the alloys over the 0-70% Fe composition range. The results of the metallographic observations are shown in Figs. 7-27 and 7-28. This "oxidation map" could be divided into two parts: a region where one-phase oxide scales form and the remaining part with two-phase scale formation. The first region includes alloys with iron content up to 10% at all oxygen pressures. The scale is a cobaltowüstite solid solution of CoO and FeO. The second region includes alloys with iron contents from 20% to 70%. Although the scales exhibit very complicated morphologies, they are comprised of only two phases, cobaltowüstite and spinel $(Co,Fe)_3O_4$. Co-Fe alloys belong to class II of the general oxidation classification, since both alloying elements react with oxygen. In fact, that the oxides of individual elements react with each other to form a solid solution or a mixed spinel classifies oxidation behaviour of these alloys as Class II_B. Further classification offers two possibilities: one-phase scale formation which describes the alloys up to 10% Fe, Class II_B^1, and two-phase scale formation which describes the alloys with iron content higher than 10%, Class II_B^2. In the latter case the second phase consisting of spinel could be present as a continuous layer, separate particles or a combination of both embedded in cobaltowüstite.

8.2.3 Correlation between Oxidation Kinetics and Scale Morphologies

A striking correspondence between the scale morphology and oxidation rate constant was observed. For low iron alloys (i.e. up to 10% Fe), the oxidation rate was increasing linearly with increasing iron content in the base alloy. The rate of increase was decreasing with decreasing oxygen pressure in the oxidizing atmosphere. At 1 atm pressure a sharp decrease in oxidation rate was observed, when iron content increased from 10% to 20%. This abrupt change can be explained by the presence of continuous layer of spinel phase in the cobaltowüstite scale illustrated in Fig. 7-29. Since the oxidation reaction remained diffusion controlled, the spinel layer acts as a barrier for cation species diffusing in the cobaltowüstite. Further additions of iron to the base alloy do not produce any significant changes in the external scale morphology. Thus, the increase in reaction rate is the result of the combined effect of diffusion blocking by a continuous layer of spinel phase and an increase increase in free energy change across the scale due to the increase in iron concentration. The change in oxidation rate due to two-phase scale formation is more gradual in oxygen atmospheres with pressure less than 1 atm. The reason for this phenomena could be found in the morphological development of the external scales. Fig. 7-41 shows that at 10^{-1} atm of oxygen pressure the continuous layer of spinel is not present. Instead, a region of discontinuous spinel particles occurs in the middle of the scale. Again, the spinel phase obstructs the diffusion, but to a lesser degree than the continuous layer, since the outer and inner cobaltowüstite layers are interconnected. If the iron content of the alloy is increased 10%, the scale develops a continuous spinel layer with a simultaneous

decrease in oxidation rate. This type of scale development was observed also at lower oxygen pressures, with the only difference that the continuous layer developed at higher iron contents in the base alloys. After appearance of this layer the increase in the rate of oxidation was similar to the 1 atm case.

5.2.4 Composition Paths

The concentration profiles measured in the cross sectioned samples of alloys oxidized for different periods of time indicate that they are not a function of time and are invariant in λ-space. Figs. 7-82 to 7-92 show that within the limits of the experimental error the interfacial concentrations as well as the profile within the scale are constant. This fact is the additional experimental evidence, that the steady state oxidation process for the investigated periods of reaction really exists and conditions of local equilibrium prevail. In the view of the theoretical considerations in Chapter III the stationary concentration profiles in the λ-space can be transposed on to the phase diagram by eliminating λ. This transposition reflects the condition of mass conservation and monotonic activity gradients for the diffusing species.

It is impractical to plot all composition paths for all investigated alloys and oxygen pressures; therefore, only schematic plots of two typical cases will be shown. Fig. 8-1 illustrates the first type of composition path which occurs in all investigated alloys (i.e. up to 10% Fe) oxidized at 10^{-4} and 10^{-3} atm oxygen pressure. Fig. 8-2 illustrates the second type of composition path which occurs in the same alloys oxidized at 10^{-2} to 1 atm of oxygen pressure. The plots are sections of

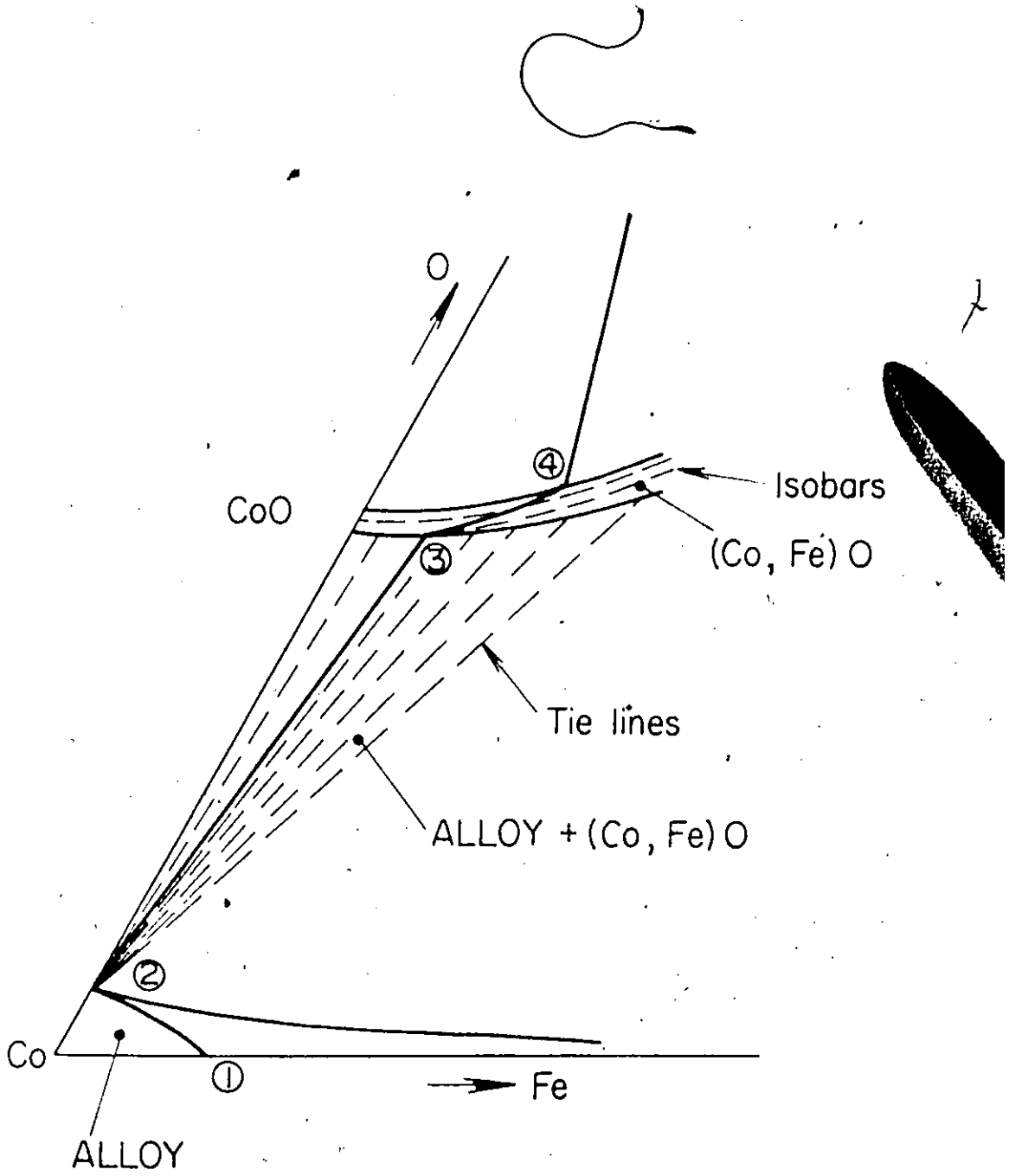

Fig. 8-1

Schematic plot of composition path on ternary isotherm for the investigated alloys oxidized in oxygen at 10^{-4} and 10^{-3} atm

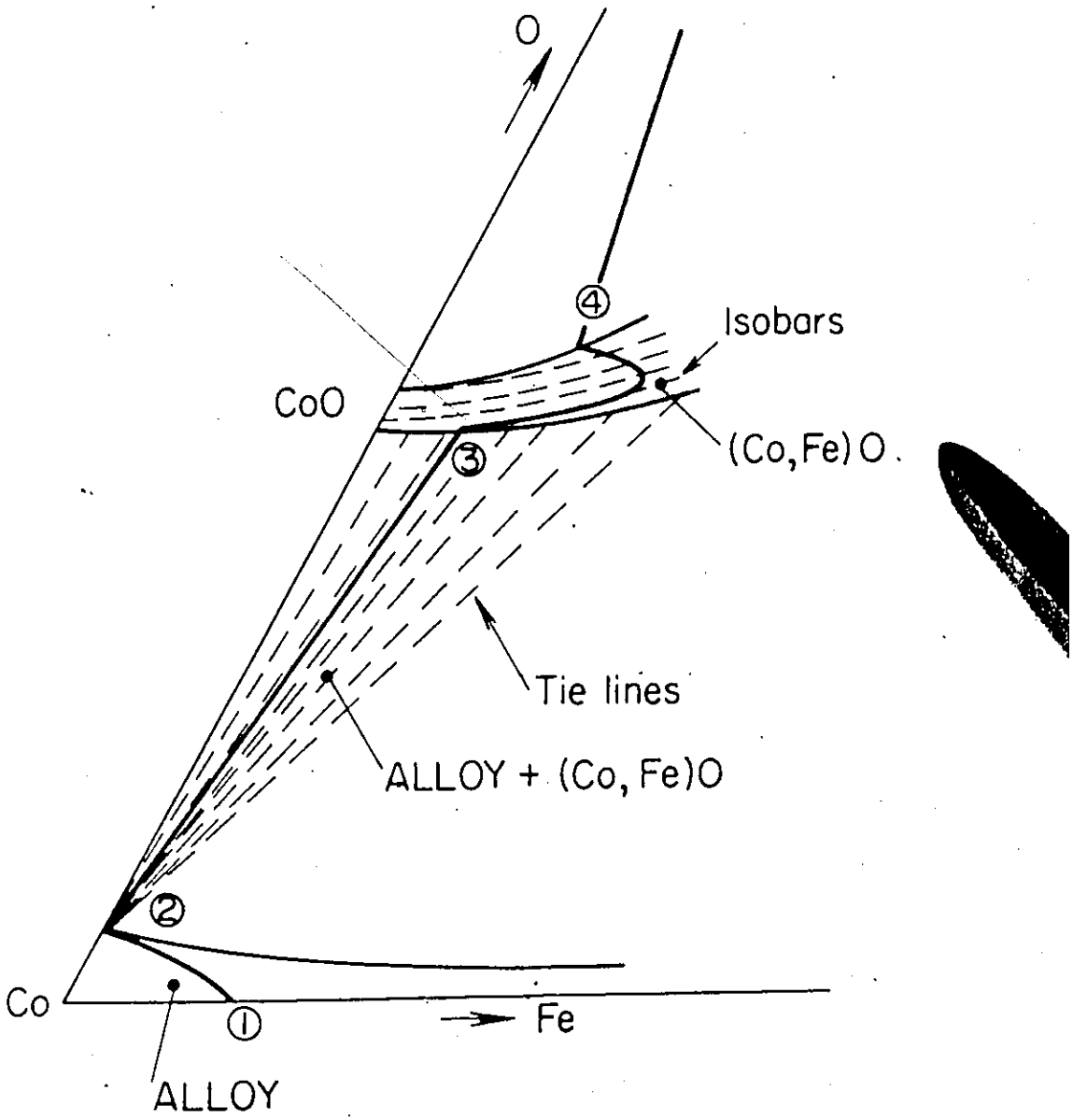

Fig. 8-2

Schematic plot of composition path on ternary isotherm for the investigated alloys oxidized in oxygen at 10^{-2} to 1 atm.

ternary Co-Fe-O diagrams at 1200°C. The numbers correspond to the interfacial compositions: 1 - composition of the base alloy, 2 - composition of the alloy at alloy-oxide interface, 3 - composition of the oxide scale at the same interface and 4 - composition of the oxide at the outer interface. The curve between 1 and 2 represents the concentration profiles in the alloy, the tie-line between 2 and 3 represents the interfacial concentrations of the two phases coexisting at equilibrium and the last part of the composition path from 3 to 4 represents the concentration profile in the oxide scale. Both composition paths illustrated in Figs. 8-1 and 8-2 show monotonically decreasing values of oxygen activity from the outer interface of the oxide, to the bulk alloy, as required from thermodynamic considerations.

The actual composition paths could be estimated from the concentration profiles in the oxide scales on alloys containing up to 10% Fe (Figs. 7-29a to 7-30e) and oxygen potential phase diagram (Fig. 5-5).

CHAPTER IX

APPLICATION OF THE DIFFUSION MODEL OF BINARY ALLOY OXIDATION TO COBALT-IRON ALLOYS: RESULTS AND DISCUSSION

9.1 Introduction

A ternary diffusion model is applied to describe the high temperature oxidation of cobalt-iron alloys when parabolic kinetics represent the growth of a single cobaltowustite scale. Equations derived by Wagner[15] for metal diffusion through p-type ternary oxide scales under chemical activity gradients are shown to lead to a description of the cation distribution in the alloy and oxide in the course of oxidation. The correlation is sought between the concentration profiles calculated from kinetic and thermodynamic data and actual profiles measured by electron probe microanalyser.

9.2 Initial Considerations

Oxidation of an Co-Fe alloy with iron content up to 10% at 1200°C is one of the limiting cases[15] of reaction classified as Class II_B^1. In this case diffusion in the alloy is slow in comparison to diffusion in the scale, i.e.

$$\tilde{D}_{FeCo}(\text{order of } 10^{-10}\text{-}10^{-11}) \ll D_{Fe}(\text{order of } 10^{-8}\text{-}10^{-9})$$

and

$$\tilde{D}_{FeCo}(\text{order of } 10^{-10}\text{-}10^{-11}) \ll D_{Co}(\text{order of } 10^{-8}\text{-}10^{-9})$$

The diffusivity constant for the alloy[99] is at least one order of magnitude lower than the diffusivity constants for iron and cobalt in the

oxide. Thus, the ratio of the fluxes of Fe and Co in the scale at y = 0 in equivalents per unit cross section per unit time must equal the ratio of the number of equivalents of Co and Fe in the bulk alloy. The material balance at the alloy-oxide interface consequently gives the relation between ξ, $\frac{d\xi}{dy}$, a_O and k' in the form of Eq. 3.52. Since there is negligible diffusion in the alloy, $\xi_{av} = \xi_{alloy}$. Similarly, the material balance at the gas-oxide interface yields a relation between the above variables in the form of Eq. 3.44, if evaporation from the surface is negligibly small.

The beauty of this limiting case of binary alloy oxidation is in the fact, that one can consider the diffusion in the scale separately, since there is negligible diffusion in the metal phase and the relations between the variables given by Eqs. (3.44) and (3.52) can be used. The necessary condition is of course, that the steady state of oxidation must be attained and local equilibrium at the interfaces must prevail.

9.3 Development of Diffusion Equations Describing Concentration Profiles in Cobaltowustite Scales on Cobalt-Iron Alloys at 1200°C

In CoO-FeO solid solutions we have $z_{Co} = z_{Fe} = |z_O| = 2$. In the following analysis A, B and X correspond to Co, Fe and O, respectively. Thus equations (3.36) and (3.37) reduce to the following expressions respectively,

$$D_{Co}(1-\xi)\left(-\frac{\partial \ell n a_{CoO}}{\partial \xi} \cdot \frac{d\xi}{dy} + \frac{d\ell n a_O}{dy}\right) + D_{Fe}\xi\left(-\frac{\partial \ell n a_{FeO}}{\partial \xi} \cdot \frac{d\xi}{dy} + \frac{d\ell n a_O}{dy}\right) = k \qquad (9.1)$$

and

$$yk\frac{d\xi}{dy} = -\frac{d}{dy}\left[D_{Fe}\xi\left(\frac{\partial \ell n a_{FeO}}{\partial \xi} \cdot \frac{d\xi}{dy} - \frac{d\ell n a_O}{dy}\right)\right] \qquad (9.2)$$

where ξ is the equivalent fraction (equal to mole fraction) of FeO in CoO-FeO mixed oxide and y and k have been defined previously.

Henry's law behaviour for FeO in CoO-FeO solid solutions has been established by Aukrust and Muan.[95,102] This can be expressed as

$$\frac{\partial \ell n a_{FeO}}{\partial \xi} = \frac{\partial \ell n \xi}{\partial \xi} = \frac{1}{\xi} \frac{\partial \xi}{\partial \xi} = \frac{1}{\xi} \tag{9.3}$$

The Gibbs-Duhem equation for the oxide may be written as

$$\frac{\partial \ell n a_{CoO}}{\partial \xi} = -\frac{\xi}{1-\xi} \frac{\partial \ell n a_{FeO}}{\partial \xi} \tag{9.4}$$

From Eqs. (9.3) and (9.4) we have

$$\frac{\partial \ell n a_{CoO}}{\partial \xi} = -\frac{1}{1-\xi} \tag{9.5}$$

Substitution of Eqs. (9.3) and (9.5) into Eq. (9.1) yields

$$(D_{Co}-D_{Fe})\frac{d\xi}{dy} + \frac{d\ell n a_O}{dy}[(1-\xi)D_{Co} + \xi D_{Fe}] = k \tag{9.6}$$

The variation of cation diffusion coefficients with ξ and a_O in the CoO-FeO mixed oxide could be expressed in general as

$$D_{Co} = D^V_{Co} \cdot N_V = D^o_{Co} \cdot \gamma \cdot a_O^n \cdot \xi^m \tag{9.7}$$

and similarly for iron cations

$$D_{Fe} = D^V_{Fe} \cdot N_V = D^o_{Fe} \cdot \gamma \cdot a_O^n \cdot \xi^m \tag{9.8}$$

Now let

$$\frac{D^o_{Fe}}{D^o_{Co}} = p = \text{constant or } f(p_{O_2}) \tag{9.9}$$

and

$$k' = \frac{k}{D^{o}_{Co}\gamma} \qquad (9.10)$$

Substitution of Eqs. (9.7), (9.8), (9.9) and (9.10) into Eq. (9.6) gives the variation of oxygen activity in the scale.

$$\frac{d\ell na_O}{dy} = [\frac{k'}{m+1} \cdot \frac{1}{a_O} + (p-1)\frac{d\xi}{dy}]/[1+(p-d)\xi] \qquad (9.11)$$

Upon substitution of various parameters above, Eq. (9.2) may be written as,

$$-yk' \frac{d\xi}{dy} \cdot \frac{d}{dy}[D^{o}_{Fe}\gamma \cdot \xi^{m+1}(\frac{1}{\xi}\cdot\frac{d\xi}{dy} - \frac{d\ell na_O}{dy})] \qquad (9.12)$$

The intended differentiation of Eq. (9.12) after substitution of Eq. (9.11) and (9.9) and rearrangement if $p = f(p_{O_2})$ leads to

$$\frac{d^2\xi}{dy^2} = \Big(-\frac{yk'}{p\, a_O^n\, \xi^{m+1}} \cdot \frac{d\xi}{dy}$$

$$-(\frac{\xi}{p}\cdot\frac{dp}{d\xi} + [(m+1)\frac{d\xi}{dy} + n\xi\frac{d\ell na_O}{dy}$$

$$\cdot(\frac{1}{\xi}\cdot\frac{d\xi}{dy} - \frac{d\ell na_O}{dy})\cdot\frac{1}{\xi}$$

$$+\frac{1}{\xi^2}(\frac{d\xi}{dy})^2 - \frac{k'}{[1+(p-1)\xi]\cdot a^n\xi^m}\cdot(\frac{m}{\xi}\frac{d\xi}{dy} + \frac{nd\ell na_O}{dy})$$

$$-(\frac{d\ell na_O}{dy})/[1+(p-1)\xi]\cdot[\frac{d\xi}{dy}(p-1) + \frac{dp}{dy}\xi]$$

$$+\frac{1}{[1+(p-1)\xi]}\cdot\frac{dp}{dy}\cdot\frac{d\xi}{dy}\Big)\cdot\frac{1}{(\frac{1}{\xi}\frac{(p-1)}{[1+(p-1)\xi]}} \qquad (9.13)$$

If the parameter p = constant and is not a function of oxygen potential, all terms from Eq. (9.13) containing $\frac{dp}{dy}$ will vanish.

Similarly, the relations derived from material balances at both interfaces, represented by Eqs. (3.47) and (3.55) could be modified in view of Eqs. (9.3),(9.5), (9.7), (9.9) and (9.10). After substitutions and rearrangement, the relation for the inner interface yields

$$\left(\frac{d\xi}{dy}\right)_{y=0} = \frac{k'}{(a_0')^n(\xi')^m} \cdot \left\{ \frac{p'\xi' - [1+(p-1).\xi]\xi_{alloy}}{p'} \right\} \qquad (9.14)$$

and for the outer interface gives

$$\left(\frac{d\xi}{dy}\right)_{y=1} = \frac{k'(1-\xi'')(p''-1)}{(a_0'')^n(\xi'')^{m-1}.p''} \qquad (9.15)$$

where the oxygen activities and iron concentrations with single prime represent the values at the alloy-oxide interface and double prime designate the values for the gas-oxide interface.

Equations (9.11) and (9.13) describe the variation of the mole fraction of FeO, ξ and oxygen potential, a_0 as a function of y. Unfortunately, the dependent variables ξ and a_0 are inseparable and an analytical solution does not exist. Therefore, these differential equations must be solved (to obtain ξ and a_0 as a function of y) simultaneously using numerical method with appropriate conditions.

9.4 Numerical Solution

Eqs. (9.11) and (9.13) developed in the previous section are ordinary first-order and second-order differential equations, respectively. In order to obtain a unique solution, it is necessary to supply additional information, namely, values of ξ, a_0 and/or their derivatives at some specific

values of y. Eq. (9.11) requires one such value and Eq. (9.13) requires at least two values to be known.

A second-order differential equation given by Eq. (9.13) may be written as a system of two first-order equations by defining a new variable ζ equal to the first derivative of the concentration. This transformation eliminates the second derivative term in Eq. (9.13) and adds a new relation to the set of equations to be solved:

$$\left(\frac{d\xi}{dy}\right) = \zeta \tag{9.16}$$

The reason for this transformation is, that the numerical methods for solution of first-order differential equations are superior in accuracy and simplicity to the methods available for solution of higher-order differential equations. Eqs. (9.11), (9.13) and (9.16) were simultaneously solved with the help of a computer using Hamming's predictor-corrector method. This routine is a stable fourth-order integration procedure. However, it is not self-starting, that is the functional values at a single previous point are not enough to get the functional values ahead. Therefore, this routine was modified and the Runge-Kutta procedure followed by one iteration step was added to the Hamming's predictor-corrector method.

In order to calculate the concentration profile in the oxide in addition to k', three additional conditions must be available. At the outer interface, the oxygen activity is known from experimental conditions, ξ'' is obtained from microprobe measurements and $\left(\frac{d\xi}{dy}\right)_{y=1}$ can be calculated from Eq. (9.15). At the alloy-oxide interface, ξ' is measured by the microprobe, a_0'' can be obtained from phase diagram Fig. (5-5) and $\left(\frac{d\xi}{dy}\right)_{y=0}$ can be calculated from Eq. (9.14).

To ensure the highest accuracy of the calculations, the profiles were calculated as an initial-value problem starting at y = 0. A "shooting method" was used to iterate an accurate value of ξ', since microprobe measurements were not accurate enough because of the interference of X-rays generated from the adjacent alloy phase of different composition. The more accurate value of ξ can be obtained upon extrapolating the measured profile to the outer interface at y = 1. This value was compared with calculated ξ'', obtained from integration procedure starting with approximate ξ'. If calculated ξ'' and measured ξ'' did not agree, the estimate of ξ' was corrected and the integration procedure across the scale carried out. This iteration loop was repeated until calculated and measured ξ'' did agree. Also values of a_0 and $\frac{d\xi}{dy}$ were obtained in the course of the calculation as a function of y. The values at the oxide-gas interface a the end of the ξ'' iteration were compared with the actual oxygen potential in the reaction atmosphere and $(\frac{d\xi}{dy})_{y=1}$ calculated from Eq. (9.15).

These calculations required, apart from k' and initial conditions, the parameter p and the concentration of defects as a function of oxygen activity. The value of k' was obtained from k_p's listed in Tables (7-1) and (7-2) using the relation:

$$k' = \frac{k_p}{2\, D^{o}_{Co^{\gamma}}} (V/16)^2 \qquad (9.17)$$

where V is the molar volume of oxide and $D^{o}_{Co^{\gamma}}$ are constants from Eq. (9.7), which have numerical values $1.46 \pm 0.04 \times 10^{-6}$ cm^2/sec and 0.60 ± 0.11, respectively. The value of the constant n which appears in all equations is 0.15 ± 0.03. The dependence of the parameter p on oxygen potential is illustrated in Fig. (5-10); the values for computer solution were supplied

from this curve as numerical values in tabular form. The detailed description of the errors involved as well as the source of all literature data are given in Chapter V.

Calculated concentration profiles in several scales are illustrated in Fig. 9-1 to 9-10. The extrapolated values of ξ'' listed in Table 9-1 were used in iterations to obtain ξ' listed in Table 9-2. In the course of the integration procedure, the values of a_0 and $\frac{d\xi}{dy}$ were obtained as a function of y. For illustration oxygen activity profiles for Co-10% Fe alloy oxidized at 10^{-3} and 1 atm are shown in Fig. 9-11 and 9-12, respectively.

The initial values of a_0'' and $(\frac{d\xi}{dy})_{y=1}$ are listed in Tables 9-3 to 9-7 together with actual experimental a_0 in reaction atmospheres and values of $(\frac{d\xi}{dy})_{y=1}$ calculated from Eq. (9.15). The relatively good agreement between iterated and experimental or calculated values offers an internal check on the validity of the utilized constants and relations obtained from literature data. The calculated oxygen activity profiles enable one to estimate the oxygen potential at each point in the scale where the maximum in the ξ profile occurs. The positions of and oxygen potentials at the maximum in scales oxidized between 10^{-2} atm to 1 atm of oxygen pressure are summarized in Table 9-8.

9.5 Comparison of Results from Theoretical Calculations and Experimental Measurements

The calculated profiles of ξ as a function of y are shown in Figs. 9-1 to 9-10 (dashed lines) together with the profiles measured by the microprobe (full lines). Good agreement was found between these profiles, which indicates internal consistency of the diffusion analysis. Considering the reliability of the data obtained from the literature, the validity of

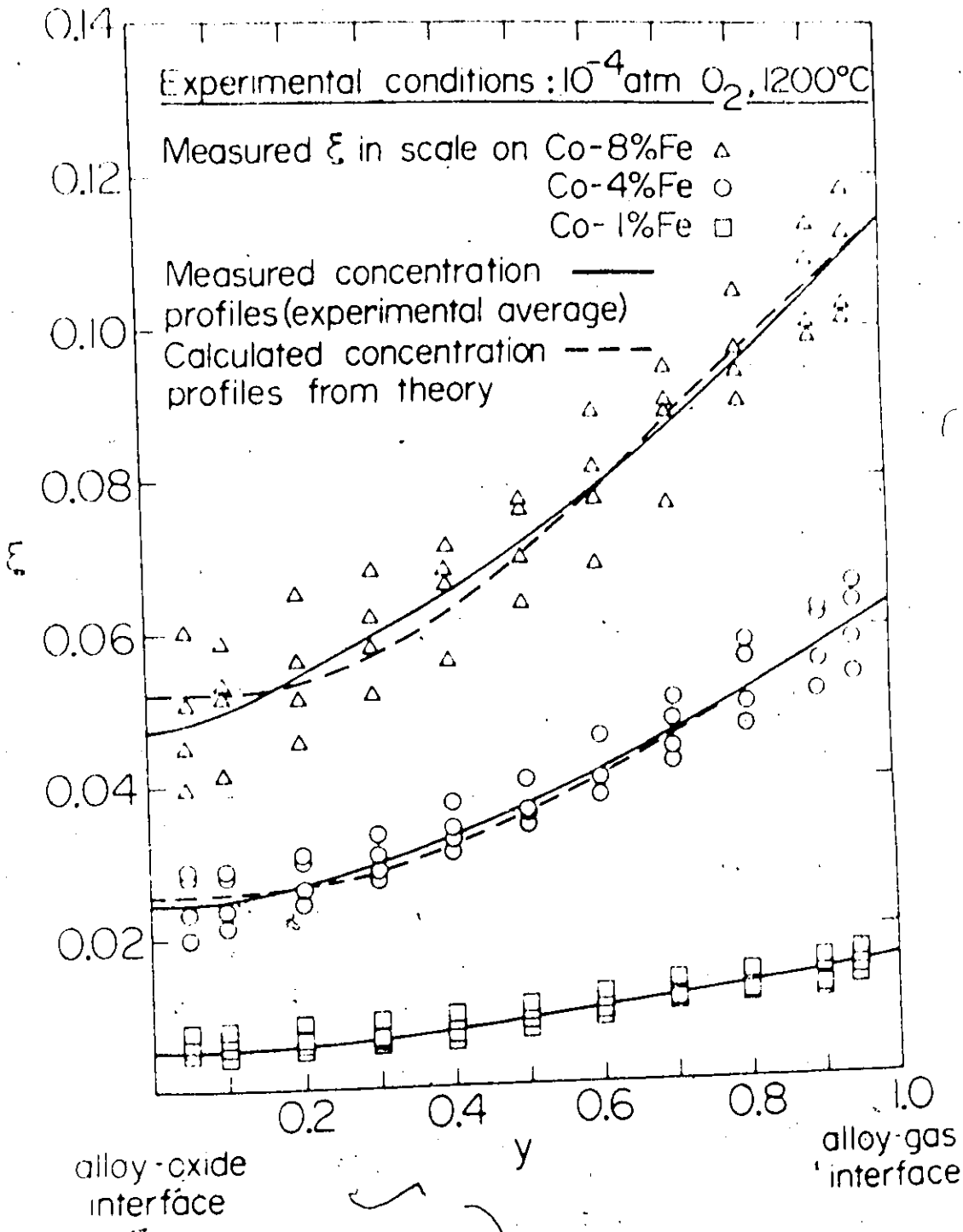

Fig. 9-1

Mole fraction of FeO, ξ, as a function of normalized distance coordinate y in the CoO-FeO oxide scale

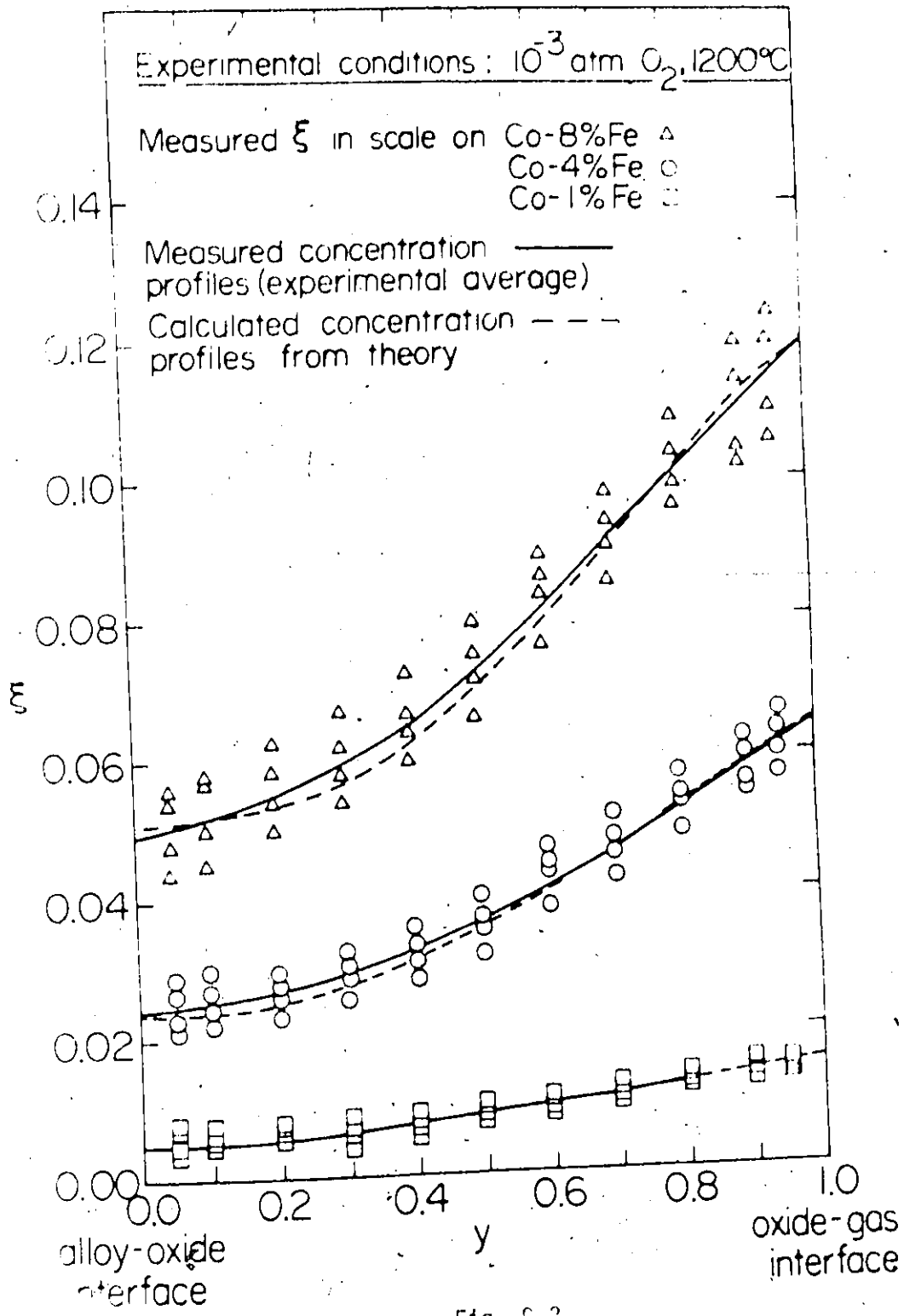

Fig. 9-2

Mole fraction of FeO, ξ, as a function of normalized distance coordinate y in the CoO-FeO oxide scale

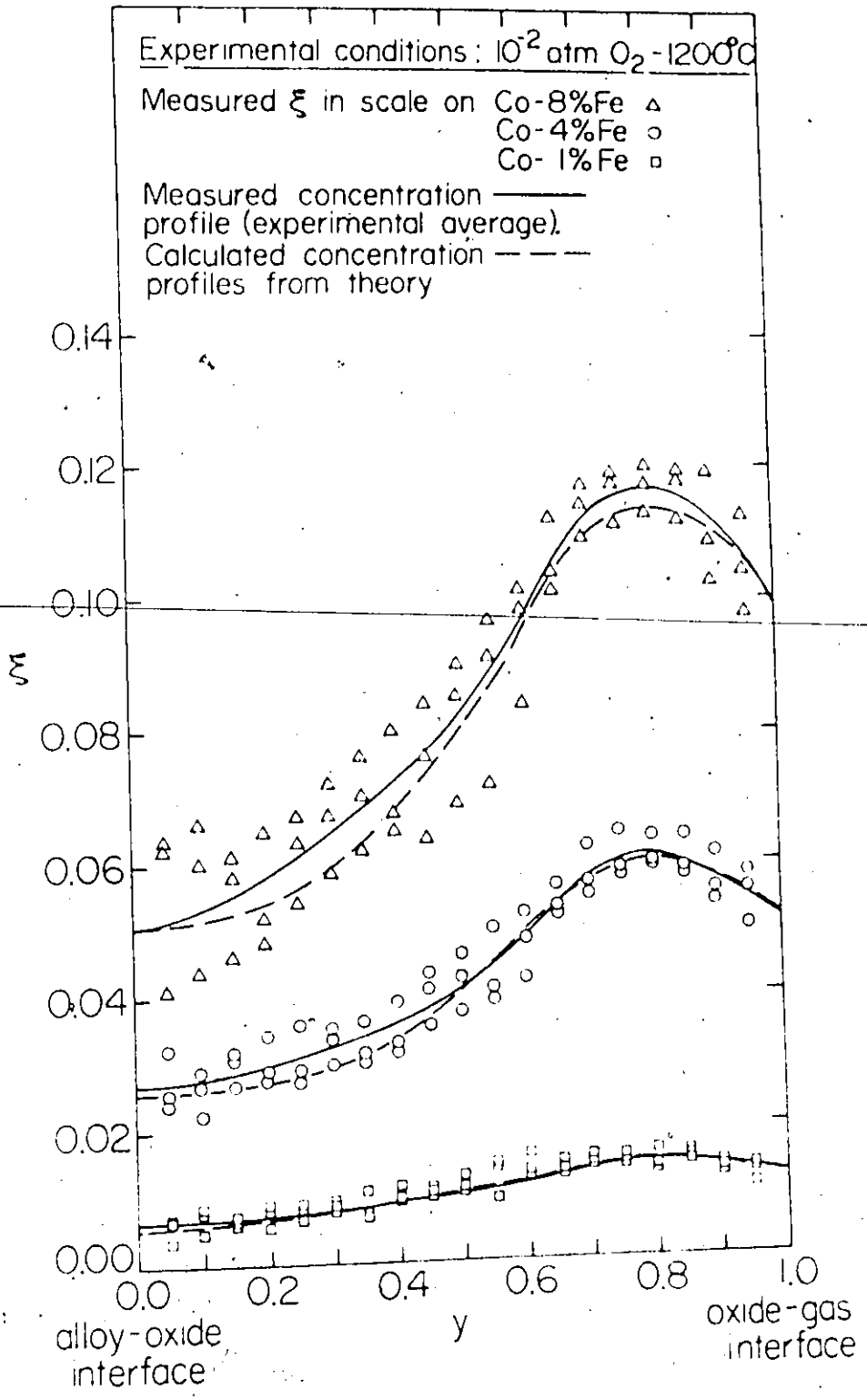

Fig. 5-3

Mole fraction of FeO, ξ, as a function of normalized distance coordinate y in the CoO-FeO oxide scale

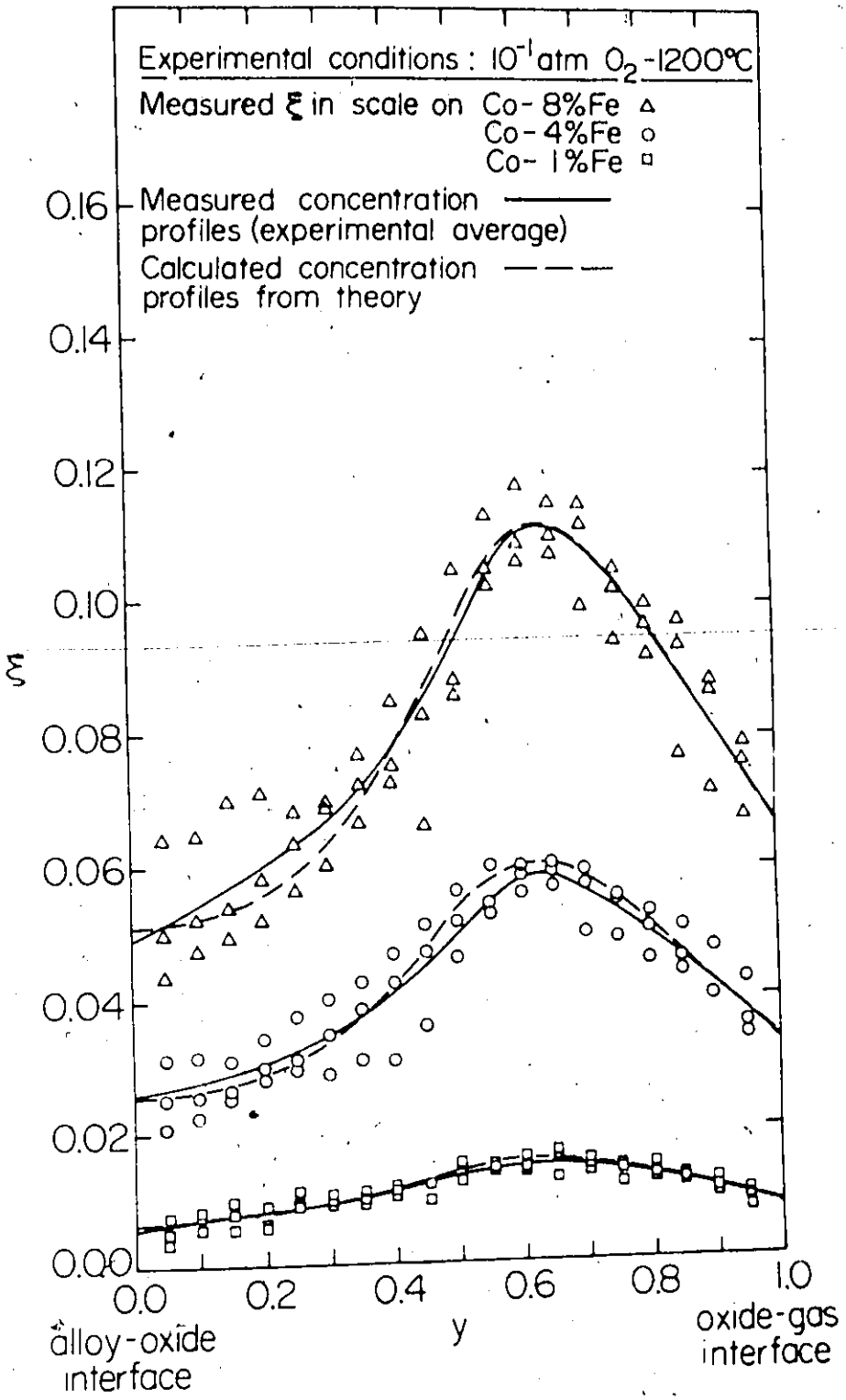

Fig. 9-4

Mole fraction of FeO, ξ, as a function of normalized distance coordinate y in the CoO-FeO oxide scale

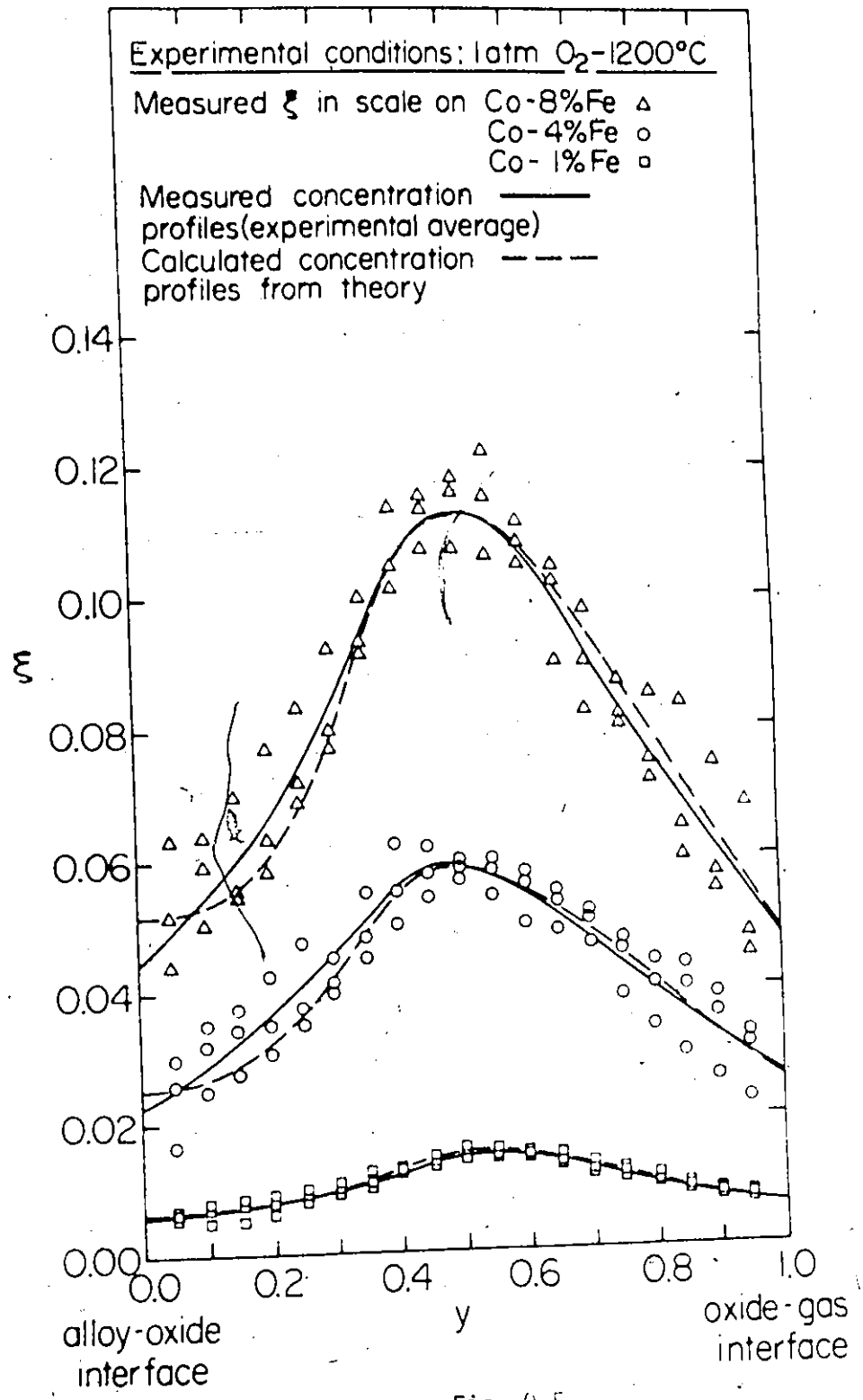

Fig. 9-5

Mole fraction of FeO, ξ, as a function of normalized distance coordinate y in the CoO-FeO oxide scale

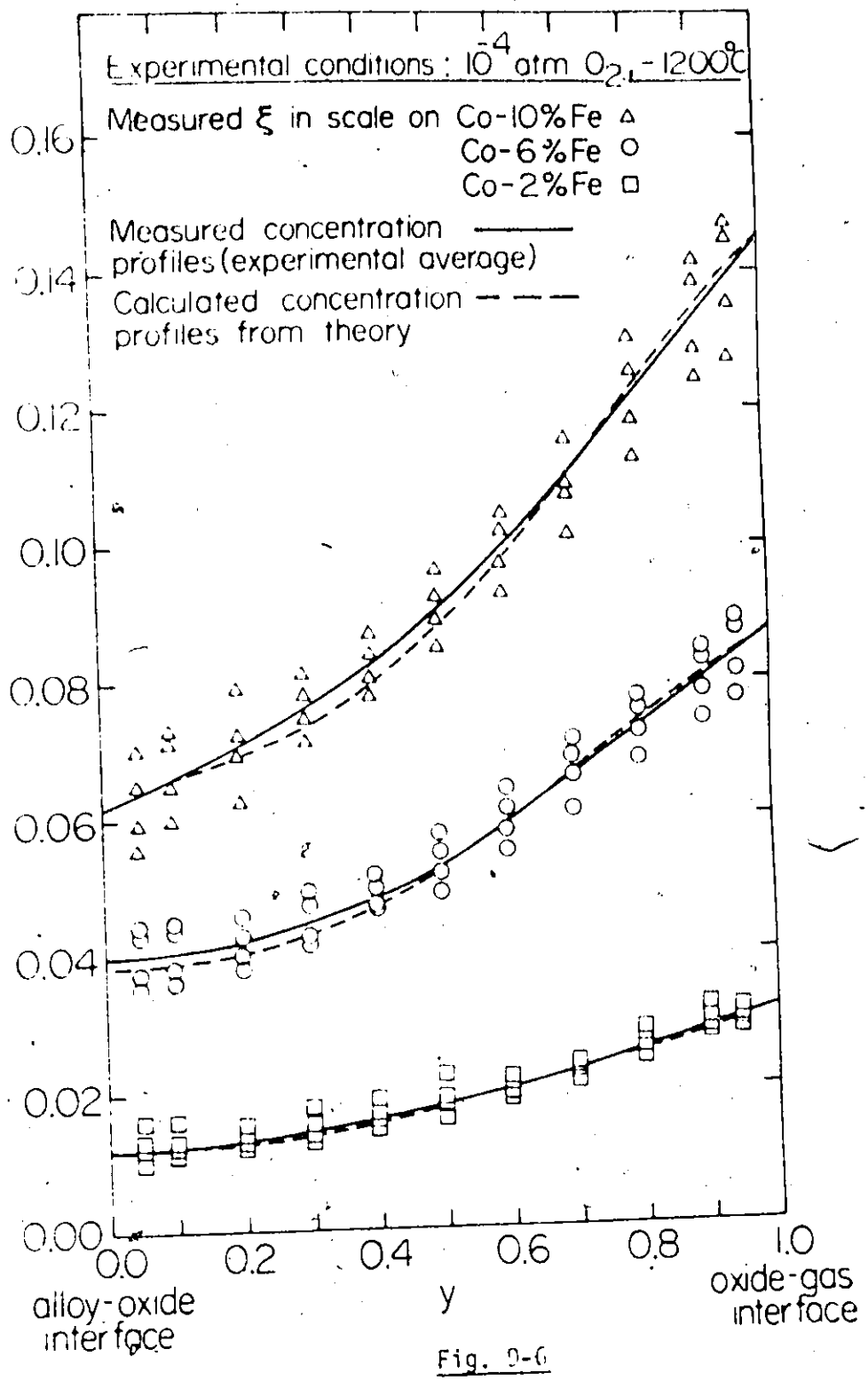

Fig. 9-6

Mole fraction of FeO, ξ, as a function of normalized distance coordinate y in the CoO-FeO oxide scale

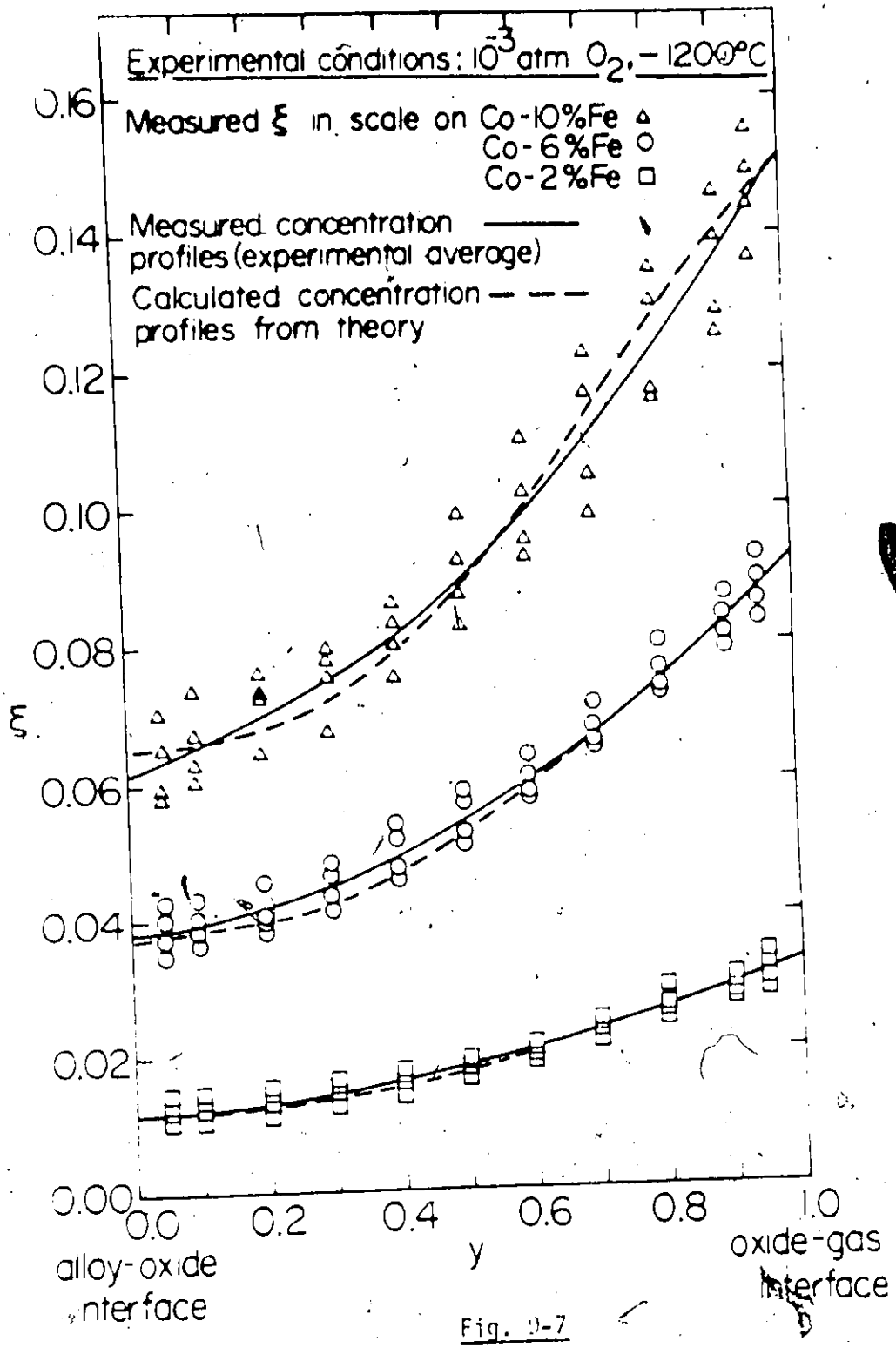

Fig. 9-7

Mole fraction of FeO, ξ, as a function of normalized distance coordinate y in the CoO-FeO oxide scale

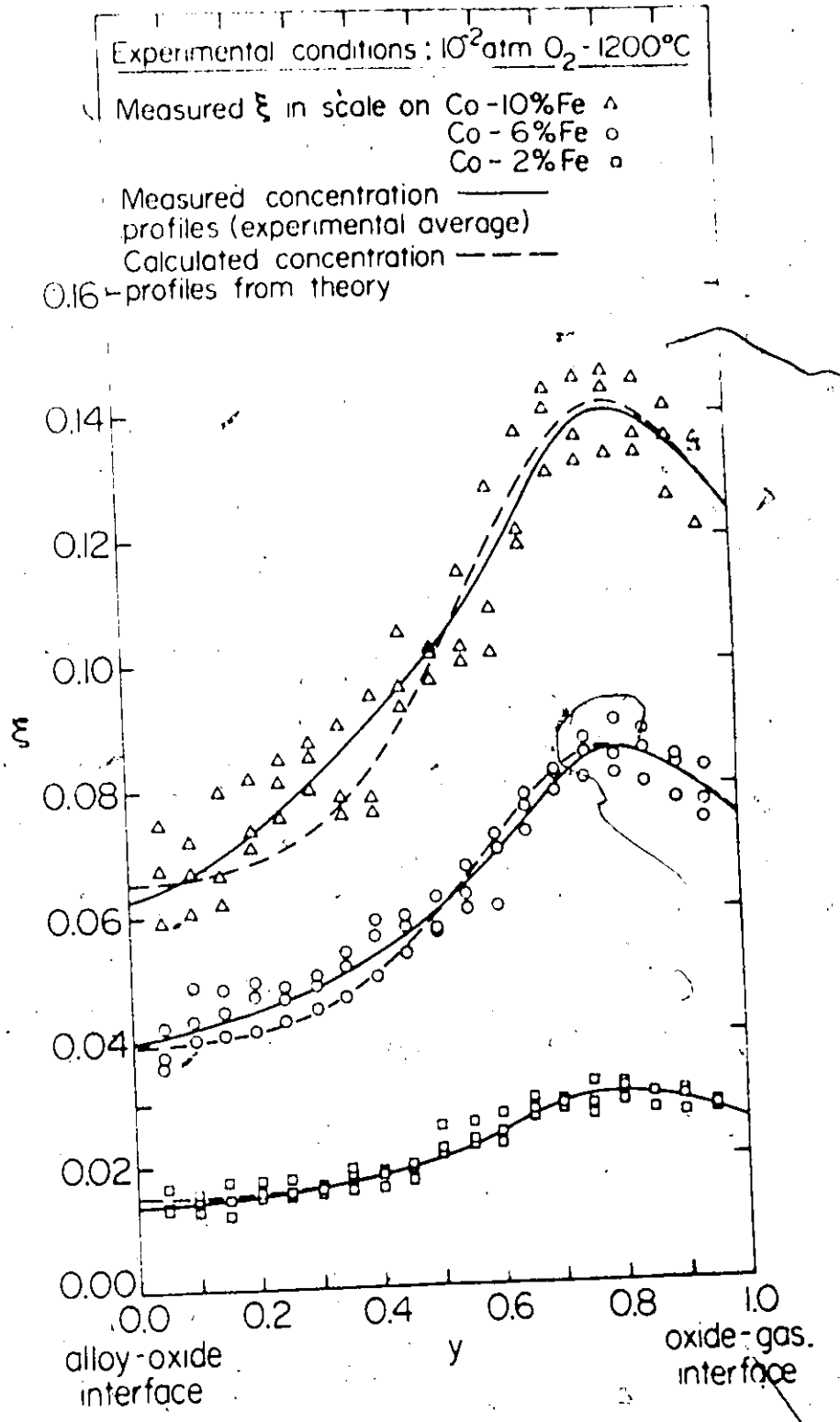

Fig. 9-8

Mole fraction of FeO, ξ, as a function of normalized distance coordinate y in the CoO-FeO oxide scale

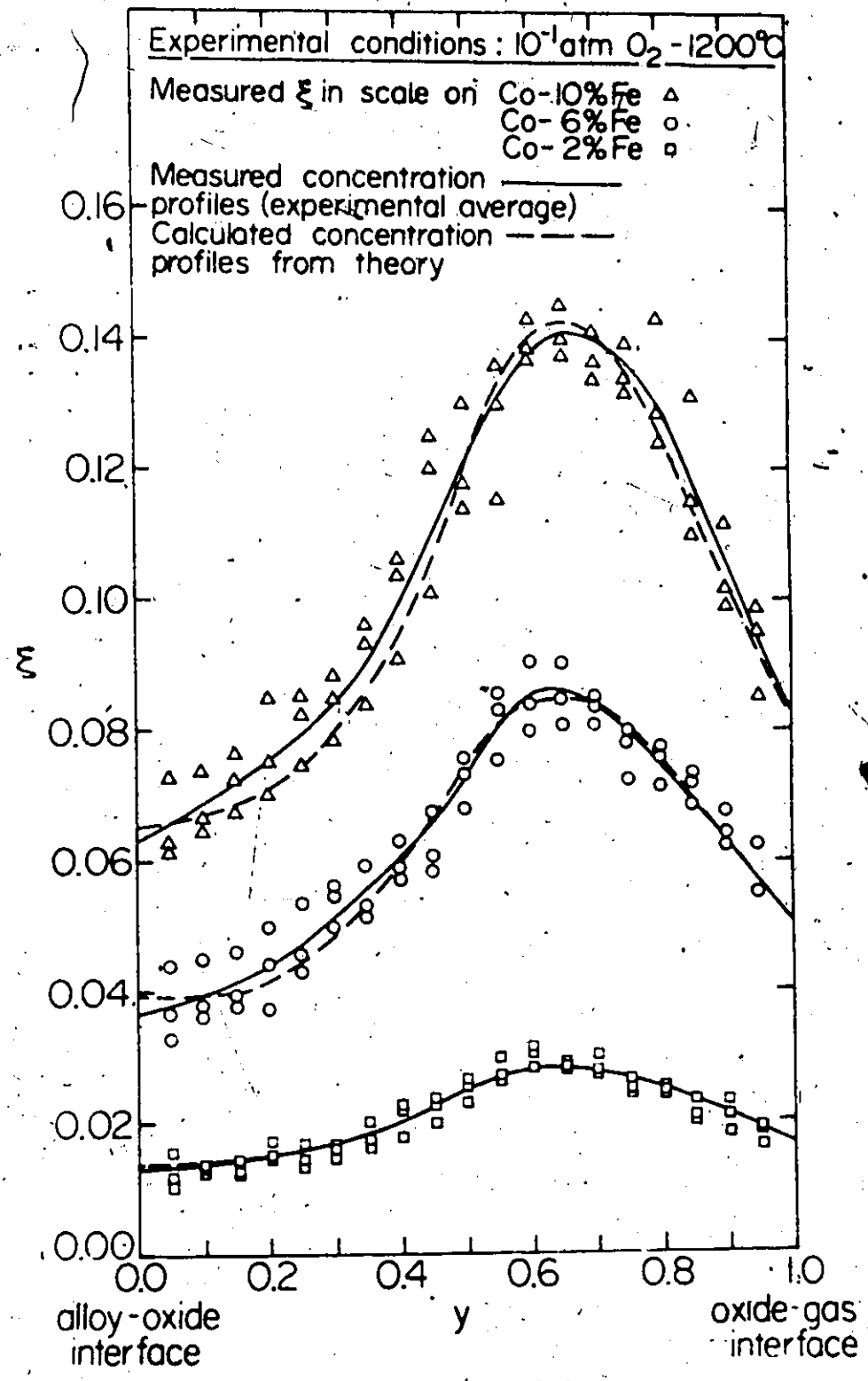

Fig. 9-9

Mole fraction of FeO, ξ_{FeO} as a function of normalized distance coordinate y in the CoO-FeO oxide scale

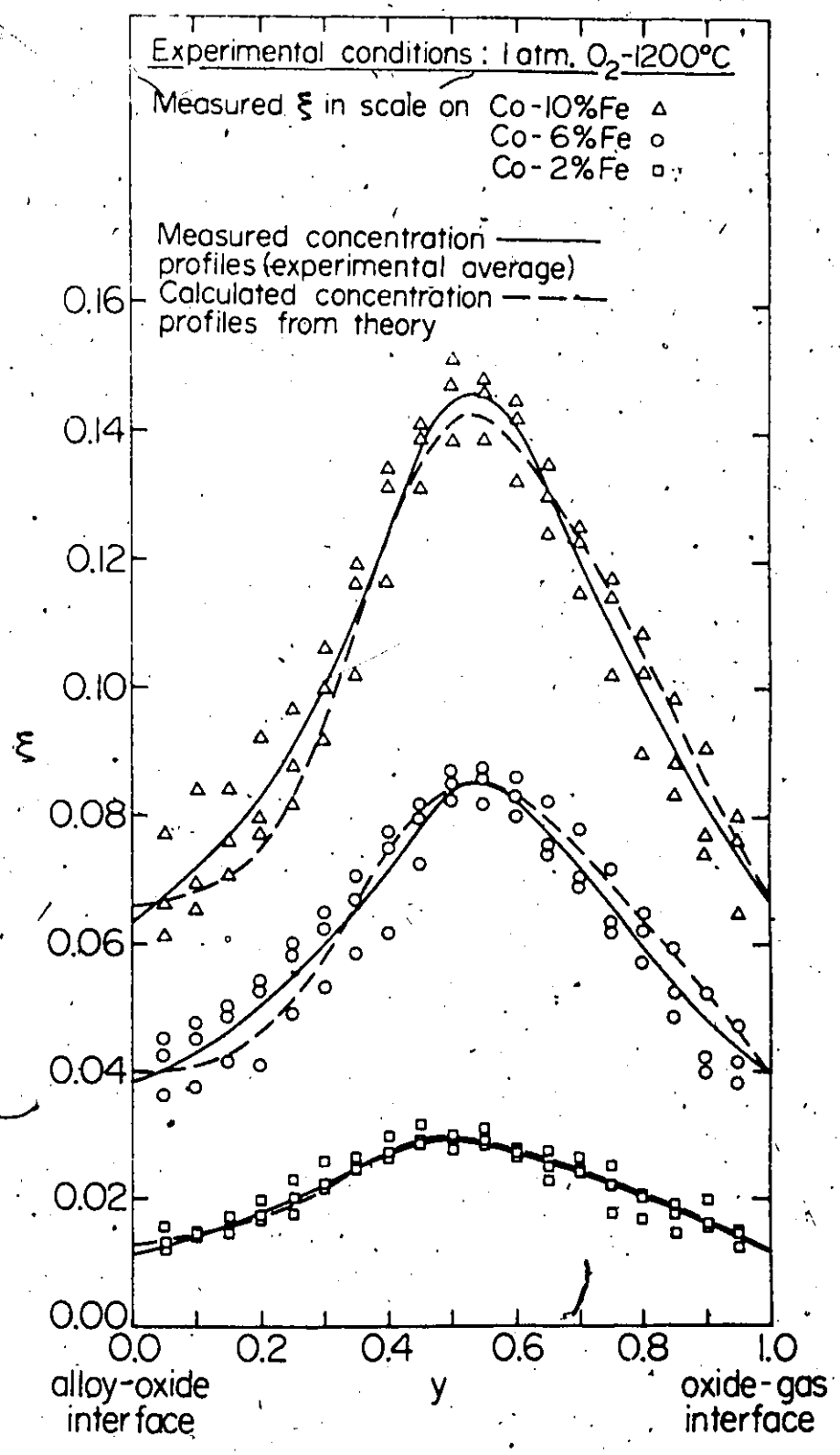

Fig. 9-10

Mole fraction of FeO, ξ, as a function of normalized distance coordinate y in the CoO-FeO oxide scale.

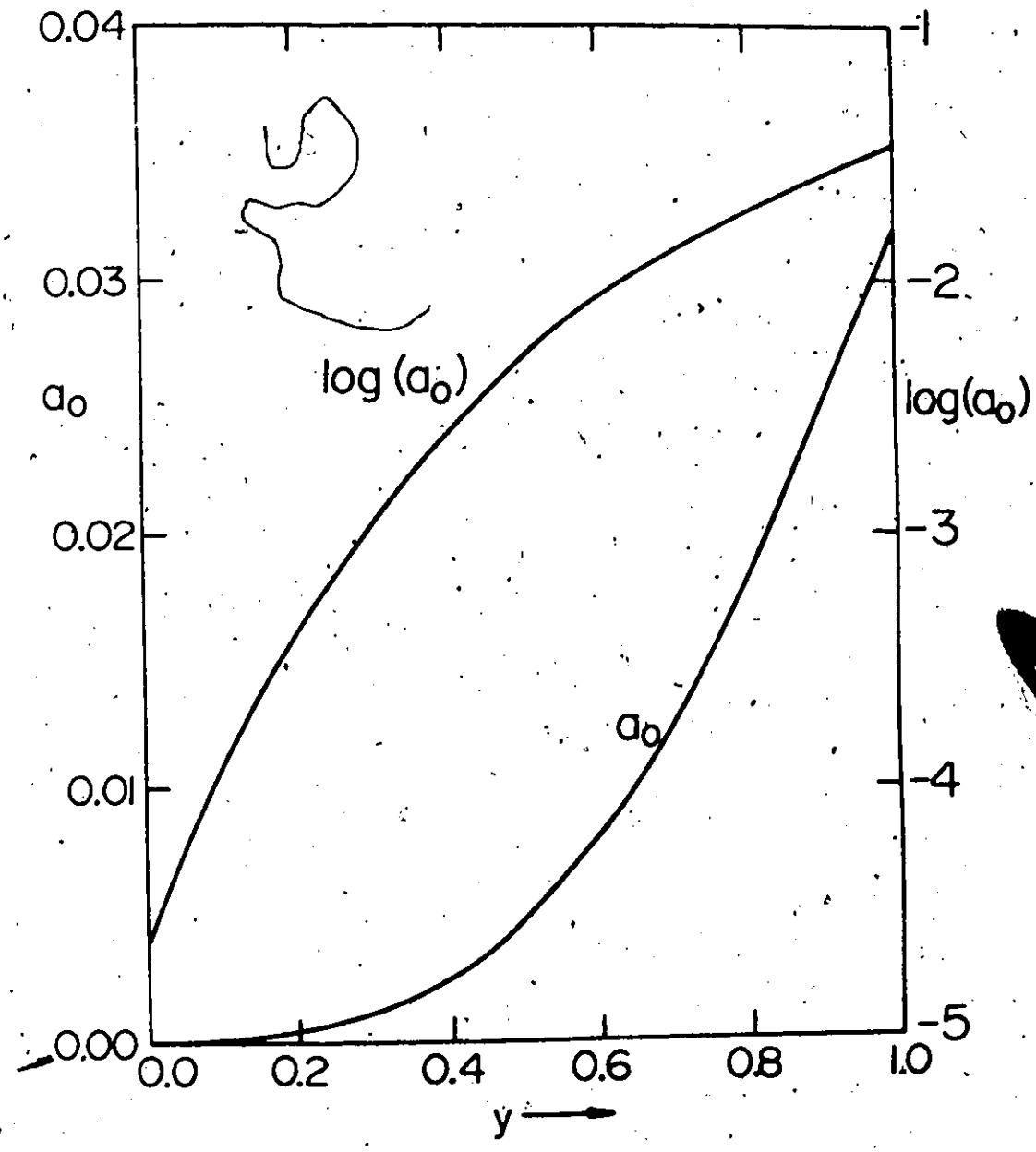

Fig. 9-11

Oxygen activity profile in (Co,Fe)O scale formed on the Co-10% Fe alloy at 10^{-3} atm oxygen pressure

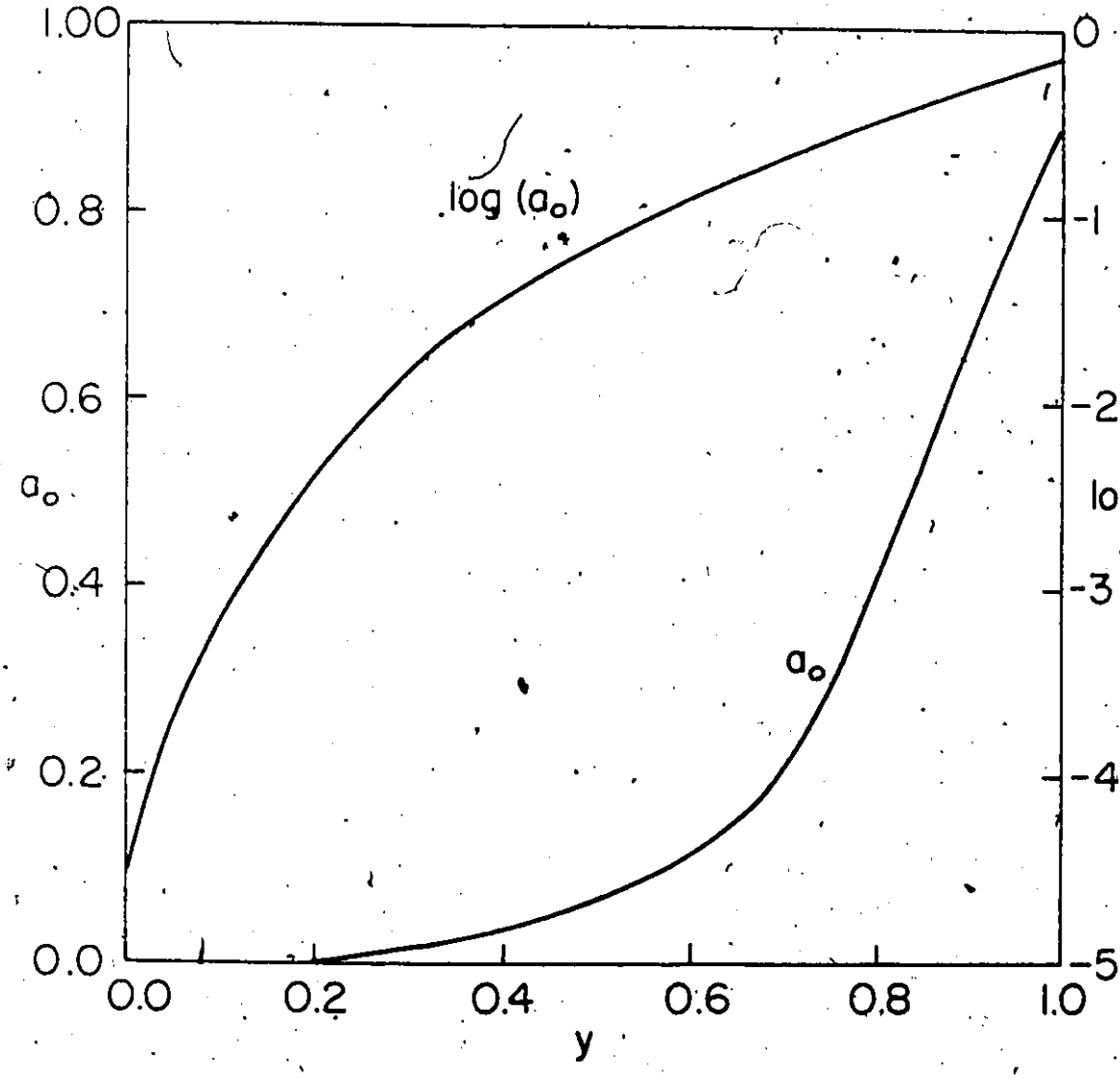

Fig. 9-12

Oxygen activity profile in (Co,Fe)O scale formed on the Co-10% Fe alloy at 1 atm oxygen pressure

Table 9-1

Extrapolated values* of ξ at the oxide-gas interface

Nominal Concentration of Iron in Alloy[%]	ξ'' Pressure of Oxygen in Reaction Atmospheres				
	10^{-4} atm	10^{-3} atm	10^{-2} atm	10^{-1} atm	1 atm
1	0.015	0.016	0.011	0.008	0.006
2	0.031	0.032	0.024	0.017	0.013
4	0.062	0.064	0.051	0.032	0.025
6	0.087	0.091	0.073	0.050	0.041
8	0.114	0.121	0.103	0.065	0.048
10	0.144	0.152	0.126	0.082	0.066

*Error ±5%

Table 9-2

Iterated values* of ξ at the alloy-oxide interface

Nominal Concentration of Iron in Alloy[%]	ξ' Pressure of Oxygen in Reaction Atmosphere				
	10^{-4} atm	10^{-3} atm	10^{-2} atm	10^{-1} atm	1 atm
1	0.0063	0.0062	0.0063	0.0063	0.0062
2	0.013	0.013	0.013	0.013	0.012
4	0.025	0.024	0.026	0.025	0.025
6	0.038	0.037	0.038	0.038	0.038
8	0.052	0.051	0.051	0.051	0.051
10	0.065	0.065	0.065	0.065	0.065

*From numerical integration yielding ξ'' equal to ξ'' from Table 9-1

Table 9-3

Nominal Concentration of Iron in Alloy[%]	a_0'' (atm$^{\frac{1}{2}}$)		$\left(\frac{d\xi}{dy}\right)_{y=1}$	
	Experimental	Iterated	Calculated from Eq. (9.15)	Iterated
1	0.010	0.006	0.015	0.016
2	0.010	0.004	0.032	0.034
4	0.010	0.011	0.057	0.056
6	0.010	0.013	0.080	0.076
8	0.010	0.008	0.103	0.107
10	0.010	0.005	0.126	0.140

Table 9-4

Nominal Concentration of Iron in Alloy[%]	a_0'' (atm$^{\frac{1}{2}}$)		$\left(\frac{d\xi}{dy}\right)_{y=1}$	
	Experimental	Iterated	Calculated from Eq. (9.15)	Iterated
1	0.03	0.02	0.017	0.018
2	0.03	0.01	0.032	0.038
4	0.03	0.05	0.061	0.056
6	0.03	0.04	0.091	0.087
8	0.03	0.08	0.118	0.102
10	0.03	0.03	0.147	0.144

Table 9-5

Nominal Concentration of Iron in Alloy[%]	a_0'' (atm$^{\frac{1}{2}}$)		$(\frac{d\xi}{dy})_{y=1}$	
	Experimental	Iterated	Calculated from Eq.(9.15)	Iterated
1	0.10	0.07	-0.014	-0.015
2	0.10	0.09	-0.027	-0.027
4	0.10	0.16	-0.048	-0.045
6	0.10	0.08	-0.072	-0.073
8	0.10	0.18	-0.094	-0.086
10	0.10	0.19	-0.105	-0.095

Table 9-6

Nominal Concentration of Iron in Alloy[%]	a_0'' (atm$^{\frac{1}{2}}$)		$(\frac{d\xi}{dy})_{y=1}$	
	Experimental	Iterated	Calculated from Eq.(9.15)	Iterated
1	0.31	0.44	-0.039	-0.037
2	0.31	0.38	-0.061	-0.058
4	0.31	0.21	-0.113	-0.119
6	0.31	0.19	-0.148	-0.159
8	0.31	0.39	-0.195	-0.189
10	0.31	0.53	-0.229	-0.2117

Table 9-7

Nominal Concentration of Iron in Alloy[%]	a_0'' (atm$^{\frac{1}{2}}$)		$(\frac{d\xi}{dy})_{y=1}$	
	Experimental	Iterated	Calculated from Eq.(9.15)	Iterated
1	1.00	0.75	-0.047	-0.083
2	1.00	0.51	-0.079	-0.053
4	1.00	1.38	-0.127	-0.121
6	1.00	1.60	-0.171	-0.159
8	1.00	1.11	-0.221	-0.218
10	1.00	0.90	-0.262	-0.266

Table 9-8

The position of the maximum* in ξ profile and corresponding oxygen potentials

Oxygen pressure in reaction atmosphere [atm]	Nominal iron content in alloy [%]	y_m Position of the maximum in ξ profile	Log pO_2 at y_m in oxygen potential gradient
0.01	1	0.52	-2.46
0.01	2	0.53	-2.31
0.01	4	0.49	-2.14
0.01	6	0.55	-2.62
0.01	8	0.51	-2.30
0.01	10	0.50	-2.23
0.10	1	0.62	-2.66
0.10	2	0.63	-2.07
0.10	4	0.62	-2.42
0.10	6	0.65	-2.78
0.10	8	0.63	-2.16
0.10	10	0.65	-2.66
1.00	1	0.78	-2.43
1.00	2	0.80	-2.58
1.00	4	0.81	-2.77
1.00	6	0.79	-2.85
1.00	8	0.82	-2.78
1.00	10	0.80	-2.46

*The average error in estimation of the position of maximum $y_m \pm 0.5$ which corresponds approximately to the deviation in log $pO_2 \pm 0.25$.

various approximations and experimental errors in measuring k_p's and the interface concentrations, the correspondence of measured and calculated profiles is satisfactory. Calculated and measured profiles correspond in both magnitude and form.

The deviations of a_0'' from the experimental value set by the oxygen pressure in the atmosphere appear to be rather serious, in some instances up to 50%. However, one has to bear in mind that the oxygen activity gradient across the scale encompasses an activity change of at least five orders of magnitude. Moreover, the cation fluxes are proportional to $\frac{d\ell n a_0}{dy}$ and not to $\frac{da_0}{dy}$. Consequently, the error in the a_0 profile is relatively low and is in accordance with the overall accuracy of the calculations. To support this assertion, one notes from Table 9-3 to 9-7 that the values of $(\frac{d\xi}{dy})_{y=1}$ calculated from Eq. 9.15 using experimental a_0'' and iterated values in the process of integration are in very good agreement. Thus, the relative deviations of iterated a_0'' do not have an important effect on the concentration gradient.

9.6 Discussion

Agreement between the theoretical calculations and the experimental results (Fig. 9-1 to 9-10) may be regarded as worthwhile support for the validity of Wagner's general treatment of binary alloy oxidation. Furthermore, the present analysis also serves to confirm the assumptions which are made regarding the nature of cobaltowüstite-(Co,Fe)O in Section 5.4.2.

Existence of uneven distributions of cations in oxide scales leads to uphill diffusion phenomena, when one of the cations is diffusing against its concentration gradient. In general, one would expect iron or cobalt

to diffuse down its own gradient. But this situation is impossible since both iron and cobalt are on the same sublattice and a decrease in concentration of one would always cause a corresponding increase in concentration of the other. This means, that no cation gradients in the oxide would be possible other than that due to nonstoichiometry, if diffusion occurs, since there is no source of either cobalt or iron in the oxide scale.

The present treatment of the problem eliminates this limitation by taking into account thermodynamic interactions between the components. This can be demonstrated by considering Eqs. 3-30 and 3-31 and the notation from Sec. 9.3 for the cations. We see that the first part of the equations describes diffusion down the activity gradient of metal cations. Since CoO-FeO solid solutions exhibit Henrian behaviour, the term $\frac{d\ell na}{d\xi}$ is always positive. Positive values of $\frac{d\xi}{dx}$ or $\frac{d\xi}{dy}$ would then lead to a negative diffusion flux. However, the second term in Eqs. 3-30 and 3-31 must be numerically greater and positive for a positive diffusion flux of J_{Fe} and J_{Co}. From this it is obvious that uphill diffusion against a metal concentration gradient is possible, but only in the presence of a sufficient oxygen activity gradient to overcome the effect of the first term.

Both cations diffuse through the oxide scale under the same oyygen activity, or vacancy concentration gradient. A relatively minor difference in jump frequencies of cobalt and iron cations results in a very significant enrichment of the more mobile constituent away from the alloy-oxide interface. The parameter p, which represents the ratio of the cation jump frequencies was used in calculations as a function of oxygen pressure. Fig. 5-10 shows and Table 5-4 lists the values of p obtained as a ratio of tracer-diffusion coefficients from the results by Crow.[85] At 1200°C the value of

p is ∿1.6 in the pressure range of oxygen from 10^{-4} to 10^{-3} atm. However, the parameter p does not remain constant and gradually changes the value to ∿0.6 at 10^{-1} atm. The value then stays constant up to 1 atm. This fact, that $f(p_{O_2})$, was taken into account in the general diffusion equations from Section 3.4.3. They were modified in Section 9.3 to yield Eqs. (9.11) and (9.13). These equations were used in numerical calculations of the concentration profiles in the scales. It was necessary to consider $p = f(p_{O_2})$ to explain the changes in the shape of the iron concentration profiles.

Two types of ξ profiles were observed in and calculated for the (Co,Fe)O scales forming on alloys containing up to 10% Fe in oxygen atmospheres with pressures ranging from 10^{-4} to 1 atm. In scales at the pressures from 10^{-4} to 10^{-3} atm the iron concentration is increasing monotonically towards the outer interface. The profile at 10^{-3} atm was more steep due to the increased oxygen activity gradient across the scale. The increase of oxygen pressure to 10^{-2} atm leads to the profile with a pronounced maximum. The appearance of the maximum in the ξ profile coincides with the change in the value of p. The maximum shifts with increasing oxygen pressure in the reaction atmosphere toward the centre of the scale. It is noteworthy that of the maxima in the profiles in scales formed at 10^{-2} to 1 atm of oxygen pressure corresponds to the value of $\log p_{O_2} \approx -2.3$ ($\ln a_O \approx -1.0$) on the oxygen activity profile. The value of p at this pressure is ≈1.0. This coincidence of the maximum in the ξ profile at the oxygen potential for $p \approx 1.0$ offers an additional substantiation to the adopted assumption that "bell type" concentration profiles are primarily due to the change in the mobilities of the cations.

Concentration profiles similar to those observed at low oxygen pressures (monotonic increase of iron concentration towards the outer interface) have been observed in oxide scales on Ni-Co,[124,125] Ni-Cr,[15] Ni-Fe[126,127] and Fe-Mn[128] alloys. The analysis involving ternary diffusion in conjunction with compositional, diffusional and thermodynamic results gave a consistent description of the oxidation phenomena. The analysis adopted in these investigations based upon ternary diffusion equations, nevertheless, is to be regarded as a simplified empirical description of the oxidation phenomena. A more fundamental analysis cannot be attempted until additional definitive knowledge becomes available on the structures, thermodynamics and mobilities of the lattice defects in solid solutions of ternary oxides.

CHAPTER X

CONCLUSIONS

The following conclusions can be presented as a result of this experimental investigation and theoretical analysis carried out on the oxidation properties of cobalt-iron alloys in oxygen atmospheres at 1200°C:

(1) The oxidation kinetics of cobalt-iron alloys with iron contents up to 70% exposed to oxygen over the pressure range 10^{-4} to 1 atm at 1200°C obey parabolic kinetics.

(2) The parabolic oxidation rate increases with increasing oxygen pressure in the reaction atmosphere. The change in reaction rate as a function of oxygen potential is most pronounced in the alloy composition range from 0 to 10% Fe. Alloys of higher iron content were less sensitive to the change in oxygen pressure.

(3) Iron additions cause a linear increase in the parabolic oxidation rate up to 10% Fe in the alloys. Further increases in the iron content in alloys cause a decrease in the oxidation rate. The extent of the iron composition range, where this decrease occurs is a function of oxygen potential in the reaction atmosphere; it is between 10 to 20% and 10% to 40% for 1 atm and 10^{-4} atm, respectively. Following this transition range iron additions to the alloys cause a moderate regular increase in oxidation rate.

(4) There are two distinct types of scales formed on cobalt-iron alloys exposed to oxygen atmospheres at 1200°C. Alloys with iron content

up to 10% exhibit one-phase (Co,Fe)O scale formation with negligible internal oxidation. This type of oxidation behaviour falls under Class II_B^1 of the general classification of alloy oxidation modes. The reaction product for alloys containing more than 10% Fe was a two-phase scale composed of (Co,Fe)O and $(Co,Fe)_3O_4$ with a small degree of internal oxidation. The oxidation mode describing this type of oxidation behaviour under the general classification is II_B^2.

(5) A direct correlation was found between the morphological development of scales and the oxidation kinetics. A region of linearly increasing oxidation rate with increasing iron concentration corresponded to single-phase scale formation. A second region of decreasing rate corresponded to two-phase scale formation with a discontinuous $(Co,Fe)_3O_4$ phase imbedded in the (Co,Fe)O scale. The third region of a moderate increase in oxidation rate with increasing iron content in the base alloy corresponded again to two-phase scale formation. However, the spinel phase formed a continuous layer on top of the (Co,Fe)O layer. The decrease in the rate of oxidation in the second and third regions was due to a blocking effect on diffusion by the $(Co,Fe)_3O_4$ phase in (Co,Fe)O since the diffusion rate in $(Co,Fe)_3O_4$ is lower than in the (Co,Fe)O phase.

(6) Concentration profiles for the metal distribution in the solid phases of reacted alloy specimens were measured by the electron microprobe technique. In the region for formation of single-phase (Co,Fe)O scales on alloys containing up to 10% iron, no pronounced concentration profiles were found in the base alloys. However, the cation concentration in (Co,Fe)O varied across the scale. Iron concentration increased with

increasing distance from the alloy-oxide interface. The increase was monotonic in scales formed at 10^{-4} and 10^{-3} atm. A maximum in the iron profile appeared in scales formed at higher pressures. The position of the maximum is a function of the oxygen potential in the reaction atmosphere. With increasing oxygen pressure, the maximum was observed to shift toward the centre of the (Co,Fe)O scale. The measured concentration profiles were found to be time invariant in y-space.

(7) The parabolic kinetics and the time invariant concentration profiles in y-space suggest that oxidation of cobalt-iron alloys with iron contents up to 10% is a steady state process and conditions of local equilibrium prevail at the interfaces and across the scale.

(8) A diffusion model based upon equations derived by Wagner[15] for metal transport through a scale under chemical activity gradients was invoked to correlate the kinetics and the concentration profiles. The modified diffusion equations were numerically solved to yield the normalized metal profiles with the boundary conditions from present experiments. The good agreement between the calculated and measured normalized metal profiles demonstrated that the theoretical analysis adopted in this work is consistent with actual physical and chemical processes occurring during the course of oxidation.

APPENDIX A

SUGGESTION FOR FUTURE WORK

A ternary diffusion model for diffusion controlled oxidation of binary alloys based on the concept of local equilibrium and ternary diffusion theory was used successfully to describe the one phase formation on metals ranging from chromium to nickel in the first transition series. Five combinations of metals Ni-Co, Ni-Cr, Ni-Fe, Fe-Mn and Co-Fe were analysed using the above mentioned model. A reasonable agreement was found between the theory and experiments in spite of serious lack of accurate and reliable data on thermodynamic, transport and defect properties of mixed oxides. There remains, nevertheless, a wide open field for investigations of these properties in concentrated solid solutions of transition metal oxides at elevated temperatures. Similar lack of data was found for solid solutions of other metal oxides. Furthermore, theoretical analysis based upon correlating diffusion and defect structure is in only the early stages of development since experimental data are only recently appearing in the scientific literature.

It would appear that the original Wagner's treatment[15] of the diffusion model for the formation of single phase scales can be extended to describe multilayer scale formation and its application to suitable experimental systems.

APPENDIX B

ERRORS IN EXPERIMENTS AND CALCULATIONS

The sources of experimental errors involved in the quantitative measurements of some physical parameters in this work will be discussed along with the limitations of the instruments and techniques used.

1. Oxidation Kinetics

The recorded oxygen uptake on the Ainsworth semiautomatic microbalance is expressed as weight gain vs. time. Vibration, oxygen flow in the reaction chamber, and electromagnetic fields inside the furnace caused small sample oscillations on the chart read-out. The maximum oscilation was ±0.25 mg. This represents a negligible error in determination of the weight gain especially in the intermediate time periods of the oxidation process. The errors associated with the initial unrecorded period of reaction were effectively eliminated by weighing the specimens before and after oxidation and plotting the weight gain curves as described in Chapter VII.

2. Parabolic Oxidation Rate Constants

From the slopes of weight gain curves plotted in parabolic form, the values of the parabolic oxidation rate constant were evaluated. The errors in k_p determination are directly related to the degree of experimental reproducibility. The factors which influence experimental reproducibility are: accuracy of temperature and oxygen pressure regulation, size of the sample, position of the sample in hot zone, etc. All these factors

are reflected in the error of the k_p evaluations (Tables 7-1 to 7-4), which is in the range from 0.5% to 10% from the arimethical average values.

3. Concentration Profiles

The precision of the concentration profile determinations from cross-sectioned oxidized samples was limited by the detection parameters of the electron probe microanalyzer and influenced by all the factors discussed in Chapters VI and IX. Figs. (7-29(a)) to (7-30(e)) show the experimental scatter. A "curve of best fit" was drawn through the experimental points, using the freehand method.[130]

The second estimate of the actual profile was obtained from the solutions of Eq. (9.11), (9.13) and (9.16) by numerical integration. This procedure was highly accurate since Hamming's predictor-corrector method allows an estimate of local truncation error at each integration step. The procedure for step size adjustment was built into the program, which assured the optimal length of integration interval and kept the truncation error under the preset tolerance. The value of the tolerance $\varepsilon = 0.0001$ was chosen in order that the last significant digit in the smallest value of the dependent variable was at least one order of magnitude higher. The rounding errors were insignificant since the CDC 3600 computer can handle much smaller numbers than those involved in present calculations. Hence, the overall errors arising from the computational procedure were insignificant. The main source of errors in these calculations were the data from the literature in the form of constants and parameters, and estimates of the interfacial concentration of FeO in cobaltowüstite.

The variance in concentration profiles was characterized by a standard deviation in ξ calculated from the estimates of the actual concentration in the normal fashion. The standard deviation from the "best fit curve" drawn through the experimental points, σ_ξ^{exp}, was taken as an error estimate in the measured profiles. This value is compared with the standard deviation, $\sigma_\xi^{theor.}$, in ξ measured by point count method from the numerically calculated profiles. It is apparent from the Figs. (9.1) to (9.10) that the two estimates of actual concentration profiles are closely comparable in size and shape. The standard deviations are in similar agreement, e.g., in case of ξ-profile in scales formed on Co-10% Fe at 10^{-3} atm O_2 $\sigma_\xi^{exp} = \pm 0.0065$ $\sigma_\xi^{theor.} = \pm 0.0076$ and in scales formed at 1 atm O_2.

$$\sigma_\xi^{exp} = \pm 0.0069 \qquad \sigma_\xi^{theor.} = \pm 0.0090$$

It could be concluded from these facts that computational procedure yields an estimate of ξ as accurate as the experimental determinations.

APPENDIX C

COMPUTER PROGRAM FOR CALCULATIONS OF CONCENTRATION PROFILES IN COBALTOWUSTITE SCALES

In this appendix, the computer program is described for numerical integration of Eqs. (9.11), (9.13) and (9.16). The purpose of the numerical calculations is to obtain an approximate solution to the system of diffusion equations with initial values. The results of the calculations are numerical values of ξ, a_O and $\frac{d\xi}{dy}$ as a function of y across the entire cobaltowüstite scale. This computation procedure was used as the major part of the iteration loop described in Chapter IX.

The computer program, written in Fortran, utilises the HPCG subroutine from IBM's Scientific subroutine package.[129] This subroutine uses Hamming's modified predictor-corrector method for solution of a general system of first-order ordinary differential equations with given initial values. The discussion of the method will be confined to the general description, since the mathematics of this method is inherently involved and would be out of the scope of this work to present it. This stable fourth-order integration procedure requires the evaluation of the differentials of functional values only per step. This is a great advantage compared with other methods of the same order of accuracy, especially the Runge-Kutta method, which requires the evaluations four times per step. Another advantage is that at each step the calculation procedure gives an estimate for the local truncation error; thus the procedure is able, without a significant amount of calculation time, to

choose and change the step size h. The estimate of the truncation error is constantly compared with a given tolerance (in program upper error bound). If the estimate of truncation error is greater than the tolerance, the integration step size is halved and the procedure computes a new value of the function at y. The estimate of truncation error for this value is again compared with the given tolerance. If it is smaller, the new computed value of the function at given y is assumed to be correct. This procedure gives a very good control over the truncation error in calculations. It has been demonstrated[129] previously that the procedure does not exceed a global relative error approximately equal to the given tolerance used in calculations. It is also very important that the starting values be accurate as possible, becuase errors in these values may increase during the computations. The accuracy of the starting values calculated by Runge-Kutta is ensured by the similar procedure of step size adjustment as in corrector-predictor method.

The entire input of the procedure is:

1. Lower and upper bound of the integration interval (y' = PRMT(1), and y" = PRMT(2)), initial step size h of independent variable (PRMT(3)), and upper error bound ε of the local truncation error (PRMT(4)).

2. Initial values of the dependent variables (ξ' = Y(1), $\ln a_0'$ = Y(2) and $(\frac{d\xi}{dy})_{y=0}$ = Y(3)) and error weights for the local truncation error in each component of the dependent variables.

3. The number of differential equations in the system (n = NDIM).

4. Two external subroutine subprograms, one is for computation of the $\frac{d\xi}{dy}$, $\frac{d\ln a_0}{dy}$ and $\frac{d^2\xi}{dy^2}$, the right-hand sides of Eqs. (9.11), (9.13) and (9.16), respectively (SUBROUTINE FCT). The second one is output subroutine

for flexibility in output (SUBROUTINE OUTP).

5. In auxiliary storage array named AUX with 16 rows and n columns.

Output is done in the following way. If a set of approximations to the dependent variables is found to be of sufficient accuracy, it is handed, together with y, derivatives of dependent variables, step size and number of bisections to the output subroutine (SUBROUTINE OUTP). This subroutine prints out the results.

The program used to calculate the concentration profile in the cobaltowüstite scale formed on 10% Fe alloy at 10^{-3} atm is shown in Table C1 with output data in Table C2 for illustration.

Table C1

Computer program used for numerical integrations

```
*************************************************************

MAIN PROGRAM
************

*************************************************************
USED SYMBOLS
PRMT(1)=LOWER BOUND OF THE INTEGRATION INTERVAL (Y=0.0)
PRMT(2)=UPPER BOUND OF THE INTEGRATION INTERVAL (Y=1.0)
PRMT(3)=INITIAL INCREMENT OF Y (STEP SIZE)
PRMT(4)=ERROR BOUND ADJUSTING THE STEP SIZE
Y(1)=NATURAL LOGARITMUS OF OXYGEN ACTIVITY
Y(2)=MOLAR FRACTION OF FEO IN COBALTOWUSTITE
Y(3)=SLOPE OF THE CONCENTRATION PROFILE
DERY(1)=ERROR WEIGHT OF Y(1)
DERY(2)=ERROR WEIGHT OF Y(2)
DERY(3)=ERROR WEIGHT OF Y(3)
P=CATION MOBILITY RATIO
DP=FIRST DERIVATIVE OF P=F( OXYGEN ACTIVITY )
NDIM=NUMBER OF EQUATIONS IN SYSTEM

*************************************************************
DIMENSION PRMT(5),DERY(3),Y(3),AUX(16,3)
EXTERNAL FCT,OUTP
PRMT(1)=0.0
PRMT(2)=1.0
PRMT(3)=0.01
PRMT(4)=0.0001
DERY(1)=0.4
DERY(2)=0.4
DERY(3)=0.2
NDIM=3
Y(1)=-10.6
Y(2)=0.065
Y(3)=-0.0634
CALL HPCG (PRMT,Y,DERY,NDIM,IHLF,FCT,OUTP,AUX)
STOP
END

*************************************************************

SUBROUTINE OUTP
***************

*************************************************************
F=0.0
IF(X.EQ.F) GO TO 21
RETURN
21 F=F+0.1
WRITE(6,20) X,Y(1),Y(2),Y(3),DERY(1),DERY(2),DERY(3),PRMT(4)
20 FORMAT(8F12.3)
RETURN
END

*************************************************************
```

(CONTINUE..)

```
*****************************************************************

SUBROUTINE FCT
**************

*****************************************************************
USED SYMBOLS
DK=PARABOLIC OXIDATION RATE CONSTANT (EQ.9.10 )
Y=DIMENSIONLESS THICKNESS OF THE SCALE Y
RM=1.0
RN=M FROM EQ.5.3
RN=N FROM EQ.5.3
DERY(1)=EQ.9.11
DERY(2)=EQ.9.16
DERY(3)=EQ.9.13

*****************************************************************
SUBROUTINE FCT (X,Y,DERY)
DIMENSION Y(3),DERY(3)
DK=0.2478
P=1.5
DP=0.0
RM=1.0
RN=0.15
A1=(P-1.0)
A2=(P-1.0)*Y(2)
A3=1.0+A2
A4=DK/((Y(2)**1)*(EXP(RN*Y(1))))
A5=A4+A1*Y(3)
A6=A5/A3
DERY(1)=A6
DERY(2)=Y(3)
X1=((RM+1.0)*(Y(3))+RN*Y(2)*A6)+Y(2)*DP/P
X2=Y(3)/Y(2)-A6
X22=((X)*A4*Y(3))/(Y(2)*P)
X3=(A6/A3)*(Y(3)*A1+DP*Y(2))
X33=(DP*Y(3))/A3
X4=(Y(3)*Y(3))/(Y(2)*Y(2))
X5=(A4/A3)*((RM/Y(2))*Y(3)+RN*A6)
X6=(1.0/Y(2))-(A1/A3)
DERY(3)=(X4-X22-((X1*X2)/Y(2))-X5-X3+X33)/X6
RETURN
END

*****************************************************************
```

Table C2

Computer output (calculated profile for Co-10% Fe alloy at 10^{-3} atm O_2)

y	$\ell n a_O$	ξ	$\frac{d\xi}{dy}$	$\frac{d\ell n a_O}{dy}$	$\frac{d^2\xi}{dy^2}$	accuracy tolerance
.000E+00	-.106E+02	.650E-01	.340E-02	.178E+02	+.512E-01	.100E-03
.100E+00	-.907E+01	.657E-01	.122E-01	.139E+02	+.131E-01	.100E-03
.200E+00	-.782E+01	.677E-01	.302E-01	.112E+02	+.229E+00	.100E-03
.300E+00	-.681E+01	.720E-01	.567E-01	.907E+01	+.289E+00	.100E-03
.400E+00	-.599E+01	.792E-01	.853E-01	.731E+01	+.269E+00	.100E-03
.500E+00	-.533E+01	.889E-01	.109E+00	.589E+01	+.193E+00	.100E-03
.600E+00	-.480E+01	.101E+00	.124E+00	.480E+01	+.107E+00	.100E-03
.700E+00	-.436E+01	.113E+00	.131E+00	.398E+01	+.337E+01	.100E-03
.800E+00	-.400E+01	.127E+00	.132E+00	.336E+01	-.107E-01	.100E-03
.900E+00	-.369E+01	.140E+00	.129E+00	.290E+01	-.418E-01	.100E-03
.100E+01	-.341E+01	.152E+00	.124E+00	.254E+01	-.607E-01	.100E-03

REFERENCES

1. G. Tamman, Z. Anorg. Chem., 111, 78 (1920).
2. N.B. Pilling, and R.E. Bedworth, J. Inst. Metals, 29, 529 (1923).
3. C. Wagner, Z. Phys. Chem., (B), 21, 25 (1933).
4. W.W. Smeltzer, R.R. Haering and J.S. Kirkaldy, Acta Met., 9, 880 (1981).
5. J.M. Perrow, W.W. Smeltzer and J.D. Embury, Acta Met., 16, 1206 (1968).
6. J. Moreau and J. Bernard, L'Oxydation des Metaux, Vol. 1., 318, Gauthier-Villars, Paris, 1962.
7. G.C. Wood, Oxidation of Metals, 2, 11 (1970).
8. L. Onsager, Ann. N.Y. Acad. Sci., 46, 241 (1945).
9. J.E. Lane, and J.S. Kirkaldy, Can. J. Phys., 42, 1643 (1964).
10. L.S. Darken, Atom Movements, ASM Publication, Cleveland, 1 (1951).
11. N.F. Mott, and R.W. Gurney, Electronic Processes in Ionic Crystals, Claredon Press, Oxford (1950).
12. C. Wagner, Thermodynamics of Alloys, Addison-Wesley Press (1952).
13. J. Stringer, Met. Rev., 11, 113 (1966).
14. K. Denbigh, The principles of chemical equilibrium, Cambridge University Press (1968).
15. C. Wagner, Corr. Sci., 9, 91 (1969).
16. F.N. Rhines, Trans. AIME, 137, 246 (1940).
17. D.E. Thomas, Trans. AIME, 191, 925 (1959).
18. J.B. Clark and F.N. Rhines, Trans. ASM, 51, 199 (1959).
19. J.S. Kirkaldy and L.C. Brown, Can. Met. Quart., 2, 89 (1963).
20. A.D. Dalvi and D.E. Coates, Oxid. Metals, 5, 113 (1972).

21. F.N. Rhines, W.A. Johnson and W.A. Anderson, Trans AIME, 147, 205 (1942).

22. L.S. Darken, Trans AIME, 150, 157 (1968).

23. C. Wagner, Z. Elektrochem., 63, 772 (1959).

24. C. Wagner, Corrosion Sci., 8, 887 (1968).

25. J.S. Kirkaldy in Oxidation of Metals and Alloys, (ASM Monograph, Cleveland, 1971), pp. 101-114.

26. J.S. Kirkaldy, Can. Met. Quart., 8, 35 (1969).

27. C. Wagner, J. Electrochem. Soc., 103, 571 (1956).

28. C. Wagner, Z. Elektrochem., 63, 950 (1959).

29. D.I. Coates and J.S. Kirkaldy, Trans ASM, 62, 426 (1969).

30. Phase diagrams for ceramists, National Bureau of Standards, Published by American Ceramic Society.

31. N.N. Greenwood, Ionic Crystals, Lattice defects and Nonstoichiometry, Butterworths, London, (1968).

32. L.S. Darken and R.W. Gurry, J. Am. Chem. Soc., 67, 1398 (1945); 68, 798 (1946).

33. K. Hauffe and Pfeiffer, Z. Metallk., 44, 27 (1953).

34. P. Vallet and P. Raccah, Mem. Sci. Rev. Met., 62, 1 (1965).

35. P. Vallet, C.r. hebd. Seanc. Acad. Sci., Paris, 261, 4396 (1966).

36. B. Swaroop and J.B. Wagner, Trans. AIME, 239, 215 (1967).

37. G.B. Barbi, J. Phys. Chem. Solids, 68, 2912 (1964).

38. H.F. Rizzo, R.S. Gordon, and I.B. Cutler, Symposium on "Mass Transport in Oxides", National Bureau Publication 296, Washington, D.C., August 1968.

39. I. Bransky and A.Z. Hed, J. Am. Cer. Soc., 57, 231 (1968).

40. H.G. Sockel and H. Schmalzried, Ber. Bunsengesellschaft, 72, 747 (1968).

41. B.E.F. Fender and F.D. Riley, J. Phys. Chem. Solids, 30, 793 (1969).

42. L. Himmel, R.F. Mehl and C.E. Birchenal, Trans AIME, 197, 822 (1953).

43. H.A. Horgard and P.N. Jensfelt, Jernkontorets Ann., 140, 467 (1956).

44. W.L. Roth, Acta Cryst., 13, 140 (1960).

45. J. Smuts, J. Iron Steel Inst., 204, 237 (1966).

46. F. Koch and J.B. Cohen, Acta Cryst., B25, 275 (1969).

47. J. Manenc, J. Bourgeot and J. Benard, Compt. Rend. Acad. Sci., Paris, 258, 4528 (1964).

48. E.R. Jette and F. Foote, J. Chem. Phys., 1, 29 (1969).

49. P. Kofstad and A.Z. Hed, J. Electrochem. Soc., 115, 102 (1968).

50. G.G. Libowitz, Symposium on "Mass Transport in Oxides", National Bureau of Standards, Special Publication No. 296, Washington, D.C., 1968.

51. R.E. Carter and Richardson, Trans. AIME, 200, 1244 (1954).

52. Ph. Desmarescaux, J.P. Bocquet, and P. Lacombe, Bull. Soc. Chim., France, 15, 1106 (1965).

53. J. Smiltens, J. Am. Chem. Soc., 79, 4877 (1957).

54. O.N. Salmon, J. Phys. Chem., 65, 550 (1961).

55. H. Schmalzried, Z. Phys. Chem. Neue Folge, 31, 184 (1962).

56. V.I. Izvekov, N.S. Gorbunov, and A.A. Babad-Zakhrapin, Fiz. Metal Metalloved., 14, 195 (1962).

57. R. Lindner, Arkiv. Kemi, 4, 381 (1952).

58. W.D. Kingery, D.C. Hill and R.P. Nelson, J. Am. Cer. Soc., 43, 473 (1960).

59. W.C. Hagel, Trans AIME, 236, 179 (1966).

60. M.H. Davies, M.T. Simnad, and C.E. Birchenall, Trans. AIME., 191, 889 (1951).

61. J. Paidassi, Rev. Met., LIV, 569 (1957).

62. N.G. Schmahl, H. Baumann, and H. Schenck, Arch. Einsenhutten., 29, 83 (1958).

63. L. Himmel, R.F. Mehl, and C.E. Birchenall, Trans. AIME, 197, 827 (1953).

64. W.E. Boggs, R.H. Kachik, and G.E. Pelissier, J. Electrochem. Soc., 112, 539 (1965).

65. W.E. Boggs, R.H. Kachik, and G.E. Pellissier, J. Electrochem. Soc., 114, 32 (1967).

66. M.J. Graham and M. Cohen, J. Electrochem. Soc., 116, 1430 (1969).

67. D. Caplan, M.J. Graham, and M. Cohen, Corrosion Sci., 10, 1 (1970).

68. R.J. Hussey and M. Cohen, J. Electrochem. Soc., 11, 699 (1971).

69. R.J. Hussey and M. Cohen, J. Electrochem. Soc., 11, 713 (1971).

70. J.C. Carbonnier and J. Bardotte, Mem. Sci. Rev. Met., 65, 423 (1968).

71. H. Pfeiffer and C. Laubmeyer, Z. Elektrochem., 59, 575 (1955).

72. N.G. Schmahl, H. Baumann and H. Schenck, Arch. Eisenhüttenw., 29, 147 (1958).

73. N.G. Schmahl, H. Küpperbusch, and H. Schenck, Arch. Eisenhüttenw., 34, 115 (1963).

74. A. Rahmel and H.J. Engell, Arch. Eisenhuttenw., 30, 743 (1959).

75. P. Belin, Corrosion Anti-Corrosion, 7, 384 (1959).

76. A.G. Goursat and W.W. Smeltzer, J. Electrochem. Soc., 120, 390 (1973).

77. H.J. Engel, Acta Met., 6, 439 (1958).

78. G. Natta and M. Strada, Gazz. Chim. Ital., 58, 419 (1928).

79. B. Fisher and D.S. Tannhauser, J. Chem. Phys., 44, 1663 (1966).

80. M.M. Henri Le Brusq, J.J. Oehlig, and F. Marion, C.R. Acad. Sci. Paris, 266, Series C, 965 (1968).

81. N.G. Eror and J.E. Wagner Jr., J. Phys. Chem. Solids, 29, 1597 (1968).

82. H.G. Sockel and H. Schmalzried, Berichte Bunsenges., 72, 745 (1968).

83. R.E. Carter and F.D. Richardson, Trans. AIME, 200, 1247 (1954); 203, 336 (1955).

84. W.K. Chen, N.L. Peterson, and W.T. Reeves, Phys. Rev., 186, 887 (1969).

85. W.B. Crow, "Report ARL-70-0090, Project No. 7021, Office of Aerospace Research, USAF., Wright-Patterson Air Force Base, Ohio (1970).

86. B.A. Thomson, Ph.D. Dissertation, Renssealaer Polytechnic Institute, 1962 (University Microfilms, Inc., Ann Arbor, Mich.).

87. W.K. Chen and R.A. Jackson, J. Phys. Chem. Solids, 30, 1309 (1969).

88. J.B. Holt, Proc. Brit. Cer. Soc., 11 157 (1967).

89. H. Schmalzried, Z. Phy. Chem., Neue Folge, 30, 1309 (1969).

90. C. Wagner, E. Koch, Z. Phys. Chem., B31, 439 (1936).

91. J. Paidassi, Dans Oxydation des Métaux, Vol. II, Paris, Gauthier et Villars, 1964, p. 126-132.

92. G.Wood, I. Wright and J. Ferguson, Corrosion Sci., 5, 645 (1965).

93. F. Morin and M. Rigaud, Can. Met. Quarterly, 9, 521 (1970).

94. R. Carter and F. Richardson, J. Metals, 6, 1244 (1954).

95. E. Aukrust and A. Muan, Trans. AIME, 230, 1395 (1964).

96. B.D. Roiter and A.E. Paladino, J. Am. Cer. Soc., 45, 218 (1962).

97. T. Satow, S. Kachi and K. Iwase, Sci. Rep. Res. Inst., Tohoku Univ., Ser. A., 8, 505 (1956).

98. W.C. Elis and E.S. Greiner, Trans. Am. Soc. Metals, 29, 415 (1941).

99. J. Badia, Diss. Thesis, University of Nancy, 47 (1969).

100. L. Boltzman, Ann. Physik, 53, 960 (1894).

101. C. Matano, Japan. Phys., 8, 109 (1933).

102. E. Aukrust and A. Muan, Trans. AIME, 227, 1378 (1963).

103. R. Schuhmann,Jr.,Acta Met., 3, 219 (1955).

104. R.F. Voitovich, Zhurnal Prikl. Khimii, 39, 565 (1966).

105. W. Hessenbruch and W. Rohn, Heraus Vakuumschmelze, p. 247 (1923-33).

106. L.S. Birks, Electrone Probe Microanalysis, Interscience, New York (1963).

107. R. Castaing, Adv. Electronic & Electron Phys., 13, 317 (1960).

108. T.D. McKinley, K.F.J. Heindrich and B. Whittry Editors, The Electron Microprobe, John Wiley, (1966).

109. A.D. Dalvi, The Electron Probe Microanalyser, McMaster University (1969).

110. C.A. Friskney and N. Haworth, Brit. J. Appl. Phys. Ser. 2, 1, 873 (1968).

111. C.A. Friskney and N. Haworth, J. Sci. Instr. Ser. 2, 1, 753 (1968).

112. P. Duncumb and S.J.B. Reed, Nat. Bur. Std., (U.S.) Spec. Publ. No. 298, (1968).

113. J. Philibert, X-Ray Optics and X-Ray Microanalysis, Proc. Third Int. Symp., Stanford 1962, Academic Press, N.Y. (1963).

114. P. Duncumb and P.K. Shields, in The Electrone Microprobe, 284, J. Wiley, N.Y. (1966).

115. M. Green and V.E. Cosslet, Proc. Phys. Soc., (London) 78, 1206 (1961).

116. G.S. Giggins, F.S. Pettit, Pratt & Whittney, Advanced Materials R & D Lab. Rep., No. 68-024, (1968).

117. G.C. Wood and T. Hodgkiess, Nature, 211,1358 (1966).

118. G.E. Zima, Trans. Am. Soc. Metals, 49, 924 (1957).

119. A.D. Dalvi and W.W. Smeltzer, J. Electrochem. Soc., 118, 1978 (1971).

120. F.R. Billman, J. Electrochem. Soc., 119, 1198 (1972).

121. C.A. Phalnikar, E.B. Evans, and W.M. Baldwin Jr., J. Electrochem. Soc., 103, 429 (1956).

122. D.P. White and G.C. Wood, J. Electrochem. Soc., 115, 133 (1968).

123. J.J. Van Den Broek and J.L. Meijering, Acta Met., 16, 375 (1968).

124. G.C. Wood and J. M. Ferguson, Nature, 208, 369 (1965).

125. A.D. Dalvi and D.E. Coates, Oxidation of Metals, 3, 203 (1971).

126. A.D. Dalvi and W.W. Smeltzer, J. Electrochem. Soc., 118, 1978 (1971).

127. A.D. Dalvi and W.W. Smeltzer, J. Electrochem. Soc., (in press).

128. P. Mayer and W.W. Smeltzer, J. Electrochem. Soc., 119, 626 (1972).

129. IBM, Scientific Subroutine Package, System 360, Version III.

130. M.R. Spiegel, Statistics, Shaum's Outline Series, McGraw-Hill Book Company.